

THE ROLE OF OUTER-SPHERE RESIDUES AND SUBSTRATE-BINDING AT THE 3-
MERCAPTOPROPIONIC ACID DIOXYGENASE (3MDO) ACTIVE SITE: A COMBINED
SPECTROSCOPIC AND COMPUTATIONAL INVESTIGATION

by

NICHOLAS JAMES YORK

BRAD S. PIERCE, COMMITTEE CHAIR

JOHN B. VINCENT

ELIZABETH T. PAPISH

PATRICK A. FRANTOM

RYAN M. SUMMERS

A DISSERTATION

Submitted in partial fulfillment of the requirements
for the degree of Doctor of Philosophy
in the Department of Chemistry
in the Graduate School of
The University of Alabama

TUSCALOOSA, ALABAMA

2021

Copyright Nicholas James York 2021
ALL RIGHTS RESERVED

ABSTRACT

Thiol Dioxygenases (TDOs) are non-heme iron enzymes that catalyze the O₂-dependent oxidation of thiol-bearing amino acid derivatives to their corresponding sulfinic acid. Recently, considerable work has been focused on this class of enzymes, as sulfur metabolite imbalances have been correlated with neurodegenerative disorders such as Alzheimer's, Parkinson's, and motor neuron disease. The active site of this enzyme class is comprised of a mononuclear Fe(II) bound by three protein derived histidine residues. A conserved feature among structurally characterized TDOs is a sequence of serine, histidine, and tyrosine residues adjacent to the iron active site, deemed the SHY motif. By far, the most well studied TDO is mammalian cysteine dioxygenase (CDO) which oxidizes L-cysteine to cysteine sulfinic acid with high substrate-specificity. Unlike CDO, bacterial 3-mercaptopropionate dioxygenase from *Azotobacter vinelandii* (Av3MDO) is a promiscuous TDO that oxidizes a variety of thiol substrates. Given both enzymes show similar active site geometries, the drastic difference in substrate specificity is not well understood.

This dissertation aims to address two unresolved topics among Av3MDO and TDOs in general. The first is the mode in which native substrate, 3MPA, binds to Av3MDO. Arguments have been made for both bidentate coordination through the substrate thiolate and carboxylate and monodentate through the thiolate only. Herein, crystallographic, spectroscopic, and computational studies are used to determine the mode of 3MPA coordination to the iron active site. Bidentate coordination was observed for a crystal structure of bound inhibitor, 3-

hydroxypropionic acid, which was used as a basis for computational models of bidentate 3MPA coordination. These models showed agreement with spectroscopic data using either nitric oxide or cyanide as spectroscopic probes.

The second aspect investigated is the role of the SHY motif in the active site. For *Av3MDO*, alterations to the SHY motif have been shown to drastically attenuate activity (k_{cat}), catalytic efficiency (k_{cat}/K_M), and formation of NO-bound ES complex. However, the interactions between the SHY motif and iron active site are not fully understood. Spectroscopic studies presented herein reveal the flexible hydrogen bonding capabilities of Tyr159 in the SHY motif and its direct influence on the electronic structure of the iron active site.

DEDICATION

To my wife, Jamie, who has stuck by me through three graduate schools and three states. Thanks for always being my pillar and best friend. I can't wait to see where life takes us.

To my family who have supported me from the beginning. Thank you for making me the person I am today. Also, I want to give a special acknowledgement to my abuela who recently passed away.

LIST OF ABBREVIATIONS AND SYMBOLS

| | |
|----------------|--|
| <i>Av</i> 3MDO | <i>Azotobacter vinelandii</i> 3-mercaptopropionate dioxygenase |
| 3MPA | continuous wave |
| TDO | thiol dioxygenase |
| SHY | serine-histidine-tyrosine |
| CDO | cysteine dioxygenase |
| ADO | 2-aminoethanethiol |
| 3SPA | 3-sulfinopropionic acid |
| CYS | cysteine |
| <i>Pa</i> 3MDO | <i>Pseudomonas aeruginosa</i> 3-mercaptopropionate dioxygenase |
| CA | cysteamine |
| EPR | electron paramagnetic resonance |
| DFT | density functional theory |
| CW | continuous wave |
| ESEEM | electron spin echo envelope modulation |
| HYSCORE | hyperfine sublevel correlation |
| 3HPA | 3-hydroxypropionic acid |
| NO | nitric oxide |
| CN | cyanide |
| CSA | cysteine sulfinic acid |

| | |
|--------|--|
| HT | hypotaurine |
| ES | enzyme-substrate |
| ET | ethanethiol |
| CASSCF | complete active space self-consistent field |
| NEVPT2 | n-electron state valence 2 nd order perturbation theory |

ACKNOWLEDGEMENTS

I want to thank my advisor, Dr. Brad Pierce, for taking me on as a graduate student. Your example as a professor and supervisor is one I hope to achieve myself. Thanks for always being willing to take the time to talk about data and make sure I actually know what is going on.

I thank my committee members, Professors Elizabeth Papish, John Vincent, Patrick Frantom, and Ryan Summers. Thank you all for supporting my research with enthusiasm and challenging me to approach problems from every angle.

I want to thank my lab mates, new and old. Dr. Sinjinee Sardar and Dr. Philip Palacios taught me everything I know about working in a lab. Dr. Molly Lockart taught me everything I know about pulsed EPR and re-taught me how to use the instrument every single time. I want to thank Jared Paris and Allison Schmittou for making coming into work an enjoyable experience.

I thank the Department of Chemistry and Biochemistry at UA for support throughout my time here. Coming into the program halfway through graduate school wasn't an easy process so I want to thank the graduate advisors, Dr. Frantom and Dr. Woski, who worked with me to figure out all the details. I also want to thank the Department of Chemistry and Biochemistry at UTA where I began graduate school with Dr. Pierce. I want to thank the department for the opportunity to teach students and be taught by some great professors. I would also like to thank the Journal of Biological Chemistry for allowing use published work in this dissertation.

Thank you to Dr. Tim Jackson at Kansas University for letting me spend time in your lab with your students to get a foundation for computational chemistry. Many of the findings in this

manuscript were possible because of the knowledge and skills I acquired during the short time in your lab.

Finally, I want to thank all the colleagues I've had the pleasure to meet through the years of graduate school. I've been lucky enough to go through with process with some great people around me.

CONTENTS

| | |
|---|------|
| ABSTRACT..... | ii |
| DEDICATION..... | iv |
| LIST OF ABBREVIATIONS AND SYMBOLS | v |
| ACKNOWLEDGEMENTS..... | vii |
| LIST OF TABLES..... | xii |
| LIST OF FIGURES | xiii |
| CHAPTER 1: INTRODUCTION..... | 1 |
| 1.1 Background of Thiol Dioxygenases and Av3MDO | 1 |
| 1.2 Promiscuous Reactivity and Substrate Binding of Av3MDO | 3 |
| 1.3 Role of The SHY Motif of Av3MDO..... | 4 |
| 1.4 Spectroscopic Studies of Thiol Dioxygenases..... | 6 |
| 1.5 Chapter Overview | 8 |
| Figures..... | 10 |
| References..... | 14 |
| CHAPTER 2: STRUCTURE OF 3-MERCAPTOPROPIONIC ACID DIOXYGENASE WITH A SUBSTRATE ANALOG REVEALS BIDENTATE SUBSTRATE BINDING AT THE IRON CENTER | 19 |
| 2.1 Introduction..... | 19 |
| 2.2 Experimental Procedures | 22 |
| 2.3 Results..... | 34 |
| 2.4 Discussion..... | 49 |

| | |
|--|------------|
| Figures..... | 53 |
| References..... | 63 |
| Appendix..... | 71 |
| CHAPTER 3: LOW-SPIN CYANIDE COMPLEXES OF <i>Av3MDO</i> REVEAL IMPACT OF OUTER-SPHERE SHY MOTIF..... | 92 |
| 3.1 Introduction..... | 92 |
| 3.2 Experimental Methods..... | 94 |
| 3.3 Results & Discussion..... | 100 |
| 3.4 Conclusion..... | 116 |
| Figures..... | 119 |
| References..... | 132 |
| Appendix..... | 137 |
| CHAPTER 4: SPECTROSCOPIC INVESTIGATION OF <i>Av3MDO</i> SIMULTANEOUSLY BOUND TO CYANIDE AND NITRIC OXIDE..... | 152 |
| 4.1 Introduction..... | 152 |
| 4.2 Materials and Methods..... | 154 |
| 4.3 Results..... | 159 |
| 4.4 Discussion..... | 168 |
| 4.5 Future Work..... | 171 |
| Figures..... | 173 |
| References..... | 188 |
| CHAPTER 5: CONCLUSIONS..... | 192 |
| 5.1 Substrate Binding to <i>Av3MDO</i> | 192 |
| 5.2 Role of the SHY Motif..... | 192 |
| 5.3 Future Directions..... | 193 |

| | |
|-----------------|-----|
| Figures..... | 195 |
| References..... | 196 |

LIST OF TABLES

| | | |
|-----|--|-----|
| 2.1 | Selected distances (<i>top</i>) and angles (<i>bottom</i>) of the Av3MDO- 3HPA complex (PDB accession code 6XB9) as compared to optimized DFT models of the iron active bound to 3HPA and 3MPA | 62 |
| 3.1 | Simulated EPR parameters for species of low spin ferric MDO when bound to cyanide | 130 |
| 3.2 | Fitted binding parameters for 3MPA to ferric enzyme (wild type, H157N and Y159F) and cyanide to each 3MPA -bound complex..... | 130 |
| 3.3 | Experimental and calculated <i>g</i> -values for 3MPA/CN-bound 3MDO species observed in EPR spectroscopy for wild type (1C), H157N (2C), and Y159F (3C) | 131 |
| 4.1 | Simulated EPR parameters for the (CN/NO)-bound ferrous 3MDO in wild-type and H157N variant..... | 186 |
| 4.2 | Calculated <i>g</i> -values for DFT optimized models of the (CN/NO)-bound 3MDO | 186 |
| 4.3 | Calculated hyperfine values and Euler angles for selected nuclei of DFT optimized models of the (CN/NO)-bound 3MDO | 187 |

LIST OF FIGURES

| | | |
|-----|--|-----|
| 1.1 | The crystal structure of mammalian <i>R. norvegicus</i> CDO (panel A) with L-cysteine (CYS) bound to iron (PDB code: 4IEV)..... | 10 |
| 1.2 | Illustrated structures of thiol substrates for <i>Av3MDO</i> | 10 |
| 1.3 | Panel A displays the crystal structure for <i>Rn</i> CDO, focused on the SHY motif and the Trp77 residue participating in the hydrogen bond network..... | 11 |
| 1.4 | EPR spectra of the (NO/ 3MPA)-bound <i>Av3MDO</i> $S = 3/2$ species for wild type and the H157N and Y159F variants. | 12 |
| 1.5 | EPR spectra of ferric mammalian CDO bound to substrate, CYS , and cyanide | 13 |
| 2.1 | Structural comparison of mammalian CDO and <i>Pseudomonas aeruginosa</i> <i>3MDO</i> active site | 53 |
| 2.2 | Structure of <i>Av3MDO</i> and its comparison to <i>Pa3MDO</i> | 54 |
| 2.3 | 3-hydroxypropionic acid (3HPA) inhibition of <i>Av3MDO</i> -catalyzed 3MPA -reactions...55 | 55 |
| 2.4 | An occluded active site channel in 3HPA -bound <i>Av3MDO</i> | 56 |
| 2.5 | Active site differences observed between 3HPA -bound <i>Av3MDO</i> and <i>Pa3MDO</i> | 57 |
| 2.6 | Overlay of 3HPA -bound <i>Av3MDO</i> complex (<i>transparent-green</i>) with a DFT optimized model (<i>white</i>) of the 3MPA -bound <i>Av3MDO</i> Fe(III)-site (RMSD, 0.417 Å).. | 58 |
| 2.7 | The optimized structure of the (3MPA /NO)-bound <i>Av3MDO</i> active site | 59 |
| 2.8 | CW EPR (A) and HYSCORE (B) spectra of (3MPA /NO)-bound <i>Av3MDO</i> iron-nitrosyl | 60 |
| 2.9 | Comparison of (3MPA /NO)-bound <i>Av3MDO</i> HYSCORE data (^1H region) collected at six field positions (173 – 200 mT) to simulations using parameters from the DFT optimized model..... | 61 |
| 3.1 | The crystal structures of inhibitor, 3HPA , bound <i>Av3MDO</i> (panel A) in the equatorial positions trans to His92 and His142. | 119 |

| | | |
|------|---|-----|
| 3.2 | X-band CW EPR of Fe(III)-Av3MDO (1) treated with a 20-fold molar excess of cyanide | 120 |
| 3.3 | An illustration of the species resulting from addition of substrate followed by cyanide (Path A) | 121 |
| 3.4 | Panel A . UV-vis spectra of Fe(III)-Av3MDO (1) with 3MPA (<i>red</i>) followed by addition of cyanide (<i>blue</i>) | 122 |
| 3.5 | X-band CW EPR of (3MPA)-bound Fe(III)-Av3MDO (1S) titrated with 5-, 20-, and 40-molar equivalents KCN | 123 |
| 3.6 | 3-pulse ESEEM spectrum of the (3MPA/CN)-Fe(III)-AvMDO (1C) at 292 mT | 124 |
| 3.7 | Comparison of 3-pulse ESEEM spectra of (3MPA/CN)-Fe(III)-AvMDO (1C) complex prepared in H ₂ O versus D ₂ O at magnetic fields spanning the region between <i>g</i> ₁ and <i>g</i> ₂ in the EPR spectrum | 125 |
| 3.8 | The EPR spectra of cyanide additions to the H157N variant | 126 |
| 3.9 | The EPR spectra of cyanide additions to the Y159F variant | 127 |
| 3.10 | Optimized structures of models 1 and 2 showing (3MPA/CN)-bound wild type-3MDO with Tyr159 donating a hydrogen bond to the axial bound cyanide (<i>top</i>) or the Nδ-His157 (<i>middle</i>) | 128 |
| 3.11 | The <i>g</i> -tensor orientations of both species 1C and 1B | 129 |
| 4.1 | Panel A displays the crystal structure of Av3MDO bound to thiocyanate in the axial position <i>trans</i> to His90 with two water/solvent ligands bound in the equatorial positions <i>trans</i> to His92 and His142. | 173 |
| 4.2 | CW EPR spectra of Fe(II)-Av3MDO mixed with 20x KCN and 10x NO (<i>trace A</i>) | 174 |
| 4.3 | CW EPR spectrum A displayed the mixture of 3MDO with cyanide and nitric oxide as shown above | 175 |
| 4.4 | CW EPR spectra of Fe(II) 3MDO mixed with natural abundance CN and NO (A) and ¹⁵ N-CN and NO (B) | 176 |
| 4.5 | HYSCORE spectra of (CN/NO)-bound Av3MDO | 177 |
| 4.6 | HYSCORE spectra for (CN/NO)-bound Fe(II)-Av3MDO collected at 344 mT | 178 |

| | | |
|------|--|-----|
| 4.7 | Field dependent HYSCORE spectra of (CN/NO)-bound Av3MDO (C ¹⁵ N/C ¹⁴ N) difference spectra | 179 |
| 4.8 | CW EPR spectrum (<i>trace A</i>) of the H157N (CN/NO)-bound Av3MDO variant | 180 |
| 4.9 | Schematic representation of possible orientations of the nitrosyl ligand on the His-bound facial triad of Av3MDO | 181 |
| 4.10 | DFT optimized structures for possible ligand arrangement for the (CN/NO)-bound Av3MDO (<i>S</i> = 1/2) species | 182 |
| 4.11 | Simulated HYSCORE spectra (red lines) based on calculated hyperfine couplings and Euler angles of ¹⁵ N-cyanide for the DFT optimized model NO/(CN) ₂ | 183 |
| 4.12 | Simulated HYSCORE spectra (red lines) based on calculated hyperfine couplings and Euler angles of ¹⁵ N-cyanide for the DFT optimized model NO/CN ₁₄₂ /Cl ₉₀ | 184 |
| 4.13 | Simulated HYSCORE spectra (red lines) based on calculated hyperfine couplings and Euler angles of ¹⁵ N-cyanide for the DFT optimized model NO/CN ₉₀ /Cl ₁₄₂ | 185 |
| 5.1 | Three modes of binding to 3MDO iron seen throughout this dissertation | 195 |

CHAPTER 1:
INTRODUCTION

1.1 Background of Thiol Dioxygenases and Av3MDO

Thiol dioxygenases (TDOs) are a class of enzymes with a mononuclear non-heme iron active site which catalyzes the O₂-dependent oxidation of thiol-bearing substrates (1). These enzymes are found in a wide range of organisms, including mammals, bacteria, fungi, and plants (2-5). Study of these enzymes has been encouraged by trends seen in neurological disorders such as Parkinson's disease, Alzheimer's disease, and motor neuron disease. Studies have shown links between these diseases and imbalances in cysteine metabolism (3,6,7). Imbalances in sulfur compound metabolism have also been seen in plasma for patients with autism and Down syndrome (8,9). Furthermore, sulfur oxidizing enzymes have also been shown to be of interest for medical applications such as cancer and inflammatory disease therapies and antimicrobial drugs (10-13). Structural and mechanistic investigation of these enzymes is vital for these purposes.

Every TDO with a published crystal structure shows two main features in the iron active site (1-3,14-16). The first is a facial triad of three protein-derived histidines that coordinate to iron, leaving three open coordination sites for solvent/substrate. The most commonly found coordination environment for Fe(II) O₂-dependent enzymes is a 2-His-1-carboxylate motif where the iron is coordinated by two histidines and either an aspartate or glutamate residue (17). The difference in iron coordination likely plays a role in the unique reactions catalyzed by TDOs. However, both coordination environments encompass a variety of reactions ranging from

hydroxylation, aliphatic desaturation, and isomerization to more exotic reactions, such as halogenation, epimerization, and aromatic ring opening (18-22). Therefore, while the mode of iron coordination is important, other relevant influences must be present among the outer sphere environment which are not directly coordinated to iron. To understand the mechanism of these enzymes' reactions, investigating the role of their respective outer sphere interactions is vital. This brings importance to the second feature shown among structurally characterized TDOs, which is a sequence of residues featuring serine, histidine, and tyrosine, dubbed the SHY motif. The SHY motif is in the outer sphere of the of the iron active site and has been shown to be important for catalytic efficiency among TDOs (15,23-25).

To date, two TDOs have been discovered among mammals: cysteine dioxygenase (CDO) and 2-aminoethanethiol dioxygenase (ADO) (1,26). CDO is by far the more well studied of the two with many investigations regarding substrate binding and selectivity, reactive intermediates, and biomimetic complexes (27-32). Studies have also been published that probe the outer sphere residues and what role they play in the reaction mechanism this enzyme catalyzes (15,24,25,29). Though the effects of removing or changing the outer sphere residues are seen in kinetic and spectroscopic studies, their exact function is still not fully understood.

A more recent system for studying TDOs and the effects of the outer sphere residues is the 3-mercaptopropionate dioxygenase (3MDO) enzyme. Av3MDO is a bacterial thiol dioxygenase from *Azotobacter vinelandii*, which natively catalyzes the conversion of 3-mercaptopropionate (**3MPA**) to 3-sulfinopropionate (**3SPA**) (33,34). In mammalian CDO, cysteine (**CYS**) is shown to bind in a bidentate fashion to iron through both the cysteine thiolate and amine groups, as seen in Figure 1.1, panel A. The native substrate of 3MDO is essentially a cysteine without the amino group. Therefore, **3MPA** must have a different mode of binding to

3MDO. For reference, the structures of discussed thiol substrates are shown in Figure 1.2. Notably, 3MDO is similar to CDO in terms of both first coordination and outer sphere environment as both feature a 3-His facial triad for iron coordination and the conserved SHY motif. The similarities can be seen from a crystal structure of a 3MDO from *Pseudomonas aeruginosa* (*Pa*3MDO), which shows a 70% sequence identity to *Av*3MDO (35). Given the overall similarity between the 3MDO and CDO, an open question remains as to why the enzymes show different reactivity. These differences in reactivity and structural environments will be elaborated upon below.

1.2 Promiscuous Reactivity and Substrate Binding of *Av*3MDO

*Av*3MDO is a promiscuous enzyme that shows catalytic turnover for a number of thiol-bearing substrates. These include native substrate, **3MPA**, as well as **CYS**, 2-aminoethanethiol (**CA**), and ethanethiol (32-34). The k_{cat} values of *Av*3MDO for **3MPA** and **CYS** are $0.45 \pm 0.06 \text{ s}^{-1}$ and $0.28 \pm 0.02 \text{ s}^{-1}$, respectively. The addition of an amino functional group for **CYS** has a negative effect on catalytic efficiency (k_{cat}/K_M) compared to no amine for **3MPA** ($2.7 \times 10^4 \pm 0.3 \times 10^4 \text{ M}^{-1}\text{s}^{-1}$ for **3MPA** vs $41.5 \pm 0.7 \text{ M}^{-1}\text{s}^{-1}$ for **CYS**). Similarly, substrate **CA**, which has an amine but no carboxylate group, shows a catalytic efficiency of $11 \pm 2 \text{ M}^{-1}\text{s}^{-1}$, which is not far off from that of **CYS**. Therefore, the absence of the carboxylate does not significantly impact the efficiency, but the presence of an amine does. The opposite effect is seen with CDO as no activity is observed for thiol-bearing substrates which lack an amine (32).

The kinetic results for *Av*3MDO suggest two things: (a) substrate amine does not directly bind to iron as the native (most efficient) substrate does not have one and (b) a carboxylate does not have to bind to iron either as **CA** does not have one. These results led to the hypothesis of substrate coordination on 3MDO being monodentate through only the thiolate. In further support

of this, O₂ consumption was observed in reactions with ethanethiol, which has no functional group to allow bidentate coordination.

Mössbauer studies were also performed with **3MPA** and **CYS**-bound Fe(II) 3MDO (16,36). **3MPA** binding results in spectral parameters that agree well with five coordinate CDO model complexes (27). On the other hand, **CYS** binding shows more similarity to six coordinate model complexes. Therefore, **3MPA** would appear to have one less coordination site. The agreement of these spectral parameters with structurally characterized models provides another compelling case for **3MPA** binding monodentate.

Recently, computational docking modeling was used to argue that **3MPA** does bind in a bidentate fashion through the thiolate and carboxylate groups. The proposal was made by Aloï et al. and argues that residue Arg168 is placed adjacent to the iron active site and interaction with substrate carboxylate would place carboxylate in a position analogous to the amine in **CYS** binding to CDO (23). The authors also suggest that if the carboxylate was to not bind with iron, the interaction between the carboxylate and Arg168 would sterically hinder binding of another ligand to that position.

The position of Arg168 does make a compelling case for bidentate coordination. However, given the kinetic and spectroscopic data described above, the idea of monodentate substrate binding cannot be dismissed. As such, investigations into the mode of substrate binding will be a recurring topic throughout the chapters to follow.

1.3 Role of The Shy Motif of Av3MDO

As mentioned above, all TDO crystal structures to date have a conserved SHY motif adjacent to the iron active site. The SHY motif has been shown to interact with the iron active site through the tyrosine residue. In CDO, for instance, perturbations to the tyrosine have directly

influenced the geometry of the substrate-bound iron active site (29). Mammalian CDO features a covalently linked Cys93-Tyr157 pair. Though not essential for activity, the k_{cat} of CDO drops by an order of magnitude when the crosslink is not allowed (29). Similar results are seen for Av3MDO when the SHY motif is altered. Variants Y159F and H157N of Av3MDO were shown to significantly decrease the k_{cat} and k_{cat}/K_M by over an order of magnitude (36). The H157N variant replaces His157 with an Asn that should be able to fulfil the role in the hydrogen bonding network as Asn is a hydrogen bond donor and acceptor. The Y159F would completely cut off the SHY motif from the iron active site. Surprisingly, both variants depreciate the activity to a somewhat equal extent ($0.092 \pm 0.003 \text{ s}^{-1}$ for H157N and $0.081 \pm 0.001 \text{ s}^{-1}$ for Y159F compared to $0.45 \pm 0.06 \text{ s}^{-1}$ for wild-type). Clearly, the exact function of the residues in the SHY motif are not fully understood.

The role to the SHY motif may be dictated by residues even farther from the iron active site. An expanded view of the SHY motif is shown for CDO and Pa3MDO in Figure 1.3. As shown for CDO in panel A, a tryptophan residue is positioned to donate a hydrogen bond from the indole nitrogen to Ser153. Hydrogens are not resolved in the X-ray diffraction of these crystals, but the hydrogen bonding orientation can be inferred based on known behaviors of residues. The indole nitrogen of Trp77 can only donate a hydrogen bond. By extension, Ser153 would donate a hydrogen bond to His155, followed by His155 to Tyr157. Tyr157 would then donate a hydrogen bond to an axial bound ligand on the iron complex, which is suspected to be where molecular oxygen binds. The presence of a hydrogen bond acceptor (Glu105) in Pa3MDO essentially forces the orientation of hydrogen bonding to reverse. Ser155 would donate to Glu105, His157 to Ser155, and Tyr159 to His157. Tyr159 is probably able to donate to both His157 and the axially bound iron ligand. Variant Y159F shows a dramatic decrease in both

activity and nitric oxide binding, suggesting the tyrosine does interact with the iron complex. This is also supported by pH dependent Mossbauer studies that show the ratio of two species of the iron complex are directly linked to the ionization of Tyr159 (36). Mammalian CDO also features the Tyr157-Cys93 crosslink which effectively locks the orientation of tyrosine in place. However, the tyrosine in 3MDO has more flexibility in both orientation and hydrogen binding partner.

These difference in the SHY motif between TDOs could help explain the different substrate selectivity shown between them. This topic will be further elaborated upon in the forthcoming chapters.

1.4 Spectroscopic Studies of Thiol Dioxygenases

Obtaining structural and electronic information from a transition metal embedded in protein structure can be a challenge. Techniques commonly used by synthetic chemists such as nuclear magnetic resonance and infrared spectroscopy can be applied but experiments need to be fine-tuned to fit the needs each individual system (37-39). As well, crystal structures can be challenging to produce and may not reflect geometries which would be seen in solution (40,41). Techniques used heavily in the work presented herein are that of electron paramagnetic resonance (EPR) spectroscopy. These techniques are advantageous in their selectivity. EPR is only sensitive to paramagnetic species, specifically iron complexes in the case of TDOs. Many studies have been done on TDOs which utilize EPR (24,28-30,33,36,42-46). For simplicity, only studies pertaining to work presented herein will be discussed in brief.

Nitric oxide has been used as a surrogate for O₂ to characterize an EPR-active form of the ES complex of various TDOs. These studies have revealed that CDO binds nitric oxide to form an $S = 1/2$ species concurrent with a ligand centered radical (28). Av3MDO produces an $S = 3/2$

species, which, according to the Feltham-Enemark formulation, can be considered as an antiferromagnetic $S = 5/2$ Fe(III) coupled to a $S = 1$ NO⁻ resulting in a ground state of $S = 3/2$ (33,47-49). These differences in electronic structure suggest the enzymes have different mechanisms of O₂ activation. Relative to the wild-type enzyme, the $S = 3/2$ EPR signal of SHY variants show deviations in spectroscopic properties. For instance, nitric oxide binding plummets with the Y159F variant, leading to speculation that Tyr159 interacts with the bound nitric oxide.

Though changes in the spectra are seen between variants in the Av3MDO nitrosyl complexes (Figure 1.4), these differences can be attributed to a single rhombic zero-field splitting parameter, E/D . While the shifts in these values are informative for acknowledging the SHY motif does interact with the nitrosyl complex, determining what geometric changes are influenced by the variants is hard.

Studies have been performed with TDOs and model complexes using cyanide as a spectroscopic probe in place of the nitric oxide O₂ surrogate (29,43). These investigations utilized cyanide as a strong field ligand to bring the ferric iron complexes to low spin $S = 1/2$. Ferric iron-cyano complexes have been shown to feature anisotropic g -values in their EPR spectra (50-52). The advantage of the $S = 1/2$ state is that the observed g -values represent the molecular response along the principle molecular axis of the Fe-site (29). Therefore, structural changes and geometric perturbations can be attributed to specific directions or even ligands on the iron complex. This is shown well in Figure 1.5 where cyanide was used on ferric CDO to gauge the effect of the Tyr157-Cys93 crosslink (29). The figure shows that both crosslinked and non-crosslinked are present in the as-isolated sample with bound **CYS** and cyanide. Systematically isolating each species shows the more anisotropic species (wider spread of g -values) is the species with a crosslink. The greatest perturbation among the species is seen in the

highest g-value ($g=2.38/2.34$). Through additional experiments and spectral simulations, the authors were able to conclude the crosslink played a role in stabilizing substrate binding to the iron active site.

When used in tandem with spectroscopic probes, density functional theory (DFT) can reveal insights to these transition metal complexes which would be hard to determine experimentally. Many studies have been performed which have been able to attribute spectroscopic features to physical parameters (24,28,42,43,45,53,54). For instance, using DFT, Fischer et al. determined the increased range of g-values for the crosslinked (CN/CYS)-bound ferric CDO mentioned above was due to a lengthening of the Fe-S bond (43). When presented with spectroscopic verification, DFT optimized structures can lead to many insights which would otherwise be unattainable. Use of nitric oxide and cyanide as spectroscopic probes in addition to computational modeling will be presented in the following chapters.

1.5 Chapter Overview

This dissertation is aimed to resolve the mode of substrate binding to Av3MDO and elucidate the effects of the SHY motif. As shown above, these two aspects are currently unresolved in the literature and vital to understand the mechanism by which Av3MDO and TDOs, in general, operate.

Chapter 2 focuses on resolving the mode of substrate binding for Av3MDO. A crystal structure is presented which features an inhibitor, 3-hydroxypropionic acid (**3HPA**), bound bidentate to iron. This mode of binding is translated to native substrate, **3MPA**, using DFT optimized structures. Using bidentate coordination as a precursor, models are optimized for the $S=3/2$ (NO/**3MPA**)-bound iron complex. These models are shown to agree well with HYSORE EPR spectra based on calculated hyperfine coupling and Euler angles.

Chapter 3 investigates the role of the SHY motif using cyanide as a spectroscopic probe. For Av3MDO, cyanide is shown to drive ferric iron to low spin $S=1/2$ with and without substrate. Variants H157N and Y159F reveal the effects of the SHY motif are seen on the (CN/3MPA)-bound enzyme. The combination of electronic absorption spectroscopy, EPR spectroscopy, and DFT optimizations verify that the effects shown in the H157N variant are due to Tyr159 shifting its hydrogen bond orientation away from the iron active site.

Chapter 4 covers a study using both nitric oxide and cyanide to simultaneously bind Av3MDO. The resulting species is an EPR-active $S=1/2$ which resembles the (NO/CYS)-bound CDO species (28). Structural identification of this species is interrogated by isotopic substitutions, computational modeling, and inducing perturbations on the iron active site by means of variants H157N and Y159F. A repeating theme of these spectroscopically validated studies is that outer sphere SHY residues influence the electronic structure of the enzymatic Fe-site. Perturbations within the SHY motif result in quantifiable changes in catalytic efficiency and substrate-specificity.

Figures

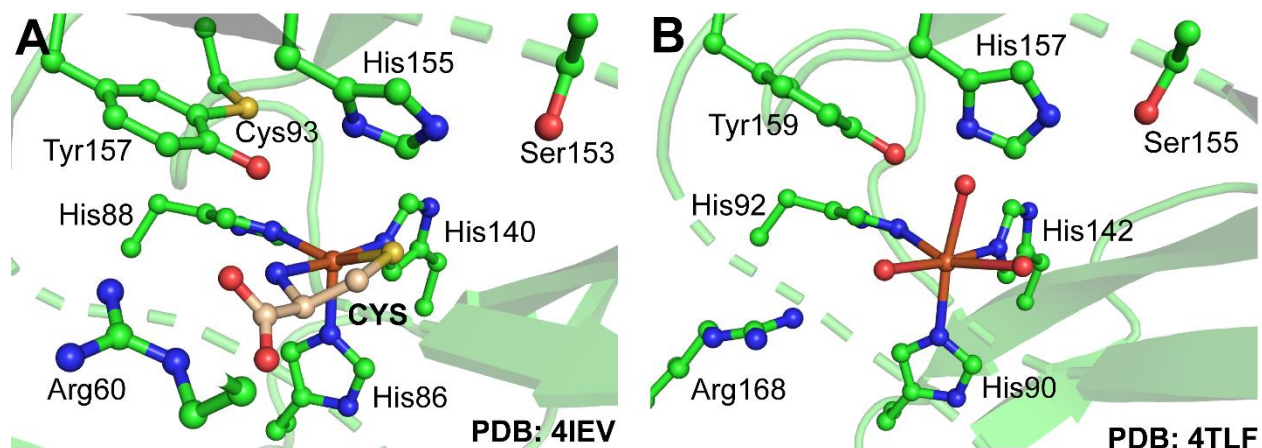


Figure 1.1: The crystal structure of mammalian *R. norvegicus* CDO (panel A) with L-cysteine (CYS) bound to iron (PDB code: 4IEV)(31). Panel B displays the crystal structure of *P. aeruginosa* 3MDO in the resting state with three waters bound to iron (PDB code: 4TLF)(16). The X-ray diffraction resolution of the crystal structures is 1.6 Å for *Rn*CDO and 2.14 Å for *Pa*3MDO.

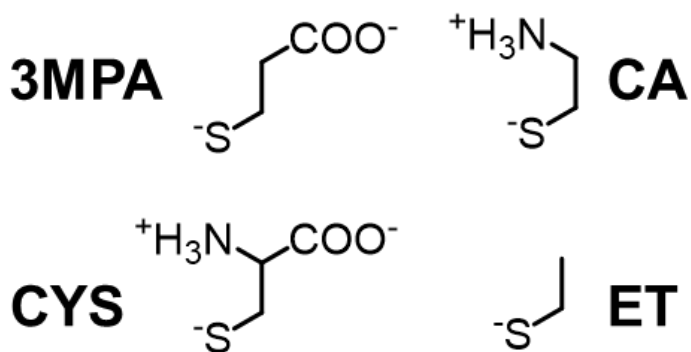


Figure 1.2: Illustrated structures of thiol substrates for *Av*3MDO. Comparisons are shown for 3-mercaptopropionic acid (3MPA), cysteine (CYS), cysteamine (CA), and ethanethiol (ET).

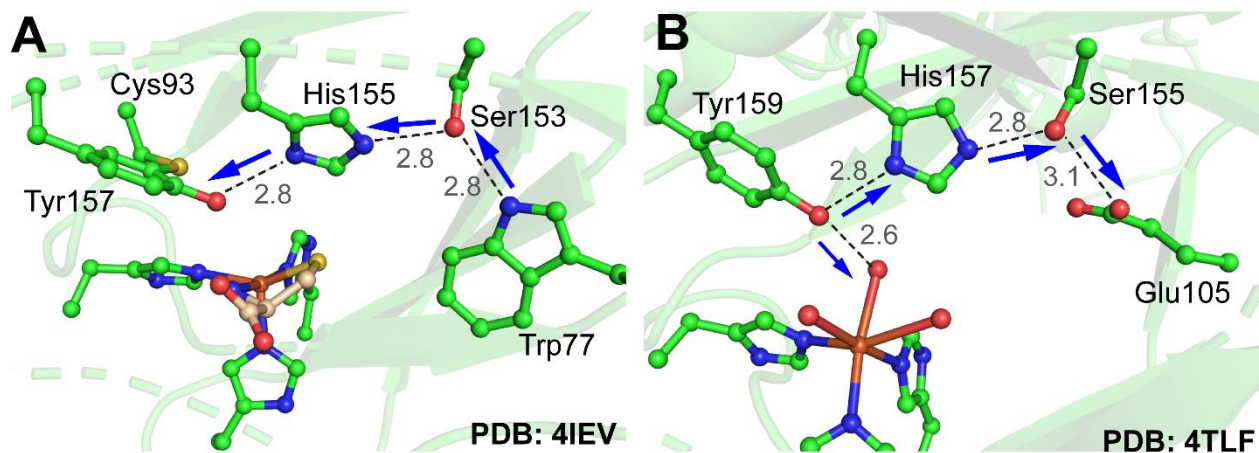


Figure 1.3: Panel A displays the crystal structure for *RnCDO*, focused on the SHY motif and the Trp77 residue participating in the hydrogen bond network (31). Panel B shows a similar view for *Pa3MDO* which shows a glutamate residue opposed to tryptophan (16). Given the indole of Trp77 acts as a hydrogen bond donor and Glu105 acts as an acceptor, the direction of likely hydrogen bond donation is indicated with blue arrows. Distances between the residues are shown in Angstrom (\AA).

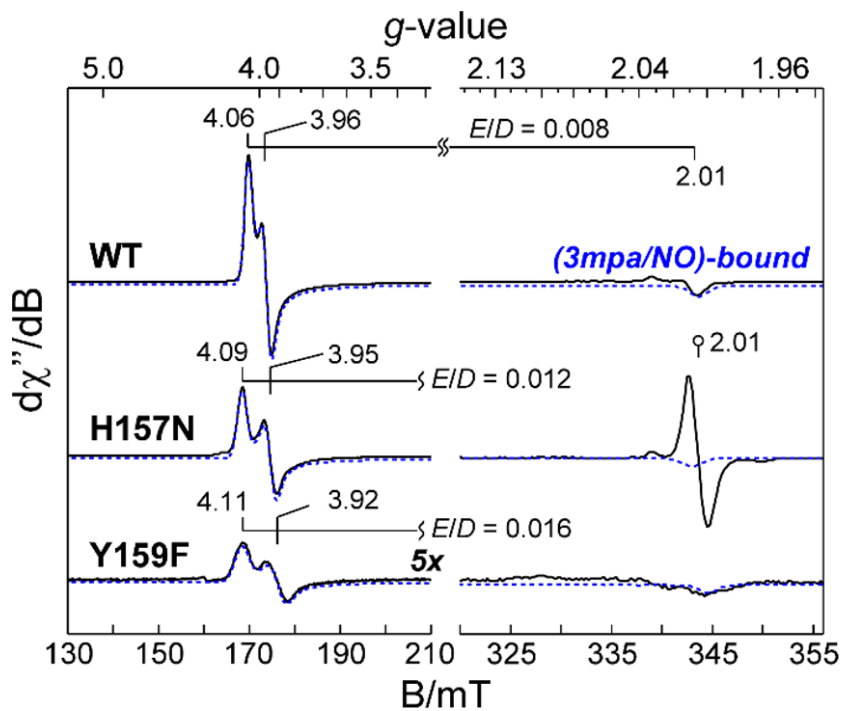


Figure 1.4: EPR spectra of the (NO/3MPA)-bound $Av3MDO$ $S=3/2$ species for wild type and the H157N and Y159F variants. Accompanying simulations are shown as blue dotted lines. The H157N variant features a signal at $g = 2.01$ which is attributed to a dinitrosyl iron contaminant. Figure adapted from reference (36).

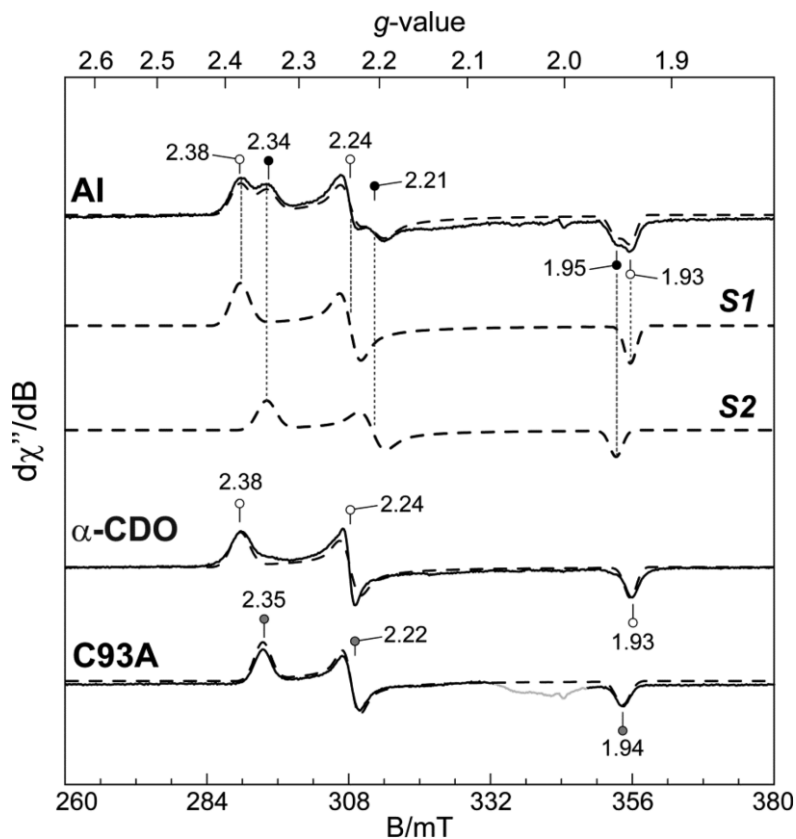


Figure 1.5: EPR spectra of ferric mammalian CDO bound to substrate, **CYS**, and cyanide. Two species are present in the as-isolated sample (AI). One species is attributed to having the Tyr159-Cys93 crosslink. This is shown by the fully modified α -CDO which was purified separately from the non-crosslinked CDO. The variant C93A was produced to compare the other signal in AI with a species which could not form a crosslink. Figure adapted from ref (29).

References

1. Simmons, C. R., Liu, Q., Huang, Q. Q., Hao, Q., Begley, T. P., Karplus, P. A., and Stipanuk, M. H. (2006) Crystal structure of mammalian cysteine dioxygenase - A novel mononuclear iron center for cysteine thiol oxidation. *J. Biol. Chem.* **281**, 18723-18733
2. Driggers, C. M., Stipanuk, M. H., and Karplus, P. A. (2015) Mammalian cysteine dioxygenase. in *Encyclopedia of Inorganic and Bioinorganic Chemistry* (Scott, R. A. ed., John Wiley & Sons, Ltd.
3. Dominy Jr, J. E., Simmons, C. R., Karplus, P. A., Gehring, A. M., and Stipanuk, M. H. (2006) Identification and characterization of bacterial cysteine dioxygenases: A new route of cysteine degradation for eubacteria. *J. Bacteriol.* **188**, 5561-5569
4. Kasperova, A., Kunert, J., Horynova, M., Weigl, E., Sebel, M., Lenobel, R., and Raska, M. (2011) Isolation of recombinant cysteine dioxygenase protein from Trichophyton mentagrophytes. *Mycoses* **54**, e456-e462
5. Weits, D. A., Giuntoli, B., Kosmacz, M., Parlanti, S., Hubberten, H.-M., Riegler, H., Hoefgen, R., Perata, P., van Dongen, J. T., and Licausi, F. (2014) Plant cysteine oxidases control the oxygen-dependent branch of the N-end-rule pathway. *Nat. Commun.* **5**, 3425-3425
6. Gordon, C., Emery, P., Bradley, H., and Waring, R. H. (1992) Abnormal sulphur oxidation in systemic lupus erythematosus. *Lancet* **339**, 25-26
7. Heafield, M. T., Fearn, S., Steventon, G. B., Waring, R. H., Williams, A. C., and Sturman, S. G. (1990) Plasma cysteine and sulphate levels in patients with motor neurone, Parkinson's and Alzheimer's disease. *Neurosci. Lett.* **110**, 216-220
8. James, S. J., Cutler, P., Melnyk, S., Jernigan, S., Janak, L., Gaylor, D. W., and Neubrandner, J. A. (2004) Metabolic biomarkers of increased oxidative stress and impaired methylation capacity in children with autism. *Am. J. Clin. Nutr.* **80**, 1611-1617
9. Deth, R., Muratore, C., Benzecry, J., Power-Charnitsky, V.-A., and Waly, M. (2008) How environmental and genetic factors combine to cause autism: A redox/methylation hypothesis. *Neurotoxicology* **29**, 190-201
10. Bhave, D. P., Muse, W. B., 3rd, and Carroll, K. S. (2007) Drug targets in mycobacterial sulfur metabolism. *Infect. Disord. Drug Targets* **7**, 140-158
11. Trachootham, D., Alexandre, J., and Huang, P. (2009) Targeting cancer cells by ROS-mediated mechanisms: a radical therapeutic approach? *Nat. Rev. Drug Discov.* **8**, 579-591

12. Winyard, P. G., Moody, C. J., and Jacob, C. (2005) Oxidative activation of antioxidant defence. *Trends in Biochemical Sciences* **30**, 453-461
13. Reddie, K. G., and Carroll, K. S. (2008) Expanding the functional diversity of proteins through cysteine oxidation. *Curr. Opin. Chem. Biol.* **12**, 746-754
14. Driggers, C. M., Hartman, S. J., and Karplus, P. A. (2015) Structures of Arg- and Gln-type bacterial cysteine dioxygenase homologs. *Protein Sci.* **24**, 154-161
15. Driggers, C. M., Kean, K. M., Hirschberger, L. L., Cooley, R. B., Stipanuk, M. H., and Karplus, P. A. (2016) Structure-Based Insights into the Role of the Cys-Tyr Crosslink and Inhibitor Recognition by Mammalian Cysteine Dioxygenase. *J. Mol. Biol.* **428**, 3999-4012
16. Tchesnokov, E. P., Fellner, M., Siakkou, E., Kleffmann, T., Martin, L. W., Aloï, S., Lamont, I. L., Wilbanks, S. M., and Jameson, G. N. (2015) The cysteine dioxygenase homologue from *Pseudomonas aeruginosa* is a 3-mercaptopropionate dioxygenase. *J. Biol. Chem.* **290**, 24424-24437
17. Kal, S., and Que, L. (2017) Dioxygen activation by nonheme iron enzymes with the 2-His-1-carboxylate facial triad that generate high-valent oxoiron oxidants. *J. Biol. Inorg. Chem.* **22**, 339-365
18. Chow, M. S., Eser, B. E., Wilson, S. A., Hodgson, K. O., Hedman, B., Fitzpatrick, P. F., and Solomon, E. I. (2009) Spectroscopy and Kinetics of Wild-Type and Mutant Tyrosine Hydroxylase: Mechanistic Insight into O₂ Activation. *J. Am. Chem. Soc.* **131**, 7685-7698
19. Chang, W.-c., Guo, Y., Wang, C., Butch, S. E., Rosenzweig, A. C., Boal, A. K., Krebs, C., and Bollinger, J. M. (2014) Mechanism of the C5 Stereoinversion Reaction in the Biosynthesis of Carbapenem Antibiotics. *Science* **343**, 1140
20. Vaillancourt, F. H., Yin, J., and Walsh, C. T. (2005) SyrB2 in syringomycin E biosynthesis is a nonheme FeII alpha-ketoglutarate- and O₂-dependent halogenase. *Proc. Natl. Acad. Sci. USA* **102**, 10111-10116
21. Li, J., van Belkum, M. J., and Vederas, J. C. (2012) Functional characterization of recombinant hyoscyamine 6 β -hydroxylase from *Atropa belladonna*. *Biorg. Med. Chem.* **20**, 4356-4363
22. Iwabuchi, T., and Harayama, S. (1998) Biochemical and Molecular Characterization of 1-Hydroxy-2-naphthoate Dioxygenase from *Nocardioïdes* sp. KP7 *J. Biol. Chem.* **273**, 8332-8336
23. Aloï, S., Davies, C. G., Karplus, P. A., Wilbanks, S. M., and Jameson, G. N. L. (2019) Substrate Specificity in Thiol Dioxygenases. *Biochemistry* **58**, 2398-2407

24. Blaesi, E. J., Fox, B. G., and Brunold, T. C. (2015) Spectroscopic and Computational Investigation of the H155A Variant of Cysteine Dioxygenase: Geometric and Electronic Consequences of a Third-Sphere Amino Acid Substitution. *Biochemistry* **54**, 2874-2884
25. Davies, C. G., Fellner, M., Tchesnokov, E. P., Wilbanks, S. M., and Jameson, G. N. L. (2014) The Cys-Tyr Cross-Link of Cysteine Dioxygenase Changes the Optimal pH of the Reaction without a Structural Change. *Biochemistry* **53**, 7961-7968
26. Dominy, J. E., Simmons, C. R., Hirschberger, L. L., Hwang, J., Coloso, R. M., and Stipanuk, M. H. (2007) Discovery and Characterization of a Second Mammalian Thiol Dioxygenase, Cysteamine Dioxygenase. *J. Biol. Chem.* **282**, 25189-25198
27. Gordon, J. B., McGale, J. P., Prendergast, J. R., Shirani-Sarmazeh, Z., Siegler, M. A., Jameson, G. N. L., and Goldberg, D. P. (2018) Structures, Spectroscopic Properties, and Dioxygen Reactivity of 5- and 6-Coordinate Nonheme Iron(II) Complexes: A Combined Enzyme/Model Study of Thiol Dioxygenases. *J. Am. Chem. Soc.* **140**, 14807-14822
28. Pierce, B. S., Gardner, J. D., Bailey, L. J., Brunold, T. C., and Fox, B. G. (2007) Characterization of the Nitrosyl Adduct of Substrate-Bound Mouse Cysteine Dioxygenase by Electron Paramagnetic Resonance: Electronic Structure of the Active Site and Mechanistic Implications. *Biochemistry* **46**, 8569-8578
29. Li, W., Blaesi, E. J., Pecore, M. D., Crowell, J. K., and Pierce, B. S. (2013) Second-Sphere Interactions between the C93–Y157 Cross-Link and the Substrate-Bound Fe Site Influence the O₂ Coupling Efficiency in Mouse Cysteine Dioxygenase. *Biochemistry* **52**, 9104-9119
30. Crawford, J. A., Li, W., and Pierce, B. S. (2011) Single Turnover of Substrate-Bound Ferric Cysteine Dioxygenase with Superoxide Anion: Enzymatic Reactivation, Product Formation, and a Transient Intermediate. *Biochemistry* **50**, 10241-10253
31. Driggers, C. M., Cooley, R. B., Sankaran, B., Hirschberger, L. L., Stipanuk, M. H., and Karplus, P. A. (2013) Cysteine Dioxygenase Structures from pH4 to 9: Consistent Cys-Persulfenate Formation at Intermediate pH and a Cys-Bound Enzyme at Higher pH. *J. Mol. Biol.* **425**, 3121-3136
32. Li, W., and Pierce, B. S. (2015) Steady-state substrate specificity and O₂-coupling efficiency of mouse cysteine dioxygenase. *Arch. Biochem. Biophys.* **565**, 49-56
33. Pierce, B. S., Subedi, B. P., Sardar, S., and Crowell, J. K. (2015) The “Gln-Type” Thiol Dioxygenase from *Azotobacter vinelandii* Is a 3-Mercaptopropionic Acid Dioxygenase. *Biochemistry* **54**, 7477-7490
34. Crowell, J. K., Sardar, S., Hossain, M. S., Foss, F. W., and Pierce, B. S. (2016) Non-chemical proton-dependent steps prior to O₂-activation limit *Azotobacter vinelandii* 3-mercaptopropionic acid dioxygenase (MDO) catalysis. *Arch. Biochem. Biophys.* **604**, 86-94

35. Tchesnokov, E. P., Fellner, M., Siakkou, E., Kleffmann, T., Martin, L. W., Aloï, S., Lamont, I. L., Wilbanks, S. M., and Jameson, G. N. L. (2015) The cysteine dioxygenase homologue from *Pseudomonas aeruginosa* is a 3-mercaptopropionate dioxygenase. *J Biol Chem.* **290**, 24424-24437
36. Sardar, S., Weitz, A., Hendrich, M. P., and Pierce, B. S. (2019) Outer-Sphere Tyrosine 159 within the 3-Mercaptopropionic Acid Dioxygenase S-H-Y Motif Gates Substrate-Coordination Denticity at the Non-Heme Iron Active Site. *Biochemistry* **58**, 5135-5150
37. Donghi, D., Johannsen, S., Sigel, R. K. O., and Freisinger, E. (2012) NMR Spectroscopy in Bioinorganic Chemistry. *CHIMIA* **66**, 791-797
38. Ronconi, L., and Sadler, P. J. (2008) Applications of heteronuclear NMR spectroscopy in biological and medicinal inorganic chemistry. *Coord. Chem. Rev.* **252**, 2239-2277
39. Alben, J. O., Choi, S. S., Adler, A. D., and Caughey, W. S. (1973) INFRARED SPECTROSCOPY OF PORPHYRINS*. *Annals of the New York Academy of Sciences* **206**, 278-295
40. Mei, Z., Treado, J. D., Grigas, A. T., Levine, Z. A., Regan, L., and O'Hern, C. S. (2020) Analyses of protein cores reveal fundamental differences between solution and crystal structures. *Proteins: Struct. Funct. Bioinform.* **88**, 1154-1161
41. Rife, J. P., Stallings, S. C., Correll, C. C., Dallas, A., Steitz, T. A., and Moore, P. B. (1999) Comparison of the Crystal and Solution Structures of Two RNA Oligonucleotides. *Biophys. J.* **76**, 65-75
42. Fischer, A. A., Stracey, N., Lindeman, S. V., Brunold, T. C., and Fiedler, A. T. (2016) Synthesis, X-ray Structures, Electronic Properties, and O₂/NO Reactivities of Thiol Dioxygenase Active-Site Models. *Inorg. Chem.* **55**, 11839-11853
43. Fischer, A. A., Miller, J. R., Jodts, R. J., Ekanayake, D. M., Lindeman, S. V., Brunold, T. C., and Fiedler, A. T. (2019) Spectroscopic and Computational Comparisons of Thiolate-Ligated Ferric Nonheme Complexes to Cysteine Dioxygenase: Second-Sphere Effects on Substrate (Analogue) Positioning. *Inorg. Chem.* **58**, 16487-16499
44. Fernandez, R. L., Dillon, S. L., Stipanuk, M. H., Fox, B. G., and Brunold, T. C. (2020) Spectroscopic Investigation of Cysteamine Dioxygenase. *Biochemistry*
45. Blaesi, E. J., Gardner, J. D., Fox, B. G., and Brunold, T. C. (2013) Spectroscopic and Computational Characterization of the NO Adduct of Substrate-Bound Fe(II) Cysteine Dioxygenase: Insights into the Mechanism of O₂ Activation. *Biochemistry* **52**, 6040-6051
46. Fischer, A. A., Lindeman, S. V., and Fiedler, A. T. (2017) Spectroscopic and computational studies of reversible O₂ binding by a cobalt complex of relevance to cysteine dioxygenase. *Dalton Trans.* **46**, 13229-13241

47. Li, M., Bonnet, D., Bill, E., Neese, F., Weyhermüller, T., Blum, N., Sellmann, D., and Wieghardt, K. (2002) Tuning the Electronic Structure of Octahedral Iron Complexes [FeL(X)] (L = 1-Alkyl-4,7-bis(4-tert-butyl-2-mercaptobenzyl)-1,4,7-triazacyclononane, X = Cl, CH₃O, CN, NO). The $S = 1/2 \rightleftharpoons S = 3/2$ Spin Equilibrium of [FeLPr(NO)]. *Inorg. Chem.* **41**, 3444-3456
48. Wanat, A., Schnepfenseper, T., Stochel, G., van Eldik, R., Bill, E., and Wieghardt, K. (2002) Kinetics, Mechanism, and Spectroscopy of the Reversible Binding of Nitric Oxide to Aqueated Iron(II). An Undergraduate Text Book Reaction Revisited. *Inorg. Chem.* **41**, 4-10
49. Sellmann, D., Blum, N., Heinemann, F. W., and Hess, B. A. (2001) Synthesis, Reactivity, and Structure of Strictly Homologous 18 and 19 Valence Electron Iron Nitrosyl Complexes. *Chem. Eur. J.* **7**, 1874-1880
50. Clay, M. D., Jenney, F. E., Hagedoorn, P. L., George, G. N., Adams, M. W. W., and Johnson, M. K. (2002) Spectroscopic Studies of *Pyrococcus furiosus* Superoxide Reductase: Implications for Active-Site Structures and the Catalytic Mechanism. *J. Am. Chem. Soc.* **124**, 788-805
51. Whittaker, J. W., and Lipscomb, J. D. (1984) 17O-water and cyanide ligation by the active site iron of protocatechuate 3,4-dioxygenase. Evidence for displaceable ligands in the native enzyme and in complexes with inhibitors or transition state analogs. *J. Biol. Chem.* **259**, 4487-4495
52. Deligiannakis, Y., Boussac, A., Bottin, H., Perrier, V., Bârzu, O., and Gilles, A.-M. (1997) A New Non-Heme Iron Environment in *Paracoccus denitrificans* Adenylate Kinase Studied by Electron Paramagnetic Resonance and Electron Spin Echo Envelope Modulation Spectroscopy. *Biochemistry* **36**, 9446-9452
53. Kumar, D., Thiel, W., and de Visser, S. P. (2011) Theoretical Study on the Mechanism of the Oxygen Activation Process in Cysteine Dioxygenase Enzymes. *J. Am. Chem. Soc.* **133**, 3869-3882
54. Fellner, M., Siakkou, E., Faponle, A. S., Tchesnokov, E. P., de Visser, S. P., Wilbanks, S. M., and Jameson, G. N. (2016) Influence of cysteine 164 on active site structure in rat cysteine dioxygenase. *J. Biol. Inorg. Chem.* **21**, 501-510

CHAPTER 2:
STRUCTURE OF 3-MERCAPTOPROPIONIC ACID DIOXYGENASE WITH A
SUBSTRATE ANALOG REVEALS BIDENTATE SUBSTRATE BINDING AT THE IRON
CENTER

2.1 Introduction

Thiol dioxygenases are a subset of non-heme mononuclear iron oxygenases that catalyze the O₂-dependent oxidation of thiol-bearing substrates to yield the corresponding sulfinic acid. Among this group, cysteine dioxygenase (CDO) (1-5) and cysteamine dioxygenase (ADO) (6,7) are responsible for the biosynthesis of cysteine sulfinic acid (**CSA**) and hypotaurine (**HT**), respectively, which are precursors for the biosynthesis of taurine (1). Among bacteria, a number of other thiol dioxygenases have been identified, including mercaptosuccinate dioxygenase (MSDO) (8) and 3-mercaptopropionate dioxygenase (3MDO) (9-14). Plant cysteine oxidases (PCO) catalyze the formation of an *N*-terminal cysteine sulfinic acid within ERF-VII transcription factors to initiate N-end rule degradation (15,16). A similar function has recently been proposed for mammalian ADO in controlling regulators of G protein signaling (17).

Over the past decade, this class of enzymes has attracted considerable attention as imbalances in L-cysteine (**CYS**) metabolism are associated with neurological diseases (5,18,19). This observation suggests a correlation between impaired sulfur metabolism, oxidative stress, and neurodegenerative disease (20,21). Consequently, enzymes involved in sulfur-oxidation and transfer are increasingly being evaluated as potential drug targets (22-25).

Across the domains of life, structurally characterized thiol dioxygenases share two major features: (1) a mononuclear non-heme iron active site coordinated by three protein derived histidine residues, and (2), a conserved sequence of outer Fe-coordination sphere amino acids (Ser-His-Tyr), the latter being adjacent to the iron site ($\sim 3 \text{ \AA}$). By analogy to the chymotrypsin-like serine proteases, the Ser-His-Tyr ('SHY') network was previously referred to as a "*catalytic triad*" (5,13,14,26-30). However, these residues appear to enhance the catalytic rate and efficiency but are not required for activity (31-34). Consequently, this hydrogen bonding network is simply referred to as the 'SHY' motif. In eukaryotic CDOs, the 'SHY' motif tyrosine (Tyr157) is covalently cross-linked with an adjacent cysteine residue (C93) to yield a C93-Y157 pair (35,36) whereas bacterial forms utilize an unmodified Tyr-residue at this position.

As shown in **Fig. 2.1A**, the substrate-bound mammalian CDO reveals a bidentate coordination of **CYS** to the mononuclear Fe-site via thiolate and neutral amine (32,37,38). Both kinetic and spectroscopic studies demonstrate additional interactions between the **CYS**-bound Fe-site and outer sphere residues (Tyr157 and Arg60) within the CDO active site (27,31). These multiple points of interaction are likely responsible for the high substrate specificity exhibited by this enzyme (35). To illustrate, cysteamine [2-aminoethanethiol, (**CA**)] is structurally similar to **CYS**, lacking only the α -carboxylate group. Therefore, it is reasonable that this substrate analogue could coordinate to the CDO Fe-site in a similar bidentate fashion as **CYS**. However, relative to **CYS**, a 10,000-fold decrease in k_{cat}/K_M was reported in steady-state reactions with **CA** (35). Therefore, removal of the **CYS**-carboxylate has a profound impact on the formation of the CDO **ES**-complex. More dramatically, no activity whatsoever is observed in reactions with similarly sized thiol-substrates lacking an amine functional group. This observation demonstrates that coordination of the substrate amine to the CDO Fe-site is required for activity. By contrast,

3MDO (**Fig. 2.1B**) is capable of accommodating a variety of thiol-bearing substrates, such as 3-mercaptopropionic acid (**3MPA**), **CYS**, and **CA** to catalyze dioxygenation over a broad pH range (10,11,13,14). While a modest decrease in k_{cat} is observed in reactions with **CA** [$0.29 \pm 0.08 \text{ s}^{-1}$] relative to **3MPA** and **CYS** [$1.0 \pm 0.1 \text{ s}^{-1}$], the vast difference in catalytic efficiency (k_{cat}/K_M) identifies **3MPA** as the preferred substrate for MDO (14). Since **3MPA** lacks an amine functional group, the first coordination sphere for the Av3MDO Fe-site cannot be equivalent to CDO.

To date, structures for the **3MPA**-bound enzyme have been unavailable; however, two models for substrate-binding at the Fe-site have been proposed. A bidentate model for **3MPA**-coordination to the Fe-site via substrate thiol and carboxylate functional groups was recently proposed by Jameson and Karplus (9). In this report, docking of **3MPA** into the *Pseudomonas aeruginosa* 3MDO (*Pa*3MDO) crystal structure led to the conclusion that a salt bridge formed between the Arg168 guanidinium group and **3MPA**-carboxylate was catalytically essential (9,10). Structurally, this model closely matches the **CYS**-bound mammalian CDO, although the relevant Arg group is in a position non-homologous to that of mammalian CDO. The proposed salt bridge provided a reasonable explanation for the decreased affinity of the enzyme for amino-bearing substrates. However, the instability of *Pa*3MDO Arg168 variants precluded experimental validation of this model by site-directed mutagenesis.

Alternatively, previous arguments suggested that **3MPA** Fe-coordination occurs via thiolate only based on the results of two key experiments (12). First, pH-dependent kinetic data for Av3MDO-catalyzed reactions with a substrate lacking a carboxyl group (cysteamine, **CA**) reveal only a modest decrease in k_{cat} -values [$v_0/[E]$, $0.29 \pm 0.08 \text{ s}^{-1}$] relative to reactions performed with **3MPA** and **CYS** [1.0 to 1.2 s^{-1}] (14). Since both CDO and 3MDO exhibit an

obligate-ordered binding of organic substrate prior to molecular oxygen, it was concluded that Fe-coordination of the substrate-carboxylate group is not required to produce the O₂-activating enzyme-substrate (**ES**) complex. Second, experiments using the O₂-mimetic nitric oxide corroborate this argument. EPR spectroscopy verified formation of a substrate-bound iron-nitrosyl species using thiol-substrates lacking carboxylate groups [such as **CA** and ethanethiol (**ET**)] (14). Therefore, direct Fe-coordination of a substrate-carboxylate is not required for converting the Fe(II) site into a NO-reactive state. These results clearly demonstrate that direct carboxylate coordination to the iron center is not obligatory to trigger oxygen activation.

In order to address this discrepancy in 3MDO substrate-binding models, the structure of Av3MDO is presented in complex with the substrate analog and competitive inhibitor, 3-hydroxypropionic acid (**3HPA**). Using the Av3MDO-**3HPA** complex as a starting point, DFT computations were performed to model the coordination of the native **3MPA** substrate. Supporting HYSCORE experiments performed on the (**3MPA/NO**)-bound Av3MDO confirm the NO-binding site and corroborate bidentate **3MPA**-coordination in the substrate-bound iron-nitrosyl site. As suggested by Jameson and Karplus, these experiments support bidentate coordination of **3MPA** with the substrate carboxylate group forming an additional interaction with Arg168 and the thiol bound at the same position as CDO.

2.2 Experimental Procedures

Protein Expression and Purification. A detailed description for the expression and purification of this enzyme has been reported elsewhere (12,14). Briefly, the Av3MDO expression vector was transformed into chemically competent BL21(DE3) *E. coli* (Novagen Cat. No. 70236-4) by heat-shock and grown overnight at 37 °C on a LB-agar plate containing 100 mg/L ampicillin (Amp). A single colony was selected for training on antibiotic in liquid LB media prior to inoculation of

the 10-L BF-110 fermenter (New Brunswick Scientific) at 37 °C. Cell growth was monitored by optical density at 600 nm (OD 600). Induction was initiated by adding 1.0 g isopropyl β -D-1-thiogalactopyranoside (IPTG), 78 mg ferrous ammonium sulfate, and 20 g casamino acids at an OD600 value of ~4. During induction, the temperature of the bioreactor was decreased from 37 °C to 25 °C and agitation was set to maintain an oxygen concentration of 20% relative to air-saturated media. Four hours post-induction, cells were harvested and pelleted by centrifugation (Beckman-Coulter Avanti J-E, JA 10.5 rotor). The resulting cell paste was stored at -80 °C.

In a typical purification, ~20 g frozen cell paste was added to extraction buffer [20 mM 4-(2-hydroxyethyl)-1-piperazineethanesulfonic acid (HEPES), 50 mM NaCl, pH 8.0]. Lysozyme, ribonuclease, and deoxyribonuclease were added to the slurry for a final concentration of 10 μ g/mL each, and the resulting slurry was stirred slowly on ice prior to pulse sonication (Bronson Digital 250/450). The insoluble debris was removed from the cell free extract by centrifugation at 48,000 x g for 1 hour at 4 °C. The supernatant was diluted 1:1 with extraction buffer and then loaded onto a DEAE sepharose fast flow anion exchange column (GE Life Sciences #17070901) pre-equilibrated with 20 mM HEPES, 50 mM NaCl, pH 8.0. The column was washed with three column volumes of extraction buffer prior to elution in a linear NaCl gradient (50 mM – 350 mM).

Fractions were collected overnight and pooled based on enzymatic activity and/or SDS PAGE as described elsewhere (12). The pooled enzyme solution was concentrated to ~50 mL using an Amicon stir cell and YM-10 ultrafiltration membrane prior to thrombin protease (Biopharma Laboratories) cleavage to remove C-terminal His-tag from the expressed enzyme. Following overnight cleavage at 4 °C, the enzyme was dialyzed against 4 L of 20 mM HEPES, 20 mM NaCl at pH 8.0 to decrease the salt content. A second DEAE column separation in a

linear gradient (50-250 mM NaCl) was used to separate the free (His)₆-tag from the purified enzyme. Pre-crystallization desalting was performed by using a Sephadex G25 column equilibrated with 20 mM HEPES, 10 mM NaCl at pH 8.0 prior to concentrating drop freezing in liquid nitrogen and storage at -80 °C. Iron content was quantified spectrophotometrically for both ferric and ferrous concentration using 2,4,6-tripyridyl-s-triazine (TPTZ) in a method previously described (14,38).

Enzyme Assays. The rate of dioxygen consumption in activity assays was determined polarographically using a standard Clark electrode (Hansatech Instruments, Norfolk, England) in a jacketed 2.5 mL cell. Reaction temperatures were fixed at 25 ± 1 °C using a 5 L circulating water bath (Grant Instruments), and O₂-electrode calibration was performed as described elsewhere (12,31,39). For all **3MPA** concentrations [7 – 1000 µM], reactions were initiated by addition of 5.0 µM Fe(II)-Av3MDO. Steady-state kinetic parameters for the enzyme used in experiments were consistent with previously published values at 25 °C [*k_{cat}*, 1.0 ± 0.1 s⁻¹; *K_M*, 13 ± 5 µM; *k_{cat}/K_M*, 72,000 ± 9,200 M⁻¹ s⁻¹] (14).

Data Analysis. Inhibition kinetic results were fit globally using the *Enzyme Kinetics Add-On* module of SigmaPlot ver. 14.0 (Systat Software Inc., Chicago, IL). In the presence of a competitive inhibitor, the Michaelis-Menten and Lineweaver-Burk equations take the form shown in equations **1** and **2**, respectively. From the analysis, kinetic parameters (*V_{max}*, *K_M*, and *K_I*) as well as the error associated with each value were determined by non-linear regression.

Equation 1.
$$v_0 = \frac{V_{max}[S]}{K_M \cdot (1 + \frac{[I]}{K_I}) + [S]}$$

Equation 2.
$$\frac{1}{v_0} = \frac{K_M \cdot (1 + \frac{[I]}{K_I})}{V_{max}} \cdot \frac{1}{[S]} + \frac{1}{V_{max}}$$

Av3MDO Crystallization. Av3MDO crystallization conditions were identified through sparse matrix trials using a number of commercially available screens. The initial hit (crystal form A) was obtained in condition 2-42 of the MIDAS screen (Molecular Dimensions), which consists of 100 mM MES pH 6, 30% w/v poly(acrylic acid sodium salt) 5100, and 10% v/v ethanol. Two μL of Av3MDO at a concentration of 40 mg/mL were mixed with 2 μL of the crystallization cocktail on a siliconized coverslip (Hampton Research), and the resulting drop was incubated over 500 μL of the same crystallization cocktail in a sealed chamber at 22 °C. Thin needle-shaped crystals with a tendency to grow in clusters were observed after a week of incubation. These initial crystals were replicated with independently prepared solutions and further optimized through streak seeding and inclusion of 50 mM MgCl_2 in the crystallization cocktail. The optimized crystals grew as thin rods over the course of a week with approximate final dimensions of 50 x 50 x (100-800) μm . Most crystals exhibited a splitting defect along their long axis. The crystals were harvested directly from the mother liquor using elliptical Microloops (Mitegen) and flash frozen in liquid nitrogen.

To obtain an alternative Av3MDO crystal form, Av3MDO was repurified by anion exchange and gel filtration chromatography in the absence of reducing agents and then concentrated to 40 mg/mL. A second crystallization hit (crystal form B) was obtained in condition E4 of the MidasPLUS screen (MD1-107, Molecular Dimensions), which consists of 100 mM HEPES pH 7, 40% v/v pentaerythritol propoxylate (5/4 PO/OH), and 0.2 M sodium thiocyanate. Two μL of Av3MDO at a concentration of 40 mg/mL were mixed with 2 μL of the crystallization cocktail on a siliconized coverslip (Hampton Research), and the resulting drop was incubated over 500 μL of the same crystallization cocktail in a sealed chamber at 22 °C. Yellowish, rod-shaped crystals with “feather-duster” growth defects on each end were observed

after 2-5 days of incubation. The growth defects were minimized by changing the HEPES, pentaerythritol propoxylate, and sodium thiocyanate concentrations to 50 mM, 44% and 0.6 M, respectively. Mature (150 x 150 x 600 μm) single crystals were harvested directly from the mother liquor using Microloops (Mitegen) and flash frozen in liquid nitrogen.

X-ray Diffraction Data Collection, Processing, and Analysis. $A\nu_3\text{MDO}$ crystal diffraction data were collected using beamlines 17-ID-2 (FMX) at the National Synchrotron Light Source (NSLS)-II, beamline 12-2 at the Stanford Synchrotron Light Source (SSRL), and beamline 24-ID-E (NE-CAT) at the Advanced Photon Source (APS). All form A $A\nu_3\text{MDO}$ crystals examined were twinned to various degrees as described in more detail below. The microfocusing capability of the FMX 17-ID-2 beamline was used to collect data from small crystal volumes to minimize contributions from twin-related domains. Initial crystals diffracted to ~ 2.7 \AA resolution and the diffraction was somewhat anisotropic, being strongest along c^* . Weak diffuse scatter was observed between reflections in h - k planes of reciprocal space. Data were indexed, integrated, and scaled using XDS (40). The data were initially processed in space group $P622$ and examination of axial reflections along c^* indicated the presence of a 6_2 or 6_4 screw axis. Analysis of the intensities with the L-test (41), as implemented in *phenix.xtriage* (42), provided strong indication that the data were twinned. The data were therefore reprocessed in space groups $P321$ and $P3$ with similar R_{merge} values for each. H-tests (43) for the four possible unique twin operators in the latter point group indicated that the crystals were tetartohedrally twinned. Crystal streak seeding and the inclusion of MgCl_2 in the crystallization cocktail substantially reduced crystal twinning and improved the data resolution to ~ 2.25 \AA . The optimized crystals remained partially merohedrally twinned with respect to operator ($k, h, -l$). The best crystals of crystal form B diffracted X-rays to ~ 2.9 \AA resolution. Data were processed in space group $P6_{(1,5)}22$.

While no twinning was detected in this crystal form, the native Patterson map suggested the presence of pseudotranslational symmetry. X-ray data collection statistics are shown in **Table A2.1**.

Structure Refinement and Analysis. Structure solution for crystal form A was carried out by molecular replacement in *Phaser* (44) using the coordinates of a related 3MDO protein (5) as a search model (PDB accession code 4TLF). Structure solution was attempted, unsuccessfully, in space groups $P6_{(2,4)}22$ before it was realized the data were twinned. Space groups $P3_{(1,2)}12$ were excluded from further consideration owing to poor merging statistics. MR trials in space groups $P3_{(1,2)}21$ led to a clear solution in space group $P3_121$ with four molecules (a pair of dimers) per asymmetric unit and a solvent content of 64%. Amino acid substitutions and model adjustments were made using *Coot* (45) and the model was refined using *Refmac* (46). After several rounds of model building and refinement R_{free} plateaued at ~37%. At this point, a majority of the strongest residual electron density was found within a large solvent channel, but it was largely uninterpretable. The possibility of rotational pseudosymmetry causing an elevation in the apparent crystal symmetry was considered, and the partially refined $A\upsilon 3\text{MDO}$ coordinates were used as a search model for molecular replacement in space group $P3_1$. *Phaser* located 12 molecules in the asymmetric unit giving a solvent content of 47%. Refinement of this new model against the $P3_1$ processed data (with R_{free} reflections transferred from the original data set after symmetry expansion to $P3_1$) resulted in an immediate reduction of R_{free} to ~28% and elimination of the residual density features noted above. RvR analysis (47) of the $P3_1$ data and calculated amplitudes as implemented in *phenix.xtriage* (42) revealed the presence of both two-fold rotational pseudosymmetry along the a and b axes together with partial merohedral twinning (k, h, -l with $\alpha \sim 0.34$). These features were also evident from inspection of Patterson self-rotation

plots which showed strong $\chi = 180^\circ$ peaks along the 'a' and 'b' axes. Together, these features accounted for the similar R_{merge} values for space groups $P3_121$ and $P3_1$. The space group assignment was further validated using Zanuda (48) and `labelit.check_pdb` symmetry (49) as well as by manual inspection of the crystal packing environment for each of the monomers in the asymmetric unit. A monomer from the $P3_1$ model was then used as a model to solve crystal form B by molecular replacement in space group $P6_122$ with four monomers in the asymmetric unit.

Refinement of both models was completed by alternating reciprocal space refinement in *Refmac*, using the amplitude-based twin refinement option in the case of crystal form A, and manual model improvements in *Coot*. Coordinate and dictionary files for the test ligands were generated using the GRADE server (Global Phasing LTD). In the case of crystal form A, inspection of residual density near the iron center revealed a large peak in the axial position and an elongated, continuous feature in the equatorial positions, indicative of a diffusible ligand set different from the three aquo complex modeled in the structure of *Pa3MDO* (**Fig. A2.1A**) (11). Indeed, placement of three water molecules poorly explained the residual density as shown in **Fig. A2.1B**. The density *trans* to His142 was flat and appeared to make a simultaneous interaction with Arg168, suggesting it could represent a carboxylate-containing ligand. Modeling of a bicarbonate at this position resulted in an excellent fit to the electron density map (**Fig. A2.1C**). However, the bicarbonate-H₂O-H₂O model resulted in residual positive density features at the axial position *trans* to His 90 as well as between bicarbonate and the water ligand *trans* to His92 in addition to an unacceptably close interaction (2.1 Å) between the non-axial water and bicarbonate ligands (**Fig. A2.1C**). Replacing the axial water with a chloride ion, which was present in the crystal mother liquor at ~100 mM concentration, fully quenched the residual density with a reasonable refined *B*-factor (**Fig. A2.1D**). Chloride binding at the equivalent site

in CDO was previously reported (27,50), which further supports the plausibility of the assignment. The difference map analysis described above suggested that the equatorial features represented a single carboxylate-containing compound. Since known components of the crystal mother liquor could not account for the electron density, further considerations were made for possible contaminants that the density could represent. 3-hydroxypropionic acid is a known precursor and contaminant of the polyacrylate used for Av3MDO crystallization, which was confirmed by mass spectrometry, and was considered the most likely source of the electron density feature (51,52). Additionally, **3HPA** is a close analog of the **3MPA** substrate of Av3MDO. Placement of **3HPA** at this position completely quenched the residual density with refined *B*-factors closely matching those of iron and its other ligands (**Fig. A2.1E and Table A2.1**). We also attempted to model **3MPA** into the density, but observed a residual density hole near the sulfur atom, which also exhibited an elevated *B*-factor relative to the remainder of the molecule (**Fig. A2.1F**).

The initial difference maps for the crystal form B model also revealed density in both the equatorial and axial positions. The equatorial features were interpreted as two coordinated water molecules while the axial density was elongated and not adequately satisfied by modeling either a single water or chloride ligand. The elongated density instead strongly suggested a bound thiocyanate ligand which was modeled with its nitrogen atom directly coordinating the iron ion based on difference map analysis and refined *B*-factors computed with the ligand modeled in either orientation.

Structure validation was carried out with the Molprobit (53) and wwPDB (54) webserver. The final model statistics are shown in **Table A2.1**. The coordinates and structure

factor amplitudes have been deposited in the Protein Data Bank under accession code 6XB9 (crystal form A) and 7KOV (crystal form B).

Mass Spectrometry. Sodium polyacrylate 5100 solution (Hampton Research) was diluted to 10% (v/v) with Millipore water. 100 μL of the resulting solution was mixed with 900 μL of HPLC-grade acetone to precipitate the acrylate polymer and the mixture was centrifuged at 17,000g for 15 min. The supernatant (10 μL) was diluted with 50% HPLC-grade methanol (90 μL), and 10 μL of the resulting solution was analyzed with LXQ Mass spectrometer (Thermo Scientific, Waltham, MA) coupled with an Ultimate 3000 HPLC system. 3HPA standard (Sigma-Aldrich) was prepared in an identical manner. Chromatography was performed with a Poroshell 120 EC C18 Column (2.7 μm , 4.6 mm \times 50 mm, Agilent Technologies, Santa Clara, CA) using a gradient mobile phase of acetonitrile/2-propanol (1/1, v/v) in water from 20% to 98% over 20 min. The flow rate was 0.6 mL/min. Ions were detected in negative mode with a normalized collision energy of 35%.

Pulsed EPR Measurements. HYSCORE measurements were made using an ELEXSYS E680 EPR spectrometer (Bruker-Biospin, Billerica, MA) equipped with a Bruker Flexline ER 4118 CF cryostat and an ER 4118X-MD4 ENDOR resonator. Measurements were made at 5 K with a nominal EPR frequency of 9.78 GHz and used a four-pulse sequence, $\pi/2-\tau-\pi/2-t_1-\pi-t_2-\pi/2-\tau$ -echo. This sequence was repeated at a rate of 1.25 kHz with values of 16 ns and 32 ns for the $\pi/2$ and π pulses, respectively. The times t_1 and t_2 were varied independently from 48 ns to 3096 ns in increments of 24 ns for a total of 128 points in each dimension. The delay time τ was set to 120 ns to maximize resolution in the ^1H region of the spectrum. HYSCORE spectra were processed using custom scripts in MATLAB (Mathworks, R2020a). Briefly, the complex raw data was phased to minimize the imaginary component, and

the background decay was subtracted in each dimension by removing a second-degree polynomial. Then, a diagonal Blackman apodization function was applied to minimize noise at larger values of t_1 and t_2 . The data were then zero-filled in both directions to 1024 points before calculating the two-dimensional Fourier transform. The absolute value of the real part of the Fourier transform is displayed. HYSORE peaks are symmetric about the frequency diagonal; however, several factors, including interference from strong nuclear modulation, can affect the intensity of each peak. As a result, real peaks are roughly symmetric about the frequency diagonal, but they can have minor intensity variations. Noise, on the other hand, is not symmetric about the diagonal. Therefore, the spectra were left unsymmetrized in order to best distinguish between signal and noise. Spectra were simulated using the “saffron” function in EasySpin, a comprehensive EPR toolbox in MATLAB (55).

HYSORE simulations on the ^1H region are based off the spin Hamiltonian

Equation 3.
$$\hat{H} = -\gamma_H \hat{I} \cdot B + \hat{S} \cdot \hat{A} \cdot \hat{I}$$

where $-\gamma_H$ is the proton gyromagnetic ratio, \hat{S} and \hat{I} are the electron and nuclear spin operators, B is the magnetic field vector, and \hat{A} is the hyperfine coupling tensor. The proton couplings were modeled using an axial dipolar tensor,

Equation 4.
$$A = [-T, -T, (2 * T)]$$

where T is the anisotropic contribution of the hyperfine interaction. The tensor was considered purely dipolar due to the distance of the coupled ^1H , which is consistent with other HYSORE analyses of $\{\text{FeNO}\}^7$ centers (56-58). The dipolar contribution, T , was calculated using the geometry-optimized DFT structure of **3MPA**-bound Av3MDO treated with NO and spin-projection factors that take into account the electronic structure of the $\{\text{FeNO}\}^7$ center (56,57).

In brief, distances between the Fe, the N, and the O of NO and each ^1H were used to calculate a T_{Fe} , T_N , and T_O according to the point-dipole approximation

Equation 5.
$$T = \left(\frac{\mu_0}{4\pi}\right) \frac{g_e g_n \beta_e \beta_n}{hr^3},$$

where μ_0 is the permittivity of free space, g_e is the electronic *g-value*, g_n is the nuclear *g-value*, β_e is the electronic Bohr magneton, β_n is the nuclear Bohr magneton, h is Planck's constant, and r is the distance from the proton to the Fe, N, or O of the $\{\text{FeNO}\}^7$ center. The dipolar contributions were then summed using spin projection factors

Equation 6.
$$T_{total} = \frac{7}{5}(T_{Fe}) - \frac{1}{5}(T_N + T_O)$$

where T_{Fe} , T_N , and T_O are the dipolar couplings resulting from the point-dipole approximation using the distance between the ^1H and the Fe, N, and O of NO, respectively. The couplings for the ^1H on His90 and His142 were varied by $\pm 0.1 \text{ \AA}$, which is the estimate of the precision of the atomic locations in the crystal structure. **Eqs. 5** and **6** were used to transform the $\pm 0.1 \text{ \AA}$ variation into the corresponding value in MHz. The other ^1H couplings were left unvaried. For each ^1H , the dipolar coupling between the ^1H and the Fe dominates **Eq. 6**; therefore, the vector connecting each ^1H and Fe is a reasonable approximation of the hyperfine interaction (57). In addition to the hyperfine coupling, HYSCORE simulations take into account the transformation of the hyperfine tensor into the magnetic axis system. This transformation is defined by a set of Euler angles (α , β , γ) in EasySpin that follow the $zy'z'$ convention. In the case of an axial hyperfine interaction, only two angles are necessary. As with other $\{\text{FeNO}\}^7$ centers, the principal axis of the zfs and the molecular z axis are nearly coincident (57,58). As a result, these Euler rotations can be approximated using polar angles φ and θ , where φ is taken as the angle between the proton and the x-z plane, and θ defines the deviation from the z-axis defined by the Fe-NO bond. An illustration below **Table A2.3** shows how these angles relate to structure for a

^1H on **3MPA**. All angles were measured based on the geometry-optimized structure using Chimera 1.14 (UCSF, San Francisco, CA) (59). While simulations were not very sensitive to the value of φ , the value of θ was varied for His90 and His142 by <10 % for the best fit.

Computational Modeling. All calculations were performed using Orca version 4.2 (60).

Starting coordinates for geometry optimizations were extrapolated from the crystal structure presented in this work and the crystal structure of *Pa3MDO*, PDB 4TLF. Optimizations were done by capping the alpha-carbons of each residue with a methyl group. Histidines directly coordinated to the iron were capped at the beta-carbon. Preliminary optimizations were done by optimizing only hydrogens and constraining the dihedral angles of capped methyl group hydrogens relative to the constrained main group atoms. These methyl groups were constrained in all geometry optimizations. Histidines coordinated to iron were protonated at the δ -position. Geometry optimizations utilized two methods. Most optimizations used the BP'86 functional with the Ahlrichs def2-tzvp basis set on iron and directly coordinated atoms and the def2-svp basis set on all other atoms (61-63). This method has been shown to work well for transition metal complexes (64). The nitroxide containing complexes used the B3LYP functional with the same basis set allocation as described earlier. B3LYP was chosen among other tested functionals (e.g. BP'86, TPSS, PBE, and PBE0), as it was the only functional which could reproduce the expected antiferromagnetically coupled $S = 3/2$ $\{\text{FeNO}\}^7$ electronic structure with $S = 5/2$ for iron and $S = -1$ on the nitrosyl ligand. Additionally, the iron nitrosyl complexes used the "broken-symmetry" approach where the wavefunction was calculated as a high spin $S = 7/2$ system before flipping the sign of the spin on the nitrosyl atoms to converge to an $S = 3/2$ system (65). All calculations utilized Grimme's D3 dispersion correction, a CPCM solvent model with $\epsilon=4$ to emulate a protein environment, and either the resolution of identity (RI) for BP'86 or

resolution of identity and chain of sphere (RIJCOSX) approximation for B3LYP with def2/J auxiliary basis sets (66-69).

Mössbauer parameters were calculated using the B3LYP functional with the CP(PPP) basis set for iron and def2-TZVP on all other atoms. Orca specific settings featured the radial integration accuracy raised to 7 for the iron atom and a TightSCF convergence threshold with Grid5 and FinalGrid7 for the whole structure. Quadrupole splitting (ΔE_Q) and η were calculated directly in Orca using the electric field gradient on the iron nucleus. The isomer shift (δ) was determined from the method described by Remolt et al. using the s electron density at the iron nucleus (70).

EPR parameters were calculated with the same method described for Mössbauer parameter, with the exception of the IGLO-II basis set used for sulfur and EPR-II used for all other atoms (CP(PPP) was still used for iron). The spin-orbit coupling part of the ZFS-tensor was calculated with the coupled-perturbed method and the spin-spin part was calculated using the spin density of “UNO” orbitals (65). Isotropic and dipolar contributions of hyperfine coupling were calculated for the nitrogens of H90, H92, H142, and Arg168 and the hydrogens of H90, H92, H142, Arg168, 3MPA, and the phenol hydrogen of Tyr159.

2.3 Results

Crystal Structure of Av3MDO in complex with 3HPA. Following extensive sparse matrix screening, a condition was identified which gave rise to well-diffracting, rod-shaped Av3MDO crystals. The optimized crystals diffracted X-rays to ~ 2.2 Å resolution and belonged to space group $P3_1$ (**Table A2.1**). Structure determination was initially complicated by the presence of tetartohedral twinning and pseudosymmetry (see **Experimental Procedures** section for further details), but eventually the structure was solved by molecular replacement and refined against

reflections extending to 2.25 Å resolution (**Table A2.1**). The polypeptide is clearly resolved except for the extreme *N*- and *C*-termini, which are omitted from the final model. The asymmetric unit of the *Av3MDO* crystals consists of 12 monomers arranged in pairs of C_2 symmetric dimers. The moderately hydrophobic dimer interface buries an average of $\sim 1,260$ Å² (1199 to 1322 Å² depending on the specific dimer pair) or $\sim 13\%$ of the total monomer surface area (71) and is structurally similar to the dimers observed for 3MDOs from other bacteria (11,26), all suggesting that it represents a physiologically relevant assembly. This finding contrasts with cysteine dioxygenases, which are monomeric proteins (72,73).

Av3MDO exhibits the classic thiol dioxygenase cupin fold consisting of three *N*-terminal alpha-helices followed by a series of 11 β -strands forming the cupin β -barrel structure that houses the enzymatic active site (**Fig. 2.2A**). Owing to the near uniformity in structure between the 12 monomers ($C\alpha$ RMSD < 0.4 Å), chain B was used as the representative monomer for structural comparisons. Among 3MDOs of known structure, *Av3MDO* exhibits greatest sequence and structural similarity to the 3MDO enzyme from *Pseudomonas aeruginosa* (*Pa3MDO*, PDB accession code: 4TLF) with 70% sequence identity and a $C\alpha$ RMSD of ~ 1 Å. The largest main chain difference is found within the Leu113-Leu117 β hairpin where the insertion of an Arg in *Pa3MDO* results in a 5.8 Å shift at the tips of the β hairpins (**Fig. 2.2B**, *asterisk*). Like in *Pa3MDO* and other thiol dioxygenases (11,26,28), the iron center of *Av3MDO* is coordinated by three His residues (90, 92, and 142) contained within the conserved cupin motifs (**Fig. 2.2C**). Although the *Av3MDO* sample used for crystallization was $\sim 36\%$ loaded with iron, the iron *B*-factors are similar to those of the surrounding His ligands when the metal is modeled at full occupancy, indicating the metal-loaded enzyme selectively crystallized (**Table A2.1**). Additionally, the metal is modeled as an Fe(III) ion given that a bulk of the iron in the enzyme

sample used for crystallization was in the ferric oxidation state. However, some portion of the iron may have been photoreduced to Fe(II) during data collection. Analysis of residual electron density maps revealed two strong features near the *Av3MDO* iron center, which could not be successfully modeled with aquo ligands as was the case for *Pa3MDO* (11) (**Fig. A2.1**). As described in detail in the **Experimental Procedures** section, these density features were modeled with chloride (*trans* to His90) and 3-hydroxypropionic acid (**3HPA**, *trans* to His 92 and 142), the latter being present as contaminant in the polyacrylate solution used for crystallization (**Figs. 2.2C, A2.1 and A2.2**).

3HPA binds to the iron center in a bidentate fashion *via* its hydroxyl and carboxylate oxygen atoms with metal-ligand bond distances of ~2.1-2.2 Å (depending on the particular monomer). The carboxylate group simultaneously engages in an ionic interaction with Arg168, which is situated adjacent to the iron center. The **3HPA** carboxylate oxygen is located ~3.1 Å from the hydroxyl group of Tyr159, which is part of the ‘SHY’ motif and is known to influence substrate binding to the iron center (12). Notably, a significant interaction was not observed for **3HPA** with Gln63, the distinguishing residue of the ‘Gln-type’ thiol dioxygenases (26). These results indicate that the carboxylate-interacting Arg residue is relocated from position 61, as found in Arg-type thiol dioxygenases, to a non-homologous position in the ‘Gln-type’ thiol dioxygenases, as was previously suggested based on docking studies of **3MPA** in *Pa3MDO* (9).

Despite the close structural resemblance of **3HPA** to the native **3MPA** substrate of 3MDOs (**Fig. 2.3, inset**), the influence of this compound on 3MDO activity has, to the authors’ knowledge, never been examined. Given its observed mode of binding to the iron center, it was hypothesized that **3HPA** could act as an inhibitor of *Av3MDO*. This was tested by carrying out *Av3MDO* steady-state assays in the presence of **3HPA** (**Fig. 2.3**). The initial rate of *Av3MDO*-

catalyzed **3MPA** reactions was previously demonstrated to be independent of oxygen concentration down to $\sim 25 \mu\text{M}$ (13). Therefore, atmospheric oxygen concentration is sufficient to saturate the enzyme kinetics. Moreover, the consumption of oxygen per 3-sulfino propionic acid (**3SPA**) produced is essentially stoichiometric (14). Crucially, no oxygen is consumed upon mixing enzyme with excess of **3HPA** (10 mM). Therefore, the initial rate of oxygen consumption was used to monitor enzymatic inhibition as a function of inhibitor concentration. A Lineweaver-Burk plot of the activity data revealed an inhibition constant (K_i) of $280 \pm 26 \mu\text{M}$ and the intersection point at the ordinate is consistent with the behavior of a classic competitive inhibitor. These results establish that **3HPA** is an effective substrate analog and that its mode of binding to Av3MDO likely mirrors that of **3MPA**.

Chloride binds to the iron center *trans* to His90 at a distance of $\sim 2.4 \text{ \AA}$ and simultaneously contacts the hydroxyl moiety of Tyr159 forming a 2.7 \AA ion-dipole interaction (**Fig. 2.2C**). This corresponds to the binding site for solvent **3** in the resting Pa3MDO structure (**Fig. 2.1B**). To distinguish this site from the other solvent-bound positions, this is referred to as the *axial* Fe-coordination site henceforth. Similar binding of chloride has been observed in structures of CDO (27,50) but not in other ‘Gln-type’ thiol dioxygenases determined to date. Activity studies carried out in the presence of increasing Cl^- show a modest degree of inhibition (30%) at the 100 mM concentration found in the crystal (**Fig. A2.3**). However, EPR experiments demonstrated that Cl^- concentration has no impact on the extent of NO-binding to the **3MPA**-bound enzyme; therefore, this chloride inhibition is unlikely to reflect competition for O_2 -binding at the iron center (*data not shown*). Possibly, Cl^- coordination is only significant for the ferric form of the enzyme, owing to its ability to provide charge balance to the Fe(III)-site. Regardless, the presence of an anionic ligand at the putative O_2 -binding site of the enzyme

supports the idea that Tyr159 could facilitate the formation of an Fe(III)-superoxo intermediate during the Av3MDO catalytic cycle via hydrogen bonding (12).

Av3MDO Active Site Accessibility. MDO homologs of Av3MDO, including Pa3MDO, exhibit active site openings on one side of the cupin beta barrel that presumably serves as the passageway for organic substrate diffusion (**Fig. 2.4A**, *left*). However, inspection of the Av3MDO structure revealed that its active site is completely sealed off to the bulk solvent (**Fig. 2.4B**, *left*). In comparison to the homologous residues of Pa3MDO, residues Tyr61, Pro88, and Phe180 of Av3MDO are shifted inward towards each other to occlude the potential passageway (**Fig. 2.4**, **A** and **B**, *right panels*). Additional variation was observed within the active site of Av3MDO as compared to Pa3MDO including rotamer differences for Phe79 and Trp81 that were found in all 12 copies within the asymmetric unit (**Fig. 2.5**). Notably, the difference in Trp81 rotameric state results in different arrangements of the ‘SHY’ motif between Av3MDO (**Fig. 2.5A**) and Pa3MDO (**Fig. 2.5B**). In the Pa3MDO structure, the Ser155 residue of this motif forms a hydrogen bond with Glu104, which simultaneously interacts with the Trp80 indole NH group. The alternative conformation of Trp81 as observed in the Av3MDO structure, results in a ~2.2 Å shift in Glu105 towards Ser153, which also has an altered conformation in the Av3MDO structure (**Fig. 2.5**), resulting in a new H-bond interaction with Ser153. These collective changes produce an extension of the ‘SHY’ motif in Av3MDO.

Because intrinsic structural differences between Av3MDO and Pa3MDO are expected to be small owing to their high sequence similarity (**Fig. 2.2A**), the possibility that the observed active site differences could arise from the bound substrate mimetic in Av3MDO was considered. To test this hypothesis, alternative crystallization conditions were identified to allow investigation of the resting-state structure of Av3MDO. Following further sparse matrix

screening, a crystallization condition was identified containing a non-polyacrylate precipitant (pentaerythritol propoxylate) as well as sodium thiocyanate that produced yellowish, rod-shaped crystals. The crystals diffracted X-rays to ~ 3 Å resolution and belonged to space group $P6_122$ with a pair of dimers (same conserved interface described above) in the asymmetric unit. Strong difference density in the equatorial positions of the iron center was adequately explained by two water molecules while the axial position contained an elongated difference peak that was too strong to represent only water or chloride (**Fig. A2.4A**). Placement of thiocyanate, a well-known Fe(III)-binding ligand present at > 0.3 M concentration in the crystal mother liquor, at this position adequately accounted for the density with reasonable refined B -factors (**Table A2.1**). Because thiocyanate is an ambivalent ligand, test refinements were carried out with the anion bound via either its nitrogen or sulfur atoms. Analysis of difference maps and refined B -factors provided strong evidence that coordination is through the nitrogen atom, which is consistent with the coordination preferences of Fe(III), a hard Lewis acid, and small molecule crystallography results for high spin, non-heme iron model compounds (74). Although this structure is not a true “resting-state” form of Av3MDO, it gave the opportunity to address the question of whether the active site closure results from **3HPA** binding.

Contrary to the hypothesis, it was observed that the active site has maintained its closed state in this new crystal form (**Fig. A2.4B**). Hence, it was concluded that the closed conformation is energetically favorable *in crystallo* and that active site closure is not strictly coupled to **3HPA** coordination. Notable differences between the two Av3MDO crystal forms included a $\sim 40^\circ$ rotation of the Phe79 C β -C γ bond away from the iron center in the **3HPA**-bound structure as well as rotamer differences for Gln63 and Ile98, which all are likely a consequence of steric factors involving the different metal-bound ligands (**Fig. A2.4A**). By contrast, the conformation

of Trp81 is identical in every copy within the asymmetric units of the two *Av*3MDO structures, suggesting it represents an intrinsic structural difference as compared to *Pa*3MDO.

Computational Modeling of the *Av*3MDO-3MPA Complex. The structure of the *Av*3MDO-**3HPA** complex revealed a bidentate coordination of **3HPA** to the Fe-site through the hydroxyl-group and proximal oxygen of the carboxylate (**Fig. 2.2C** and **Fig. 2.5A**). Given the near structural equivalence of **3MPA** and the competitive inhibitor **3HPA**, a logical argument for bidentate **3MPA**-coordination within the enzymatic site can be made. Based on this hypothesis, the optimal 3MDO Fe-site geometry was determined for the bidentate *Av*3MDO-**3MPA** complex through density functional theory (DFT) calculations using the coordinates from the **3HPA**-bound *Av*3MDO crystal structure as a starting point. A truncated model for the inhibitor-bound active site, comprised of iron, His residues 90, 92, and 142, chloride, and Arg168, was generated and geometry-optimized with both **3HPA** and **3MPA** bound to the iron. Selected first-coordination sphere distances are presented in **Table A2.2** for the *Av*3MDO-**HPA** complex, **CYS**-bound CDO, synthetic non-heme mononuclear iron model complexes, and our computational models. Although the bulk oxidation state observed for *Av*3MDO was ferric prior to crystallization, the possibility of reduction by the synchrotron source could not be ruled out.

The pKa of the **3HPA**-hydroxyl (14.4-15.1) is expected to be much higher than the **3MPA**-thiol (~8) (75). While it is unlikely that the Fe-bound **3HPA**-hydroxyl is deprotonated, pKa-values for metal-coordinated water can decrease by several pH-units (76,77). To corroborate the ionization state of the **3HPA** inhibitor, optimized DFT models for the deprotonated (**3HPA²⁻**)- and protonated (**3HPA¹⁻**)-hydroxyl group were made with ferric and ferrous iron for comparison to the crystallographic results (**Table 2.1**). While the overall structures were similar (**Fig. A2.5**), the protonated (**3HPA¹⁻**)-bound model exhibited the lowest

RMSD values relative to crystallographic coordinates. Moreover, optimized bond distances and angles closely match what is observed for the Av3MDO-**3HPA** complex. From this it was concluded that the **3HPA**-inhibitor coordinates bidentate to the Fe-site through carboxylate and neutral hydroxyl-groups. For simplicity, all calculations and **3HPA**-bound structures discussed henceforth refer solely to the **3HPA**¹⁻ form in which the hydroxyl group is protonated. However, the calculated structural perturbations incurred by altering the oxidation state of the iron (+II versus +III) site fall within the inherent error (~0.1 Å) of the crystal structure. Therefore, neither oxidation state can be ruled out on the basis of these calculations.

Given the ambiguous oxidation state of the iron site, **3MPA**-bound structures were optimized in both the ferric and ferrous states. **Fig. 2.6** illustrates the Fe-sites for the Av3MDO-**3HPA** XRD structure and the DFT optimized **3MPA**-bound model. Selected bond distances and angles for both optimized structures are provided in **Table 2.1** for comparison. DFT-optimized structures show a shorter bond length between the iron and **3HPA**-hydroxyl than with the corresponding **3MPA**-thiolate [2.23 versus 2.32 Å, respectively for ferric and 2.26 vs 2.33 Å for ferrous]. Similarly, the distance separating the substrate carboxylate O-atom from the Fe-site (Fe-O_{carbox}) is closer for the ferric **3HPA**-bound model [2.08 for **3MPA** versus 1.97 Å for **3HPA**]. The trend is more drastic in the ferrous state with 2.25 Å for **3HPA** and 2.51 Å for **3MPA**. The longer bond length for the **3MPA**-bound structure is likely be attributed to (1) electrostatic interaction of the anionic carboxylate group with the adjacent cationic Arg168, and (2) inclusion of three negative charges [Cl⁻ and **3HPA**²⁻ (or **3MPA**²⁻)] in the Fe(II) coordination sphere. However, charge neutrality is easily remedied by loss of a chloride ligand in the ferrous enzyme. For both ferric computational models, these distances are shorter than observed in the Av3MDO-**3HPA** complex (~2.17 Å) while the both ferrous models are longer, but are well

within the estimated coordinate error of the crystal structure ($\sim 0.1 \text{ \AA}$). Similarly, the average Fe- N_{His} and Fe-Cl bond lengths for the **3MPA**-bound complex are largely invariant and any deviations observed fall well within the coordinate error of the *Av3MDO-3HPA* complex. For comparison, selected bond distances for thiolate-bound non-heme ferric thiol dioxygenase enzymes and model complexes are provided in **Table A2.2**.

Regardless of iron oxidation state (+II or +III), all optimized structures modeled (**3HPA**²⁻, **3HPA**¹⁻, and **3MPA**) predict a bidentate Fe-coordination *via* a single carboxylate O-atom and terminal oxide/hydroxyl or thiolate. As predicted by Aloï *et al.* (9), this places the substrate-carboxylate in a favorable position for electrostatic stabilization by cationic Arg168. Taken together with the XRD structure of the *Av3MDO-3HPA* complex, these optimized DFT structures infer that the native **3MPA** substrate coordinates to the *Av3MDO* iron site in a bidentate fashion as well.

Modeling of the (3MPA/NO)-bound *Av3MDO*. Nitric oxide is frequently used as a surrogate for molecular oxygen when characterizing non-heme iron oxidase/oxygenases. These experiments provide an excellent handle for EPR spectroscopy as the resulting iron-nitrosyl {FeNO}⁷ species is paramagnetic ($S = 3/2$). According to the Feltham–Enemark notation (78), the ground state $S = 3/2$ spin-manifold is produced by an antiferromagnetic coupling between a high-spin Fe(III) ($S = 5/2$) and a bound NO⁻ anion ($S = 1$). Moreover, given the similarity of the NO electronic structure to O₂, the resulting **(3MPA/NO)**-bound *Av3MDO* ternary complex likely provides insight into transient iron-oxo species produced during native turnover with oxygen. The **3MPA**-bound iron nitrosyl form of *Av3MDO* has been extensively characterized by EPR and Mössbauer spectroscopies (12,14). Such data provides an opportunity to validate computational models by comparing predicted spectroscopic properties to experimental values.

To this end, we studied whether bidentate iron coordination of **3MPA** is retained in the (**3MPA/NO**)-bound ternary complex. Starting from the optimized *Av3MDO-3MPA* model, a new structure for the (**3MPA/NO**)-bound *Av3MDO* active site was modeled and optimized. As shown in **Figure 2.7**, nitric oxide was placed in putative oxygen binding site *trans* to His90, essentially displacing the axial chloride in previous models. This positioning of NO is also consistent with previous EPR experiments which suggest that hydrogen-bonding from Tyr159 stabilizes NO-binding within the active site (12). The outer sphere Tyr159 was included in optimized models to account for this interaction.

The precise orientation of hydrogen bonding between Tyr159 and Fe-bound nitric oxide is not known. Therefore, an energy surface (79-81) for Tyr159 hydrogen bonding was generated from the *Av3MDO-3HPA* complex to evaluate likely H-bond acceptors (*Appendix*). As shown in **Fig. A2.6C**, an energy minimum is observed for H-bond donation from Tyr159 to the Fe-bound Cl atom for both ferrous and ferric oxidation states. Potentially, substitution of the axial chloride ligand for NO could alter the direction of the Tyr159 H-bond to favor donation to H157. However, this would be inconsistent with the previous EPR and Mössbauer results. Moreover, as both chlorine and nitrosyl ligands have an equivalent formal charge (-1), a reasonable argument can be made that H-bond donation from Tyr159 would similarly favor axially bound NO over His157. **Table A2.3** illustrates the influence of Tyr159 H-bond orientation on selected geometric parameters in the optimized (**3MPA/NO**)-bound *Av3MDO* Fe-site.

As an initial validation of the model, Mössbauer spectroscopic parameters were calculated for the optimized (**3MPA/NO**)-bound active site structures allowing comparison to the experimental values. As shown in **Table A2.4**, the isomer shift (δ) and quadrupole splitting (ΔE_Q) observed for the (**3MPA/NO**)-bound enzyme are reasonably reproduced by all optimized

models. In particular, ΔE_Q is highly sensitive to the nature and symmetry of ligands directly coordinated to the Fe-site. Thus, the closeness of calculated ΔE_Q -values strongly support the hypothesis of a bidentate **3MPA**-coordination within the (**3MPA**/NO)-bound enzyme. Overall, the ΔE_Q and asymmetry parameter (η) are best fit in optimized structures with Tyr159 donating a hydrogen bond to the N-atom of nitric oxide. However, the observed deviations among optimized structures largely fall within experimental error. Therefore, while the calculated Mössbauer parameters are entirely consistent with the optimized model shown in **Fig. 2.7**, the orientation of Tyr159 hydrogen bond donation cannot be definitively assigned based solely on these results.

HYSCORE of the (3MPA/NO)-bound Av3MDO. As noted above, characterization using continuous-wave (CW) EPR spectroscopy has been reported for iron-nitrosyl produced by treating **3MPA**-bound Av3MDO with nitric oxide (12). The CW EPR spectrum, shown in **Figure 2.8 (panel A)**, has observed g -values of 4.06, 3.96, and 2.01, consistent with a nearly axial ($E/D = 0.008$) $S = 3/2$ iron-nitrosyl site. Further, the measured axial zero field splitting ($D = 10 \pm 2 \text{ cm}^{-1}$) confirms that this signal is derived from a transition within the ground $|m_s = \pm 1/2\rangle$ doublet (38). These parameters are consistent with other spectroscopically and crystallographically characterized $S = 3/2$ iron-nitrosyl complexes (82,83). Crucially, the observed CW spectrum is nearly homogeneous and exhibits only minor contributions from known dinitrosyl (DNIC) complexes localized near $g = 2$. As a result, this complex is ideal for further characterization by hyperfine sublevel correlation spectroscopy (HYSCORE).

HYSCORE is a two-dimensional, four-pulse EPR technique that directly probes magnetic nuclei coupled to paramagnetic centers. This is an exceptionally sensitive technique that has the resolution necessary to distinguish and characterize individual nuclei. The magnitude of coupling

for each magnetic nucleus is highly dependent on the distance separating it from the paramagnetic center and its position relative to the magnetic axis. Similar HYSCORE experiments have been performed on a variety of non-heme enzymes to provide structural details about the (substrate/NO)-bound active site geometry (12,56-58,83-85). Moreover, relative to Mössbauer spectroscopy, HYSCORE is much more sensitive to subtle structural perturbations in the outer coordination sphere of the Fe-site, allowing for a more robust validation of the optimized (3MPA/NO)-bound Av3MDO structure.

Figure 2.8 (panel **B**) shows a representative HYSCORE spectrum of the (3MPA/NO)-bound Av3MDO complex. This spectrum was measured at 175 mT near the low-field edge of the CW EPR spectrum (**Fig. 2.8A**) where no contribution is present from the small proportion of DNIC that appears near $g = 2$ (12,38). The spectrum can be divided into two quadrants, the (-, +) quadrant, or the left half of the spectrum, and the (+, +) quadrant, or the right half of the spectrum. HYSCORE peaks appear in pairs that are reflected along the frequency diagonal at or near the nuclear Larmor frequency. The spectrum in **Fig. 2.8B** encodes precise information about the nuclei coupled to the $S = 3/2$ center. The spectrum is comprised of multiple, overlapping peaks characteristic of coupled ^{14}N and ^1H from the coordinated histidine ligands, NO, 3MPA, and other nearby residues making up the second coordination sphere. The peaks in the (-, +) quadrant represent strongly coupled ^{14}N nuclei; these peaks arise from nuclei where the hyperfine couplings are much greater than the ^{14}N Larmor frequency at 175 mT, ~ 0.54 MHz. These peaks are characteristic of what is observed for directly coordinated ^{14}N from histidine ligands (58,86). The (+, +) quadrant contains peak from weakly-coupled nuclei, namely those where the ^{14}N Larmor frequency is greater than the hyperfine coupling. **Fig. 2.8B** shows several overlapping peaks in the (+, +) quadrant below ~ 4 MHz; these peaks can be attributed to weakly-

coupled ^{14}N . In general, the remote ^{14}N of histidine ligands in metalloenzymes has a much weaker hyperfine coupling than the directly-coordinated ^{14}N (86). For example, the remote ^{14}N in histidine residues coordinated to the diiron site of the hydroxylase component of methane monooxygenase was found to have an isotropic coupling of 0.8 MHz, whereas the coordinated nitrogen had a coupling of 13.0 MHz (87). Therefore, the peaks in the (+, +) quadrant below 4 MHz are likely the remote ^{14}N on the three coordinated histidine ligands, although there could be a small contribution from second-sphere residues. In addition to ^{14}N , the (+, +) quadrant reveals multiple pairs of coupled ^1H peaks that are shifted from the ^1H Larmor frequency by significant dipolar couplings. The most intense region of the ^1H spectrum is an arc centered near (5, 12) MHz (ν_1, ν_2) that curves in towards the frequency diagonal. For simplicity, the coordinates refer to the peak that is on the high frequency side (larger ν_2) of the diagonal since each peak is nearly symmetric about the diagonal. The arc consists of several underlying peaks with similar anisotropic hyperfine couplings. There are two additional sets of peaks with frequencies of (6, 9) and (7, 8) MHz; these are more weakly-coupled ^1H as they appear closer to the ^1H Larmor frequency along the diagonal.

In order to derive specific structural information from HYSCORE results, computational simulations were carried out for comparison to the experimental spectrum. In this case, the observed HYSCORE spectrum depends on several discrete factors. For an $I = 1/2$ nucleus like ^1H , the peak positions are largely determined by the hyperfine coupling and the position of each nucleus with respect to the magnetic axis system. Beyond these parameters, additional complications arise for ^{14}N ($I = 1$) quadrupole nuclei. For this reason, attention was focused solely on the ^1H region of the spectrum. DFT calculations provide the geometry-optimized model from which distances and positions of each coupled ^1H can be derived. As such, it is possible to

simulate the HYSCORE spectrum by including all protons in the calculated model. However, the strongest couplings dominate the spectrum and the simulated intensity, which makes the intensity of weakly-coupled protons difficult to distinguish. Accordingly, simulations focused on eight individual ^1H with larger dipolar couplings (T_{total} derived from **Eq. 6**, and listed in **Table A2.5**). These protons are located on the coordinated histidine residues and on C3 of **3MPA**.

Figure 2.9 shows HYSCORE spectra and simulations at magnetic fields spanning the low-field region of the EPR spectrum. The simulations take into account eight protons with axial hyperfine couplings, each with a hyperfine tensor and a set of angles that relate the Fe- ^1H vector and the magnetic axis system. Many of these peaks overlap due to the similarities in dipolar couplings. *Appendix Figures A2.7-A2.10* illustrate the individual contributions for each simulated ^1H to the overall ^1H HYSCORE spectrum. The hyperfine tensors and Euler angles, listed in *Appendix (Table A2.5)*, were both derived directly from the DFT-optimized structure (see *Experimental Procedures* for details).

The intensity of a ^1H HYSCORE peaks depends in part on measurement conditions, but the shape of the contours, or the peak “footprint”, shows the range of observed nuclear frequencies, which is largely independent of measurement conditions. Consequently, HYSCORE spectra are simulated by matching the peak locations and shapes rather than the intensities. The simulations in **Figure 2.9**, plotted as black contours, match the observed experimental contour shapes well. While the overlap of ^1H peaks in the HYSCORE spectra limit the ability to optimize simulated contributions from individual ^1H nuclei, the calculated parameters obtained from our computational model reasonably reproduce the entire ^1H region of the observed spectra collected at multiple magnetic field positions. This later point is crucial as HYSCORE simulations are sensitive to changes in the hyperfine tensor and nuclear positions. To illustrate, **Fig. A2.11**

demonstrates how the simulated peaks for each ^1H can shift considerably with relatively small changes in hyperfine coupling and/or its position relative to the magnetic axis. Accordingly, the fact that the simulations shown in **Fig. 2.9** reasonably overlay onto the experimental peaks across multiple magnetic fields confirms that the calculated model produces reasonable distances and locations for the ^1H included in simulations. The protons in the optimized model that are not included in these simulations produce peaks that are too weak to resolve in the presence of the intense peaks from strongly-coupled protons. The **3MPA** protons on C2 fall into this category. Therefore, deuterium exchange experiments were performed as additional corroboration of bidentate **3MPA** coordination. These experiments uniquely identify any solvent-based ligands that would be present in the case of monodentate **3MPA** coordination. In principle, monodentate **3MPA**-coordination would be evident from the absence of strongly coupled ^1H peaks in samples prepared in $^2\text{H}_2\text{O}$ -buffer. In order to test this, samples of (**3MPA/NO**)-bound AvMDO were prepared in $^2\text{H}_2\text{O}$ -buffer in order to observe Fe-coordinated solvent ligands and exchangeable protons via lost peaks in the ^1H HYSCORE spectrum. However, as shown in **Fig. A2.11**, no such difference is observed in $^2\text{H}_2\text{O}$ samples. This observation is consistent with the absence of solvent-derived ligands directly coordinated to the Fe-site. Moreover, the observed non-exchangeable behavior is consistent with what is expected for each simulated group (**Table A2.5**).

Despite the inability to resolve the ^1H peaks associated with **3MPA** C2, a monodentate coordination of **3MPA** can be reasonably ruled out as this would significantly alter the position and distance of the **3MPA** C3 protons. Therefore, the ability to simulate the ^1H HYSCORE spectra collected at multiple magnetic fields along with the absence of exchangeable Fe-bound solvent ligands provides ample validation of the optimized (**3MPA/NO**)-bound Av3MDO Fe-site

model shown in **Fig. 2.7**. Collectively, these results corroborate that the bidentate inhibitor coordination reflected in the *Av*3MDO-**3HPA** complex is retained in the **3MPA**-bound **ES**-complex.

2.4 Discussion

Substrate-Coordination at the *Av*3MDO Fe-site. The structure of *Av*3MDO in complex with **3HPA** and corroborating DFT computational modeling of the **3MPA**-bound Fe-site are consistent with the bidentate substrate binding model proposed by Jameson and Karplus (9), where the substrate carboxylate group simultaneously interacts with iron as well as a nearby Arg168 residue. Interestingly, this Arg is non-homologous to the Arg residue employed by CDO to bind the carboxylate group of **CYS**, demonstrating the phenomenon of active site plasticity within different lineages of thiol dioxygenases (88). Given the ambiguous oxidation state in the *Av*3MDO-**3HPA** complex, additional spectroscopic validation was performed to independently corroborate the nature of **3MPA** coordination at the enzymatic Fe-site. Computationally predicted Mössbauer parameters (δ and ΔE_Q) for the optimized (**3MPA/NO**)-bound *Av*3MDO site (**Fig. 2.7**) are consistent with reported experimental values, thereby providing support for a similar **3MPA** coordination as that present in the *Av*3MDO-**3HPA** complex. Moreover, the closeness of simulated HYSCORE ^1H -couplings from coordinated His residues (His90, His92, and His142) and **3MPA** C3 to observed spectra collected across multiple field positions makes a powerful argument for the validity of the optimized (**3MPA/NO**)-bound *Av*3MDO active site model. Further, since coordination of NO to the Fe-site defines the primary magnetic axis, ^1H HYSCORE simulations also verify NO (and likely also dioxygen) binds to the axial Fe-site *trans* to His90. While ^1H -peaks associated with **3MPA** C2 are too weak to resolve, the absence of a difference in peaks between $^2\text{H}_2\text{O}/\text{H}_2\text{O}$ HYSCORE spectra demonstrates that no solvent-derived

ligands are in the *Av*3MDO **ES** complex, further supporting the conclusion of bidentate coordination of the native **3MPA** substrate at the enzymatic Fe-site. Collectively, the combined crystallographic, spectroscopic, and computational results provide an experimentally verified model for **3MPA**-binding within the *Av*3MDO active site resolving a debate in the literature regarding the denticity of substrate binding.

The chelate effect associated with bidentate **3MPA** Fe-coordination likely explains the ~2000-fold increase in the K_M value obtained in **CA**-reactions [0.013 ± 0.005 versus 26.5 ± 5 mM] (14). As mentioned in the **Introduction** section, this possibility was previously disregarded on the basis of kinetic and CW EPR studies performed on *Av*3MDO using multiple thiol-bearing substrates (**3MPA**, **CYS**, **CA**, and **ET**) (14). Taken together with the results presented here, it is evident that while bidentate coordination of the native **3MPA** substrate is favored, it is not obligatory for catalysis or O₂-activation. For substrates lacking a carboxylate functional group, only coordination of a thiolate (presumably *trans* to H92) is required for gating O₂-activation. This behavior is unlike mammalian CDO, which is highly specific for the L-isomer of **CYS** (35). Despite the ability to activate oxygen, *Av*3MDO reactions with non-carboxylate-bearing substrates are significantly uncoupled. For instance, in assays with **3MPA** and **CYS**, the consumption of molecular oxygen is essentially stoichiometric with formation of the sulfinic acid. However in reactions with **CA**, the coupling efficiency decreased by more than half [$40 \pm 9\%$] (14). Similarly, in reactions with the aromatic substrate 2-mercaptoanaline (**2MA**), O₂-consumption was observed without formation of a sulfinic acid product. Instead, the majority products of this reaction appear to be hydrogen peroxide and **2MA**-disulfide (89,90). By contrast, no oxygen consumption is observed in *Av*3MDO reactions with inhibitor (**3HPA**) in the absence of substrate. Similarly, no formation of iron-nitrosyl species is observed by EPR upon

addition of nitric oxide to Av3MDO in the presence of excess **3HPA**. Therefore, thiol Fe-coordination is essential for initiating O₂-activation; however, coordination of the substrate-carboxylate appears to attenuate non-productive ‘*off pathway*’ reactions following binding of O₂ to the **ES**-complex.

Orientation of Hydrogen Bonding Network. The Av3MDO-**3HPA** structure reveals an apparent change in the directionality of the ‘SHY’ proton relay network relative to the eukaryotic **CYS**-bound CDO. As shown in **Fig. A2.6A**, Trp77 of the mammalian CDO serves as an H-bond donor to Ser153 (W77 → S153). This dictates the direction of proton donation toward the Fe-site (*dashed blue lines*). By contrast, Glu105 of the Av3MDO-**3HPA** complex (**Fig. A2.6B**) is an H-bond acceptor, thus reversing (H157 → Ser155 → Glu105) hydrogen bond donation (*dashed red lines*). This leaves Tyr159 in a favorable position to donate a hydrogen atom to either His157 (*red*) or the axial Fe-bound chloride (*blue*). Previous studies reported for both Av3MDO and *Mus musculus* CDO that perturbations within the ‘SHY’ motif directly influence substrate-specificity and denticity of Fe-coordination, nitric oxide affinity and the oxygen *K_M*-value (12), as well as “*coupling*”; which is defined as the molar ratio of O₂-consumed per sulfinic acid produced (35). Despite these observations, the functional role of this conserved proton relay network remains poorly understood. An obvious question is whether the orientation of the Tyr159 H-bond donation plays any role in gating O₂-activation to coordination of the substrate at the Fe-site.

Energy surface scan calculations on the optimized Av3MDO-**3HPA** complex (**Fig. A2.6C**) predict Tyr159 H-bond donation to the Fe-bound chloride ligand is more stable relative to the Tyr159 → His157 configuration. This conclusion is consistent with previously reported both EPR and Mössbauer studies verifying direct interaction between the SHY Tyr-residue and enzymatic Fe-site (12,14,31). However, the particular atom (N or O) receiving the hydrogen

bond and how it would translate to catalytically relevant molecular oxygen remains unsettled.

While attempts were made to directly observe and assign the Tyr159 hydroxyl proton by HYSORE spectroscopy, the peaks overlapped with other weakly-coupled ^1H that had anisotropic hyperfine couplings of < 1 MHz. These more distant ^1H , which include the ^1H on the remote nitrogen of the three histidine residues and the ^1H on Arg168, overlap near the matrix ^1H peak that occurs at the nuclear Larmor frequency along the diagonal (Shown in **Fig. A2.13**).

Accordingly, the direction of the Tyr159 H-bond donation could not be corroborated spectroscopically.

Implications of the Closed Active Site Cavity Observed for Av3MDO. A notable finding from the structural analysis of Av3MDO was its lack of a patent tunnel for substrate diffusion to the active site. This observation was consistent across all crystallographically independent protomers of both Av3MDO crystal forms. This structural uniformity suggests that the closed conformation could be adopted in the solution form of the enzyme, although the fact that it is observed in both the presence and absence of **3HPA** seems to rule out the possibility that active site closure could be triggered by substrate binding. Such a uniformly occluded conformation has not, to the authors' knowledge, been observed for other thiol dioxygenases, although two of the four the subunits of the Pa3MDO crystal structure do appear to be occluded. Clearly, the active site must communicate with the bulk solvent to allow organic substrate entry, and the tunnel described in **Fig. 2.4** is the best candidate for such a role given its appropriate size and orientation with respect to the iron center. Discerning the relevance of the closed conformation observed for Av3MDO to the thiol dioxygenase catalytic cycle will require further research.

Figures

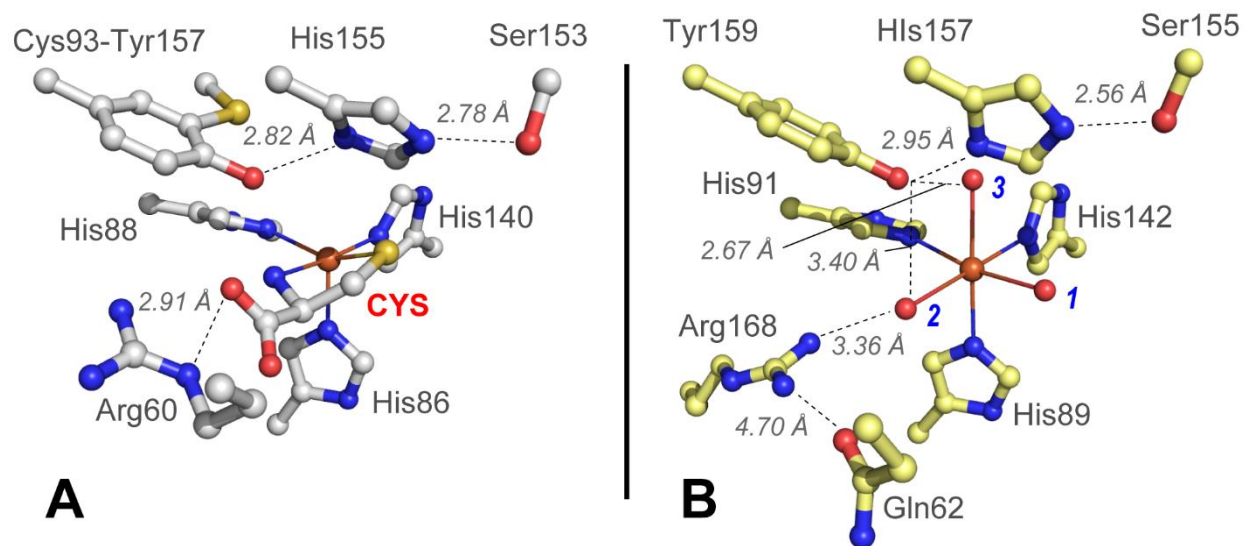


Figure 2.1: Structural comparison of mammalian CDO and *Pseudomonas aeruginosa* 3MDO active site. **A.** 1.6 Å X-ray diffraction structure of CYS-bound *Rattus norvegicus* CDO (PDB accession code 4IEV) (91). Selected atomic distances are designated by dashed lines. **B.** 2.14 Å X-ray diffraction structure of the *Pseudomonas aeruginosa* 3MDO active site (PDB 4TLF) (11). Fe-coordinated solvent ligands designated (1-3) for clarity (blue).

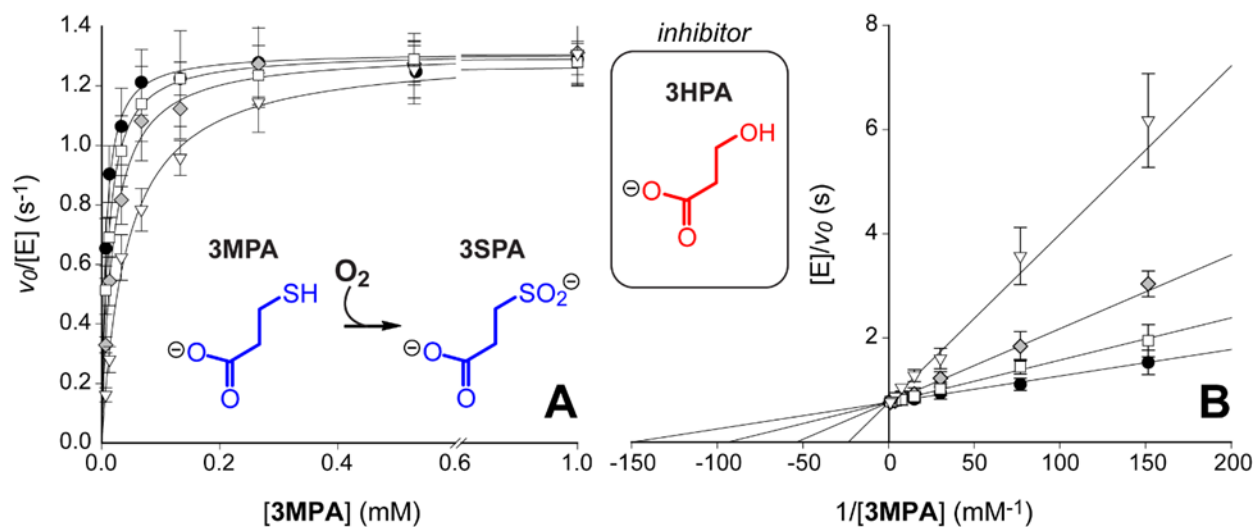


Figure 2.3: 3-hydroxypropionic acid (3HPA) inhibition of Av3MDO-catalyzed 3MPA-reactions. Kinetic data were collected in the presence of 167 μM (white square), 500 μM (grey diamond), and 1500 μM (white triangle) 3HPA for comparison to the uninhibited enzyme (black circle). SigmaPlot was used to globally fit enzyme kinetics in either Michaelis-Menten (A) or Lineweaver-Burk (B) fashion assuming a fully competitive model of inhibition. The resulting least-square fits (solid-lines) are overlaid on kinetic data to obtain values for k_{cat} , K_M , and K_I , as well as the error associated with each parameter [1.31 ± 0.01 s⁻¹, 6.7 ± 0.4 μM, and 280 ± 26 μM, respectively]. Michaelis-Menten results (A) are presented with a gap ranging from 0.6 to 0.8 mM 3MPA to avoid data crowding at low concentration.

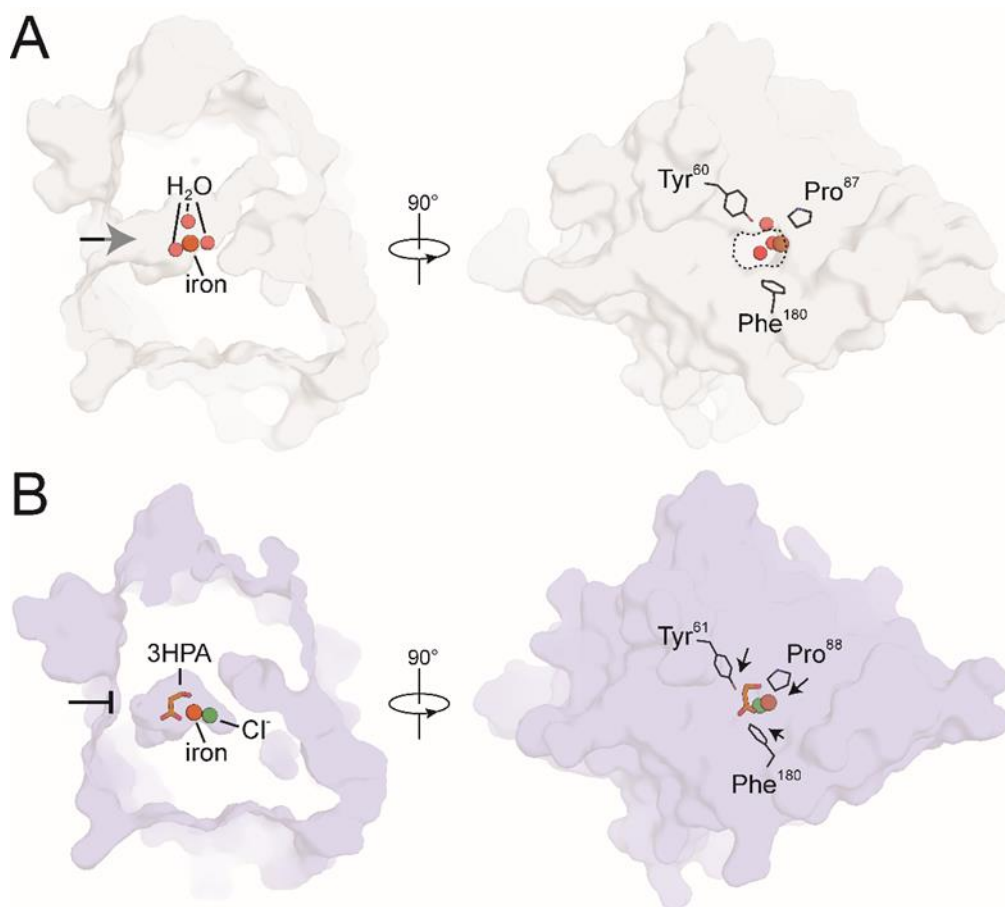


Figure 2.4: An occluded active site channel in *3HPA*-bound *Av3MDO*. In contrast to the resting-state structure of *Pa3MDO* (**A**) in which the active site is readily accessible to organic substrate through a passageway marked by an arrow on the left view and a dashed circle on the right view, the active site of *Av3MDO* (**B**) is completely sealed to bulk solvent due to positional differences in Tyr⁶¹, Pro⁸⁸, and Phe¹⁸⁰ (directionality differences with respect to the corresponding residues in *Pa3MDO* indicated by arrows). The structures are shown as Connolly surfaces.

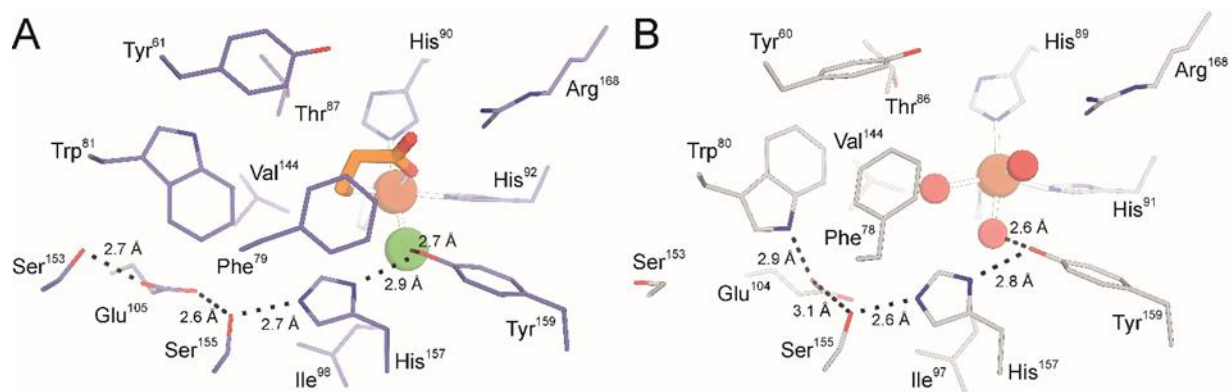


Figure 2.5: Active site differences observed between **3HPA**-bound Av3MDO and Pa3MDO. Comparison of the **3HPA**-bound structure of Av3MDO (**A**) and the resting-state structure of Pa3MDO (**B**) reveals active site conformational differences in Phe79/Phe78 and Trp81/Trp80 and a rearrangement of the ‘SHY’ H-bonding network with Glu105 interacting with Ser153 and Ser155 in the Av3MDO structure.

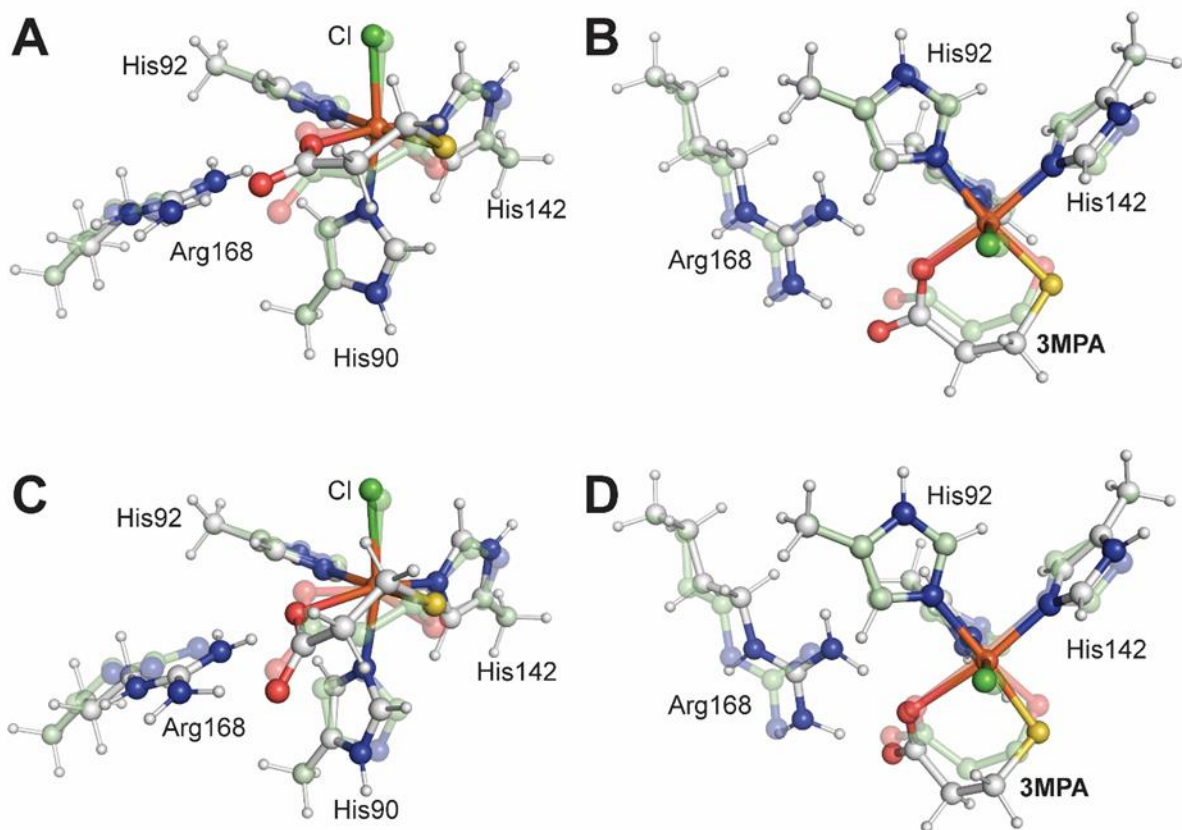


Figure 2.6: Overlay of 3HPA-bound Av3MDO complex (*transparent-green*) with a DFT optimized model (*white*) of the 3MPA-bound Av3MDO Fe(III)-site (RMSD, 0.417 Å). Shown from a side-on view (A) and following 90° rotation (B) through the bond of His142 (which is excluded from the image). These views are replicated in panels C and D for the ferrous optimized model. Selected distances, angles, and RMSD values are presented in Table 2.1 for comparison.

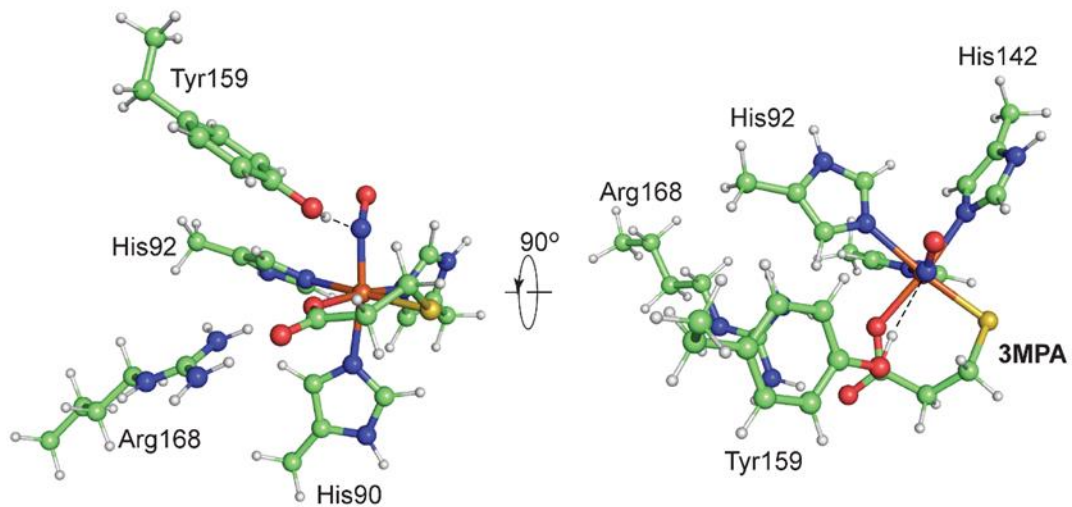


Figure 2.7: The optimized structure of the (3MPA/NO)-bound Av3MDO active site. The left panel displays a side view highlighting the axial nitric oxide ligand. The right panel rotates the structure to more clearly show bidentate coordination of 3MPA and Tyr159 hydrogen bond donation to the nitrogen of the NO ligand.

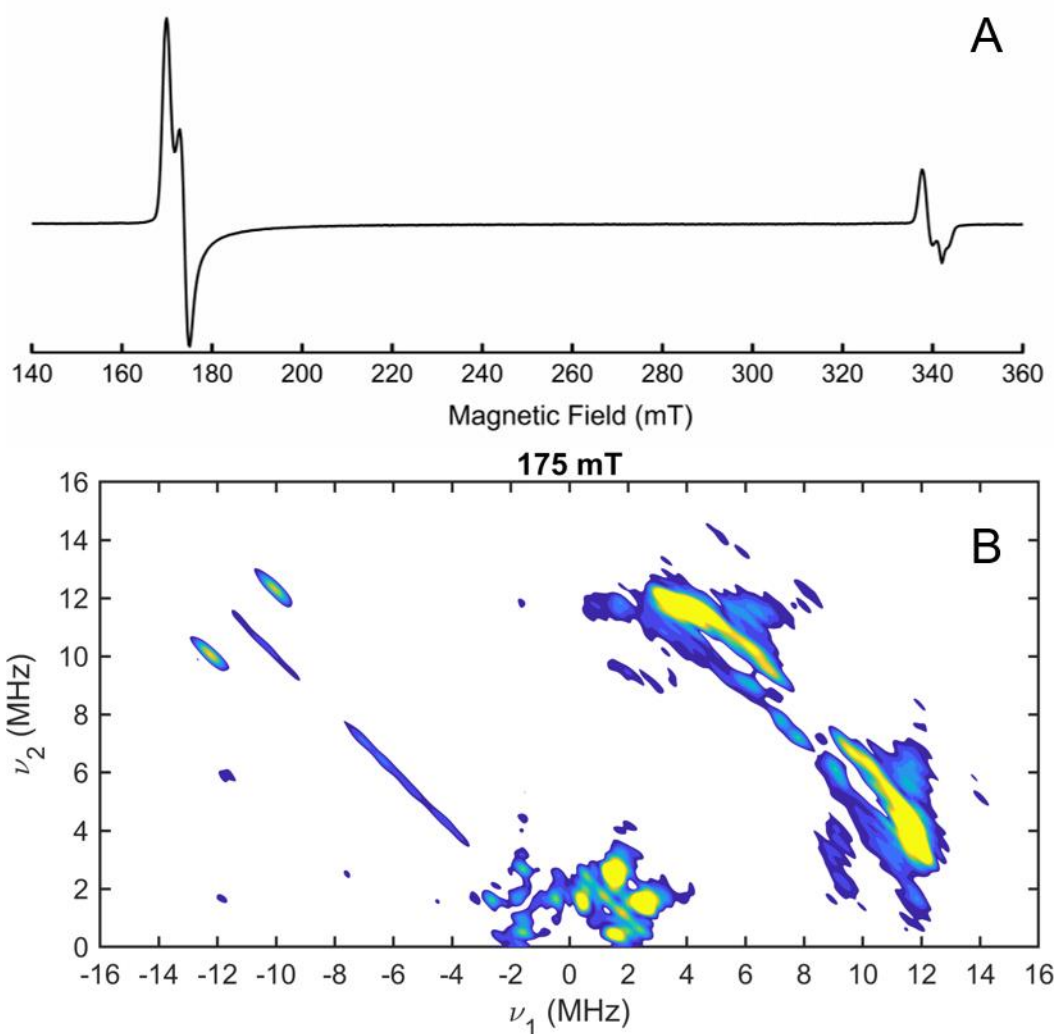


Figure 2.8: CW EPR (**A**) and HYSORE (**B**) spectra of (3MPA/NO)-bound Av3MDO iron-nitrosyl. The instrumental parameters for (**A**) (previously reported) are described in detail elsewhere (12). The data in (**B**) were collected with the following instrumental parameters: microwave frequency, 9.78 GHz; field position of 175 mT; temperature, 5 K; pulse repetition rate, 1.25 kHz; τ , 120 ns. Additional instrumental parameters are described in detail in *Experimental Procedures*.

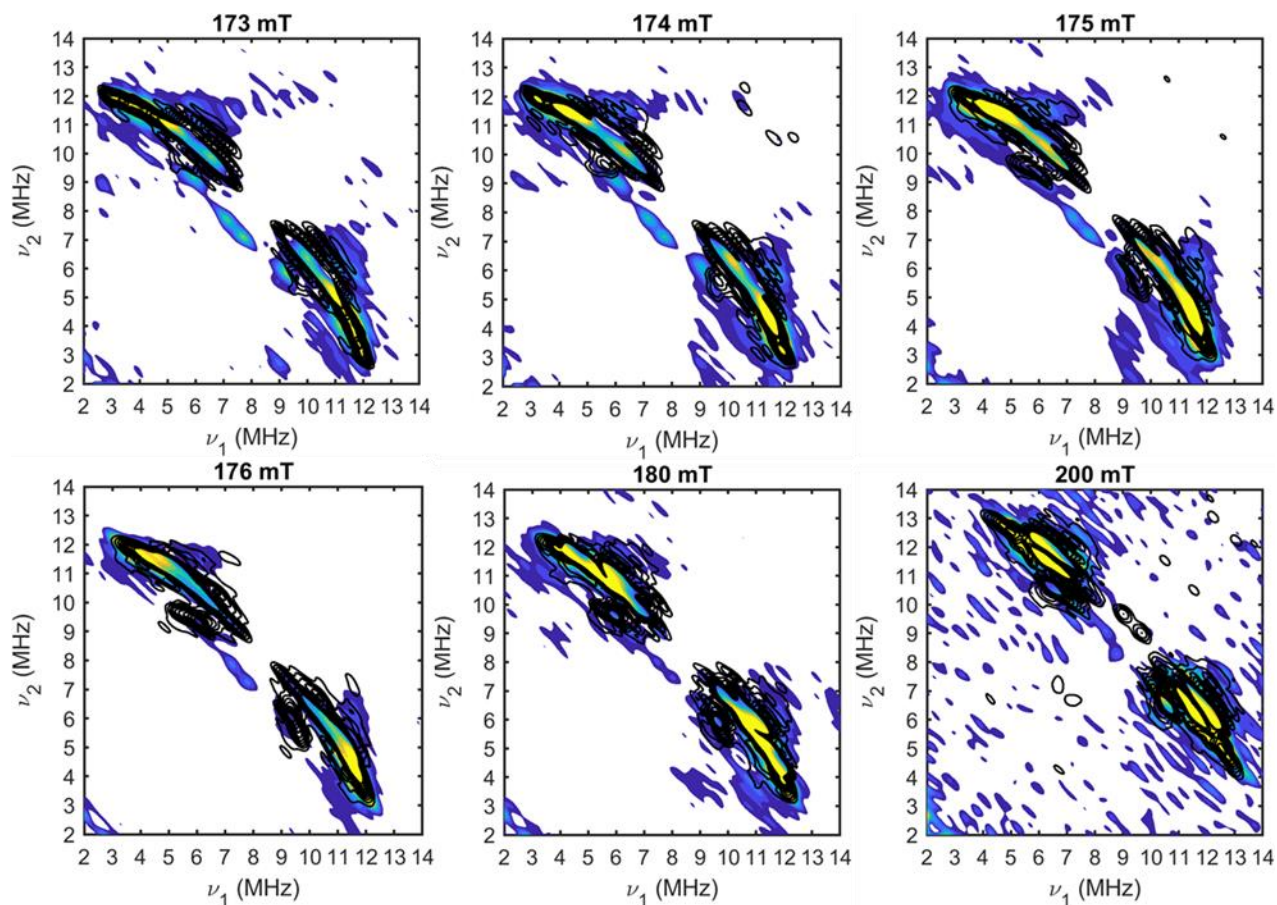


Figure 2.9: Comparison of (3MPA/NO)-bound Av3MDO HSCORE data (^1H region) collected at six field positions (173 – 200 mT) to simulations using parameters from the DFT optimized model. In each panel, experimental spectra are represented by the color contours whereas simulations are overlaid in black contours. Data were collected from 173 – 200 mT using the following instrumental parameters: microwave frequency, 9.78 GHz; temperature, 5 K; pulse repetition rate, 1.25 kHz; τ , 120 ns. Additional instrumental parameters are described in detail in *Experimental Procedures*.

| | 6XB9 | Fe(III) 3HPA ²⁻ | Fe(III) 3HPA ¹⁻ | Fe(III) 3MPA | Fe(II) 3HPA ²⁻ | Fe(II) 3HPA ¹⁻ | Fe(II) 3MPA |
|---|-------|--------------------------------------|--------------------------------------|------------------------|-------------------------------------|-------------------------------------|-----------------------|
| RMSD ^b | - | 0.382 | 0.248 | 0.417 | 0.517 | 0.357 | 0.547 |
| <i>Distance</i> (Å) | | | | | | | |
| Fe-O/S distance (Å) | 2.16 | 1.87 | 2.23 | 2.32 | 1.91 | 2.26 | 2.33 |
| Fe-O _(carb) ^a (Å) | 2.17 | 2.14 | 1.97 | 2.08 | 2.55 | 2.25 | 2.51 |
| Fe-Cl (Å) | 2.36 | 2.36 | 2.28 | 2.36 | 2.60 | 2.38 | 2.47 |
| Fe-His _(Ave) | 2.16 | 2.18 | 2.13 | 2.20 | 2.17 | 2.15 | 2.19 |
| Fe-H90 | 2.15 | 2.17 | 2.17 | 2.19 | 2.18 | 2.16 | 2.20 |
| Fe-H92 | 2.16 | 2.20 | 2.08 | 2.21 | 2.18 | 2.11 | 2.22 |
| Fe-H142 | 2.16 | 2.17 | 2.13 | 2.19 | 2.16 | 2.19 | 2.15 |
| <i>Angles</i> ∠ (°) | | | | | | | |
| Fe-O/S-C _α | 92.5 | 120.6 | 113.0 | 96.7 | 117.7 | 111.6 | 98.4 |
| H90-Fe-Cl | 175.7 | 171.8 | 174.0 | 169.3 | 169.6 | 171.5 | 166.3 |
| H92-Fe-O/S | 171.1 | 177.9 | 174.1 | 171.9 | 168.2 | 179.3 | 175.9 |
| O _(carb) -Fe-O/S | 101.1 | 92.1 | 85.1 | 96.4 | 82.6 | 88.6 | 88.8 |
| 3HPA/3MPA C ₁ -C ₂ -C ₃ | 114.6 | 116.9 | 115.6 | 119.3 | 116.5 | 117.8 | 117.6 |

^a Fe-O_(carb) designates the distance separating the Fe(III)-site from the **3HPA** (or **3MPA**) carboxylate O-atom. ^b. Hydrogens and all constrained atoms were excluded from RMSD calculations.

Table 2.1: Selected distances (*top*) and angles (*bottom*) of the Av3MDO-**3HPA** complex (PDB accession code 6XB9) as compared to optimized DFT models of the iron active bound to **3HPA** and **3MPA**. The **3HPA**-inhibitor was modeled as both the protonated and deprotonated alcohol (**3HPA**¹⁻ and **3HPA**²⁻) for comparison.

References

1. Stipanuk, M. H. (2004) Sulfur Amino Acid Metabolism: Pathways for Production and Removal of Homocysteine and Cysteine. *Annu Rev Nutr.* **24**, 539-577
2. Ewetz, L., and Sorbo, B. (1966) Characteristics of the Cysteinesulfinate-Forming Enzyme System in Rat Liver. *Biochim Biophys Acta.* **128**, 296-305
3. Sorbo, B., and Ewetz, L. (1965) The Enzymatic Oxidation of Cysteine to Cysteinesulfinate in Rat Liver. *Biochem Biophys Res Commun.* **18**, 359-363
4. Lombardini, J. B., Singer, T. P., and Boyer, P. D. (1969) Cysteine Oxygenase. *J Biol Chem.* **244**, 1172-1175
5. Dominy, J. E., Jr., Simmons, C. R., Karplus, P. A., Gehring, A. M., and Stipanuk, M. H. (2006) Identification and Characterization of Bacterial Cysteine Dioxygenases: a New Route of Cysteine Degradation for Eubacteria. *J Bacteriol.* **188**, 5561-5569
6. Fernandez, R. L., Dillon, S. L., Stipanuk, M. H., Fox, B. G., and Brunold, T. C. (2020) Spectroscopic Investigation of Cysteamine Dioxygenase. *Biochemistry* **59**, 2450-2458
7. Dominy, J. E., Simmons, C. R., Hirschberger, L. L., Hwang, J., Coloso, R. M., and Stipanuk, M. H. (2007) Discovery and Characterization of a Second Mammalian Thiol Dioxygenase, Cysteamine Dioxygenase. *J Biol Chem.* **282**, 25189-25198
8. Brandt, U., Schürmann, M., and Steinbüchel, A. (2014) Mercaptosuccinate Dioxygenase, a Cysteine Dioxygenase Homologue, from *Variovorax paradoxus* Strain B4 Is the Key Enzyme of Mercaptosuccinate Degradation. *J Biol Chem.* **289**, 30800-30809
9. Aloï, S., Davies, C. G., Karplus, P. A., Wilbanks, S. M., and Jameson, G. N. L. (2019) Substrate Specificity in Thiol Dioxygenases. *Biochemistry* **58**, 2398-2407
10. Fellner, M., Aloï, S., Tchesnokov, E. P., Wilbanks, S. M., and Jameson, G. N. L. (2016) Substrate and pH-Dependent Kinetic Profile of 3-Mercaptopropionate Dioxygenase from *Pseudomonas aeruginosa*. *Biochemistry* **55**, 1362-1371
11. Tchesnokov, E. P., Fellner, M., Siakkou, E., Kleffmann, T., Martin, L. W., Aloï, S., Lamont, I. L., Wilbanks, S. M., and Jameson, G. N. L. (2015) The cysteine dioxygenase homologue from *Pseudomonas aeruginosa* is a 3-mercaptopropionate dioxygenase. *J Biol Chem.* **290**, 24424-24437
12. Sardar, S., Weitz, A., Hendrich, M. P., and Pierce, B. S. (2019) Outer-Sphere Tyrosine 159 within the 3-Mercaptopropionic Acid Dioxygenase S-H-Y Motif Gates Substrate-Coordination Denticity at the Non-Heme Iron Active Site. *Biochemistry* **58**, 5135-5150
13. Crowell, J. K., Sardar, S., Hossain, M. S., Foss Jr, F. W., and Pierce, B. S. (2016) Non-chemical proton-dependent steps prior to O₂-activation limit *Azotobacter vinelandii* 3-

- mercaptopropionic acid dioxygenase (MDO) catalysis. *Arch Biochem Biophys.* **604**, 86-94
14. Pierce, B. S., Subedi, B. P., Sardar, S., and Crowell, J. K. (2015) The “Gln-Type” Thiol Dioxygenase from *Azotobacter vinelandii* Is a 3-Mercaptopropionic Acid Dioxygenase. *Biochemistry* **54**, 7477-7490
 15. Weits, D. A., Giuntoli, B., Kosmacz, M., Parlanti, S., Hubberten, H.-M., Riegler, H., Hoefgen, R., Perata, P., van Dongen, J. T., and Licausi, F. (2014) Plant cysteine oxidases control the oxygen-dependent branch of the N-end-rule pathway. *Nat Commun.* **5**, 3425
 16. White, M. D., Klecker, M., Hopkinson, R. J., Weits, D. A., Mueller, C., Naumann, C., O'Neill, R., Wickens, J., Yang, J., Brooks-Bartlett, J. C., Garman, E. F., Grossmann, T. N., Dissmeyer, N., and Flashman, E. (2017) Plant cysteine oxidases are dioxygenases that directly enable arginyl transferase-catalysed arginylation of N-end rule targets. *Nat Commun.* **8**, 14690
 17. Masson, N., Keeley, T. P., Giuntoli, B., White, M. D., Puerta, M. L., Perata, P., Hopkinson, R. J., Flashman, E., Licausi, F., and Ratcliffe, P. J. (2019) Conserved N-terminal cysteine dioxygenases transduce responses to hypoxia in animals and plants. *Science* **365**, 65-69
 18. Gordon, C., Emery, P., Bradley, H., and Waring, H. (1992) Abnormal sulfur oxidation in systemic lupus erythematosus. *Lancett* **229**, 25-26
 19. Heafield, M. T., Fearn, S., Steventon, G. B., Waring, R. H., Williams, A. C., and Sturman, S. G. (1990) Plasma cysteine and sulfate levels in patients with motor neurone, Parkinson's and Alzheimer's disease. *Neurosci Lett.* **110**, 216-220
 20. James, S. J., Cutler, P., Melnyk, S., Jernigan, S., Janak, L., Gaylor, D. W., and Neubrandner, J. A. (2004) Metabolic biomarkers of increased oxidative stress and impaired methylation capacity in children with autism. *Am J Clin Nutr.* **80**, 1611-1617
 21. Deth, R., Muratore, C., Benzecry, J., Power-Charnitsky, V.-A., and Waly, M. (2008) How environmental and genetic factors combine to cause autism: A redox/methylation hypothesis. *Neurotoxicology* **29**, 190-201
 22. Reddie, K. G., and Carroll, K. S. (2008) Expanding the functional diversity of proteins through cysteine oxidation. *Curr Opin Chem Biol.* **12**, 746-754
 23. Winyard, P. G., Moody, C. J., and Jacob, C. (2005) Oxidative activation of antioxidant defence. *Trends Biochem Sci.* **30**, 453-461
 24. Trachootham, D., Alexandre, J., and Huang, P. (2009) Targeting cancer cells by ROS-mediated mechanisms: a radical therapeutic approach? *Nat Rev Drug Discov* **8**, 579-591
 25. Behave, D. P., Muse, W. B., and Carroll, K. S. (2007) Drug Targets in Mycobacterial Sulfur Metabolism. *Infect Disord Drug Targets.* **7**, 140-158

26. Driggers, C. M., Hartman, S. J., and Karplus, P. A. (2015) Structures of Arg- and Gln-type bacterial cysteine dioxygenase homologs. *Protein Sci* **24**, 154-161
27. Driggers, C. M., Kean, K. M., Hirschberger, L. L., Cooley, R. B., Stipanuk, M. H., and Karplus, P. A. (2016) Structure-Based Insights into the Role of the Cys–Tyr Crosslink and Inhibitor Recognition by Mammalian Cysteine Dioxygenase. *J Mol Biol.* **428**, 3999-4012
28. Simmons, C. R., Liu, Q., Huang, Q., Hao, Q., Begley, T. P., Karplus, P. A., and Stipanuk, M. H. (2006) Crystal Structure of Mammalian Cysteine Dioxygenase: A NOVEL MONONUCLEAR IRON CENTER FOR CYSTEINE THIOL OXIDATION. *J Biol Chem.* **281**, 18723-18733
29. Davies, C. G., Fellner, M., Tchesnokov, E. P., Wilbanks, S. M., and Jameson, G. N. L. (2014) The Cys-Tyr Cross-Link of Cysteine Dioxygenase Changes the Optimal pH of the Reaction without a Structural Change. *Biochemistry* **53**, 7961-7968
30. Blaesi, E. J., Fox, B. G., and Brunold, T. C. (2015) Spectroscopic and Computational Investigation of the H155A Variant of Cysteine Dioxygenase: Geometric and Electronic Consequences of a Third-Sphere Amino Acid Substitution. *Biochemistry* **54**, 2874-2884
31. Li, W., Blaesi, E. J., Pecore, M. D., Crowell, J. K., and Pierce, B. S. (2013) Second-sphere interactions between the C93-Y157 cross-link and the substrate-bound Fe site influence the O₂-coupling efficiency in mouse cysteine dioxygenase. *Biochemistry* **52**, 9104-9119
32. Ye, S., Wu, X. a., Wei, L., Tang, D., Sun, P., Bartlam, M., and Rao, Z. (2007) An Insight into the Mechanism of Human Cysteine Dioxygenase: Key Roles of the Thioether-Bonded Tyrosine-Cysteine Cofactor. *J Biol Chem.* **282**, 3391-3402
33. Dominy, J. E., Hwang, J., Guo, S., Hirschberger, L. L., Zhang, S., and Stipanuk, M. H. (2008) Synthesis of Amino Acid Cofactor in Cysteine Dioxygenase Is Regulated by Substrate and Represents a Novel Post-translational Regulation of Activity. *J Biol Chem.* **283**, 12188-12201
34. Njeri, C. W., and Ellis, H. R. (2014) Shifting redox states of the iron center partitions CDO between crosslink formation or cysteine oxidation. *Arch Biochem Biophys.* **558**, 61-69
35. Li, W., and Pierce, B. S. (2015) Steady-state substrate specificity and O₂-coupling efficiency of mouse cysteine dioxygenase. *Arch Biochem Biophys.* **565**, 49-56
36. Easson, L. H., and Stedman, E. (1933) Studies on the relationship between chemical constitution and physiological action: Molecular dissymmetry and physiological activity. *Biochem J* **27**, 1257-1266

37. McCoy, J. G., Bailey, L. J., Bitto, E., Bingman, C. A., Aceti, D. J., Fox, B. G., and Phillips, G. N., Jr. (2006) Structure and mechanism of mouse cysteine dioxygenase. *Proc Natl Acad Sci USA*. **103**, 3084-3089
38. Pierce, B. S., Gardner, J. D., Bailey, L. J., Brunold, T. C., and Fox, B. G. (2007) Characterization of the Nitrosyl Adduct of Substrate-Bound Mouse Cysteine Dioxygenase by Electron Paramagnetic Resonance: Electronic Structure of the Active Site and Mechanistic Implications. *Biochemistry* **46**, 8569-8578
39. Crowell, J. K., Li, W., and Pierce, B. S. (2014) Oxidative uncoupling in cysteine dioxygenase is gated by a proton-sensitive intermediate. *Biochemistry* **53**, 7541-7548
40. Kabsch, W. (2010) XDS. *Acta Crystallogr. Sect. D. Biol. Crystallogr.* **66**, 125-132
41. Padilla, J. E., and Yeates, T. O. (2003) A statistic for local intensity differences: robustness to anisotropy and pseudo-centering and utility for detecting twinning. *Acta Crystallogr. Sect. D. Biol. Crystallogr.* **59**, 1124-1130
42. Zwart, P. H., Grosse-Kunstleve, R. W., Lebedev, A. A., Murshudov, G. N., and Adams, P. D. (2008) Surprises and pitfalls arising from (pseudo)symmetry. *Acta Crystallogr. Sect. D. Biol. Crystallogr.* **64**, 99-107
43. Yeates, T. O. (1997) Detecting and overcoming crystal twinning. *Methods Enzymol.* **276**, 344-358
44. McCoy, A. J., Grosse-Kunstleve, R. W., Adams, P. D., Winn, M. D., Storoni, L. C., and Read, R. J. (2007) Phaser crystallographic software. *J. Appl. Crystallogr.* **40**, 658-674
45. Emsley, P., Lohkamp, B., Scott, W. G., and Cowtan, K. (2010) Features and development of Coot. *Acta Crystallogr. Sect. D. Biol. Crystallogr.* **66**, 486-501
46. Murshudov, G. N., Skubak, P., Lebedev, A. A., Pannu, N. S., Steiner, R. A., Nicholls, R. A., Winn, M. D., Long, F., and Vagin, A. A. (2011) REFMAC5 for the refinement of macromolecular crystal structures. *Acta Crystallogr. Sect. D. Biol. Crystallogr.* **67**, 355-367
47. Lebedev, A. A., Vagin, A. A., and Murshudov, G. N. (2006) Intensity statistics in twinned crystals with examples from the PDB. *Acta Crystallogr. Sect. D. Biol. Crystallogr.* **62**, 83-95
48. Lebedev, A. A., and Isupov, M. N. (2014) Space-group and origin ambiguity in macromolecular structures with pseudo-symmetry and its treatment with the program Zanuda. *Acta Crystallogr. Sect. D. Biol. Crystallogr.* **70**, 2430-2443
49. Poon, B. K., Grosse-Kunstleve, R. W., Zwart, P. H., and Sauter, N. K. (2010) Detection and correction of underassigned rotational symmetry prior to structure deposition. *Acta Crystallogr. Sect. D. Biol. Crystallogr.* **66**, 503-513

50. Fellner, M., Siakkou, E., Faponle, A. S., Tchesnokov, E. P., de Visser, S. P., Wilbanks, S. M., and Jameson, G. N. (2016) Influence of cysteine 164 on active site structure in rat cysteine dioxygenase. *J. Biol. Inorg. Chem.* **21**, 501-510
51. Kumar, V., Ashok, S., and Park, S. (2013) Recent advances in biological production of 3-hydroxypropionic acid. *Biotechnol. Adv.* **31**, 945-961
52. Jers, C., Kalantari, A., Garg, A., and Mijakovic, I. (2019) Production of 3-Hydroxypropanoic Acid From Glycerol by Metabolically Engineered Bacteria. *Front. Bioeng. Biotechnol.* **7**, 124
53. Williams, C. J., Headd, J. J., Moriarty, N. W., Prisant, M. G., Videau, L. L., Deis, L. N., Verma, V., Keedy, D. A., Hintze, B. J., Chen, V. B., Jain, S., Lewis, S. M., Arendall, W. B., 3rd, Snoeyink, J., Adams, P. D., Lovell, S. C., Richardson, J. S., and Richardson, D. C. (2018) MolProbity: More and better reference data for improved all-atom structure validation. *Protein Sci.* **27**, 293-315
54. Read, R. J., Adams, P. D., Arendall, W. B., 3rd, Brunger, A. T., Emsley, P., Joosten, R. P., Kleywegt, G. J., Krissinel, E. B., Lutteke, T., Otwinowski, Z., Perrakis, A., Richardson, J. S., Sheffler, W. H., Smith, J. L., Tickle, I. J., Vriend, G., and Zwart, P. H. (2011) A new generation of crystallographic validation tools for the protein data bank. *Structure* **19**, 1395-1412
55. Stoll, S., and Schweiger, A. (2006) EasySpin, a comprehensive software package for spectral simulation and analysis in EPR. *J. Magn. Reson.* **178**, 42-55
56. Martinie, R. J., Livada, J., Chang, W.-c., Green, M. T., Krebs, C., Bollinger, J. M., and Silakov, A. (2015) Experimental Correlation of Substrate Position with Reaction Outcome in the Aliphatic Halogenase, SyrB2. *J Am Chem Soc.* **137**, 6912-6919
57. McCracken, J., Casey, T. M., and Hausinger, R. P. (2020) ¹H-HYSCORE Reveals Structural Details at the Fe(II) Active Site of Taurine:2-Oxoglutarate Dioxygenase. *Appl Magn Reson.*
58. McCracken, J., Eser, B. E., Mannikko, D., Krzyaniak, M. D., and Fitzpatrick, P. F. (2015) HYSCORE Analysis of the Effects of Substrates on Coordination of Water to the Active Site Iron in Tyrosine Hydroxylase. *Biochemistry* **54**, 3759-3771
59. Pettersen, E. F., Goddard, T. D., Huang, C. C., Couch, G. S., Greenblatt, D. M., Meng, E. C., and Ferrin, T. E. (2004) UCSF Chimera—A visualization system for exploratory research and analysis. *J Comput Chem.* **25**, 1605-1612
60. Neese, F. (2017) Software update: the ORCA program system, version 4.0. *WIREs Comput Mol Sci.* **8**, e1327
61. Weigend, F., and Ahlrichs, R. (2005) Balanced basis sets of split valence, triple zeta valence and quadruple zeta valence quality for H to Rn: Design and assessment of accuracy. *Phys Chem Chem Phys.* **7**, 3297-3305

62. Becke, A. D. (1986) Density functional calculations of molecular bond energies. *J Chem Phys.* **84**, 4524-4529
63. Perdew, J. P. (1986) Density-functional approximation for the correlation energy of the inhomogeneous electron gas. *Phys Rev B.* **33**, 8822-8824
64. Bühl, M., and Kabrede, H. (2006) Geometries of Transition-Metal Complexes from Density-Functional Theory. *J Chem Theory Comput.* **2**, 1282-1290
65. Ye, S., Price, J. C., Barr, E. W., Green, M. T., Bollinger, J. M., Krebs, C., and Neese, F. (2010) Cryoreduction of the NO-Adduct of Taurine: α -Ketoglutarate Dioxygenase (TauD) Yields an Elusive {FeNO}₈ Species. *J Am Chem Soc.* **132**, 4739-4751
66. Vahtras, O., Almlöf, J., and Feyereisen, M. W. (1993) Integral approximations for LCAO-SCF calculations. *Chem Phys Lett.* **213**, 514-518
67. Kendall, R. A., and Früchtl, H. A. (1997) The impact of the resolution of the identity approximate integral method on modern ab initio algorithm development. *Theor Chem Acc.* **97**, 158-163
68. Neese, F., Wennmohs, F., Hansen, A., and Becker, U. (2009) Efficient, approximate and parallel Hartree–Fock and hybrid DFT calculations. A ‘chain-of-spheres’ algorithm for the Hartree–Fock exchange. *Chem Phys.* **356**, 98-109
69. Grimme, S., Antony, J., Ehrlich, S., and Krieg, H. (2010) A consistent and accurate ab initio parametrization of density functional dispersion correction (DFT-D) for the 94 elements H-Pu. *J Chem Phys.* **132**, 154104
70. Römelt, M., Ye, S., and Neese, F. (2009) Calibration of modern density functional theory methods for the prediction of ⁵⁷Fe Mössbauer isomer shifts: meta-GGA and double-hybrid functionals. *Inorg. Chem.* **48**, 784-785
71. Krissinel, E., and Henrick, K. (2007) Inference of macromolecular assemblies from crystalline state. *J. Mol. Biol.* **372**, 774-797
72. McCoy, J. G., Bailey, L. J., Bitto, E., Bingman, C. A., Aceti, D. J., Fox, B. G., and Phillips, G. N., Jr. (2006) Structure and mechanism of mouse cysteine dioxygenase. *Proc. Natl. Acad. Sci. USA* **103**, 3084-3089
73. Driggers, C. M., Stipanuk, M. H., and Karplus, P. A. (2015) Mammalian cysteine dioxygenase. in *Encyclopedia of Inorganic and Bioinorganic Chemistry* (Scott, R. A. ed., John Wiley & Sons, Ltd.
74. Abibat Salaudeen, A., Kilner, C. A., and Halcrow, M. A. (2008) Mononuclear and dinuclear iron thiocyanate and selenocyanate complexes of tris-pyrazolylmethane ligands. *Polyhedron* **27**, 2569-2576

75. Silva, A. M. N., Kong, X., and Hider, R. C. (2009) Determination of the pKa value of the hydroxyl group in the α -hydroxycarboxylates citrate, malate and lactate by ^{13}C NMR: implications for metal coordination in biological systems. *BioMetals* **22**, 771-778
76. Brines, L. M., Coggins, M. K., Poon, P. C. Y., Toledo, S., Kaminsky, W., Kirk, M. L., and Kovacs, J. A. (2015) Water-Soluble Fe(II)–H₂O Complex with a Weak O–H Bond Transfers a Hydrogen Atom via an Observable Monomeric Fe(III)–OH. *J Am Chem Soc.* **137**, 2253-2264
77. Tyler, L. A., Noveron, J. C., Olmstead, M. M., and Mascharak, P. K. (2003) Modulation of the pKa of Metal-Bound Water via Oxidation of Thiolato Sulfur in Model Complexes of Co(III) Containing Nitrile Hydratase: Insight into Possible Effect of Cysteine Oxidation in Co–Nitrile Hydratase. *Inorg Chem.* **42**, 5751-5761
78. Enemark, J. H., and Feltham, R. D. (1974) Principles of structure, bonding, and reactivity for metal nitrosyl complexes. *Coord Chem Rev.* **13**, 339-406
79. Dajnowicz, S., Parks, J. M., Hu, X., Gesler, K., Kovalevsky, A. Y., and Mueser, T. C. (2017) Direct evidence that an extended hydrogen-bonding network influences activation of pyridoxal 5'-phosphate in aspartate aminotransferase. *J Biol Chem.* **292**, 5970-5980
80. Bykov, D., Plog, M., and Neese, F. (2014) Heme-bound nitroxyl, hydroxylamine, and ammonia ligands as intermediates in the reaction cycle of cytochrome c nitrite reductase: a theoretical study. *J Biol Inorg Chem* **19**, 97-112
81. Kampa, M., Lubitz, W., van Gastel, M., and Neese, F. (2012) Computational study of the electronic structure and magnetic properties of the Ni–C state in [NiFe] hydrogenases including the second coordination sphere. *J Biol Inorg Chem* **17**, 1269-1281
82. Brown, C. D., Neidig, M. L., Neibergall, M. B., Lipscomb, J. D., and Solomon, E. I. (2007) VTVH-MCD and DFT Studies of Thiolate Bonding to {FeNO}7/{FeO₂}₈ Complexes of Isopenicillin N Synthase: Substrate Determination of Oxidase versus Oxygenase Activity in Nonheme Fe Enzymes. *J Am Chem Soc.* **129**, 7427-7438
83. Arciero, D. M., Lipscomb, J. D., Huynh, B. H., Kent, T. A., and Münck, E. (1983) EPR and Mössbauer studies of protocatechuate 4,5-dioxygenase. Characterization of a new Fe²⁺ environment. *J Biol Chem.* **258**, 14981-14991
84. Mitchell, A. J., Dunham, N. P., Martinie, R. J., Bergman, J. A., Pollock, C. J., Hu, K., Allen, B. D., Chang, W.-C., Silakov, A., Bollinger, J. M., Jr., Krebs, C., and Boal, A. K. (2017) Visualizing the Reaction Cycle in an Iron(II)- and 2-(Oxo)-glutarate-Dependent Hydroxylase. *J Am Chem Soc.* **139**, 13830-13836
85. Yu, C.-P., Tang, Y., Cha, L., Milikisiyants, S., Smirnova, T. I., Smirnov, A. I., Guo, Y., and Chang, W.-c. (2018) Elucidating the Reaction Pathway of Decarboxylation-Assisted Olefination Catalyzed by a Mononuclear Non-Heme Iron Enzyme. *J Am Chem Soc.* **140**, 15190-15193

86. Dikanov, S. A., Davydov, R. M., Gräslund, A., and Bowman, M. K. (1998) Two-Dimensional ESEEM Spectroscopy of Nitrogen Hyperfine Couplings in Methemerythrin and Azidomethemerythrin. *J Am Chem Soc.* **120**, 6797-6805
87. Hendrich, M. P., Fox, B. G., Andersson, K. K., Debrunner, P. G., and Lipscomb, J. D. (1992) Ligation of the diiron site of the hydroxylase component of methane monooxygenase. An electron nuclear double resonance study. *J Biol Chem.* **267**, 261-269
88. Todd, A. E., Orengo, C. A., and Thornton, J. M. (2002) Plasticity of enzyme active sites. *Trends Biochem Sci* **27**, 419-426
89. Morrow, W. P., Sardar, S., Thapa, P., Hossain, M. S., Foss, F. W., and Pierce, B. S. (2017) Thiol dioxygenase turnover yields benzothiazole products from 2-mercaptoaniline and O₂-dependent oxidation of primary alcohols. *Arch Biochem Biophys.* **631**, 66-74
90. Gordon, J. B., McGale, J. P., Prendergast, J. R., Shirani-Sarmazeh, Z., Siegler, M. A., Jameson, G. N. L., and Goldberg, D. P. (2018) Structures, Spectroscopic Properties, and Dioxygen Reactivity of 5- and 6-Coordinate Nonheme Iron(II) Complexes: A Combined Enzyme/Model Study of Thiol Dioxygenases. *J Am Chem Soc.* **140**, 14807-14822
91. Driggers, C. M., Cooley, R. B., Sankaran, B., Hirschberger, L. L., Stipanuk, M. H., and Karplus, P. A. (2013) Cysteine Dioxygenase Structures from pH4 to 9: Consistent Cys-Persulfenate Formation at Intermediate pH and a Cys-Bound Enzyme at Higher pH. *J Mol Biol.* **425**, 3121-3136

Appendix

Table A2.1. X-ray diffraction data collection and structure refinement statistics

| <i>Data collection and processing¹</i> | | |
|---|--------------------------------|--------------------------------------|
| Crystal | 3-HPA complex (crystal form A) | Thiocyanate complex (crystal form B) |
| X-ray source | NSLS-II (FMX 17-ID-2) | APS (NE-CAT 24-ID-E) |
| Wavelength (Å) | 0.979339 | 0.979180 |
| Space group | <i>P</i> 3 ₁ | <i>P</i> 6 ₁ 22 |
| Unit cell lengths (Å) | a = 178.22, c = 75.92 | a = 102.18, c = 301.93 |
| Resolution (Å) [†] | 50 – 2.25 (2.39 – 2.25) | 50 – 2.95 (3.13 – 2.95) |
| Unique reflections | 127,973 (20,673) | 20,505 (3,185) |
| Multiplicity | 4.4 (4.4) | 12.9 (13.4) |
| Completeness (%) | 99.9 (99.8) | 99.8 (99.2) |
| $\langle I/\sigma I \rangle$ | 6.35 (0.78) | 12.9 (0.98) |
| $R_{\text{merge}}I$ (%) | 15.0 (164.2) | 18.5 (288.3) |
| CC _{1/2} (%) | 99.3 (48.4) | 99.9 (46.8) |
| Wilson <i>B</i> factor (Å ²) | 55 | 86 |
| <i>Refinement</i> | | |
| Resolution (Å) | 46.26 – 2.25 | 49.88 – 2.95 |
| No reflections [‡] | 121,709 (6,243) | 19,476 (1,026) |
| $R_{\text{work}}/R_{\text{free}}$ (%) [‡] | 19.6 (22.6) | 21.4 (24.1) |
| Twin law (α) [∇] | k, h, -l (0.34) | N/A |
| No. atoms | 18,870 | 6,166 |
| Protein | 18,374 | 6,124 |
| Iron | 12 | 4 |
| 3-Hydropropionic acid | 72 | --- |
| Chloride/thiocyanate | 13 (Cl ⁻) | 12 (SCN ⁻) |
| Water | 395 | 24 |
| $\langle B\text{-factor} \rangle$ (Å ²) | 57 | 105 |
| Protein | 57 | 105 |
| Iron | 52 | 86 |
| 3-Hydroxypropionic acid | 53 | --- |
| Chloride/thiocyanate | 63 | 122 |
| Water | 50 | 81 |
| RMS deviations | | |
| Bond lengths (Å) | 0.006 | 0.003 |
| Bond angles (°) | 1.27 | 1.22 |
| Ramachandran plot (% favored/outliers)* | 96.4/0 | 94.0/0 |
| Molprobit score (%) | 100 | 100 |
| PDB accession code | 6XB9 | 7KOV |

¹Data were collected from a single crystal

[†]Values in parentheses are for the highest resolution shell of data

[‡]Values in parentheses are the number of reflections used for cross-validation

[∇]Twin fraction was refined in REFMAC based on the observed and calculated amplitudes

Table A2.2. Comparison of *Av*3MDO bond distances with other thiolate-bound non-heme iron complexes. Distances are shown for the iron to bound thiolate (Fe-S), either bidentate bound substrate carboxylate, amine, or equivalent (Fe-O or Fe-N_{amine}), and average iron to histidine or equivalent nitrogen. All units are in Ångströms.

| | Fe-S | Fe-O | Fe-N _{amine} | Fe-N _{his ave} | ref |
|---|-------------------|-------------------|-----------------------|-------------------------|-----------|
| <i>Av</i> MDO- 3HPA complex ^a | 2.16 ^b | 2.17 | - | 2.16 | This work |
| Fe^{II} structures | | | | | |
| <i>Av</i> MDO 3HPA ¹⁻ -bound ^c | 2.26 ^b | 2.25 | - | 2.15 | This work |
| <i>Av</i> MDO 3HPA ²⁻ -bound ^c | 1.91 ^b | 2.55 ^d | - | 2.17 | This work |
| <i>Av</i> MDO 3MPA -bound ^c | 2.33 | 2.51 ^d | - | 2.19 | This work |
| <i>Rn</i> CDO cysteine-bound ^a | 2.35 | - | 2.35 | 2.17 | (1) |
| [Fe ^{II} (2-MTS)(^{Ph} 2TIP)]BPh ₄ ^a | 2.32 | 2.12 | - | 2.16 | (2) |
| [Fe ^{II} (CysOEt)(^{Ph} 2TIP)]BPh ₄ ^a | 2.31 | - | 2.26 | 2.17 | (3) |
| [Fe ^{II} (Me ₃ TACN)(abt)(OTf)] ^a | 2.44 | - | 2.23 | 2.25 | (4) |
| [Fe ^{II} (Me ₃ TACN)(abt ^{CF3})(OTf)] ^a | 2.43 | - | 2.24 | 2.24 | (4) |
| [Fe ^{II} (iPr ₃ TACN)(abt)(OTf)] ^a | 2.36 | - | 2.26 | 2.20 | (4) |
| [Fe ^{II} (iPr ₃ TACN)(abt ^{CF3})(OTf)] ^a | 2.38 | - | 2.27 | 2.20 | (4) |
| Fe^{III} structures | | | | | |
| <i>Av</i> 3MDO 3HPA ¹⁻ -bound ^c | 2.23 ^b | 1.97 | - | 2.13 | This work |
| <i>Av</i> 3MDO 3HPA ²⁻ -bound ^c | 1.87 ^b | 2.14 | - | 2.18 | This work |
| <i>Av</i> 3MDO 3MPA -bound ^c | 2.32 | 2.08 | - | 2.20 | This work |
| [Fe ^{III} (2-MTS)(^{Ph} 2TIP)]-CN ^c | 2.20 | 1.96 | - | 2.17 | (2) |
| [Fe ^{II} (CysOEt)(^{Ph} 2TIP)]-CN ^c | 2.18 | - | 2.05 | 2.17 | (2) |
| (L-Cys/CN)-CDO cross-linked ^c | 2.28 | - | 2.09 | 2.07 | (5) |
| (L-Cys/CN)-CDO non-cross-linked ^c | 2.26 | - | 2.11 | 2.05 | (5) |

^a Distances obtained from crystal structure. ^b 3-oxide of **3HPA** instead of sulfur. ^c Distances obtained from computational methods. ^d The longer Fe-O_(carboxylate) distance of 2.51 - 2.55 Å can likely be attributed to the electrostatic interaction of the anionic carboxylate group with adjacent Arg168. This is more pronounced when coordinating three anionic ligands due to the excess negative charge surrounding the Fe(II)-site. This suggests that chloride is an unfavorable ligand for the catalytically relevant **3MPA**-bound *Av*3MDO Fe(II)-site.

Table A2.3. Geometric properties of the DFT optimized (**3MPA/NO**)-Fe(II) Av3MDO models. Three structures were optimized differing in the hydrogen bond donation of the Tyr159 hydroxyl group.

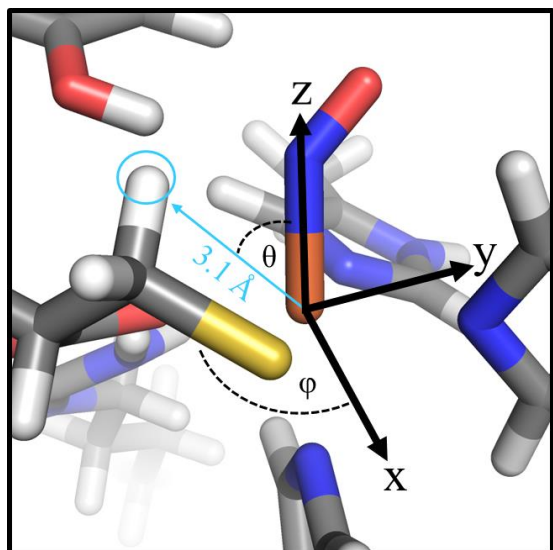
| | Tyr-OH → N(NO) | Tyr-OH → O(NO) | Tyr-OH → Nδ-His157 |
|--|----------------|----------------|--------------------|
| <i>Distance (Å)</i> | | | |
| Fe-S | 2.38 | 2.40 | 2.41 |
| Fe-O _(carb) | 2.08 | 2.08 | 2.11 |
| Fe-N(NO) | 1.89 | 1.84 | 1.82 |
| N-O | 1.18 | 1.18 | 1.17 |
| Fe-His _(Ave) | 2.21 | 2.23 | 2.24 |
| Fe-H90 | 2.19 | 2.23 | 2.19 |
| Fe-H92 | 2.24 | 2.26 | 2.29 |
| Fe-H142 | 2.21 | 2.20 | 2.23 |
| Tyr-OH-X ^a | 2.11 | 1.98 | 1.78 |
| <i>Angles ∠ (°)</i> | | | |
| Fe-S-C _α | 95.7 | 97.8 | 94.0 |
| Fe-N-O | 138.7 | 145.7 | 151.0 |
| H90-Fe-N(NO) | 170.0 | 176.8 | 168.9 |
| H92-Fe-S | 174.8 | 175.2 | 173.9 |
| O _(carb) -Fe-S | 95.0 | 93.8 | 95.3 |
| 3MPA C ₁ -C ₂ -C ₃ | 120.4 | 120.1 | 118.8 |

^a X refers to the hydrogen binding partner of the Tyr157 hydroxyl group, being either the nitrogen or oxygen of nitric oxide or the δ-nitrogen of His157.

Table A2.4. Calculated vs experimental Mössbauer parameters for wild-type **3MPA**-bound MDO with added nitric oxide. Calculations are based on bidentate bound **3MPA** with nitrosyl group in the axial position *trans* to His90. Percent error shown in parentheses.

| | Isomer shift δ (mm/s) | Quadrupole splitting, ΔE _Q (mm/s) | asymmetry (η) | Ref |
|----------------------------------|--------------------------|--|------------------|-----------|
| Experimental | 0.60 | 1.52 | 0.4 | (6) |
| Tyr-OH---N _(nitrosyl) | 0.550 (8.4%) | 1.474 (3.0%) | 0.546 | This work |
| Tyr-OH---O _(nitrosyl) | 0.554 (7.7%) | 1.325 (12%) | 0.686 | This work |
| Tyr-OH---His157 | 0.585 (2.5%) | 1.611 (6.0%) | 0.593 | This work |

Table A2.5. The dipolar coupling in MHz and polar angles in degrees for each ^1H included in HYSCORE simulations. Shown below are the polar angles that relate a ^1H on **3MPA** to magnetic axis system. The angle φ represents rotation in x-y plane, whereas θ is the deviation from the z axis defined by the Fe-NO bond.



| ^1H | $T(\text{MHz})$ | $\varphi (^{\circ})$ | $\theta (^{\circ})$ | Distance from Fe (\AA) |
|-------------------|-----------------|----------------------|---------------------|-----------------------------------|
| His90 | 2.37 | 35 | 110 | 3.4 |
| His90 | 2.40 | 160 | 140 | 3.4 |
| His92 | 2.36 | 110 | 63 | 3.3 |
| His92 | 2.30 | 80 | 92 | 3.5 |
| His142 | 2.34 | 40 | 128 | 3.5 |
| His142 | 1.36 | 165 | 58 | 3.3 |
| C3 of 3MPA | 1.16 | 115 | 79 | 4.2 |
| C3 of 3MPA | 2.54 | 120 | 59 | 3.1 |

Supplemental Figures

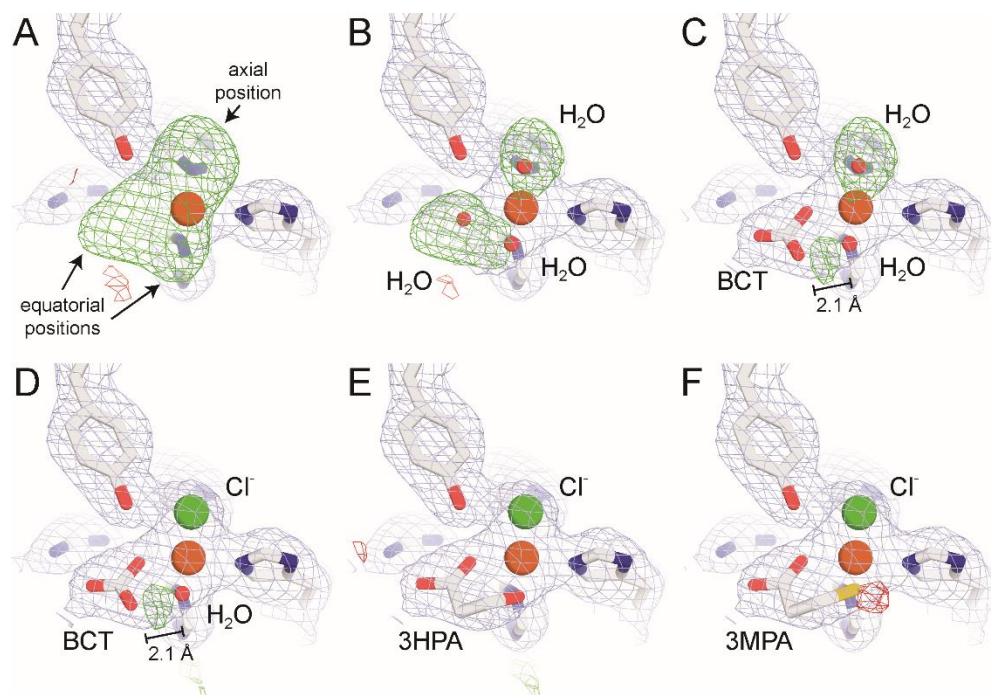


Figure A2.1. Av3MDO active site difference density modeling. In all panels the blue mesh represents sigma A-weighted $2F_o - F_c$ density for chain B of the structure contoured at 1 RMSD and the green and red mesh represent NCS-averaged, sigma A-weighted $F_o - F_c$ density contoured at +8 and -8 RMSD respectively. **A.** Map before modeling the open coordination sites. **B.** Updated maps following refinement with three aquo ligands modeled. The three aquo model poorly accounts for the difference map feature. **C.** Updated maps following refinement with two aquo ligands and one bicarbonate (BCT) modeled. **D.** Updated maps following refinement with one aquo ligand, one chloride (Cl⁻) and bicarbonate modeled. Chloride fully accounts for the difference density at the axial coordination site. Note the unacceptably close contact between bicarbonate and the modeled solvent and the residual strong positive density between these two moieties. **E.** Updated maps following refinement with one chloride (Cl⁻) and 3-hydroxypropionic acid (3HPA) modeled. This model fully accounts for the active site density. **F.** Updated maps following refinement with one chloride (Cl⁻) and 3-mercaptopropionic acid (3MPA) modeled. Note the difference map hole at the S atom confirming the presence of a lower Z atom (e.g. oxygen) at that site.

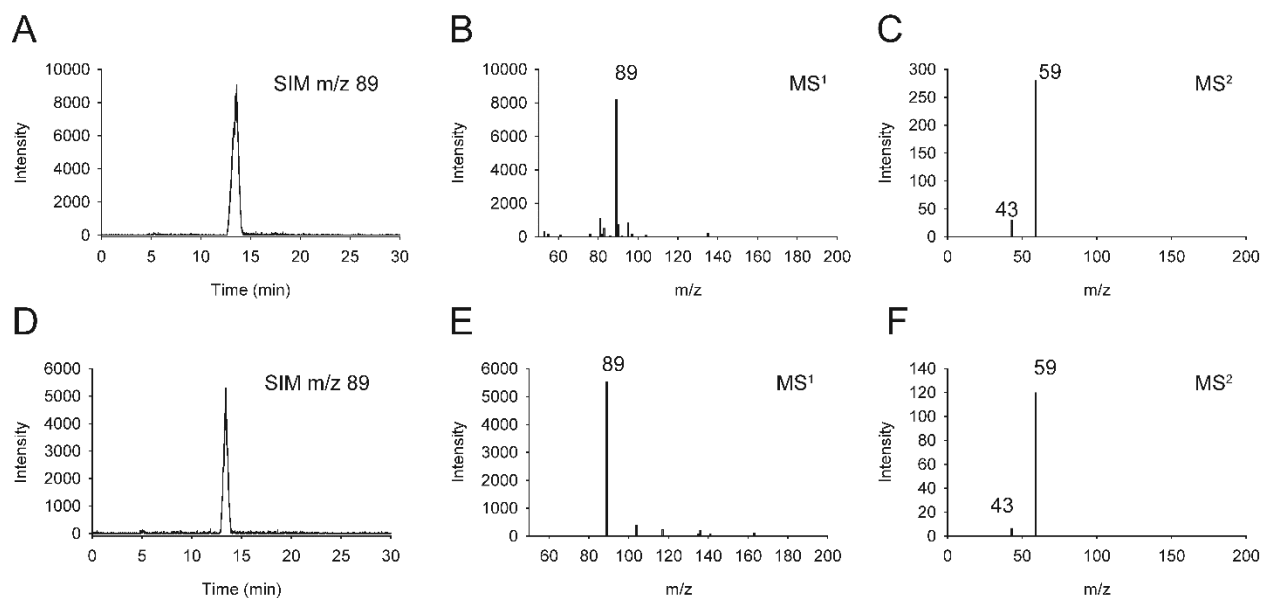


Figure A2.2. Mass spectrometry detection of **3HPA** in sodium polyacrylate 5100 solution used for *Av3MDO* crystallization. **A.** Negative ion-mode LC-MS of 3HPA standard with selective ion monitoring (SIM) of $m/z = 89$ species corresponding to deprotonated 3HPA. **B.** MS¹ spectrum of the SIM m/z 89 peak. **C.** MS² spectrum showing fragmentation of the m/z 89 precursor ion to form $m/z = 59$ ($-\text{H}_2\text{CO}$) and 43 ($-\text{HCOOH}$) species. **D.** LC-MS of the polyacrylate solution extract carried out in this same manner as (**A**) showing a single SIM m/z 89 peak with a retention time and fragmentation pattern (panels **E** and **F**) matching those of the 3HPA standard. No SIM m/z 89 peak was observed in control samples with acrylate extract or 3HPA standard omitted. By comparison of the SIM m/z 89 peak areas the concentration of 3HPA in the polyacrylate extract was estimated to be ~ 20 mM.

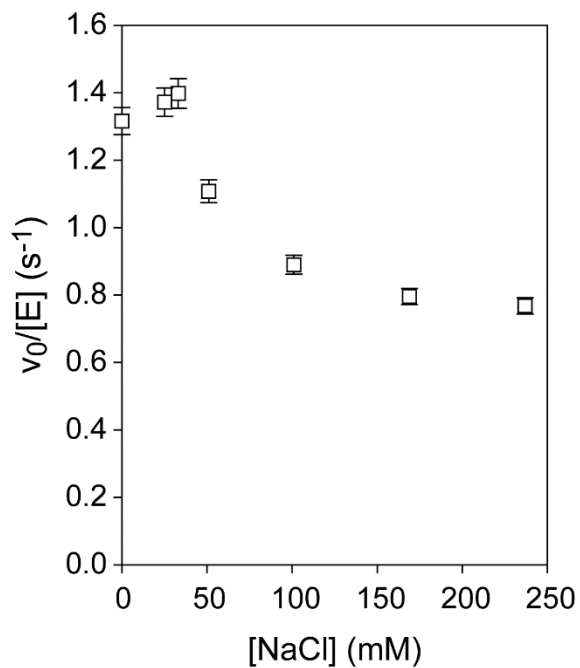


Figure A2.3. Inhibition of Av3MDO catalyzed oxidation of **3MPA** with increasing NaCl concentration. Assays were performed at fixed and saturated **3MPA** concentration (1 mM) in a buffered 20 mM HEPES pH 8 solution at fixed temperature ($25 \pm 1 \text{ }^\circ\text{C}$). Salt concentrations were varied from 0 to 240 mM.

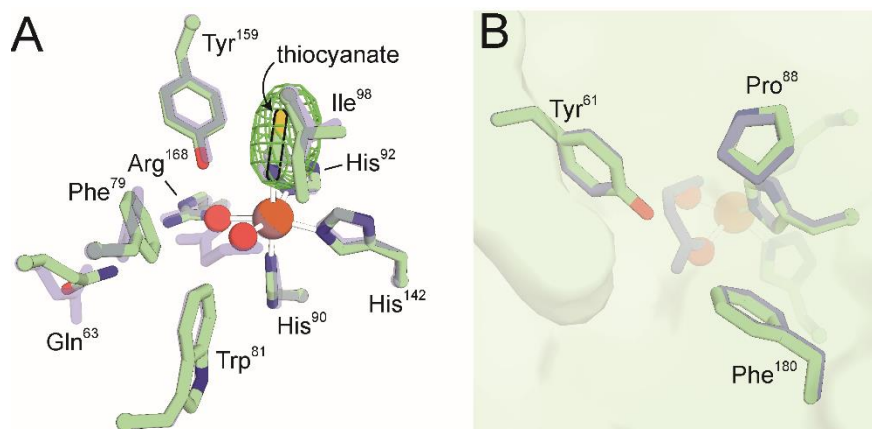


Figure A2.4. Crystal structure of Av3MDO in complex with thiocyanate (green) and its comparison to the 3HPA-bound Av3MDO structure (grey). **A.** Active site comparison between the two structure showing conformational differences in Gln63, Phe79, and Ile98. The green mesh represents unbiased, NCS-averaged, sigma A-weighted Fo-Fc electron density in the axial coordination position supporting the modeling of thiocyanate at this site. **B.** The tunnel providing access to the active site remains occluded in the thiocyanate-bound Av3MDO structure with the gatekeeper residues Tyr61, Pro88, and Phe180 found in nearly identical positions as compared to the 3HPA-bound structure.

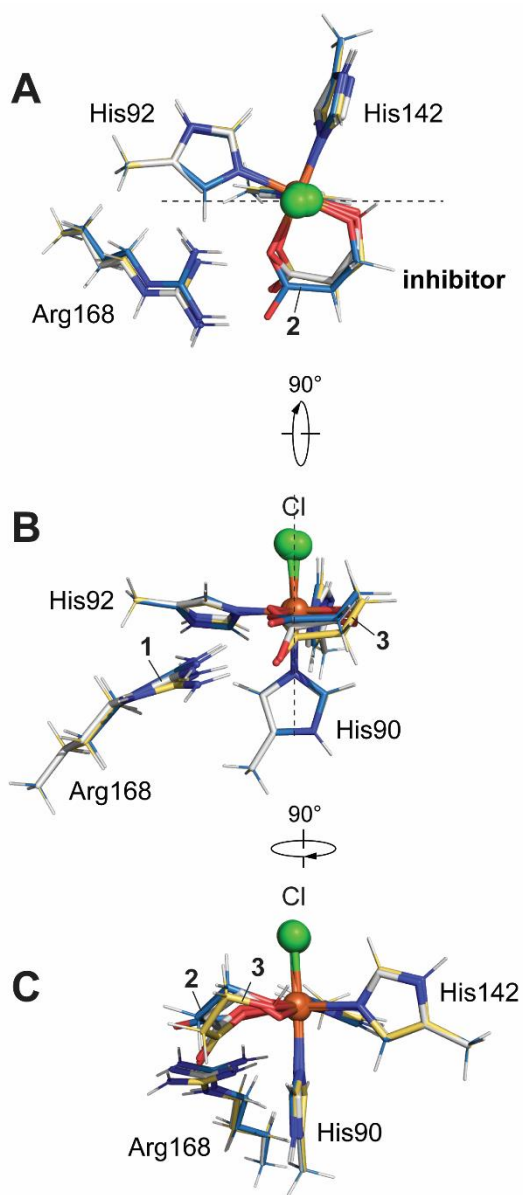


Figure A2.5. Selected viewpoints (A-C) of the Av3MDO-3HPA complex ([1], code 6XB9, shown in white) overlaid on DFT optimized structures for the 3HPA-bound Fe-site. Structures for the deprotonated ([2], 3HPA²⁻, blue carbon atoms) and protonated ([3], 3HPA¹⁻, yellow carbon atoms) inhibitor alcohol are presented for comparison. The top-down view shown in panel A aligns all structures along the [His90-Fe-Cl] axis. Panel B illustrates a 90° rotation of A along the perpendicular axis (dashed line). Clockwise rotation (-90°) of B around the [His90-Fe-Cl] axis results in Panel C. Selected distances, angles, and RMSD values are presented in Table 2.1 for comparison.

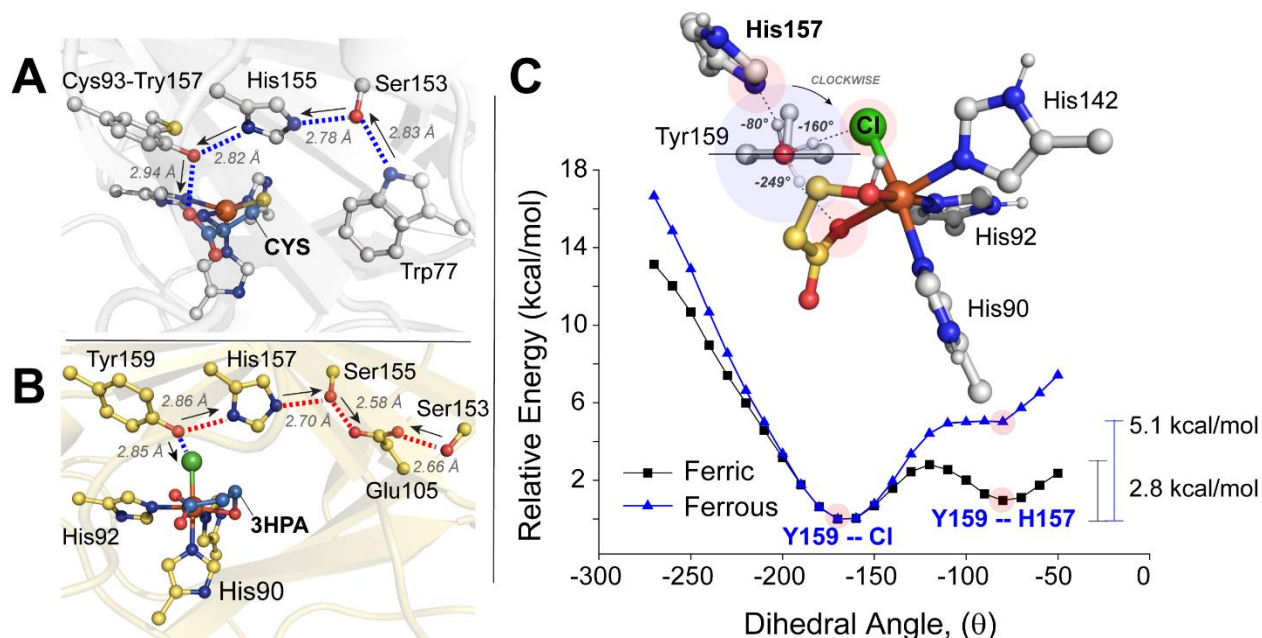


Figure A2.6. Comparison of **CYS**-bound rat CDO (**A**, PDB 4IEV) and **3HPA**-bound Av3MDO (**B**, PDB 6XB9) structures highlighting the extended proton relay network for each enzyme. **C**. Energy surface for Tyr159 H-bond donation/acceptor interactions as a function of dihedral bond angle. Given the ambiguous oxidation state of the Fe-site in the SXB9 structure, relaxed surface scan calculations were performed for both ferrous (*blue*) and ferric (*black*) states.

Orientation of Y159 hydrogen bond. Multiple pH-dependent kinetic studies verify that both Tyr159 and His157 of Av3MDO are protonated in the catalytically active state (6-8). The crystal structures for the Av3MDO-**3HPA** complex presents three possible proton-acceptors for Tyr159. The N δ -atom of His157 (2.86 Å), the chloride bound to the axial Fe- site (2.85 Å), and the proximal **3HPA**-carboxylate O-atom (3.01 Å). Alternatively, the directionality of the proton relay network could be reversed by N δ -His157 donation of an H-bond to the Tyr159 phenol O-atom. This leaves Tyr159 free to donate a hydrogen bond to either the axial chloride or the **3HPA**-carboxylate.

The energy surface for potential Tyr159 H-bond acceptors was evaluated using a relaxed surface scan (9-11) of the Av3MDO-**3HPA** complex. Calculations included Fe-coordinated histidine residues (His90, His92, and His142), the ‘SHY’ motif (Tyr159, His157, and Ser155), Arg168, **3HPA**⁻¹, and chlorine with coordinates taken from the Av3MDO crystal structure. All hydrogens were optimized while constraining the crystal structure coordinates. The Tyr159 phenol hydrogen was varied in orientation by varying the dihedral angle defined by the Tyr159 atoms C ϵ -C ξ -O η -H. Where C ϵ denotes the Tyrosine ϵ -carbon in closest proximity to H157. The path of the relaxed surface scan placed the phenol hydrogen oriented towards the N δ -atom of His157, axial iron-bound chlorine, and **3HPA**-carboxyl group while keeping the crystal structure rigid. This calculation was done for both Fe(II) and Fe(III) oxidation states to evaluate its influence (if any) on the preferred H-bond orientation. It should be noted that this model does not account for rotation of the tyrosine aromatic ring or other geometric perturbations and thus the values should be considered qualitative.

As illustrated above (**Figure A2.6C**, *black*) for the ferric state, an activation barrier of 2.8 kcal/mol is calculated for the Tyr159 \rightarrow His157 configuration from Tyr159 \rightarrow Cl. Given the small energy barrier and overall energy difference of >1 kcal/mol, it is reasonable that Tyr159 could alternate between donating a hydrogen bond to both His157 and the more preferred iron-bound chlorine. By contrast, the proximal O-atom of the **3HPA**-carboxylate is a poor H-bond acceptor for Tyr159 and is unfavorable in this model. The ferrous state (**Fig. A2.6C**, *blue*) calculations show a more dramatic bias towards Tyr159 \rightarrow Cl donation. The energy difference between donation towards Cl or His157 is approximately 5 kcal/mol. Qualitatively the activation barrier is also approximately 5 kcal/mol as the Tyr159 \rightarrow His157 orientation is not in a local minimum. Based on these observations, it can be argued that Tyr159 donates an H-bond to the

iron-bound Cl-atom in the *Av*3MDO-**3HPA** complex. Potentially, substitution of the axial chloride ligand for NO could alter the orientation of the Tyr159 H-bond to favor donation to H157. However, this would be inconsistent with previous EPR studies which demonstrate attenuated NO-binding for the Y159F variant (and to a lesser extent H157N). Moreover, as both chlorine and nitrosyl ligands have an equivalent formal charge (-1), an argument can be made that H-bond donation from Tyr159 would similarly favor axially bound NO over His157.

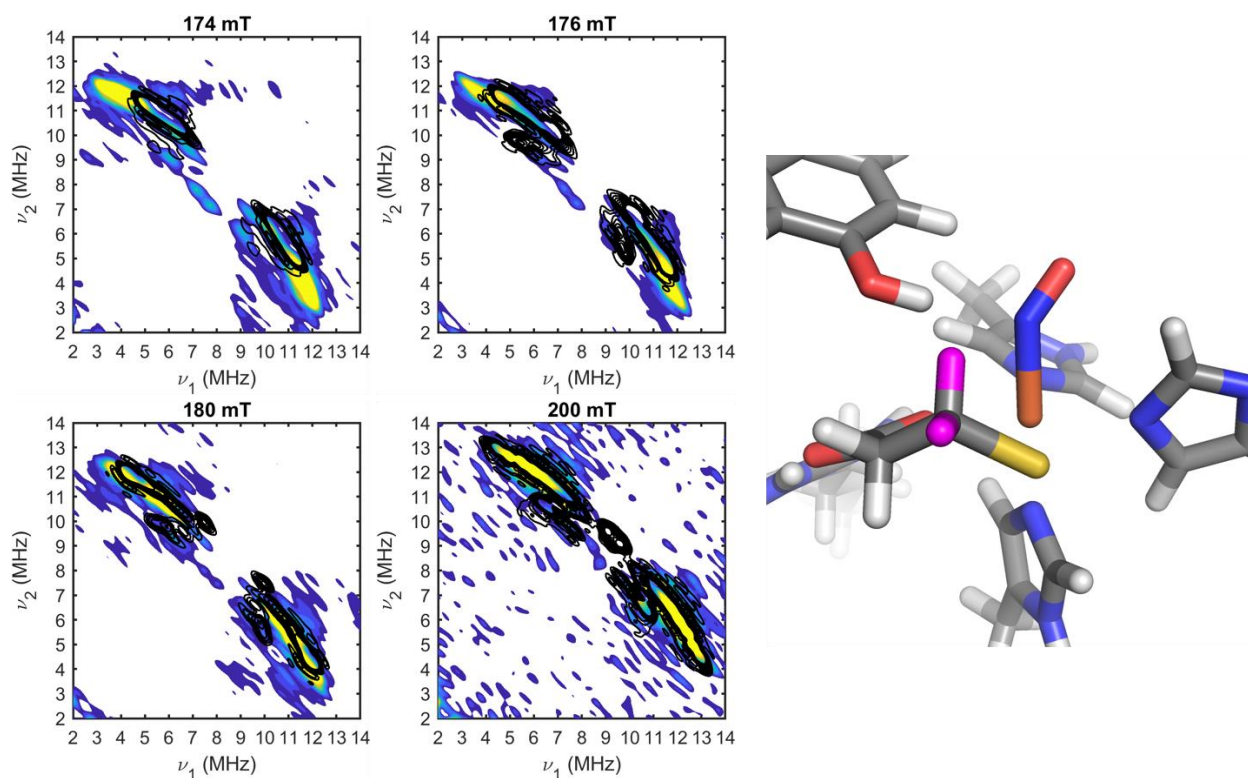


Figure A2.7. HYSCORE spectra and simulations of the ^1H on **3MPA** (shown in magenta) at 174, 176, 180, and 200 mT. Experimental spectra appear as color contours; simulations are overlaid as black contour lines. The anisotropic hyperfine couplings and the positions of each nucleus relative to the magnetic axis system are listed in **Table A2.5**.

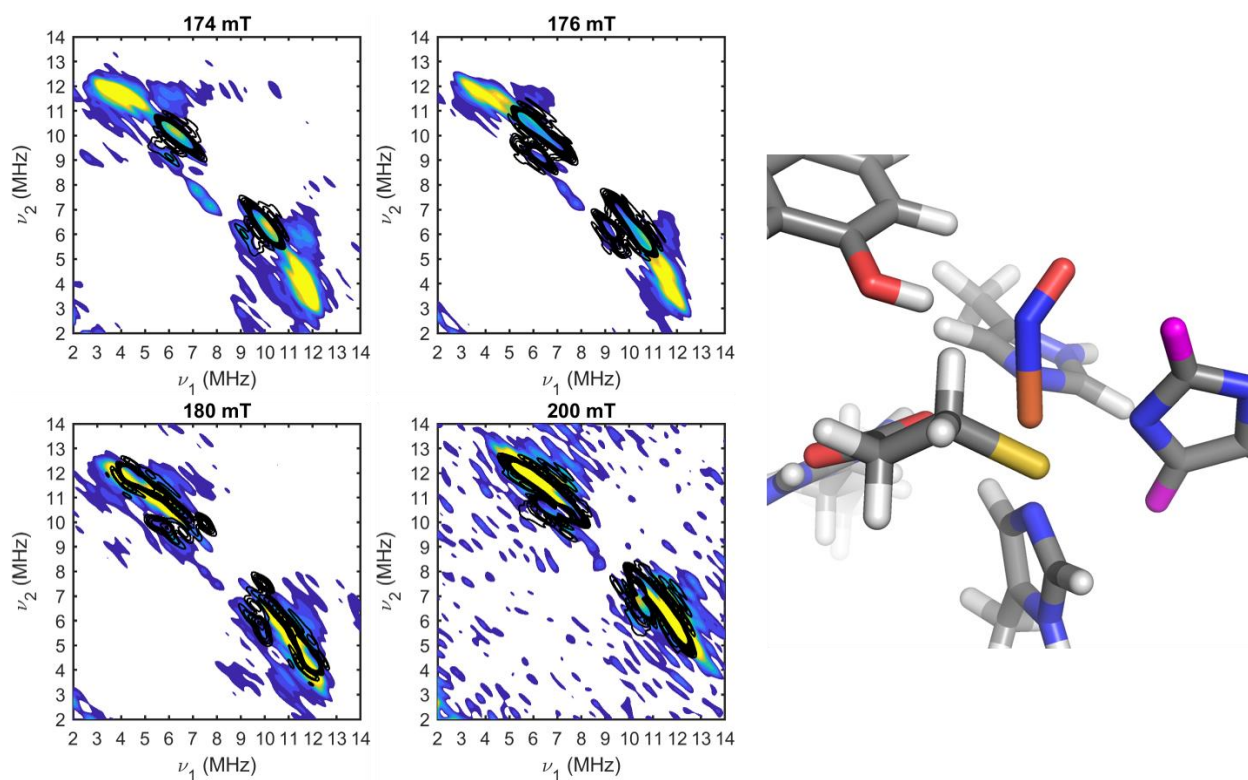


Figure A2.8. HSCORE spectra and simulations of the ^1H on His142 (*shown in magenta*) at 174, 176, 180, and 200 mT. Experimental spectra appear as color contours; simulations are overlaid as black contour lines. The anisotropic hyperfine couplings and the positions of each nucleus relative to the magnetic axis system are listed in **Table A2.5**.

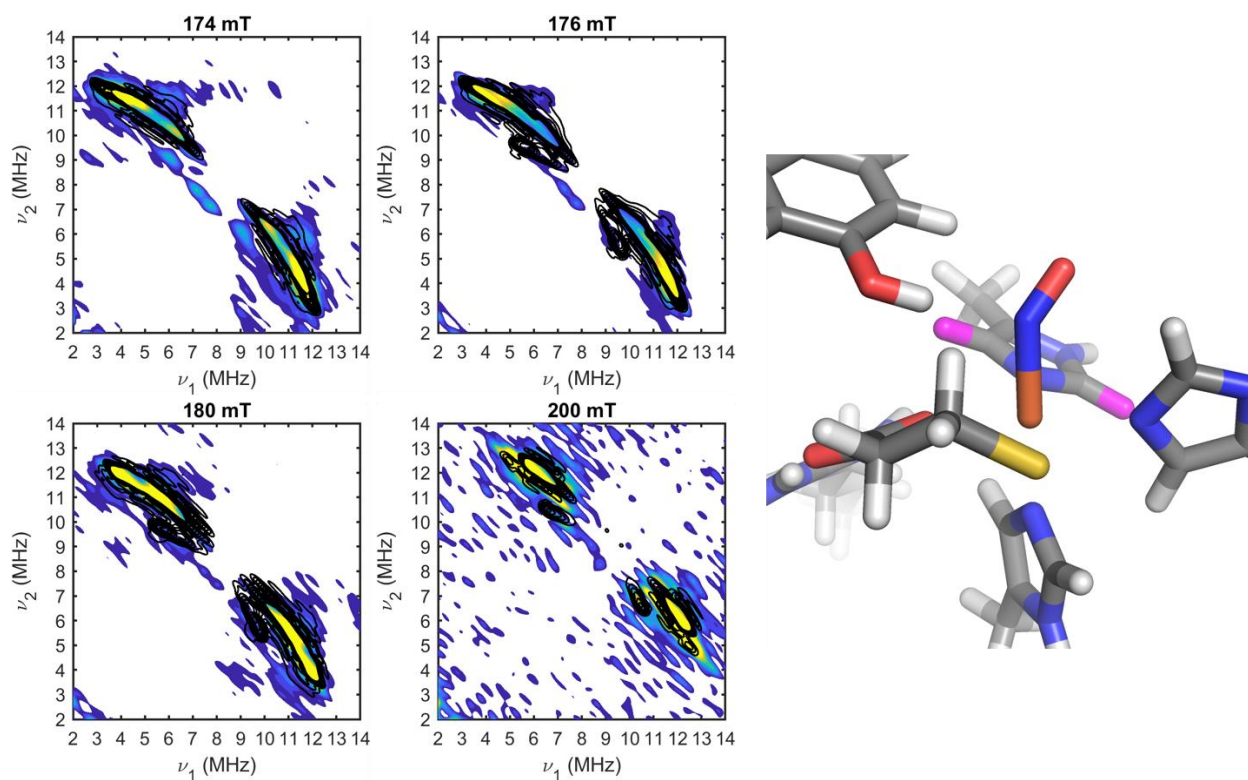


Figure A2.9. HYSCORE spectra and simulations of the ^1H on His92 (*shown in magenta*) at 174, 176, 180, and 200 mT. Experimental spectra appear as color contours; simulations are overlaid as black contour lines. The anisotropic hyperfine couplings and the positions of each nucleus relative to the magnetic axis system are listed in **Table A2.5**.

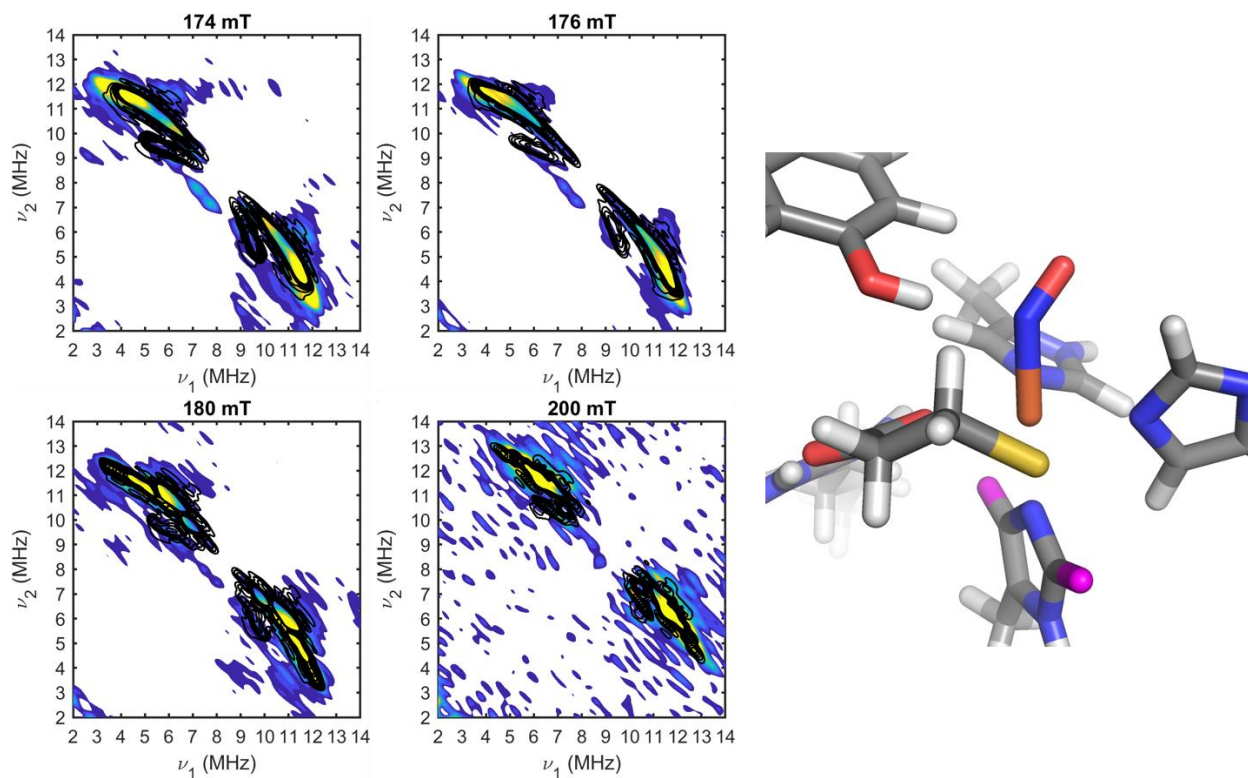


Figure A2.10. HYSORE spectra and simulations of the ^1H on His90 (*shown in magenta*) at 174, 176, 180, and 200 mT. Experimental spectra appear as color contours; simulations are overlaid as black contour lines. The anisotropic hyperfine couplings and the positions of each nucleus relative to the magnetic axis system are listed in **Table A2.5**.

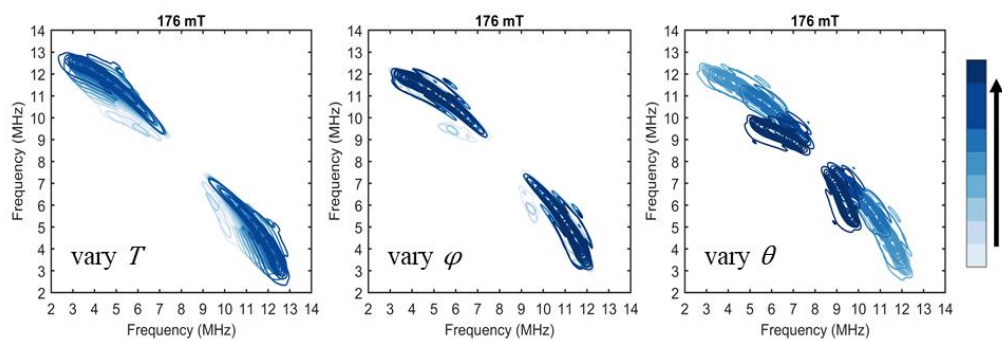


Figure A2.11. HSCORE simulations of the closest ^1H on **3MPA** at 176 mT. Color gradient represents the simulations that result from increasing the value of T in increments of 0.25 MHz (left) and the angles φ and θ in increments of 15° (center and right, respectively).

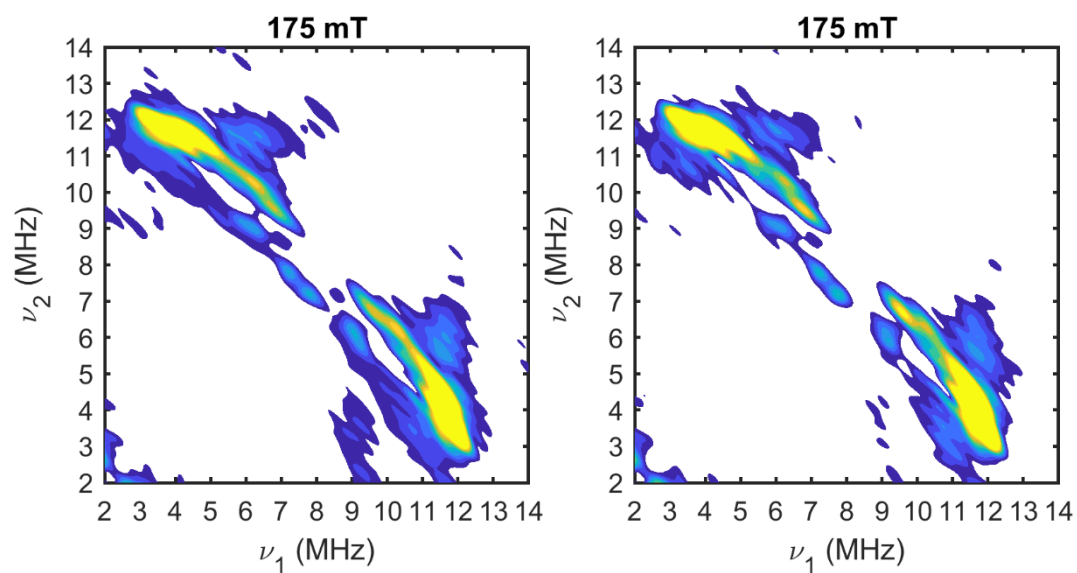


Figure A2.12. HSCORE spectra (at 175 mT) for (3MPA/NO)-bound Av3MDO prepared in $^1\text{H}_2\text{O}$ (*left*) buffer as compared to samples exchanged into $^2\text{H}_2\text{O}$ buffer (*right*). The absence of ^1H peaks lost upon exchange into deuterated buffer suggests no solvent-derived ligands are coordinated to the Fe-site.

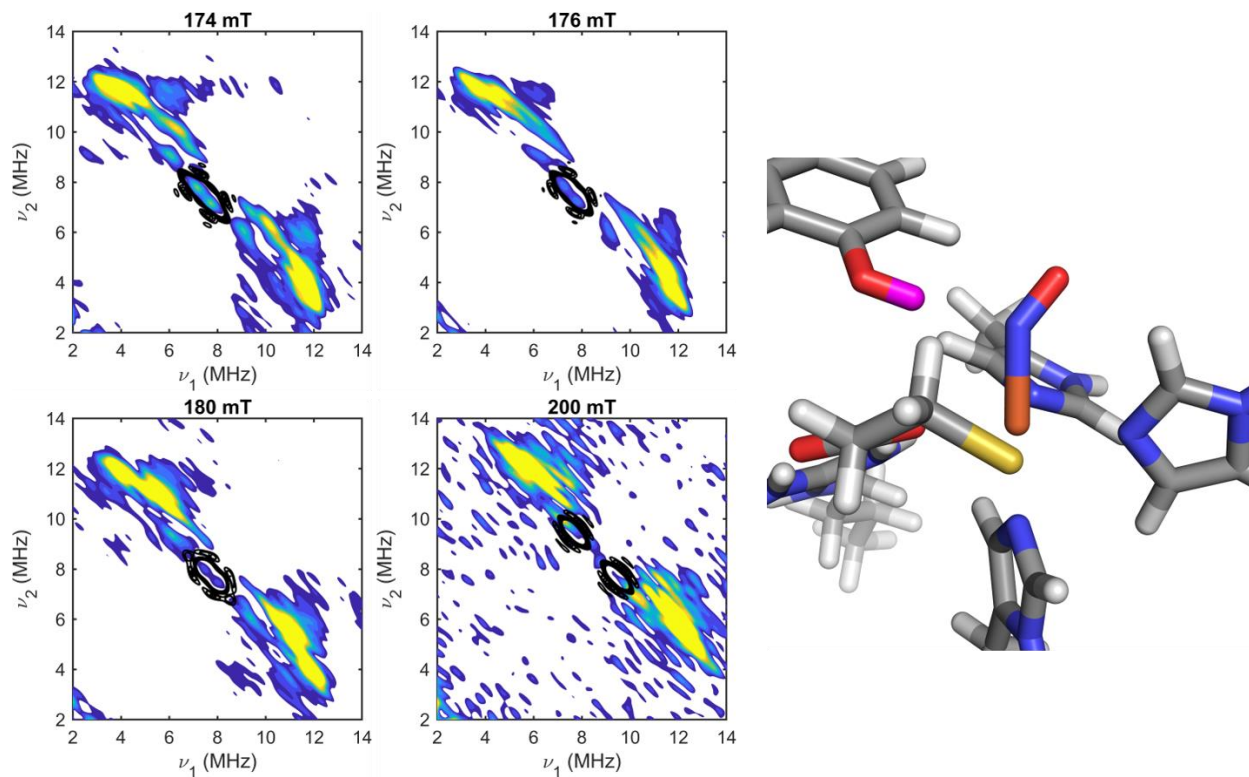


Figure A2.13. HYSORE spectra and simulations of the ^1H on the hydroxyl group of Tyr159 (shown in magenta) at 174, 176, 180, and 200 mT. Experimental spectra appear as color contours; simulations are overlaid as black contour lines. The simulations were calculated with an anisotropic hyperfine coupling of 0.95 MHz and values of 40° and 20° for θ and ϕ , respectively.

Copyright Information

The content of this chapter was accepted to the Journal of Biological Chemistry as of February 26, 2021.

The article is currently published online and cited as:

York NJ, Lockart MM, Sardar S, Khadka N, Shi W, Stenkamp RE, Zhang J, Kiser PD, Pierce BS, Structure of 3-mercaptopropionic acid dioxygenase with a substrate analog reveals bidentate substrate binding at the iron center, Journal of Biological Chemistry (2021), doi: <https://doi.org/10.1016/j.jbc.2021.100492>.

This article was published under the open access CC-BY license. The publisher allows use of such published work as indicated in the following statement:

“This is an open access article distributed under the terms of the Creative Commons CC-BY license, which permits unrestricted use, distribution, and reproduction in any medium, provided the original work is properly cited.

You are not required to obtain permission to reuse this article.”

Journal of Biological Chemistry is part of Elsevier publishing which issues the following statements regarding use of your published article in a dissertation/thesis.

“As an Elsevier journal author, you have the right to Include the article in a thesis or dissertation (provided that this is not to be published commercially) whether in full or in part, subject to proper acknowledgment; see the Copyright page for more information. No written permission from Elsevier is necessary.

This right extends to the posting of your thesis to your university’s repository provided that if you include the published journal article, it is embedded in your thesis and not separately downloadable.”

References

1. Driggers, C. M., Stipanuk, M. H., and Karplus, P. A. (2015) Mammalian cysteine dioxygenase. in *Encyclopedia of Inorganic and Bioinorganic Chemistry* (Scott, R. A. ed., John Wiley & Sons, Ltd.
2. Fischer, A. A., Miller, J. R., Jodts, R. J., Ekanayake, D. M., Lindeman, S. V., Brunold, T. C., and Fiedler, A. T. (2019) Spectroscopic and Computational Comparisons of Thiolate-Ligated Ferric Nonheme Complexes to Cysteine Dioxygenase: Second-Sphere Effects on Substrate (Analogue) Positioning. *Inorg Chem.* **58**, 16487-16499
3. Fischer, A. A., Stracey, N., Lindeman, S. V., Brunold, T. C., and Fiedler, A. T. (2016) Synthesis, X-ray Structures, Electronic Properties, and O₂/NO Reactivities of Thiol Dioxygenase Active-Site Models. *Inorg Chem.* **55**, 11839-11853
4. Gordon, J. B., McGale, J. P., Prendergast, J. R., Shirani-Sarmazeh, Z., Siegler, M. A., Jameson, G. N. L., and Goldberg, D. P. (2018) Structures, Spectroscopic Properties, and Dioxygen Reactivity of 5- and 6-Coordinate Nonheme Iron(II) Complexes: A Combined Enzyme/Model Study of Thiol Dioxygenases. *J Am Chem Soc.* **140**, 14807-14822
5. Li, W., Blaesi, E. J., Pecore, M. D., Crowell, J. K., and Pierce, B. S. (2013) Second-Sphere Interactions between the C93–Y157 Cross-Link and the Substrate-Bound Fe Site Influence the O₂ Coupling Efficiency in Mouse Cysteine Dioxygenase. *Biochemistry* **52**, 9104-9119
6. Sardar, S., Weitz, A., Hendrich, M. P., and Pierce, B. S. (2019) Outer-Sphere Tyrosine 159 within the 3-Mercaptopropionic Acid Dioxygenase S-H-Y Motif Gates Substrate-Coordination Denticity at the Non-Heme Iron Active Site. *Biochemistry* **58**, 5135-5150
7. Crowell, J. K., Sardar, S., Hossain, M. S., Foss Jr, F. W., and Pierce, B. S. (2016) Non-chemical proton-dependent steps prior to O₂-activation limit *Azotobacter vinelandii* 3-mercaptopropionic acid dioxygenase (MDO) catalysis. *Arch Biochem Biophys.* **604**, 86-94
8. Pierce, B. S., Subedi, B. P., Sardar, S., and Crowell, J. K. (2015) The “Gln-Type” Thiol Dioxygenase from *Azotobacter vinelandii* Is a 3-Mercaptopropionic Acid Dioxygenase. *Biochemistry* **54**, 7477-7490
9. Dajnowicz, S., Parks, J. M., Hu, X., Gesler, K., Kovalevsky, A. Y., and Mueser, T. C. (2017) Direct evidence that an extended hydrogen-bonding network influences activation of pyridoxal 5'-phosphate in aspartate aminotransferase. *J Biol Chem.* **292**, 5970-5980
10. Bykov, D., Plog, M., and Neese, F. (2014) Heme-bound nitroxyl, hydroxylamine, and ammonia ligands as intermediates in the reaction cycle of cytochrome c nitrite reductase: a theoretical study. *J Biol Inorg Chem* **19**, 97-112

11. Kampa, M., Lubitz, W., van Gestel, M., and Neese, F. (2012) Computational study of the electronic structure and magnetic properties of the Ni–C state in [NiFe] hydrogenases including the second coordination sphere. *J Biol Inorg Chem* **17**, 1269-1281

CHAPTER 3:
LOW-SPIN CYANIDE COMPLEXES OF 3MDO REVEAL IMPACT OF OUTER-SPHERE
SHY MOTIF

3.1 Introduction

Thiol dioxygenases (TDOs) are a class of enzymes which oxidize thiol substrates to their corresponding sulfinic acid derivatives (1-6). Imbalances of sulfur compounds have been correlated to neurological diseases such as Alzheimer's, Parkinson's, and neurodegenerative diseases (7-9). Therefore, these enzymes are of interest due to potential medicinal implications with said diseases as well as anti-inflammatory therapies, anticancer therapies, and antimicrobials (10-13). Two thiol dioxygenases currently known within mammals: cysteine dioxygenase (CDO) and cysteamine dioxygenase (ADO) (2,3,14). Both enzymes have shown high specificity with their respective substrates (15,16). However, the substrate specificity is not well understood as the iron coordination environment of TDOs are seemingly quite similar. Each TDO shows iron coordinated to a facial triad of histidine residues and a conserved sequence of residues serine, histidine, and tyrosine which form an SHY motif.

Recently, a new avenue to explore the mechanism of thiol dioxygenases has been given in the enzyme 3-mercaptopropionate dioxygenase (3MDO). This enzyme, isolated from *Azotobacter vinelandii*, has shown promiscuous thiol dioxygenase chemistry with cysteine, cysteamine, and its native substrate, 3-mercaptopropionate (6,17). Chapter 2 showed bidentate coordination of the inhibitor, 3-hydroxypropionic acid (**3HPA**), shown in **Figure 3.1**, panel A.

3HPA is bound to iron by both its terminal hydroxyl group and carboxylate in the equatorial positions trans to His92 and His142, respectively. Coincidentally, **3HPA** is a structural analog of native substrate, **3MPA**, differing only in a terminal hydroxyl instead of a thiol. Because of this similarity, the authors hypothesized **3MPA** would bind in a similar manner. Structural DFT models were used to confirm bidentate coordination of **3MPA** in tandem with HYSORE spectroscopy. An interesting feature of the crystal structure was a chloride ligand bound to the axial iron position. This ligand was in closest proximity to the SHY motif (Figure 3.2), which has shown to be important in both substrate binding and catalytic turnover (18). The effect of hydrogen bonding within the SHY motif and how it connects to the active site was a topic of consideration in the last chapter. However, the mode of hydrogen bonding from the Tyr159 residue could not be definitively assigned as multiple orientations were found to reasonably replicate experimental parameters.

The work presented herein is an effort to elucidate more structural information of the substrate bound active site. Specifically, the orientation of the SHY motif and its influence on the iron active site. For this purpose, cyanide was used to produce EPR-active $S = 1/2$ ferric **3MDO** complexes. The use of cyanide as a spectroscopic probe has been used for mammalian CDO to gauge the influence of a Tyr157-Cys93 covalent crosslink on the iron active site (19). Cyanide was not shown to bind to resting ferric CDO, however, a crystal structure shows coordination of thiocyanate to *Av3MDO* as seen in **Figure 3.1**, panel **B**. An $S = 1/2$ species has the advantage of anisotropic g -values which are more sensitive to geometric perturbations than comparable complexes of high spin of which the spectra is dominated by rhombic zero-field splitting parameters (E/D). Herein, the effects of altering the SHY motif are shown through variants

H157N and Y159F that, respectively, alter and cut off the hydrogen bonding network from the iron active site.

3.2 Experimental Methods

Enzyme purification and expression. The purification and expression procedure used for this enzyme is described elsewhere (6). To summarize, *Av3MDO* was expressed in competent BL21(DE3) *E. coli* cells. Cells were grown with agitation at 37 °C in a 1 L of LB media with 100 mg/L of ampicillin to an OD600 of ~1 before transferring to a 10 L BF-110 fermenter. Upon reaching OD600 of ~4, induction was started by addition of 1 g isopropyl β -D-1-thiogalactopyranoside (IPTG), 78 mg ferrous ammonium sulfate, and 20 g casamino acids and reducing the temperature to 25 °C. Cells were harvested after 4 hours, pelleted by centrifugation, and frozen at -80 °C.

For purification, cells were thawed in 20 mM 4-(2-hydroxyethyl)-1-piperazineethanesulfonic acid (HEPES), 50 mM NaCl, pH 8.0 and lysed by sonication with added lysozyme, ribonuclease, and deoxyribonuclease at 10 mg/L each. The slurry was then centrifuged, and the supernatant was loaded onto a DEAE Sepharose fast flow anion exchange column. The protein was eluted on a 50 – 350 mM NaCl linear gradient. Fractions were collected and pooled based on SDS-page. The enzyme was then concentrated to ~50 mL before cutting the His-tag with bovine thrombin protease overnight. The solution was then concentrated to ~ 5 mL before being frozen in liquid nitrogen and stored at -80 °C.

Iron content was quantified for both Fe(II) and Fe(III) content using 2,4,6-tripyridyl-s-triazine (TPTZ) in a method previously described (4,6). A typical purification yields 80-95% ferric iron with the remainder being ferrous.

UV-Visible. UV-vis measurements were taken on an Agilent 8453 photodiode array spectrometer using ES Quartz cuvettes. All solutions were prepared in working buffer 20 mM HEPES (pH 8.0) and 50 mM NaCl. MDO was thawed and diluted to a concentration of 120 μ M ferric iron. Substrate, **3MPA**, was prepared in a 120 mM stock solution in working buffer brought back to pH 8.0. Cyanide stock was prepared with 120 mM sodium cyanide in 100 mM HEPES (pH 8.0) and 50 mM NaCl. One minute was allowed for equilibration between additions of both substrates and cyanide to the enzyme solution before taking a measurement.

A sample of as isolated enzyme was used as a baseline in all spectra. Binding curves were produced using the max absorbance for each set of spectra. Fitting of the binding curves were done using Equation 1.

$$[EL] = \frac{\sqrt{(B_{max}+K_d+[L])-(B_{max}+K_d+[L])^2-4\cdot B_{max}\cdot[L]}}{2} - n \cdot [L] \quad \text{Equation 1.}$$

K_d is the dissociation constant, B_{max} is the concentration of iron which acts as receptor to each ligand, $[L]$ is the concentration of ligand being added (**3MPA**, cys, or cyanide), and n is a small correction factor. B_{max} was allowed to vary in order to gain better fitting curves. Some titrations showed a decrease in signal at high ligand concentration instead of converging to a maximum. This correction, n , adds a linear negative slope to help fit the curves at higher ligand concentration.

CW EPR spectroscopy. X-Band CW EPR spectroscopy was done on a Bruker EMX Plus with a bimodal resonator and an oxford ESR900 cryostat and Oxford ITC 03 temperature controller for low temperature spectra acquisition. Samples were frozen in 4 mm diameter Wilmad-Labglass EPR tubes. Simulations of EPR spectra were done on Spincount (version 6.2.6907.24939)

developed by Professor Michael Hendrich at Carnegie Mellon University by utilizing the general spin Hamiltonian seen in Equation 2.

$$\hat{H} = \mathbf{D} \left[\hat{S}_Z^2 - \frac{S(S+1)}{3} \right] + \mathbf{E} \left(\hat{S}_X^2 + \hat{S}_Y^2 \right) + \beta \mathbf{B} \cdot \mathbf{g} \cdot \mathbf{S} \quad \text{Equation 2.}$$

Variables D and E are respectively the axial and rhombic zero-field splitting parameters and g is the g -tensor. For a system of $S = 1/2$, both the D and E terms go to zero, and only the Zeeman (right) term remains.

Samples with ferric enzyme were made with Fe(III) concentrations of 300 μM and varying ratios of substrate and cyanide to represent different points of saturation based on the previously acquired UV-Vis data. Substrates and cyanide were added from stock solutions of 375 mM **3MPA** and 300mM sodium cyanide.

Pulsed EPR Spectroscopy. Electron spin echo envelope modulation (ESEEM) spectra were measured using an ELEXSYS E680 EPR spectrometer (Bruker-Biospin, Billerica, MA) equipped with a Bruker Flexline ER 4118 CF cryostat. ESEEM measurements were made at 5 K at seven magnetic fields spanning the region between g_1 and g_2 (g_{max} and g_{mid} , respectively). Data were collected using a three pulse stimulated echo sequence, $\pi/2-\tau-\pi/2-T-\pi/2-\tau+T$ -echo, where $\pi/2$ represents a 16 ns microwave pulse, and T and τ represent delays between the pulses. The delay time τ was set to 136 ns, and the pulse sequence was repeated at a rate of 0.5 kHz. Spectra were processed using Xepr (Bruker-Biospin, Billerica, MA) and custom scripts in MATLAB (Mathworks, 2020a). In brief, spectra were phased to minimize the imaginary

component of the signal before removing the imaginary part. Then, the natural log was taken, and the result was fit to a second-order polynomial, which was then subtracted to remove the background echo decay. A sine bell apodization function was then applied to the spectra to minimize noise at longer times. The result was zero-filled to 1024 points, and the fast Fourier transform was calculated. The spectra are plotted as the magnitude of the real part of the Fourier transform. Plots were made using OriginPro version 2019 (OriginLab, Northhampton MA). Samples for 3p-ESEEM were prepared in 3 mm quartz tubes with 1 mM Fe (III) 3MDO.

Computational model selection. Coordinates were extrapolated from the crystal structure of *Av*MDO (pdb: 6XB9). This structure features inhibitor, 3-hydroxypropionic acid (3HPA), bound bidentate to iron with a chloride bound to the axial position. This arrangement mimics the proposed substrate binding model of **3MPA** to the iron active site. The model features the thiolate bound trans to His92 and the carboxylate of **3MPA** bound trans to His142, leaving the axial position, trans to His90, for molecular oxygen. Previous, computational studies have shown native substrate is able to bind iron similar to that of the inhibitor featured in the crystal structure.

Therefore, the computational models used herein take the coordinates of the iron, 3HPA, chloride, His90, His92, His142, Arg168, Tyr159, His157, and Ser155. Arg168 was included due to its apparent interaction with the iron bound carboxylate group of 3HPA and, presumably, **3MPA**. The SHY motif was included to see what interactions, if any, would be encountered by ligands directly bound to the iron. The outer sphere residues (Arg168, Tyr159, His157, and Ser155) were capped at their respective α -carbons as methyl groups. The histidines directly coordinating to iron (His90, His92, His142) were capped at their beta carbons. 3HPA was converted to **3MPA** by simply displacing the terminal hydroxyl oxygen with a sulfur. The residues were then fully protonated with His90, His92, and His142 protonated at the delta-

nitrogen and His157 at the epsilon-nitrogen. Sulfur was left deprotonated. Preliminary optimization of only hydrogens restricted the dihedral angle of the methyl capped hydrogens in relation to the constrained main group elements. This kept the orientation of the methyl capped hydrogens consistent with the original C-N and C-C_(carboxyl) bonds which were truncated. Chloride was displaced by cyanide with a Fe-C bond length of 1.8 Å for models of cyanide bound to the ES complex.

Quantum calculations. All calculations were done using Orca version 4.2.(20) All geometry optimizations were performed using the BP '86 functional.(21,22) Ahlrich's def2-TZVP basis set was used on iron, sulfur and all atoms directly coordinated to iron.(23) Def2-SVP was used on all other atoms. Optimizations also included Grimme's D3 dispersion energy correction, a CPCM potential with epsilon=4 to simulate a protein environment, and the resolution of identity (RI) approximation.(24-26) The capped methyl groups were restricted in the optimizations to preserve the overall orientation of the enzyme active site.

Single point calculations were performed to obtain spectroscopic parameters. DFT was used to calculate *g*-values using the optimized structures. The electronic structure was calculated using the PBE0 hybrid functional.(27,28) The core potential CP(PPP) and IGLO-II basis sets were used on iron and sulfur, respectively.(29,30) All other atoms utilized the EPR-II basis sets (31). These basis sets have more flexibility in the core orbitals for more accurate hyperfine coupling values. The integration grid was set to "Grid5" and "FinalGrid7" in Orca with the radial integration grid of iron set to 7. The Resolution of Identity Chain of Spheres (RIJCOSX) approximation was used with the Def/2 auxiliary basis set.(32) The *g*-values were determined from spin orbit coupling calculated using the coupled-perturbed self-consistent field equations.(33-36) The *g*-tensor origin was placed on the center of spin density. Separate

calculations were attempted with the default origin position (center of electric charge) and directly on the iron atom. All attempts showed negligible changes to the calculated *g*-values.

The spectroscopic properties were also calculated using a complete active space self-consistent field method with the *n*-electron valence state 2nd order perturbation theory energy correction (CASSCF/NEVPT2).(37,38) Recently, this method was utilized by Fischer et al. to calculate *g*-values of both biomimetic synthetic complexes and computationally optimized models of substrate bound cysteine dioxygenase with a bound cyanide ligand.(39) Of the biomimetic complexes, one was structurally similar to the proposed substrate binding model of **3MPA** to 3MDO, having a ligand bound bidentate through a thiolate and carbonyl. The authors of this work used a (11,13) CASSCF active space (11 electrons, 13 orbitals) which included five 3d orbitals, five 4d orbitals, and three ligand binding orbitals. The authors iteratively increased the size of the active space, starting from a minimal (5,5) active space with only the 3d iron orbitals. A similar procedure was performed herein and will be discussed in subsequent sections. In each CASSCF calculation, 10 doublet roots were calculated. Initial calculations used a def2-SVP basis set which was expanded to the def2-TZVP basis set. Differences in calculated *g*-values are minimal due to CASSCF calculation's basis set stability (37). Starting orbitals were taken from quasi-restricted orbitals (QROs) from single point DFT calculations.(40)

The models used for CASSCF calculations were further truncated to include the iron, directly bound histidines (His90, His92, and His142), **3MPA**, and other ligands bound to the iron (cyanide, water, hydroxide). CASSCF/NEVPT2 calculations are computationally more expensive than DFT and also depend on the size of the basis set. The outer sphere residues (Arg168, Tyr159, His157, and Ser155) were included in the calculations as point charges. As such, perturbations to the active space orbitals of interest could still be considered while keeping

the computational cost relatively low. The Mulliken atomic charges were extrapolated from the previous DFT geometry optimizations. The charges were included iteratively, as will be discussed in Results.

3.3 Results & Discussion

Cyanide binding to Fe(III)-*Av*3MDO [1]. In the catalytically active ferrous oxidation state, *Av*3MDO exhibits an obligate ordered coordination of **3MPA**-substrate prior to nitric oxide and dioxygen (6,18). Interestingly, the Fe(III)-bound form of mammalian CDO (*Mm*CDO) exhibits similar behavior when binding cyanide (19). Given the nearly equivalent first Fe-coordination sphere of these enzymes, an obvious question is whether *Av*3MDO is capable of binding cyanide in the absence of substrate. As shown in **Figure 3.2** (trace **1**), Fe(III)-*Av*3MDO (referred to as **1** henceforth) exhibits no visible absorption features. Consequently, CW X-band EPR spectroscopy was used to following cyanide binding in the ferric enzyme. Frozen samples of **1** exhibit a broad isotropic resonance at $g \sim 4.26$ typical of a high spin $S = 5/2$ Fe(III) center at the rhombic limit ($E/D \sim 0.33$). Such signals are largely unremarkable in that they cannot be differentiated from adventitious Fe(III). However, addition of excess sodium cyanide results in the loss of the $g \sim 4.26$ high spin Fe(III) signal and formation of new $S = 1/2$ signals observed near $g = 2.0$. Addition of a 20-fold excess of cyanide relative to **1** results in the two spectroscopically distinct, rhombic $S = 1/2$ signals shown in **Figure 3.2**. The relative contribution from each rhombic species (designated **1A** and **1B**) can be deconvoluted by spectroscopic simulation. The minor fraction, designated species (**1A**), has observed g -values (g_1 , g_2 , and g_3) of 2.38, 2.22, and 1.89, this species contributes only 23% to the total spin quantitation. The overall span in g -values ($g_1 -$

$g_3 = 0.49$) is consistent with those reported for other non-heme iron enzymes containing a low-spin ferric site (19,39,41-43). Species **1B** represents the majority fraction (77%) and exhibits a larger range of g -values (2.53, 2.19, and 1.84). Despite the higher anisotropy, the span in g -values (0.69) is also consistent with a low spin ferric iron site. Interestingly, the ratio of these two species is largely fixed regardless of cyanide concentration suggesting **1A** and **1B** are in equilibrium with each other. On the basis of these results, it can be concluded that *Av*3MDO is capable of binding cyanide in the absence of substrate. Additional experiments (*outlined below*) confirm that both low-spin ferric species (**1A** and **1B**) represent different CN-coordination modes within the *Av*3MDO active site.

Cyanide binding to the Fe(III)-*Av*3MDO-3MPA complex [1S]. As illustrated in **Scheme 1 (ii)**, addition of substrate (**3MPA**) to **1** results in the formation of a catalytically inert oxidized enzyme-substrate complex [Fe(III)-*Av*3MDO-**3MPA**, designated **1S**]. Similar to the Fe(III)-form of *Mm*CDO, coordination of the **3MPA**-thiolate to the Fe(III)-site results in a charge transfer band observable by UV-visible spectroscopy at 584 nm (19). Structural and spectroscopic characterization of synthetic model complexes of the substrate-bound 3MDO indicate that this absorption feature can be attributed to a LMCT between the bound thiolate S-atom and Fe(III)-site (44). As illustrated in **Figure 3.4**, this absorption feature can be used to monitor the formation of **1S** upon titration of **1** with **3MPA**. Full saturation of this absorption feature is observed at ~10-fold molar excess of **3MPA** relative to **1**. **Equation 1** was used to fit the increase in absorbance with substrate to obtain a binding constant for **3MPA** ($K_d \sim 540 \pm 10 \mu\text{M}$). At saturating **3MPA**-concentration, it can be assumed that all of the enzyme present in solution is in the form of *Av*3MDO-**3MPA** complex. As discussed below, the concentration of **1S** was also confirmed by CW EPR spectroscopy and analytical simulations to ensure the

accuracy. Based on the concentration of **2** and the maximum absorbance, the molar extinction coefficient for the 584 nm LMCT band ($2970 \pm 20 \text{ M}^{-1}\text{cm}^{-1}$) was determined. For comparison, the corresponding LMCT observed in the Fe(III)-*Mm*CDO-L-Cys complex is red-shifted to 650 nm with slightly lower (~25%) extinction coefficient ($2,200 \text{ M}^{-1}\text{cm}^{-1}$) (19).

As shown in **Figure 3.4**, addition of cyanide at saturating concentrations of **3MPA** results in a red shift in the LMCT band to 696 nm. Stacked difference spectra highlight the loss of the original 584 nm absorption associated with **1S** upon increasing equivalents of cyanide. Since addition of cyanide to **1** yields no absorption features, the resulting red shift in λ_{max} confirms simultaneous binding of both cyanide and **3MPA**. Consequently, formation of the cyano-bound Fe(III)-*Av*3MDO-**3MPA** complex (termed **1C**) can be monitored by UV-visible spectroscopy as described above. **Figure 3.4** reveals that the binding affinity of **2** for cyanide is relatively poor ($K_d \sim 2.3 \text{ mM}$), with only partial saturation observed at a 40-fold molar excess relative to **1S**. Beyond which, some loss in 696 nm absorbance is observed which may reflect loss of **3MPA**-coordination or iron from the *Av*3MDO active site.

EPR spectroscopy was also used to monitor **3MPA** and cyanide binding at the Fe(III)-*Av*3MDO active site. As stated previously, in the absence of substrate the observed spectra for **1** is nondescript and indistinguishable for adventitiously bound ferric iron. However, addition of a 10-fold molar excess **3MPA** relative to **1** results the spectrum shown in **Figure 4.5 (panel A)**. Relative to the signal observed for Fe(III)-*Av*3MDO, the spectrum observed for **2** is vastly sharper and exhibits clearly defined rhombic *g*-values at 4.44, 4.31, and 4.27. An additional weak resonance can be observed at $g \sim 9.66$ at temperatures below 10 K. While the spin-state of **1S** remains the same as for **1** ($S = 5/2$), coordination of the **3MPA** results in perturbation to zero field splitting parameters (D and E/D). The magnitude of the axial-zero field splitting term ($|D| =$

$1.1 \pm 0.1 \text{ cm}^{-1}$) for **1S** was determined by fitting the temperature normalized intensity of the $g_{ave} = 4.34$ signal to a Boltzmann population distribution for a 3-level system. A quantitative simulation (*blue dashed line*) is overlaid on the data for comparison. These features and the increase in spin orbit coupling observed upon **3MPA**-coordination closely parallels what has been reported for L-Cys binding to Fe(III)-*MmCDO* (19). **Table 3.1** lists all the relevant spectroscopic parameters for **2** determined from EPR simulation.

Samples of **1S** were treated with a 5-, 20-, and 40-fold molar excess of cyanide relative to enzyme and allowed to equilibrate for 20-minutes on ice prior to refreezing and data collection. As shown in Figure 4.5, the high spin $g_{ave} \sim 4.34$ signal associated with **1S** is attenuated with increasing cyanide concentration, and two new signals grow in near $g \sim 2$. At low cyanide additions (5-fold molar excess), only one signal is observed with g -values of 2.39, 2.24, and 1.92. As this signal is distinct from the previously described low-spin ferric iron species (**1A** and **1B**), it is reasonable to conclude that this signal represents the low-spin (**3MPA/CN**)-bound Fe(III)-*Av3MDO* observed at 696 nm by UV-visible spectroscopy. The overlaid spectroscopic simulation provides an analytical determination of concentration from which a molar extinction coefficient ($\epsilon_{696} = 1800 \pm 10 \text{ M}^{-1}\text{cm}^{-1}$) can be determined for (**3MPA/CN**)-bound Fe(III)-*Av3MDO*. For simplicity, this species will be referred to as **1C**.

As shown in Figure 4.5 (panel **B**), the concentration of **1C** remains largely constant at higher concentrations of added cyanide (20- and 40-fold molar excess). Instead, an additional signal is observed with g -values matching those previously attributed to **1B** (1.84, 2.18, and 2.53). Comparison of the microwave power required for half-saturation ($P_{1/2}$) at g_1 ($0.91 \pm 0.1 \text{ mW}$) and g_3 ($0.96 \pm 0.2 \text{ mW}$) are also equivalent to **1B**, suggesting that these are indeed the same species. From this observation, it can be concluded that coordinated **3MPA** ligand is displaced

from the ferric site at high cyanide concentration. To maintain charge balance, displacement of the **1C** 3MPA^{2-} dianion would require coordination of at least two cyanide ligands in **1B**. This explains the inability to obtain saturating **1C** formation in UV-visible experiments performed at high cyanide concentrations. A summary of these reactions is presented in **Figure 3.3**.

Assuming an equivalent bidentate **3MPA** Fe(III)-coordination as reported previously (Chapter 2), only one coordination site (*trans* to H90) remains accessible for cyanide binding. For clarity, this site is henceforth referred to as the axial binding to distinguish it from the equatorial, substrate-binding sites. Incidentally, this is the same Fe-binding site occupied by the π -accepting thiocyanate ligand in the crystal structure (PDB code: 7HOV) shown in **Figure 3.1B**. It is therefore reasonable to conclude that the structure of the (**3MPA/CN**)-bound Fe(III)-Av3MDO site (**1C**) represents the sum of the two structures shown in **Figure 3.1**. With **3MPA** occupying the equatorial Fe-sites and cyanide at the axial Fe-coordination site. However, the structure of **1A** and **1B** remain less well defined. Both species must have at least one cyanide ligand to push the Fe(III)-site low spin, but beyond this only some qualitative inferences can be made. For instance, based on the arguments presented above, **1B** likely feature at least two cyanide ligands bound to the Fe-site but their specific binding locations are not known. In an effort to provide more information regarding these species EPR experiments with isotopic substitutions were made using $^2\text{H}_2\text{O}$ and K^{13}CN .

Substitution with $^2\text{H}_2\text{O}$ buffer is often used to in EPR experiments to identify Fe-bound solvent ligands. There is a near 7-fold decrease in gyromagnetic ratio of ^2H ($I = 1$) relative to ^1H ($I = 1/2$) resulting in a significantly lower magnitude of hyperfine splitting. While these are frequently unresolved in CW EPR, samples prepared in $^2\text{H}_2\text{O}$ will have decreased linewidth relative to $^1\text{H}_2\text{O}$. By contrast, the magnetic ^{13}C ($I = 1/2$) present in samples prepared from K^{13}CN

should exhibit a broadening effect due to the interaction of the magnetic nuclei with the paramagnetic metal.

As shown in **Figure A3.1**, samples containing a mixture of **1A** and **1B** were prepared in $^2\text{H}_2\text{O}$ buffer or using K^{13}CN for comparison. A summary of these results is presented in **Table A3.1**. Most notably, species **1A** and **1B** exhibits minor shifts in g -values ($\Delta g \sim 0.003$ to 0.008) when prepared in $^2\text{H}_2\text{O}$ buffer. Further, a noticeable decrease in linewidth was observed for **1A** along the g_2 -principle axis. Indeed, **1B** exhibits a decrease in the full width at half-maximum (FWHM) along g_2 of 3 mT. A similar, albeit smaller effect (0.6 mT) is observed for **1B** along the same g_2 -principle axes. These findings are consistent with $^1\text{H}/^2\text{H}$ exchange within the first coordination sphere of the Fe(III)-site, suggesting that both **1A** and **1B** are coordinated by at least one water/hydroxide in addition to at least one cyanide ligand.

As **1A** and **1B** are both low-spin Fe(III) species both must have at least one cyanide ligand. Regardless, only minor perturbations were observed in the line width of **1A** prepared with K^{13}CN . By contrast, as illustrated in **Figure A3.1**, **1B** exhibited significant line broadening along the g_2 -axis. By comparison to **1A**, the larger increase in observed line width for **1B** prepared with K^{13}CN could be attributed to multiple Fe-bound cyanide ligands present on **1B**. This conclusion fits nicely with the observation that **1B** is produced by displacement of **3MPA** from **1C** by excess cyanide. However, this could also be attributed to greater alignment of the **1B** g -tensor with the molecular axis of the Fe-site. In which case, direct comparison of isotopic effects can be misleading. Consequently, isotopic CW EPR experiments on **1A** and **1B** offer only limited utility with regard to the speciation of CN-bound Fe(III)-Av3MDO in the absence of substrate.

Electron spin echo envelope modulation (ESEEM) experiments were performed to further interrogate the first coordination sphere of (**3MPA/CN**)-Fe(III)-Av3MDO (**1C**). ESEEM

is a pulsed EPR technique that directly observes magnetic nuclei that are coupled to the unpaired spin via hyperfine couplings. Consequently, ESEEM measurements are a useful and popular tool for characterizing metalloenzyme structure (45,46). In an ESEEM experiment, coupled nuclei are identified by their periodic modulation of the electron spin echo as a function of time (47-49). Typically, the time domain spectrum is Fourier transformed into a frequency domain spectrum in which peaks from individual nuclei appear at their respective ENDOR frequencies (50).

Several coupled magnetic nuclei are present in complex **1C**. **Figure 3.5** shows the 3-pulse ESEEM spectrum of **1C** at 292 mT, which falls near g_1 in the EPR spectrum (**Fig. 3.5**). Peaks below 8 MHz represent coupled ^{14}N nuclei ($I = 1$) that are close to the low-spin Fe(III) center. These include the ^{14}N on coordinated histidine residues, on the second-sphere arginine residue, and on the coordinated cyanide.

In addition to ^{14}N , a few ^1H ($I = 1/2$) peaks that fall near the ^1H Larmor frequency (~ 12.4 MHz at this magnetic field). These are from ^1H that are near the Fe center, namely those on the histidine residues and on **3MPA**. While many of these peaks overlap, any exchangeable ^1H should disappear in deuterated samples. Therefore, measurements on deuterated samples made under the same conditions reveal if a solvent-based ligand like H_2O or OH^- is coordinated to the Fe(III) center. **Figure 3.7** shows a comparison of $^1\text{H}/^2\text{H}$ ESEEM spectra taken at magnetic fields spanning the region between g_1 and g_2 . While there is a decrease in the intensity of ^{14}N peaks in the ^2H sample, the peaks in the ^1H region of the spectra (~ 12.4 MHz) are nearly superimposable. Typically, $^2\text{H}/^1\text{H}$ ratio spectra are used to divide out ^1H modulation and isolate ^2H peaks that can then be simulated. However, because the ^2H samples exhibit less intensity in the ^{14}N region, ratio spectra are dominated by ^{14}N peaks. Therefore, in this case, the comparison of $^1\text{H}/^2\text{H}$ spectra is most practical for determining coupled exchangeable ^1H . As shown in **Fig. 3.7**, no strongly-

coupled ^1H peaks disappear in the deuterated sample, which suggests there is not a solvent-based ligand coordinated to the Fe(III) center in species **1C**. These observations are consistent with the simultaneous binding of **3MPA** and CN^- in species **1C** and rule out the possibility of a solvent-based ligand.

Cyanide binding to H157N and Y159F Fe(III)-Av3MDO variants. Following the same procedure as described above for cyanide additions to the wild-type enzyme. EPR samples of cyanide-bound Fe(III)-Av3MDO were prepared for both H157N and Y159F variants. These studies serve two purposes. First, both variants alter the conserved SHY hydrogen bonding network which interacts directly with the non-heme iron site even in the absence of substrate (18). Therefore, any deviation in the g -values observed in wild-type and variant low-spin iron species can be used to confirm that the signals originate within the enzymatic active site rather than adventitiously bound iron. Second, in previously reported EPR studies, it was observed that the amount of iron-nitrosyl species produced in samples prepared from the H157N and Y159F variant of Av3MDO is significantly lower than observed for the wild-type enzyme (18). Moreover, the variant $S = 3/2$ $\{\text{FeNO}\}^7$ EPR signals exhibited greater rhombic distortion as compared to wild-type enzyme. These findings suggest that the conserved SHY H-bonding network is crucial for stabilizing NO binding at the non-heme iron site. Therefore, these studies provide an additional method to investigate the how interaction between the Fe-site and the SHY H-bonding network influence coordination of ligands at the Fe-site.

As shown in **Figure 4.8**, treatment of H157N Av3MDO with a 40-fold molar excess of cyanide results in the formation to two sets of rhombic g -values (2.48, 2.18, and 1.87) and (2.54, 2.21, and 1.84) consistent with low-spin iron. To differentiate these species from those observed

in the wild-type enzyme, these are simply referred to as **2A** and **2B**, respectively. Of note, the g -values observed for **2B** are quite similar to wild-type **1B** with a minor shift in g_2 ($\Delta g_2 = 0.026$) with increased line width as well as a lesser shift in g_1 ($\Delta g_1 = 0.005$). This suggests that **1B** and **2B** likely have a similar first Fe-coordination sphere, albeit with some minor structural perturbations induced by perturbations within the SHY H-bonding network. By contrast, wild-type **1A** and **2A** exhibit vastly divergent g -values and no apparent overlap in corresponding g -values. As with the wild-type enzyme, the relative concentration of each species (0.75 eq. **2A** to 0.25 eq. **2B**) determined by spectroscopic simulation is largely insensitive to cyanide concentration. However, whereas **1B** represents the majority product in the wild-type enzyme, this trend is apparently reversed for H157N. Regardless, the shift in EPR signals observed in cyanide treated Fe(III)-Av3MDO samples prepared from the H157N variant confirms that wild-type signals **1A** and **1B** indeed originate within the enzymatic active site.

Up to this point, EPR spectroscopy reveals two distinct cyanide binding modes within the wild-type Av3MDO and H157N variant. Presumably, each species representing cyanide coordination at a different Fe-site or potentially multiple CN-ligands bound simultaneously. However, cyanide additions made to the Y159F variant of Fe(III)-Av3MDO result in three distinct low-spin rhombic ($S = 1/2$) species are observed with g -values of (2.33, 2.14, and 1.94), (2.42, 2.20, and 1.90), and (2.47, 2.17, and 1.87). These signals are shown in Figure 3.9 and will be referred to as **3A₁^F**, **3A₂^F**, and **3B^F** henceforth. Species **3B** exhibits the least spread in g -values ($g_1 - g_3 = 0.39$) and has no obvious analogue in either the wild-type or H157N variant. However, all three g -values for **3A₁** exhibit only modest deviations relative to wild-type **1A** (Δg_1 , Δg_2 , and $\Delta g_3 = 0.07$, -0.02 , and 0.01). Similarly, Y159F species **3A₂** correlates closely with **2A** with deviations in g_1 , g_2 , and g_3 of -0.01 , -0.01 , and 0.00 , respectively. Additional features observed

near $g \sim 2.25$ and 2.01 (designated by \circ) suggest the presence of an additional $S = 1/2$ species however its contribution to the overall spectrum is negligible. For comparison, **Table 3.1** summarizes the simulation parameters for all low-spin ($S = 1/2$) ferric Av3MDO signals.

Addition of cyanide to H157N and Y159F Av3MDO pre-incubated with **3MPA** yields rhombic $S = 1/2$, signals which can be attributed to each (**3MPA/CN**)-bound variant. UV-visible and EPR spectroscopy was used to follow coordination of **3MPA** and cyanide at the enzymatic Fe-site as described above for the wild-type enzyme. For brevity, only the (**3MPA/CN**)-bound Fe(III)-Av3MDO species are described below. However, a summary of all UV-visible and EPR results obtained from variants can be found in *Appendix*, **Figures A3.2-A3.6**.

Among samples of (**3MPA/CN**)-bound Fe(III)-Av3MDO prepared from the H157N and Y159F variant (termed **2C** and **3C**, respectively), perturbations to both UV-visible and EPR features are readily apparent in the **3MPA**- and (**3MPA/CN**)-bound sites. For instance, maximum absorbance for **2C** was observed at 670 nm; representing a -26 nm red shift relative to wild-type **1C**. The line width (169 nm) of this absorption feature is quite similar to wild-type suggesting the formation of a homogeneous (**3MPA/CN**)-bond Fe-site. Indeed, as shown in **Figure A3.5**, the observed g -values for **2C** (2.39, 2.30, and 1.93) are quite similar to wild-type **1C**, except that the middle g_2 resonance is shifted up-field relative to **1C** (2.240). Simulations of **2C** reveal that g -strain along g_1 is significantly higher for H157N relative to the wild-type enzyme. This implies structural heterogeneity along the g_1 -molecular axis, potentially indicating a change in H-bond donation from the outer Fe-coordination sphere. Crucially, samples prepared from the H157N variant exhibits homogenous binding of **3MPA** and cyanide. Meaning that only one species is observed in which **3MPA** and cyanide are simultaneously bound to the Fe-site (species **2C**). Another feature that parallels the wild-type enzyme is the formation of a new $S =$

1/2 signal (designated **2B**) upon addition of excess cyanide to the H157N (**3MPA/CN**)-bound **2C**. As with the wild-type enzyme, this suggests that displacement of **3MPA** from the Fe-site by cyanide yields both **1B** and **2B**.

By contrast, UV-visible spectra of **3C** exhibits a broad absorption feature at 684 nm (a -12 nm red-shift relative to **1C**) with a substantially broader peak (337 nm), this could suggest heterogeneous binding of **3MPA** and/or CN within the Y159F variant. Surprisingly, the observed *g*-values of **3C** (2.40, 2.26, and 1.92) closely match those observed with wild-type **1C**. Thus despite the vastly attenuated **3C** signal relative to wild-type and H157N, the active site geometry of the (**3MPA/CN**)-bound Fe-site is not vastly perturbed. This implies that the role of Tyr159 is to facilitate ligand binding at the Fe-site without altering significantly the geometry of the enzyme-substrate complex. Isotopic substitutions were not attempted with H157N and Y159F variants due to their lower **3MPA**- and cyanide binding affinities and heterogeneity of signals.

Computational results: 3MPA/CN-bound wild type Av3MDO (1C). The chosen model for the **3MPA**-bound Fe(III)-Av3MDO is based on the Av3MDO crystal structure of in complex with the competitive inhibitor 3-hydroxypropionic acid (**3HPA**) (Chapter 2). In this report, computationally models were generated for coordination of the native **3MPA**-substrate and spectroscopically validated by HYSCORE and Mössbauer spectroscopies. This model is similar to what was proposed Jameson and Karplus *et al.* where **3MPA** is bound bidentate with thiolate trans to His92 and the carboxylate bound trans to His142.(51) For optimization of the **1C** structure, a cyanide ligand was placed in the axial position analogous to the Fe-bound thiocyanate ligand in **Figure 1B**, essentially displacing nitric oxide from the previous NO-bound model.

After assigning the first coordination ligands, consideration was put into the outer sphere residues. The cationic Arg168 residue is expected to interact with the adjacent **3MPA** carboxylate as shown previously (Chapter 2). What remains to be determined is the influence of the outer-sphere SHY hydrogen bonding network on the observed *g*-values of **1C**. As it stands, Tyr159 can either donate a hydrogen bond to the axial bound ligand or to the delta-nitrogen of His157 within the SHY motif. Therefore, two optimizations were performed with the inclusion of Arg168 and the SHY motif to reflect these possibilities. In the first model (*1*) shown in **Figure 3.10**, the Tyr159 phenol hydroxyl group (Tyr159-OH) donating a hydrogen bond to the axial cyanide ligand. By contrast, model (*2*), shows the Tyr159-OH donating to the δ -nitrogen of His157. Previous work suggested the possibility of an equilibrium between Tyr159-OH donating to His157 and the axial bound chloride identified in the crystal structure of the *Av*3MDO-3HPA complex (pdb code, 6XB9) (Chapter 2). Therefore, both arrangements are possible with possible with anionic cyanide in place of chloride. For both optimized models, EPR *g*-values were calculated using DFT methods. The resulting values are shown in **Table 3.3**. Neither model (*1*) or (*2*) accurately reproduce the *g*-values seen experimentally with DFT methods. This disagreement in DFT predicted *g*-values is not uncommon among low-spin cyano-species was observed in our previous characterization of the (CYS/CN)-bound *Mm*CDO.(19)

Recently, Fischer and Brunold *et al.* reported the use of CASSCF/NEVPT2 calculations to provide a much greater agreement between computationally predicted and experimentally observed *g*-values among synthetic model complexes of the (**3MPA/CN**)-bound 3MDO active site (39). Therefore, this same methodology was applied here to the optimized structures for model (*1*) and (*2*).

As shown in **Table A3.2**, initial calculations were performed without contributing outer-sphere residues (Arg168, Tyr159, His157, and Ser155) using a minimal active space (5,5). Using (n-electron, n-orbital) nomenclature, the (5-5) active space represents 5 electrons and five 3d iron orbitals. Improvements in the accuracy of each calculation can then be gauged by a decreasing RMSD value comparing calculated and experimental *g*-values. For instance, a greater agreement in prediction of *g*-values was obtained with inclusion of three occupied ligand bonding orbitals, representing an (11, 8) active space. Inclusion of outer sphere residues as point charges also results in higher agreement with experimentally observed *g*-values. In the aforementioned work presented by Fischer and Brunold et al., addition of five (4d-orbitals) to provide a (11,13) active space provided the best agreement with their observed *g*-values.(39) However, in this instance, expansion to (11,13) active space substantially decreases agreement between predicted and observed *g*-values. Given the similarities in structures, this result was unexpected. However, it has been observed that CASSCF studies on transition metal complexes can be highly system dependent when choosing optimal active space orbitals.(37) Moreover, the *g*-values for species **1C** presented herein are more anisotropic with a higher g_1-g_3 than what is reported for the model complex analogous to (3MPA/CN)-3MDO (0.47 for **1C** vs 0.27 for the model complex) (39). Therefore, the *g*-values reported in **Table 3.3** were calculated using the optimal (11,8) active space which include outer sphere point charges. **Table A3.2** illustrates the calculated *g*-values for each step in the optimizing the active space and basis set.

As noted above, two modes of **1C** were optimized to account for differences in the H-bond donation of Tyr159. In model 1 (**M1**), Tyr159 H-bond donation to the axial Fe-bound cyanide ligand is modeled, whereas (**M2**) represents Tyr159 H-bond donation to the adjacent His157 residue. In this case, model (**M1**) provides a greater agreement with the experimentally

observed g -values with a nearly 2-fold decrease in RMSD [0.018 for (*M1*) versus 0.033 for (*M2*)]. Of note, (2) provides a closer match to the g -values observed for **2C** in the H157N variant suggesting the loss of H-bond donation in H157N to the axial Fe-bound cyanide ligand.

Computational Results: 3MPA/CN-bound H157N (2C) and Y157F (3C) Av3MDO. In the H157N variant, the outer sphere SHY motif has been augmented to a SNY motif. This perturbation is reflected in the observed g -values of **2C** by a g -shift in g_2 from 2.24 to 2.30. Like wild type, the outer sphere interactions in the H157N 3MDO variant were investigated by building of models and evaluated based on their agreement with spectroscopic g -values. The case of H157N was more complicated as the asparagine could be either a hydrogen bond acceptor or donor to the adjacent Tyr159. Therefore, four models were optimized to account for each possibility.

Illustrations of each model for the H157N variant is shown in **Figure A3.7**. Each model for **2C** has cyanide and **3MPA** bound to iron as seen in wild type. Coordinates of the Asn157 residue were initially obtained by the mutagenesis function in Pymol (v2.2.3) with PDB: 6XB9.(52) Model **3** is similar to model **2**, wherein Tyr159-OH donates towards the Asn157 carbonyl group, leaving the cyanide unperturbed. model **4** has Tyr159-OH donating to the cyanide, as in model **1**. It is also possible to flip the orientation of the Asn157 so the amide group is closest to the tyrosine and cyanide ligand. In this orientation, both the Tyr159-OH and Asn157-NH₂ could donate towards the cyanide, as seen in model **5**. Finally, model **6** features the Asn157-NH₂ donating to the Tyr159 oxygen and the Tyr159-OH donating to cyanide. Attempts were also made to optimize Tyr159-OH donate to the Asn157 amide group. However, these optimizations converged as variations of model **6**.

The CASSCF/NEVPT2 process was repeated for these models using a (11-8) active space and point charges in the place of the outer sphere residues. The resulting calculated g -values are shown in **Table 3.3**. Model **3** shows the best agreement between calculated and experimental values. Similarly, if one looks at the shift in experimental and calculated g -values comparing H157N to wildtype, the agreement is also best with model **3** (**Table A3.2**). Therefore, both the direct comparison of g -values of this species and trend seen in the change of g -values between variants agree with this model. Notably, model **3** is the only arrangement which does not feature a hydrogen bond being donated to the cyanide ligand. This agrees with the trend seen above where model **2** also closely reproduced the g -values of the H157N variant. As such, the optimized structure assigned as **2C** is shown in **Figure 3.7** (bottom).

Previously, UV-vis spectra of MDO titrated with **3MPA** followed by cyanide showed a shift in the LMCT band of S \rightarrow Fe. The wild type **1C** had a λ_{\max} of 696 nm while the H157N **2C** had a λ_{\max} of 670 nm. The energy difference between these wavelengths is 1.6 kcal/mol. This destabilization could be due to a loss of a hydrogen bond. Both the UV-vis spectra and calculated g -values support the theory of the (**3MPA/CN**)-bound MDO complex losing a hydrogen bond to the cyanide in the H157N variant.

The Y159F variant of 3MDO eliminates the possibility of hydrogen bond donation from the SHY motif to the iron active site by replacing the tyrosine phenol with a phenyl group. However, the g -values observed from **3C** are quite similar to **1C**. The diagnostic g -shift for the g_2 signal is not observed in great magnitude as in the H157N variant. In fact, the g -values do not largely shift from those seen in wild type. This creates a dilemma as the phenylalanine replacing tyrosine has no means of donating a hydrogen bond.

The previous UV-vis titrations showed a λ_{max} of 684 nm for the (**3MPA/CN**)-bound Y159F 3MDO vs 696 nm for wild type. The difference in energy between these wavelengths is 0.76 kcal/mol; lower in magnitude than for H157N. Therefore, it was speculated that in the absence of tyrosine, another moiety could be donating a hydrogen bond in its place, albeit with a weaker interaction. Two models, shown in Figure A3.8, attempt to replicate the effects of the Y159F variant. However, neither model reaches *g*-value agreement to experimental values shown above. Therefore, the structure of **3C** and its interactions with the outer sphere remain unresolved.

Computational Results: CN-bound *A*v3MDO (1B**)** It was reasoned that **1B** was the result of cyanide displacing substrate and would therefore have at least two cyanides bound to iron. Using this postulate, multiple structures were optimized for both two and three cyanides bound to replicate **1B**. In the case of two cyanides, both the positions and identity of a third ligand were considered (water, hydroxide, chloride). A five-coordinate structure was also considered. CASSCF/NEVPT2 calculated *g*-values were determined for the resulting structures. A summary of this work is shown in the Appendix and **Table A3.3**. In short, the orientation of ligands was determined have cyanide bound to the equatorial positions (*trans* to His92 and His142) with hydroxide bound axially (*trans* to His90). The *g*-values were best replicated to experimental when hydroxide is donating a hydrogen bond to the phenol oxygen of Tyr159, which in turn, donates a hydrogen bond to His157. The *g*-values were calculated to show very good agreement with an RMSD of 0.013. This structure was replicated for the H157N variant in the same way as for species **2C** and calculated *g*-values similarly showed good agreement with experimental values.

Though attempts were made, the identity of species **1A** is still unresolved. The g -values are more similar to species **1C** than **1B** which suggests one cyanide is bound. However, the orientation and identity of the other ligands is still unknown. D₂O substitution experiments suggest there is at least one ligand with an exchangeable proton, but further investigation would likely be beyond the scope of this work. Similarly, the H157N and Y159F cyano species seen without substrate (**2A**, **3A₁^F**, **3A₂^F**, **3B^F**) were not investigated computationally due to the high number of possible orientations and lack of spectroscopic information.

3.4 Conclusion

Cyanide was shown to bind ferric 3MDO without the presence of substrate. As such, the effects of the SHY motif were able to be interrogated for the resting state enzyme. Both wild type and the H157N variant revealed two $S = 1/2$ species in the presence of cyanide. However, the Y159F variant revealed at least three different cyanide-bound species. Clearly, the absence of the Tyr159 interaction with the iron complex severely impacts the manner in which incoming ligands bind to iron. Tyr159 likely gates the binding of ligands to preferred coordination sites resulting in the two stable configurations represented by **1A** and **1B**. Then removal of this interaction results in seemingly random assortment of cyanide binding.

The effects of the SHY motif can be seen on the (CN/3MPA)-bound species by the large shift in the g_2 signal when comparing the wild type to the H157N variant. DFT optimizations with CASSCF/NEVPT2 single point calculations were able to accurately replicate the experimental g -values for both species. **Figure 3.9** shows that the calculated g -tensor orientation is consistent with the g_2 signal being colinear with the Fe-CN bond. These calculations showed the shift was due to a reorientation of the Tyr159 residue of the SHY motif. In wild type it was

determined that Tyr159 donates a hydrogen bond to the axially bound cyanide ligand. Upon substituting His157 for an asparagine, the Tyr159 phenol redirects to donate a hydrogen bond to the carbonyl of Asn157. Previously, it was thought that the H157N variant altered the hydrogen bond network of the SHY motif by a small geometric perturbation which would still allow Tyr159 to interact with the iron complex. However, data presented above shows the H157N variant effectively cuts off interaction of the Tyr159 residue from the iron active site. This agrees well with kinetic studies showing the H157N and Y159F have similar activities ($k_{cat} = 0.092$ vs 0.081 s^{-1}) and catalytic efficiencies ($k_{cat}/K_M = 7800$ vs $9000 \text{ M}^{-1}\text{s}^{-1}$) as both variants effectively remove hydrogen bond donation from Tyr159 to the active site.

It is peculiar that both the H157N and Y159F variant remove hydrogen bond donation of Tyr159 from the active site but only Y159F result in the multitude of cyanide bound species. This behavior may be explained by the mode in which the hydrogen bond is removed. The phenyl functional group of the Y159F variant has no means of hydrogen bonding. Whereas the Tyr159 may still accept a hydrogen bond from a ligand bound to the iron complex. Indeed, this is seen for structural assignment of **1B** when an axial bound hydroxide donates a hydrogen bond to Tyr159. The structure of **1B** is shown in **Figure 3.9** with its corresponding g-tensor orientation. This model shows an interaction possible in both wild type and the H157N variant which is impossible for the Y159F variant. Therefore, the means of directing ligand binding may be from Tyr159 accepting a hydrogen bond and thus stabilizing the axially bound hydroxide/water ligand.

As presented herein, Tyr159 of the SHY motif can interact with the iron active site as both a donor and acceptor of a hydrogen bond. This is a stark contrast to mammalian CDO which, based on the orientation of the SHY motif hydrogen bonding network (see Chapter 1),

would only act as a donor to the iron active site. Therefore, these insights may help to reason the difference in substrate specificity between the two enzymes.

Figures

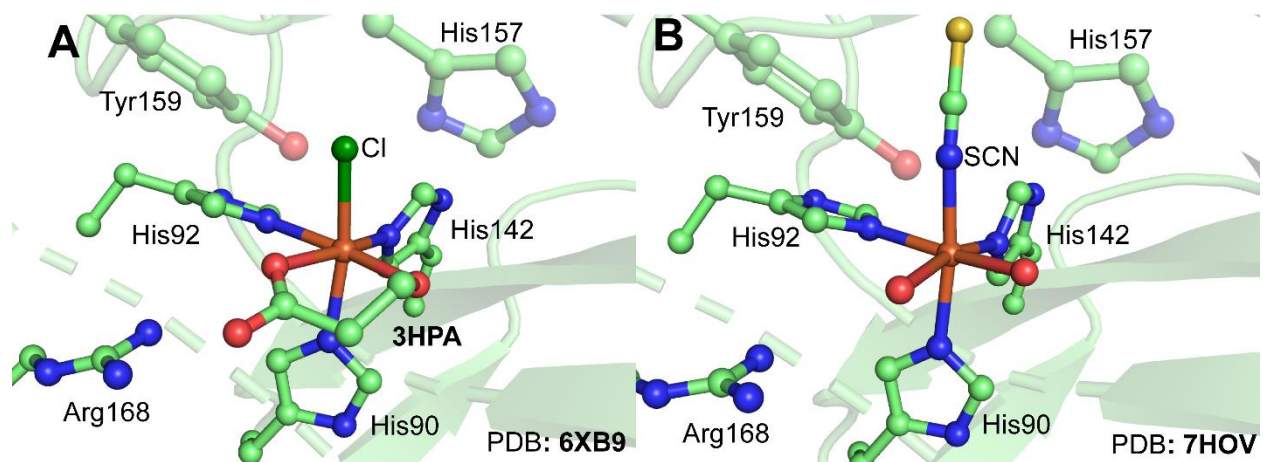


Figure 3.1: The crystal structures of inhibitor, **3HPA**, bound *Av3MDO* (panel A) in the equatorial positions trans to His92 and His142. Panel B shows the crystal structure of SCN⁻ bound to the axial position trans to His90.

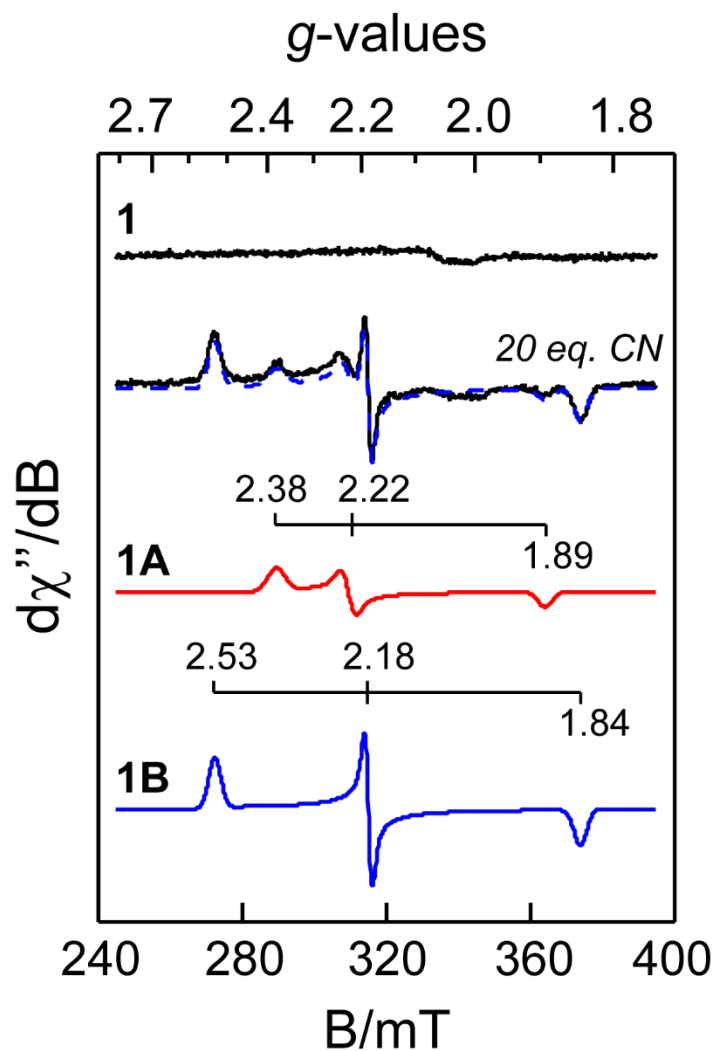


Figure 3.2 X-band CW EPR of Fe(III)-Av3MDO (**1**) treated with a 20-fold molar excess of cyanide. A two component simulation (*dashed lines*) for cyano-bound Fe(III)-Av3MDO is overlaid on the data. Instrumental conditions: microwave frequency, 9.64 GHz, microwave power, 40 μ W; modulation amplitude, 0.9 mT; temperature, 10 K. Simulation parameters for **1A** and **1B** provided in **Table 3.1**.

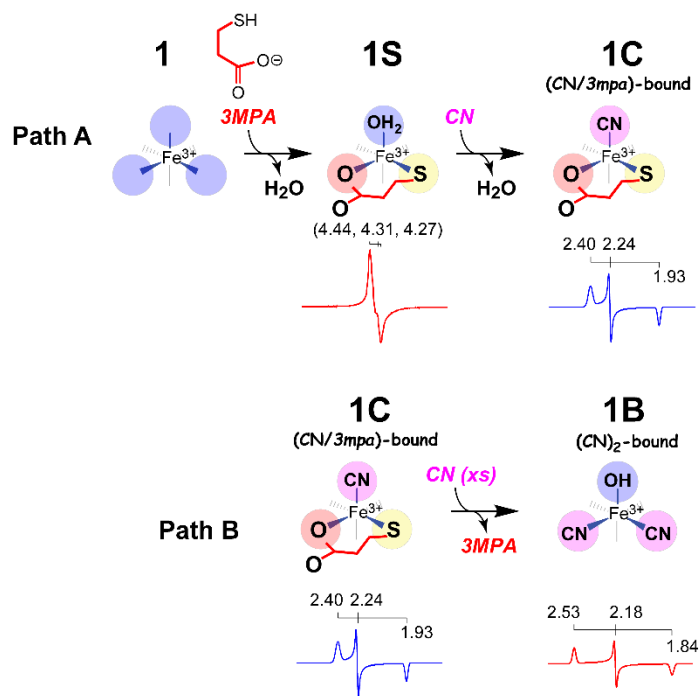


Figure 3.3 An illustration of the species resulting from addition of substrate followed by cyanide (**Path A**). Subsequent addition of excess cyanide to the (CN/3MPA)-bound species results in displacement of 3MPA (**Path B**).

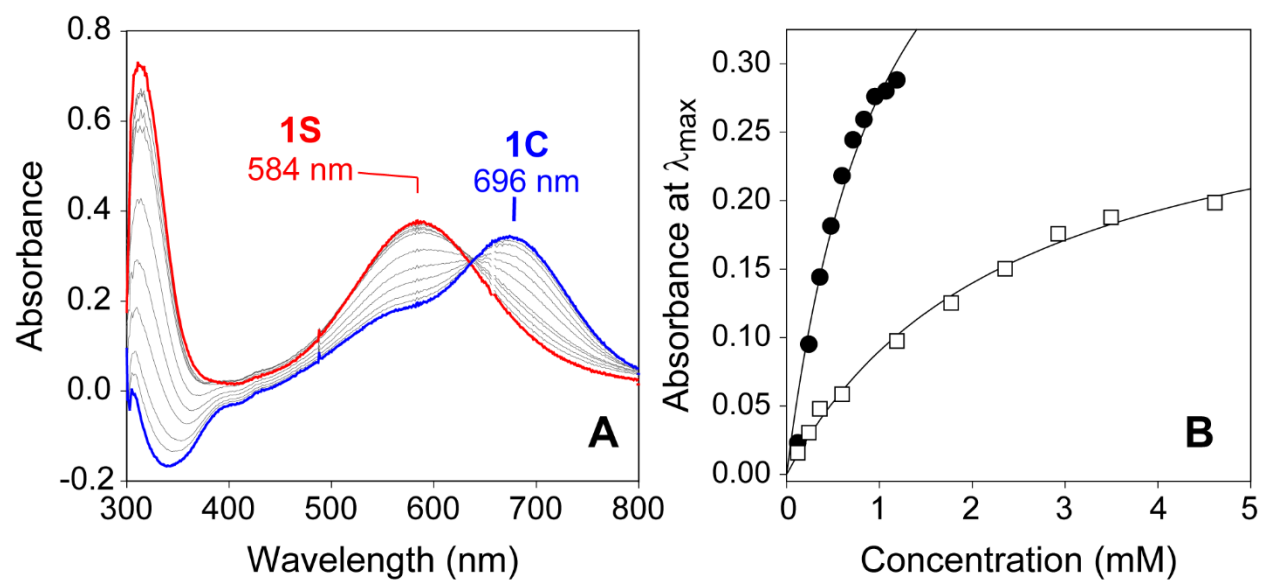


Figure 3.4: Panel A. UV-vis spectra of Fe(III)-Av3MDO (**1**) with **3MPA** (*red*) followed by addition of cyanide (*blue*). For clarity, the initial **1** complex was used to blank **3MPA** and KCN addition spectra. Panel B illustrates the change in λ_{\max} for **1S** (584 nm) and **1C** (696 nm) with increasing **3MPA** (*circle*) and KCN additions (*square*).

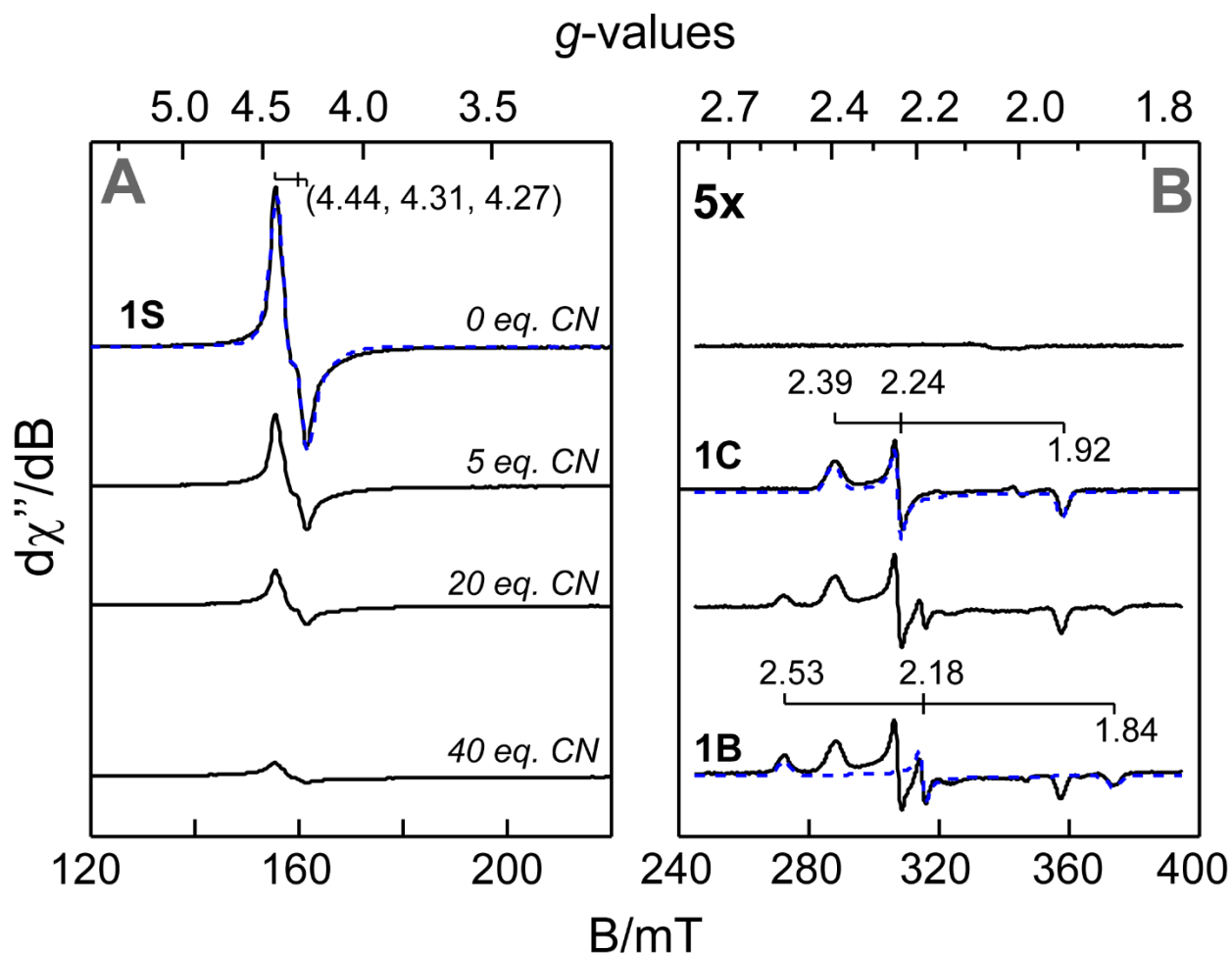


Figure 3.5 X-band CW EPR of (3MPA)-bound Fe(III)-Av3MDO (**1S**) titrated with 5-, 20-, and 40-molar equivalents KCN. Panel **A** highlights the loss of the high-spin (3MPA)-bound Fe(III)-Av3MDO with increasing cyanide concentration. Panel **B** illustrates the initial formation of the a low-spin (3MPA/CN)-Fe(III)-Av3MDO (**1C**) complex followed by formation of the **1B** cyano-species at elevated cyanide concentration. The scale of panel **B** was multiplied by 5-fold for clarity. EPR simulations (*dashed lines*) are overlaid on data for comparison. Instrumental conditions: microwave frequency, 9.64 GHz, microwave power, 20 mW (**A**) 40 μ W (**B**); modulation amplitude, 0.9 mT; temperature, 10 K. Simulation parameters for **1C** provided in **Table 3.1**.

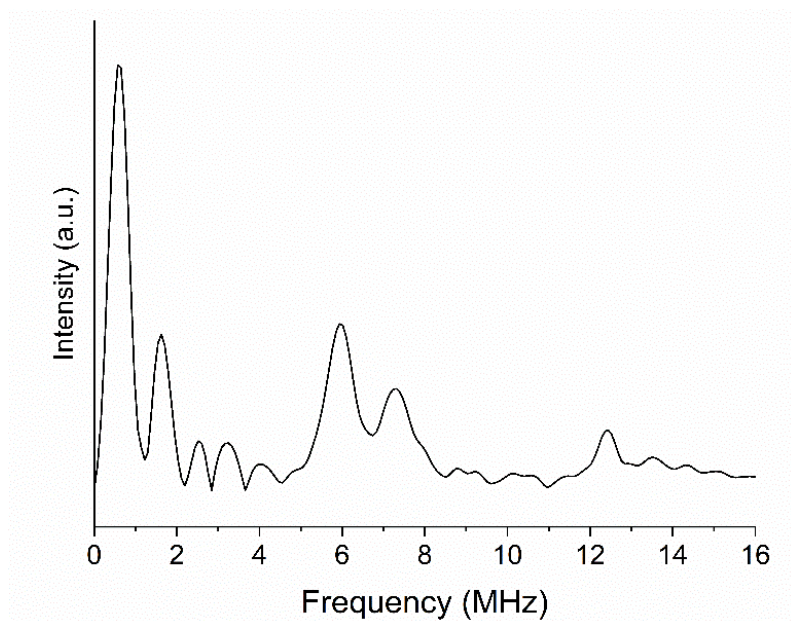


Figure 3.6. 3-pulse ESEEM spectrum of the **(3MPA/CN)-Fe(III)-AvMDO (1C)** at 292 mT. Instrument parameters: microwave frequency, 9.78 GHz; field position of 292 mT; temperature, 5 K; pulse repetition rate, 0.5 kHz; τ , 136 ns.

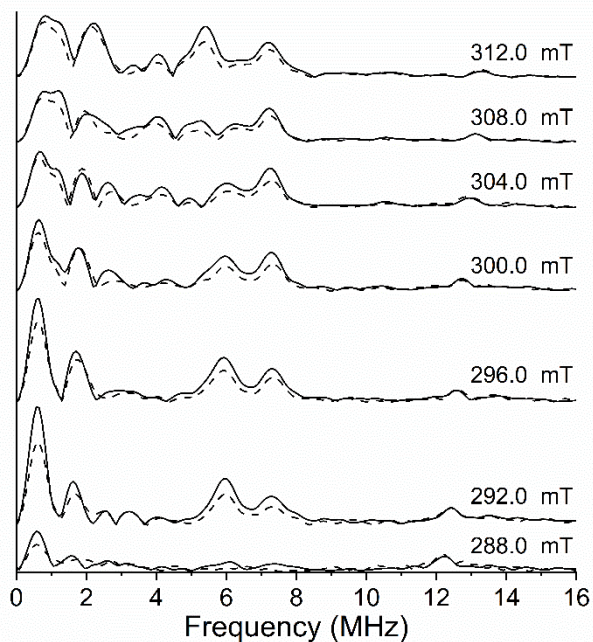


Figure 3.7. Comparison of 3-pulse ESEEM spectra of (3MPA/CN)-Fe(III)-AvMDO (1C) complex prepared in H₂O versus D₂O at magnetic fields spanning the region between g_1 and g_2 in the EPR spectrum. Spectra of the complex in H₂O are plotted as solid lines, and spectra of the complex in D₂O are plotted as dashed lines

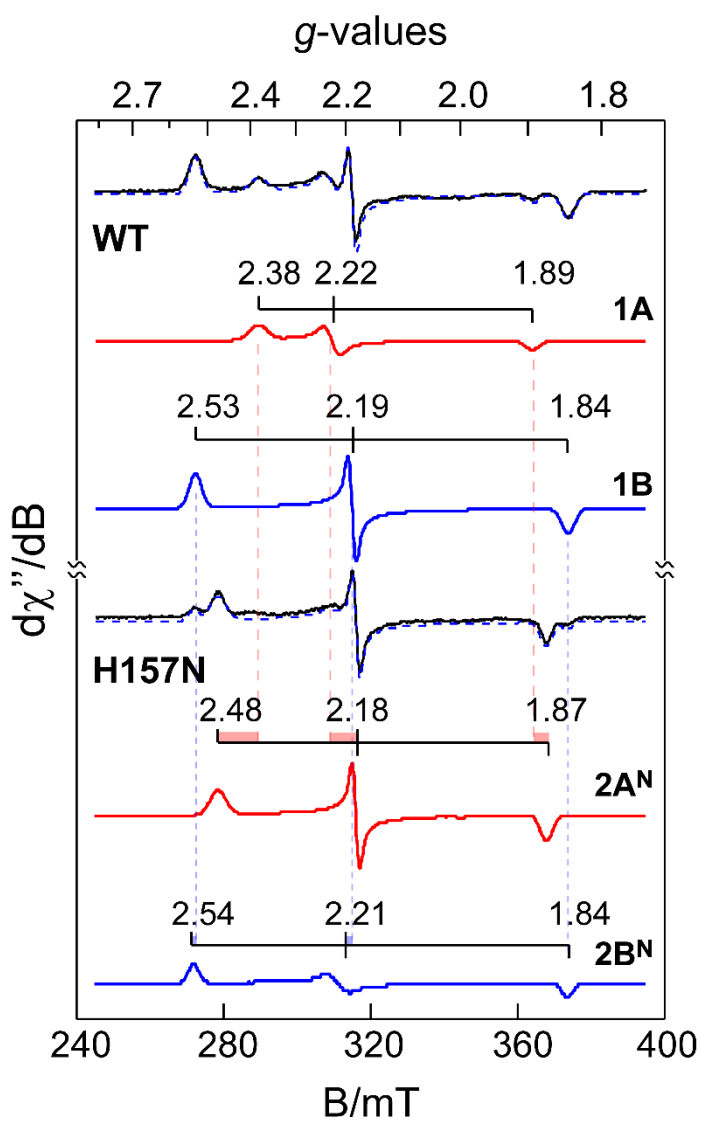


Figure 3.8 The EPR spectra of cyanide additions to the H157N variant. Two species are revealed through simulation (blue dashed line). Species 2A^N (red) and 2B^N (blue) are shown and compared to the correlating wild type species.

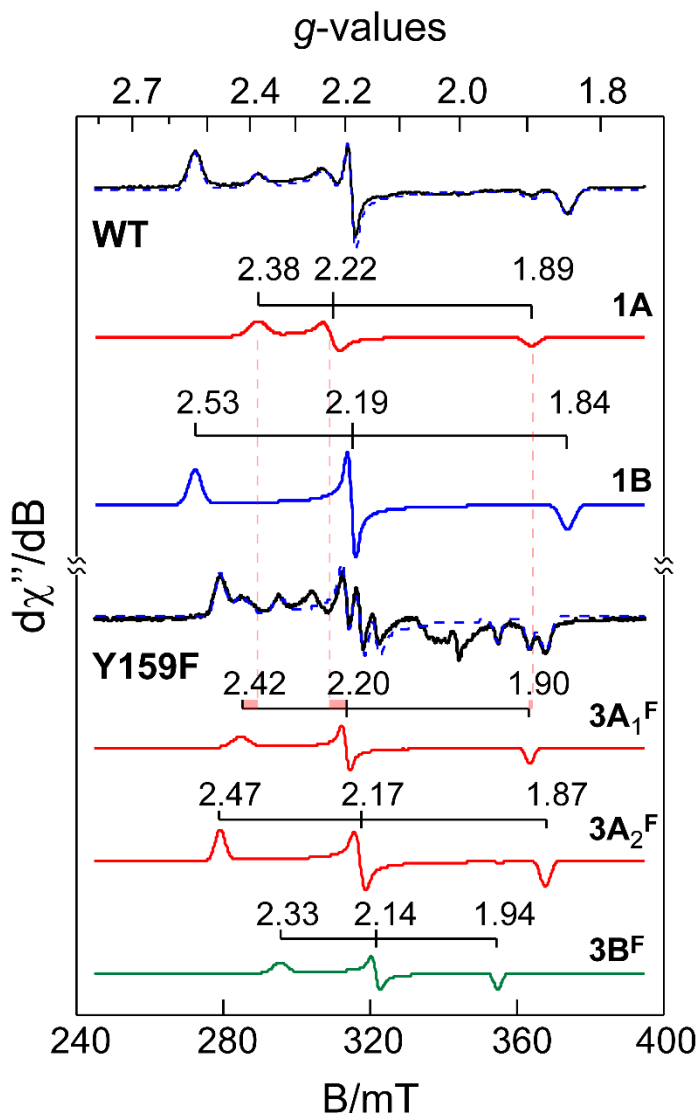


Figure 3.9 The EPR spectra of cyanide additions to the Y159F variant. Three species are revealed through simulation (blue dashed line). Species $3A_1^F$ and $3A_2^F$ (red) are labeled based on similarity to species **1A** and **2A**, respectively. Species $3B^F$ shows no similarity to other $S = 1/2$ 3MDO species.

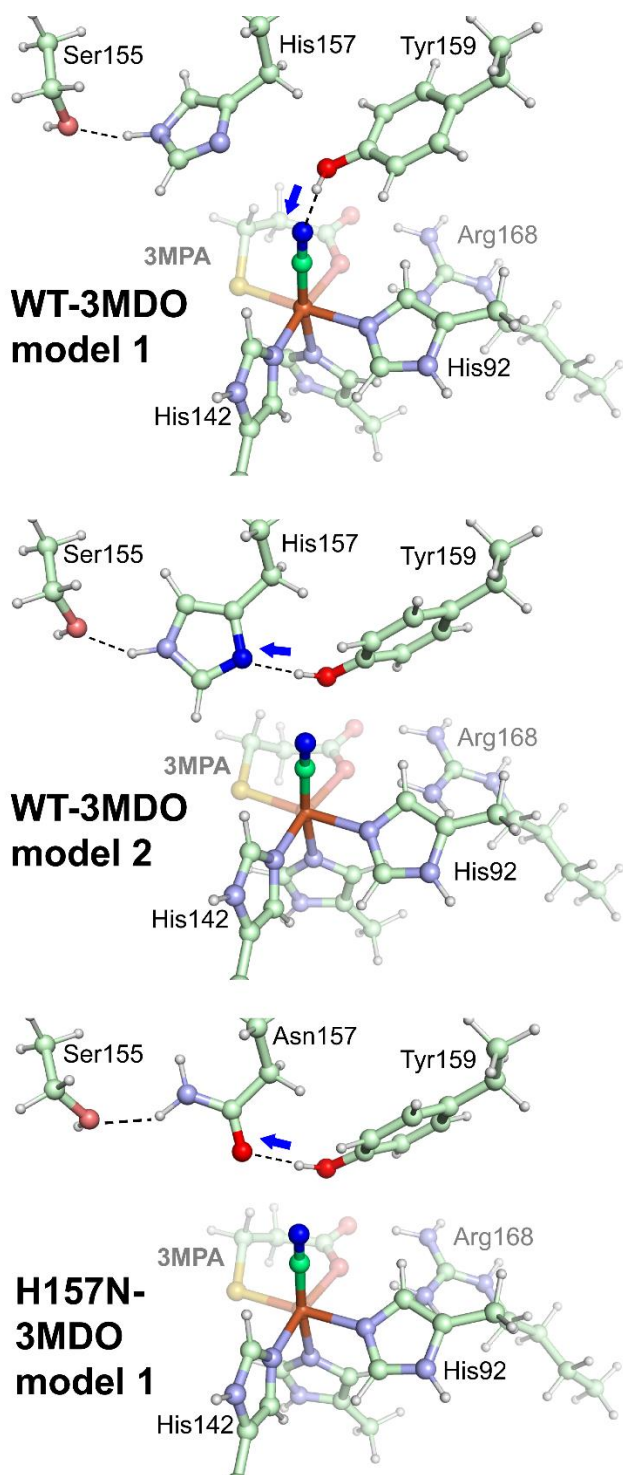


Figure 3.10: Optimized structures of models 1 and 2 showing (3MPA/CN)-bound wild type-3MDO with Tyr159 donating a hydrogen bond to the axial bound cyanide (*top*) or the N δ -His157 (*middle*). The optimized structure of (3MPA/CN)-bound H157N-3MDO is shown (*bottom*) as the assigned structure based on *g*-value agreement.

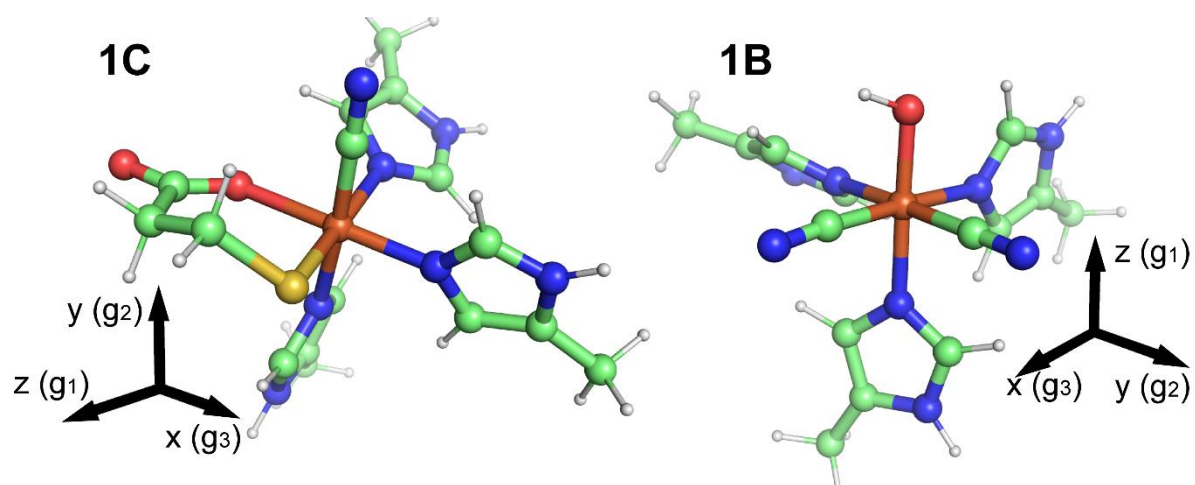


Figure 3.11: The g -tensor orientations of both species **1C** and **1B**.

| Sample+CN | Species | g_z | g_y | g_x | σg_x | σg_y | σg_z |
|------------|------------------------------|-------|-------|-------|--------------|--------------|--------------|
| MDO | 1A | 2.382 | 2.226 | 1.892 | 0.018 | 0.011 | 0.010 |
| | 1B | 2.531 | 2.188 | 1.843 | 0.014 | 0.002 | 0.008 |
| MDO+3MPA | 1C | 2.394 | 2.240 | 1.928 | 0.017 | 0.005 | 0.007 |
| | 1B | 2.531 | 2.188 | 1.843 | 0.014 | 0.002 | 0.008 |
| H157N | 2A | 2.476 | 2.180 | 1.873 | 0.018 | 0.001 | 0.008 |
| | 2B | 2.536 | 2.214 | 1.844 | 0.012 | 0.016 | 0.006 |
| H157N+3MPA | 2A | 2.470 | 2.180 | 1.874 | 0.014 | 0.002 | 0.007 |
| | 2B | 2.524 | 2.242 | 1.847 | 0.019 | 0.008 | 0.008 |
| | 2C | 2.394 | 2.295 | 1.932 | 0.027 | 0.010 | 0.010 |
| Y159F | 3A ₂ ^F | 2.469 | 2.172 | 1.874 | 0.010 | 0.006 | 0.006 |
| | 3A ₁ ^F | 2.422 | 2.198 | 1.896 | 0.019 | 0.002 | 0.004 |
| | 3B ^F | 2.333 | 2.143 | 1.942 | 0.013 | 0.003 | 0.004 |
| Y159F+3MPA | 3A ₂ ^F | 2.472 | 2.170 | 1.875 | 0.011 | 0.006 | 0.009 |
| | 3A ₁ ^F | 2.421 | 2.198 | 1.898 | 0.020 | 0.001 | 0.001 |
| | 3B ^F | 2.336 | 2.142 | 1.941 | 0.017 | 0.005 | 0.006 |
| | 3C | 2.399 | 2.259 | 1.919 | 0.017 | 0.005 | 0.005 |

Table 3.1: Simulated EPR parameters for species of low spin ferric MDO when bound to cyanide.

| | K_d (μM) | B_{max} (μM) | R^2 | λ_{max} (nm) | ϵ ($\text{M}^{-1}\text{cm}^{-1}$) |
|-----------------|-------------------------|------------------------------------|-------|-----------------------------|--|
| WT + 3MPA | 539 | 206 | 0.948 | 584 | 2970 |
| WT-3MPA + CN | 2250 | 184 | 0.995 | 696 | 1800 |
| H157N+3MPA | 229 | 154 | 0.965 | 550 | - |
| H157N-3MPA+CN | 3000 | 165 | 0.995 | 670 | - |
| Y159F + 3MPA | 328 | 125 | 0.971 | 689 | - |
| Y159F-3MPA + CN | 3200 | 185 | 0.981 | 684 | - |

Table 3.2: Fitted binding parameters for 3MPA to ferric enzyme (wild type, H157N and Y159F) and cyanide to each 3MPA-bound complex. Also included are the λ_{max} for each LMCT band and calculated extinction coefficients for wild type species.

| Species | Model | g_z | g_y | g_x | RMSD |
|-----------|-------|-------|-------|-------|-------|
| 1C | exp | 2.394 | 2.240 | 1.928 | - |
| | 1 | 2.371 | 2.248 | 1.944 | 0.018 |
| | 2 | 2.400 | 2.298 | 1.932 | 0.033 |
| | 1 DFT | 2.152 | 2.125 | 2.015 | 0.164 |
| | 2 DFT | 2.149 | 2.131 | 2.017 | 0.165 |
| 2C | exp | 2.394 | 2.295 | 1.932 | - |
| | 3 | 2.371 | 2.280 | 1.940 | 0.016 |
| | 4 | 2.361 | 2.249 | 1.948 | 0.034 |
| | 5 | 2.374 | 2.260 | 1.947 | 0.025 |
| | 6 | 2.350 | 2.263 | 1.937 | 0.031 |
| 3C | exp | 2.399 | 2.259 | 1.919 | - |
| | 7 | 2.331 | 2.239 | 1.954 | 0.046 |
| | 8 | 2.364 | 2.291 | 1.938 | 0.030 |

Table 3.3: Experimental and calculated g -values for 3MPA/CN-bound 3MDO species observed in EPR spectroscopy for wild type (**1C**), H157N (**2C**), and Y159F (**3C**).

References

1. Stipanuk, M. H. (2004) SULFUR AMINO ACID METABOLISM: Pathways for Production and Removal of Homocysteine and Cysteine. *Annu. Rev. Nutr.* **24**, 539-577
2. Simmons, C. R., Liu, Q., Huang, Q. Q., Hao, Q., Begley, T. P., Karplus, P. A., and Stipanuk, M. H. (2006) Crystal structure of mammalian cysteine dioxygenase - A novel mononuclear iron center for cysteine thiol oxidation. *J. Biol. Chem.* **281**, 18723-18733
3. Dominy, J. E., Simmons, C. R., Hirschberger, L. L., Hwang, J., Coloso, R. M., and Stipanuk, M. H. (2007) Discovery and Characterization of a Second Mammalian Thiol Dioxygenase, Cysteamine Dioxygenase. *J. Biol. Chem.* **282**, 25189-25198
4. Pierce, B. S., Gardner, J. D., Bailey, L. J., Brunold, T. C., and Fox, B. G. (2007) Characterization of the Nitrosyl Adduct of Substrate-Bound Mouse Cysteine Dioxygenase by Electron Paramagnetic Resonance: Electronic Structure of the Active Site and Mechanistic Implications. *Biochemistry* **46**, 8569-8578
5. Tchesnokov, E. P., Fellner, M., Siakkou, E., Kleffmann, T., Martin, L. W., Aloji, S., Lamont, I. L., Wilbanks, S. M., and Jameson, G. N. (2015) The cysteine dioxygenase homologue from *Pseudomonas aeruginosa* is a 3-mercaptopropionate dioxygenase. *J. Biol. Chem.* **290**, 24424-24437
6. Pierce, B. S., Subedi, B. P., Sardar, S., and Crowell, J. K. (2015) The "Gln-Type" Thiol Dioxygenase from *Azotobacter vinelandii* Is a 3-Mercaptopropionic Acid Dioxygenase. *Biochemistry* **54**, 7477-7490
7. Gordon, C., Emery, P., Bradley, H., and Waring, R. H. (1992) Abnormal sulphur oxidation in systemic lupus erythematosus. *Lancet* **339**, 25-26
8. Heafield, M. T., Fearn, S., Steventon, G. B., Waring, R. H., Williams, A. C., and Sturman, S. G. (1990) Plasma cysteine and sulphate levels in patients with motor neurone, Parkinson's and Alzheimer's disease. *Neurosci. Lett.* **110**, 216-220
9. Dominy Jr, J. E., Simmons, C. R., Karplus, P. A., Gehring, A. M., and Stipanuk, M. H. (2006) Identification and characterization of bacterial cysteine dioxygenases: A new route of cysteine degradation for eubacteria. *J. Bacteriol.* **188**, 5561-5569
10. Bhave, D. P., Muse, W. B., 3rd, and Carroll, K. S. (2007) Drug targets in mycobacterial sulfur metabolism. *Infect. Disord. Drug Targets* **7**, 140-158
11. Trachootham, D., Alexandre, J., and Huang, P. (2009) Targeting cancer cells by ROS-mediated mechanisms: a radical therapeutic approach? *Nat. Rev. Drug Discov.* **8**, 579-591
12. Winyard, P. G., Moody, C. J., and Jacob, C. (2005) Oxidative activation of antioxidant defence. *Trends Biochem. Sci* **30**, 453-461

13. Reddie, K. G., and Carroll, K. S. (2008) Expanding the functional diversity of proteins through cysteine oxidation. *Curr. Opin. Chem. Biol.* **12**, 746-754
14. Fernandez, R. L., Dillon, S. L., Stipanuk, M. H., Fox, B. G., and Brunold, T. C. (2020) Spectroscopic Investigation of Cysteamine Dioxygenase. *Biochemistry*
15. Li, W., and Pierce, B. S. (2015) Steady-state substrate specificity and O₂-coupling efficiency of mouse cysteine dioxygenase. *Arch. Biochem. Biophys.* **565**, 49-56
16. Naik, S. G., Wang, Y., Davis, I., Chan, Y., Griffith, W. P., and Liu, A. (2020) Characterization of the nonheme iron center of cysteamine dioxygenase and its interaction with substrates. *J. Biol. Chem.* **295**, 11789-11802
17. Crowell, J. K., Sardar, S., Hossain, M. S., Foss, F. W., and Pierce, B. S. (2016) Non-chemical proton-dependent steps prior to O₂-activation limit *Azotobacter vinelandii* 3-mercaptopropionic acid dioxygenase (MDO) catalysis. *Arch. Biochem. Biophys.* **604**, 86-94
18. Sardar, S., Weitz, A., Hendrich, M. P., and Pierce, B. S. (2019) Outer-Sphere Tyrosine 159 within the 3-Mercaptopropionic Acid Dioxygenase S-H-Y Motif Gates Substrate-Coordination Denticity at the Non-Heme Iron Active Site. *Biochemistry* **58**, 5135-5150
19. Li, W., Blaesi, E. J., Pecore, M. D., Crowell, J. K., and Pierce, B. S. (2013) Second-Sphere Interactions between the C93–Y157 Cross-Link and the Substrate-Bound Fe Site Influence the O₂ Coupling Efficiency in Mouse Cysteine Dioxygenase. *Biochemistry* **52**, 9104-9119
20. Neese, F. (2017) Software update: the ORCA program system, version 4.0. *Wiley Interdiscip. Rev. Comput. Mol. Sci.* **8**, e1327
21. Becke, A. D. (1986) Density functional calculations of molecular bond energies. *J. Chem. Phys.* **84**, 4524-4529
22. Perdew, J. P. (1986) Density-functional approximation for the correlation energy of the inhomogeneous electron gas. *Phys. Rev. B: Condens. Matter* **33**, 8822-8824
23. Weigend, F., and Ahlrichs, R. (2005) Balanced basis sets of split valence, triple zeta valence and quadruple zeta valence quality for H to Rn: Design and assessment of accuracy. *Phys. Chem. Chem. Phys.* **7**, 3297-3305
24. Vahtras, O., Almlöf, J., and Feyereisen, M. W. (1993) Integral approximations for LCAO-SCF calculations. *Chem. Phys. Lett.* **213**, 514-518
25. Kendall, R. A., and Früchtl, H. A. (1997) The impact of the resolution of the identity approximate integral method on modern ab initio algorithm development. *Theor. Chem. Acc.* **97**, 158-163

26. Grimme, S., Antony, J., Ehrlich, S., and Krieg, H. (2010) A consistent and accurate ab initio parametrization of density functional dispersion correction (DFT-D) for the 94 elements H-Pu. *J. Chem. Phys.* **132**, 154104
27. Perdew, J. P., Ernzerhof, M., and Burke, K. (1996) Rationale for mixing exact exchange with density functional approximations. *J. Chem. Phys.* **105**, 9982-9985
28. Adamo, C., and Barone, V. (1999) Toward reliable density functional methods without adjustable parameters: The PBE0 model. *J. Chem. Phys.* **110**, 6158-6170
29. Neese, F. (2002) Prediction and interpretation of the ^{57}Fe isomer shift in Mössbauer spectra by density functional theory. *Inorg. Chim. Acta* **337**, 181-192
30. Schindler, M., and Kutzelnigg, W. (1982) Theory of magnetic susceptibilities and NMR chemical shifts in terms of localized quantities. II. Application to some simple molecules. *J. Chem. Phys.* **76**, 1919-1933
31. (1995) *Recent Advances in Density Functional Methods*, Vol. Volume 1, WORLD SCIENTIFIC
32. Neese, F., Wennmohs, F., Hansen, A., and Becker, U. (2009) Efficient, approximate and parallel Hartree–Fock and hybrid DFT calculations. A ‘chain-of-spheres’ algorithm for the Hartree–Fock exchange. *Chem. Phys.* **356**, 98-109
33. Neese, F. (2001) Prediction of electron paramagnetic resonance g values using coupled perturbed Hartree–Fock and Kohn–Sham theory. *J. Chem. Phys.* **115**, 11080-11096
34. Neese, F. (2003) Quantum chemical calculations of spectroscopic properties of metalloproteins and model compounds: EPR and Mössbauer properties. *Curr. Opin. Chem. Biol.* **7**, 125-135
35. Neese, F. (2003) Metal and ligand hyperfine couplings in transition metal complexes: The effect of spin–orbit coupling as studied by coupled perturbed Kohn–Sham theory. *J. Chem. Phys.* **118**, 3939-3948
36. Sinnecker, S., Neese, F., Noodleman, L., and Lubitz, W. (2004) Calculating the Electron Paramagnetic Resonance Parameters of Exchange Coupled Transition Metal Complexes Using Broken Symmetry Density Functional Theory: Application to a MnIII/MnIV Model Compound. *J. Am. Chem. Soc.* **126**, 2613-2622
37. Singh, S. K., Atanasov, M., and Neese, F. (2018) Challenges in Multireference Perturbation Theory for the Calculations of the g-Tensor of First-Row Transition-Metal Complexes. *J. Chem. Theory Comput.* **14**, 4662-4677
38. Singh, S. K., Eng, J., Atanasov, M., and Neese, F. (2017) Covalency and chemical bonding in transition metal complexes: An ab initio based ligand field perspective. *Coord. Chem. Rev.* **344**, 2-25

39. Fischer, A. A., Miller, J. R., Jodts, R. J., Ekanayake, D. M., Lindeman, S. V., Brunold, T. C., and Fiedler, A. T. (2019) Spectroscopic and Computational Comparisons of Thiolate-Ligated Ferric Nonheme Complexes to Cysteine Dioxygenase: Second-Sphere Effects on Substrate (Analogue) Positioning. *Inorg. Chem.* **58**, 16487-16499
40. Neese, F. (2006) Importance of Direct Spin-Spin Coupling and Spin-Flip Excitations for the Zero-Field Splittings of Transition Metal Complexes: A Case Study. *J. Am. Chem. Soc.* **128**, 10213-10222
41. Clay, M. D., Jenney, F. E., Hagedoorn, P. L., George, G. N., Adams, M. W. W., and Johnson, M. K. (2002) Spectroscopic Studies of *Pyrococcus furiosus* Superoxide Reductase: Implications for Active-Site Structures and the Catalytic Mechanism. *J. Am. Chem. Soc.* **124**, 788-805
42. Deligiannakis, Y., Boussac, A., Bottin, H., Perrier, V., Bârzu, O., and Gilles, A.-M. (1997) A New Non-Heme Iron Environment in *Paracoccus denitrificans* Adenylate Kinase Studied by Electron Paramagnetic Resonance and Electron Spin Echo Envelope Modulation Spectroscopy. *Biochemistry* **36**, 9446-9452
43. Whittaker, J. W., and Lipscomb, J. D. (1984) 17O-water and cyanide ligation by the active site iron of protocatechuate 3,4-dioxygenase. Evidence for displaceable ligands in the native enzyme and in complexes with inhibitors or transition state analogs. *J. Biol. Chem.* **259**, 4487-4495
44. Fischer, A. A., Stracey, N., Lindeman, S. V., Brunold, T. C., and Fiedler, A. T. (2016) Synthesis, X-ray Structures, Electronic Properties, and O₂/NO Reactivities of Thiol Dioxygenase Active-Site Models. *Inorg. Chem.* **55**, 11839-11853
45. Van Doorslaer, S. (2008) Continuous wave and pulsed EPR analyses of metalloproteins. in *Electron Paramagnetic Resonance: Volume 21*, The Royal Society of Chemistry. pp 162-183
46. Prisner, T., Rohrer, M., and MacMillan, F. (2001) PULSED EPR SPECTROSCOPY: Biological Applications. *Annu. Rev. Phys. Chem.* **52**, 279-313
47. Mims, W. B. (1972) Envelope Modulation in Spin-Echo Experiments. *Physical Review B* **5**, 2409-2419
48. Dikanov, S. A., and Tsvetkov, Y. (1992) *Electron Spin Echo Envelope Modulation (ESEEM) Spectroscopy*, Taylor & Francis
49. Schweiger, A. J., G. (2001) *Principles of Pulse Electron Paramagnetic Resonance*, Oxford University Press, UK
50. Harmer, J., Mitrikas, G., and Schweiger, A. (2009) Advanced Pulse EPR Methods for the Characterization of Metalloproteins. in *High Resolution EPR: Applications to Metalloenzymes and Metals in Medicine* (Berliner, L., and Hanson, G. eds.), Springer New York, New York, NY. pp 13-61

51. Aloï, S., Davies, C. G., Karplus, P. A., Wilbanks, S. M., and Jameson, G. N. L. (2019) Substrate Specificity in Thiol Dioxygenases. *Biochemistry* **58**, 2398-2407
52. Schrodinger, LLC. (2015) The PyMOL Molecular Graphics System, Version 1.8.

Appendix

Summary of UV-vis Results for H157N and Y159F Variants. Additions of **3MPA** and cyanide to ferric 3MDO were repeated for the H157N and Y159F variants. Enzyme concentration and stock substrate/cyanide concentrations were prepared as described in the methods section. As with wild type, additions of **3MPA** were performed first to determine the saturating relative concentration. **3MPA** binding to H157N 3MDO was evidenced by a LMCT band with a max wavelength of 550 nm. Substrate binding was shown to saturate at 10 molar eq. to enzyme. Cyanide was added to H157N preincubated with 10x **3MPA**. Increasing equivalents of cyanide showed a red shift of the max wavelength to 670 nm, as shown in **Figure A3.3** (panel B). Using Equation 1 (main text), a binding curve was constructed for both **3MPA** and cyanide binding and relevant parameters are displayed in **Table 3.2**. Similar to wild type, tight binding was observed for **3MPA** with a K_d of 229 μ M. Cyanide binding never appeared to reach full saturation with a K_d of 3 mM.

Comparable ferric iron concentrations with Y159F 3MDO showed drastically lower absorbance values compared to **3MPA**-bound wild type and H157N 3MDO. Nevertheless, LMCT bands were observed at 689 nm with increasing addition of **3MPA** and similarly showed saturating binding at 10 molar eq. relative to enzyme (**Figure A3.4**, panel A). This λ_{max} is considerably higher in wavelength compared to wild type and H157N. The line width was measured to be 336 nm, which is much greater than that seen for either wild type or H157N; 222 and 169 nm, respectively. This broadening effect would contribute to the overall lower absorbance at λ_{max} and may be due to species heterogeneity. Cyanide binding again never fully saturates with a K_d of 3.2 mM at 684 nm. A notable feature though wild type and both variants is the line width of the CN-**3MPA**-bound 3MDO LMCT band being relatively constant. Line

widths for this species are 96, 118, and 126 nm for wild type, H157N, and Y159F, respectively. This suggests that while there may be heterogeneity among the **3MPA**-bound species, there is only one orientation for simultaneous binding of **3MPA** and cyanide.

Summary of EPR Experiments with H157N and Y159F Variants. Cyanide addition to ferric 3MDO was repeated for variants H157N and Y159F. The H157N $S = 5/2$ as-isolated signal shown in **Figure A5.5** features multiple peaks with high rhombicity ($E/D \sim 0.33$). Simulations were not attained on this species due to overlapping heterogeneous signals. Cyanide addition showed a decrease in the $S = 5/2$ signal and two cyanide-bound low spin species in the $g = 2$ region labeled **2A** and **2B**. **2B** shows g -values of 2.54, 2.21, 1.84 which is very similar to **1B** seen in wild type. The g_2 signal is shifted up-field and shows increased g -strain. Species **2A** appears to be unique with g -values (2.48, 2.18, 1.87).

Substrate addition to H157N 3MDO showed an increase in signal at the $S=5/2$ high rhombic region ($g = 4.3$) similar to wild type. Some as-isolated signal is still present, signifying decreased binding affinity of **3MPA** relative to wild-type. Addition of cyanide to this species shows three $S = 1/2$ cyanide bound species. Two of which are **2A** and **2B**, seen without substrate. The third set of g -values (2.39, 2.30, 1.93) is attributed to the (**3MPA**/CN)-bound H157N 3MDO species, denoted **2C**. **2C** is similar to **1C** seen in wild type, but with a shifted g_2 signal. **2A** and **2B** are shown in both low and high relative cyanide concentrations, likely due to binding of as-isolated ferric enzyme which did not bind to substrate.

Ferric Y159F 3MDO shows a weak $S = 5/2$ rhombic signal at $g = 4.3$. This signal lacks discerning features which is typical of adventitious ferric iron. Upon adding cyanide, the $g = 4.3$ signal attenuates and multiple cyanide-bound species are shown at $g = 2$. At least three low spin species are observed and simulated as shown in **Figure A3.6**. The first species, denoted **3A_I^F**, is

similar in g -values to **1A** seen in wild type. Each g -value shows minor shifts but the comparison shown in **Table 3.1** reveals the signals are reminiscent of each other. The second species denoted **3A₂^F**, is very similar to **2A** shown in the H157N variant. These g -values are remarkably close to one another and are shown in **Table 3.1**. Given the structural identity of **1A** and **2A** are unresolved, the implications of seeing similar species in the Y159F variant are limited. The third species, **3B^F**, is a unique signal with no other counterpart. The g -values (2.33, 2.14, 1.94) show a lower g -spread ($g_1 - g_3 = 0.39$) than any other cyanide bound species presented. Other signals were observed but were unable to be accounted for by simulation. These are shown near $g = 2.25$ and $g = 2.001$. The signal at $g = 2.25$ appears to be a derivative signal in accord with a g_2 signal for an anisotropic low spin species. The signal at $g = 2.001$ is overlapped with a broad signal seen in other samples as well. This broad signal is likely due to adventitious ferric iron bound to added cyanide.

No change in the high spin ferric signal is observed with addition of substrate. Based on UV-vis data it is likely that **3MPA**-binding is both low and heterogeneous in nature. Nevertheless, cyanide was added to Y159F saturated with **3MPA**. A single new species, **3C**, was observed in the $g = 2$ region. The aforementioned low spin cyanide-bound species were also in the sample. Fortunately, **3C** showed g -values (2.40, 2.26, 1.92) with little overlap of previous species on the already crowded spectrum. Simulations were able to isolate the (**3MPA**/CN)-bound Y159F species as shown in **Figure A3.6**. The g -values are similar to the wild type counterpart, **1C**, attributed to simultaneous **3MPA** and cyanide binding. Only one new signal was observed when adding cyanide and **3MPA** to Y159F **3MDO**. This agrees well with UV-vis results which showed a LMCT band for the (**3MPA**/CN)-bound species with a line width similar

to both wild type and H157N which also only showed one (**3MPA/CN**)-bound species in EPR (**1C** and **2C**).

Summary of computational investigation of 1B It was previously inferred that species **1B** likely had two cyanide ligands bound, whereas species **1A** and **1C** only had one. Using this postulate, predicting a structure for **1B** became simplified as five of possibly six coordinated ligands are known (two cyanides and three histidines). Furthermore, the histidines are arranged as a facial triad, leaving the opposite facial arrangement for variation. Besides cyanide being bound to the iron active site, chloride, water, and hydroxide were also attempted as possible ligands. A three cyanide-bound complex was also considered. Optimized structures were produced with each ligand. Various orientations were considered as well. For instance, hydroxide was placed trans to His90 with cyanide ligands placed in the remaining positions. Then hydroxide was placed trans to His92, followed by His142. This procedure was performed for water and chloride ligands as well. The influence of the SHY motif was left out of the preliminary structures to increase throughput. Initial CASSCF/NEVPT2 calculations were done with a (5,5) minimal active space. Chloride and water ligands were subsequently ruled out due to overly high anisotropy g -values with high RMSDs. Only complexes with a hydroxide ligand gave g -values with agreement less than 0.1 RMSD. Similarly, no 5-coordinate structures produced g -values with RMSD less than 0.1. Therefore, only 6-coordinate structures containing two cyanides and one hydroxide ligand were considered. From these postulates, only three structural candidates remained. These are shown in **Figure A3.9**. From here, each structure was validated by addition of Arg168 and SHY motif point charges. Since the Tyr159-OH may or may not donate a hydrogen bond to the axial ligand, both instances would need to be considered. The hydroxide ligand could potentially donate a hydrogen bond to the Tyr159 oxygen. Two structures were optimized for model 9 which features a hydroxide in the axial position. The first with the hydroxide ligand donating a hydrogen bond to the Tyr159 phenol, which, in turn, donates a hydrogen bond to His157. This arrangement is shown in **Figure A3.9** as model 9-1. The second arrangement (9-2) has Tyr159 donating a hydrogen bond to the axial hydroxide ligand.

At this point, the remaining structure's predicted g -values were recalculated with an optimized (9,12) active space. This included five 3d orbitals, two ligand bonding orbitals, and five 4d orbitals. These orbitals were found to have the most impact on the calculated g -values.

Of the remaining structures, each was compared to **1B** g -values. From this data, a single candidate stands out in agreement for species **1B**. The structure labeled 9-1 has the lowest RMSD value and was identified as the most likely structure of species **1B**. The calculated g -values for models shown in **Figure A3.9** are shown in **Table A3.4**. As such, species **1B** was determined to be comprised of two cyanides bound trans to His142 and His92 with a hydroxide ligand trans to His90 which donates a hydrogen bond to Try159.

| Species | Isotope | g_1 | g_2 | g_3 | σg_1 | σg_2 | σg_3 |
|-----------|----------------------|-------|-------|-------|--------------|--------------|--------------|
| 1A | - | 2.382 | 2.226 | 1.892 | 0.018 | 0.011 | 0.010 |
| | ^{13}CN | 2.382 | 2.228 | 1.895 | 0.019 | 0.011 | 0.009 |
| | D_2O | 2.376 | 2.231 | 1.897 | 0.013 | 0.010 | 0.006 |
| 1B | - | 2.531 | 2.188 | 1.843 | 0.014 | 0.002 | 0.008 |
| | ^{13}CN | 2.528 | 2.187 | 1.845 | 0.018 | 0.006 | 0.010 |
| | D_2O | 2.523 | 2.188 | 1.849 | 0.014 | 0.003 | 0.008 |
| 1C | - | 2.394 | 2.240 | 1.928 | 0.017 | 0.005 | 0.007 |
| | ^{13}CN | 2.398 | 2.242 | 1.927 | 0.019 | 0.005 | 0.008 |
| | D_2O | 2.387 | 2.241 | 1.927 | 0.018 | 0.008 | 0.001 |

Table A3.1: Simulated EPR parameters of cyano-bound low spin ferric wild type MDO species with ^{13}CN , D_2O , and natural abundance isotope conditions.

| Model ^a | | g_z | g_y | g_x | RMSD |
|------------------------------------|-------------------------------|-----------------|-------|-------|-------|
| 1C | EXP | 2.397 | 2.241 | 1.928 | - |
| 1 | (5,5) gas phase | 2.428 | 2.323 | 1.929 | 0.051 |
| | (5,5) SHY (Tyr-OH→CN) | 2.419 | 2.288 | 1.939 | 0.031 |
| | (11,8) SHY (Tyr-OH→CN) | 2.372 | 2.255 | 1.941 | 0.019 |
| | TZVP (11,8) SHY (Tyr-OH→CN) | 2.371 | 2.248 | 1.944 | 0.018 |
| | (11,13) SHY (Tyr-OH→CN)) | 2.250 | 2.166 | 1.952 | 0.096 |
| | TZVP (11,13) SHY (Tyr-OH→CN)) | 2.248 | 2.164 | 1.949 | 0.097 |
| | 2 | (5,5) gas phase | 2.451 | 2.369 | 1.921 |
| (5,5) SHY (Tyr-OH→His157) | | 2.446 | 2.370 | 1.923 | 0.080 |
| (11,8) SHY (Tyr-OH→ His157) | | 2.399 | 2.299 | 1.932 | 0.034 |
| TZVP (11,8) SHY (Tyr-OH→ His157) | | 2.408 | 2.298 | 1.932 | 0.033 |
| (11,13) SHY (Tyr-OH→ His157)) | | 2.266 | 2.196 | 1.975 | 0.084 |
| TZVP (11,13) SHY (Tyr-OH→ His157)) | | 2.267 | 2.197 | 1.973 | 0.084 |

Table A3.2: Calculated g -values of Models 1 and 2 for the structural determination of $S = 1/2$ species **1C**. Effects of orbital active space, basis set, and outer sphere point charges are shown.

| Model | g_z | g_y | g_x | RMSD |
|----------|---------|--------|--------|-------|
| exp | -0.0033 | 0.0545 | 0.0040 | - |
| 3 | 0.000 | 0.032 | -0.004 | 0.014 |
| 4 | -0.010 | 0.001 | 0.004 | 0.031 |
| 5 | 0.003 | 0.011 | 0.004 | 0.025 |
| 6 | -0.021 | 0.015 | -0.006 | 0.026 |

Table A3.3: The experimental difference in g -values between wild type species **1C** and H157N species **2C** as compared to calculated differences of modeled complexes calculated by CASSCF/NEVPT2 methods.

| Model ^a | | g_z | g_y | g_x | RMSD |
|--------------------|--|-------|-------|-------|-------|
| 1B | EXP | 2.531 | 2.188 | 1.843 | - |
| 9 | (5,5) gas phase | 2.466 | 2.261 | 1.887 | 0.062 |
| | (5,5) Arg168 | 2.472 | 2.237 | 1.894 | 0.053 |
| | (9-1) (5,5) SHY (OH→Tyr-OH→His157) | 2.448 | 2.228 | 1.868 | 0.055 |
| | (9-1) (9,7) SHY (OH→Tyr-OH→His157) | 2.525 | 2.236 | 1.855 | 0.029 |
| | (9-1) (9,12) SHY (OH→Tyr-OH→His157) | 2.508 | 2.198 | 1.856 | 0.016 |
| | (9-1) TZVP (9,12) SHY (OH→Tyr-OH→His157) | 2.548 | 2.201 | 1.838 | 0.013 |
| | (9-2) (5,5) SHY (Tyr-OH→OH) | 2.519 | 2.260 | 1.873 | 0.046 |
| | (9-2) (9,7) SHY (Tyr-OH→OH) | 2.583 | 2.271 | 1.861 | 0.057 |
| | (9-2) (9,12) SHY (Tyr-OH→OH) | 2.549 | 2.220 | 1.870 | 0.026 |
| | (9-2) TZVP (9,12) SHY (Tyr-OH→OH) | 2.591 | 2.224 | 1.853 | 0.041 |
| 10 | (5,5) gas phase | 2.406 | 2.232 | 1.896 | 0.082 |
| | (5,5) Arg168 | 2.459 | 2.278 | 1.872 | 0.069 |
| | (5,5) SHY (Tyr-OH→CN) | 2.465 | 2.252 | 1.871 | 0.055 |
| | (9,7) SHY (Tyr-OH→CN) | 2.512 | 2.256 | 1.869 | 0.044 |
| | (9,12) SHY (Tyr-OH→CN) | 2.485 | 2.219 | 1.881 | 0.039 |
| | TZVP (9,12) SHY (Tyr-OH→CN) | 2.522 | 2.235 | 1.862 | 0.030 |
| 11 | (5,5) gas phase | 2.418 | 2.211 | 1.909 | 0.076 |
| | (5,5) Arg168 | 2.380 | 2.202 | 1.914 | 0.097 |
| | (5,5) SHY (Tyr-OH→CN) | 2.389 | 2.188 | 1.926 | 0.095 |
| | (9,7) SHY (Tyr-OH→CN) | 2.442 | 2.198 | 1.922 | 0.069 |
| | (9,12) SHY (Tyr-OH→CN) | 2.430 | 2.186 | 1.912 | 0.070 |
| | TZVP (9,12) SHY (Tyr-OH→CN) | 2.459 | 2.197 | 1.897 | 0.052 |
| H157N | EXP | 2.536 | 2.214 | 1.844 | - |
| H157N | TZVP (9,12) SNY (OH→Tyr-OH→Asn157) | 2.545 | 2.206 | 1.843 | 0.007 |

^a SHY refers to the inclusion of point charges from the Ser155, His157, and Tyr159 residues.

Table A3.4: Workflow of CASSCF/NEVPT2 calculated g-values for identification of species **1B**. The flow for each species depicts the addition of Arg168 points charges, followed by the point charges of the SHY motif. This was followed by optimization of the active space orbitals, going from a (5,5) minimal active space to a (9,7) active space with ligand orbitals, to a (9,12) active space with additional d-orbitals. Calculations were performed with the def2-SVP basis set except where noted with TZVP.

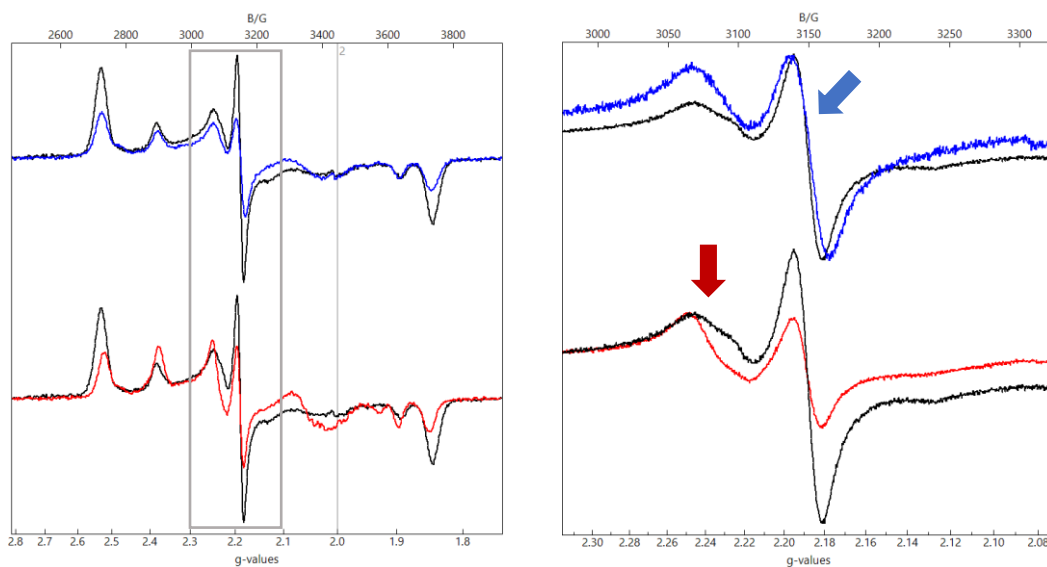


Figure A3.1: EPR spectra of wild type MDO with 40x cyanide compared to addition of ^{13}C cyanide (blue) and in D_2O buffer (red). The relative concentrations of species 1A and 1B are inconsistent through each sample. Therefore, the spectra are scaled to match intensity for comparison of individual g-values. Notable, changes are displayed on the right figure where the g_y signal of species 1B shows a broadening effect with ^{13}C cyanide (blue arrow). Also shown is a sharpening effect for the g_y signal of species 1A (red arrow) in D_2O buffer.

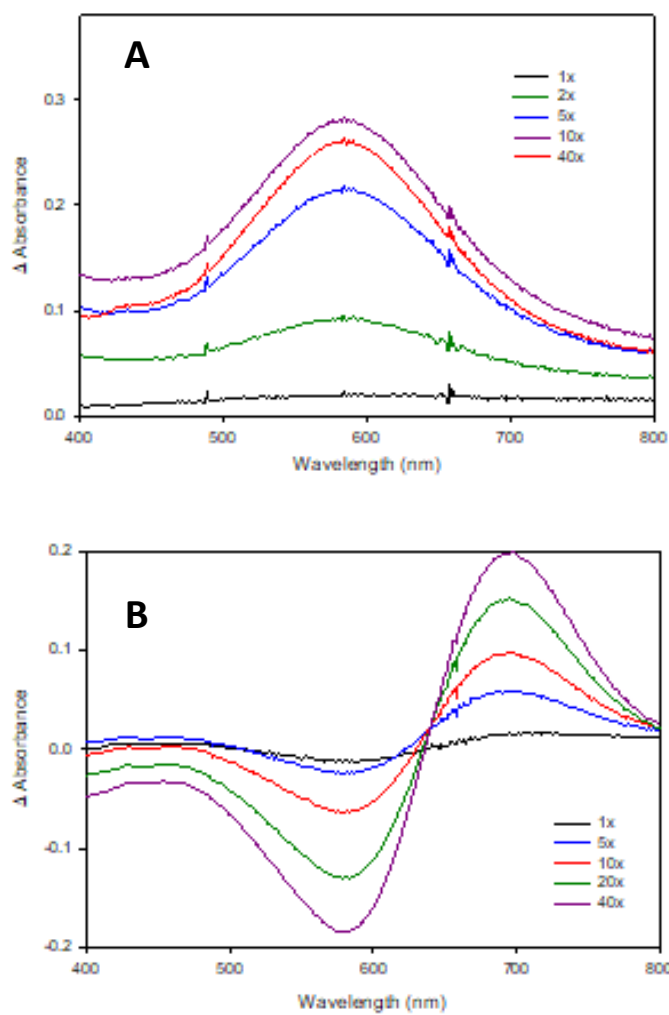


Figure A3.2: UV-vis difference spectra of ferric wild type 3MDO titrated with **3MPA** (A). The spectrum of as-isolated 3MDO was subtracted as the baseline. Using saturating conditions of **3MPA**, cyanide was titrated to the **3MPA**-bound 3MDO (C) For B, **3MPA**-bound MDO was subtracted as the baseline.

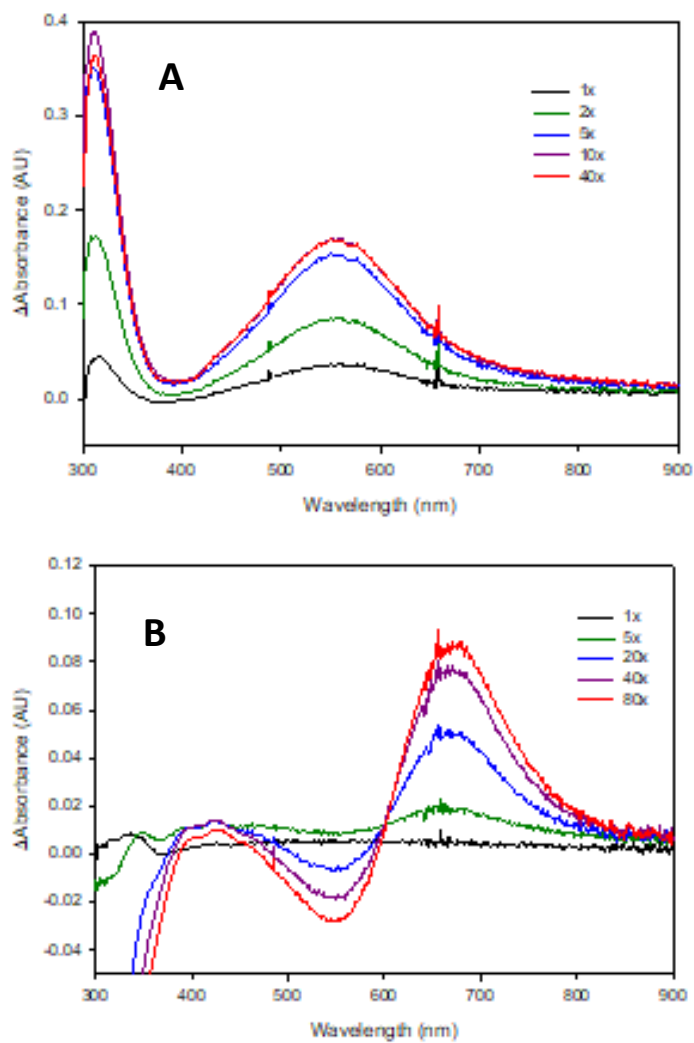


Figure A3.3: UV-vis difference spectra of ferric H157N 3MDO titrated with **3MPA** (A). The spectrum of as-isolated 3MDO was subtracted as the baseline. Using saturating conditions of **3MPA**, cyanide was titrated to the **3MPA**-bound MDO (B). For B, **3MPA**-bound 3MDO was subtracted as the baseline.

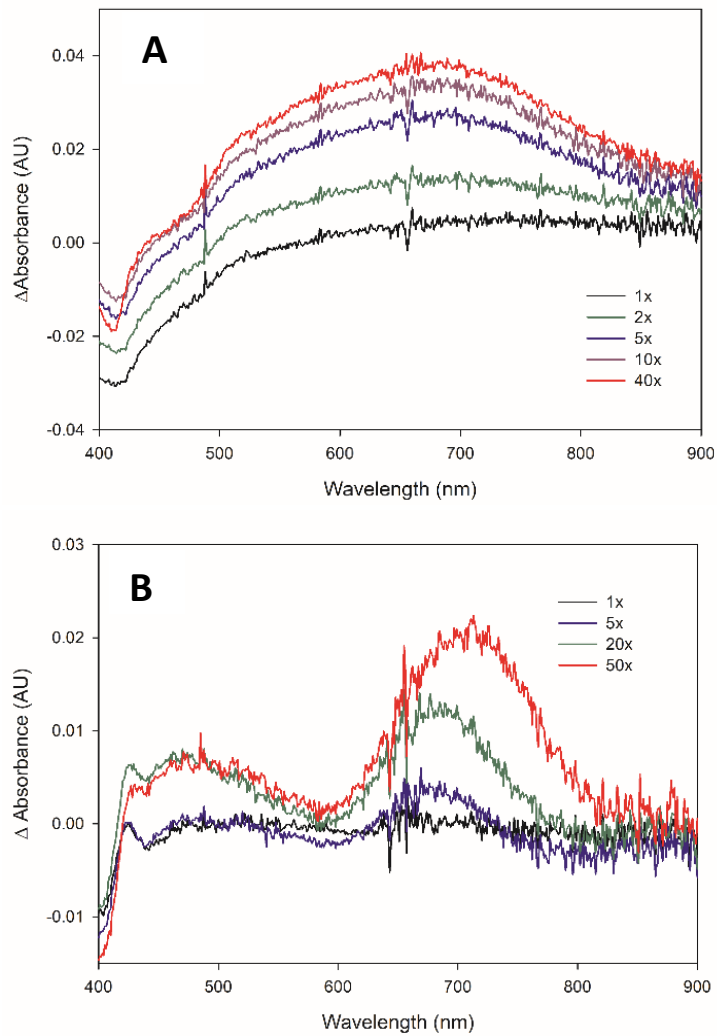


Figure A3.4: UV-vis difference spectra of ferric Y159F 3MDO titrated with **3MPA** (A). The spectrum of as-isolated 3MDO was subtracted as the baseline. Using saturating conditions of **3MPA**, cyanide was titrated to the **3MPA**-bound 3MDO (B). For B, **3MPA**-bound 3MDO was subtracted as the baseline.

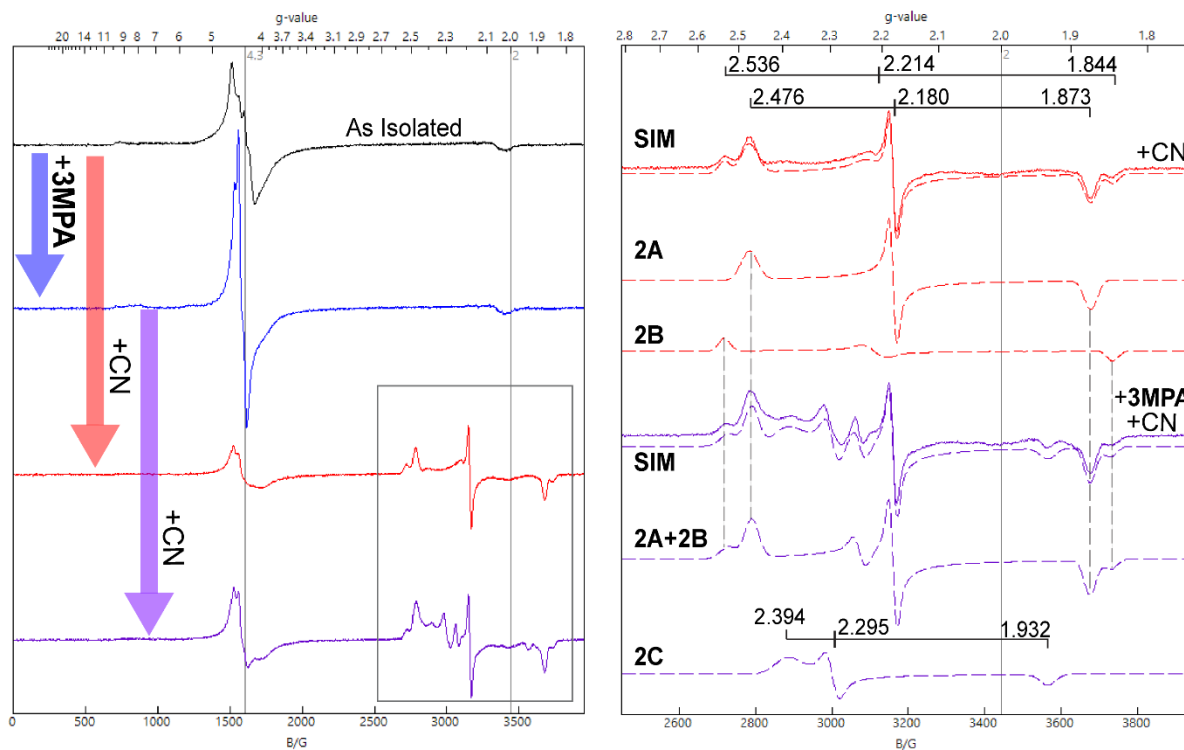


Figure A3.5: EPR spectra showing the full spectrum (left panel) of the as-isolated ferric H157N 3MDO (black), after being subjected to **3MPA** (blue), cyanide (red), and cyanide after **3MPA** (purple). The right panel shows the simulated $S=1/2$ species resulting from cyanide additions (red) and **3MPA** and cyanide additions (purple). Additions of cyanide shows two species, 2A and 2B. These species also appear in the presence of substrate along with a new species, 2C, which is attributed to be the (CN/**3MPA**)-bound species.

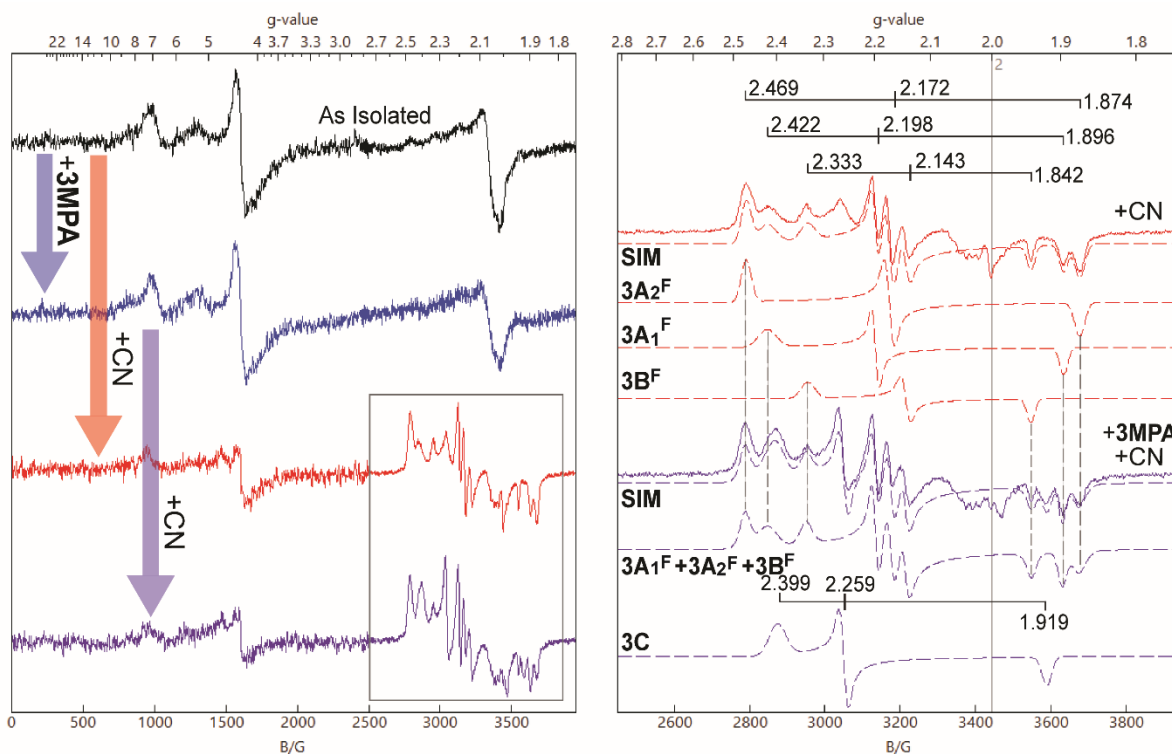


Figure A3.6: EPR spectra showing the full spectrum (left panel) of the as-isolated ferric Y159F 3MDO (black), after being subjected to **3MPA** (blue), cyanide (red), and cyanide after **3MPA** (purple). The right panel shows the simulated $S = 1/2$ species resulting from cyanide additions (red) and **3MPA** and cyanide additions (purple). Additions of cyanide shows three species, $3A_1^F$, $3A_2^F$, and $3B^F$. These species also appear in the presence of substrate along with a new species, **3C**, which is attributed to be the (CN/**3MPA**)-bound species.

Figure A3.7 Illustrated models of optimized structures for the (CN/3MPA)-bound H157N 3MDO active site.

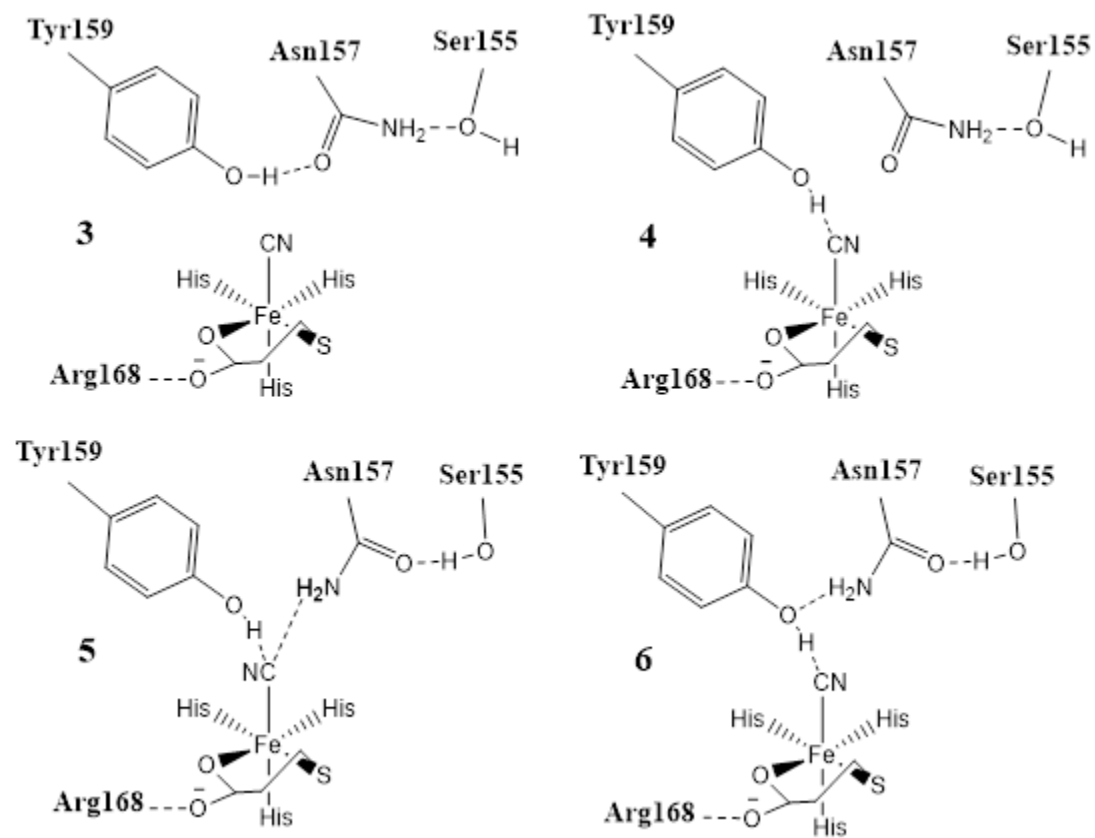


Figure A3.8. Illustrated models of optimized structures for the (CN/3MPA)-bound Y159F 3MDO active site.

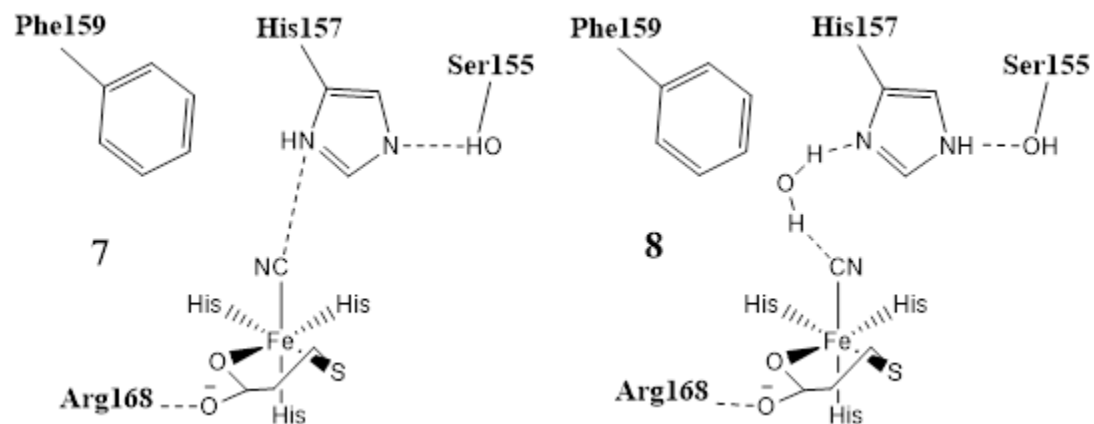
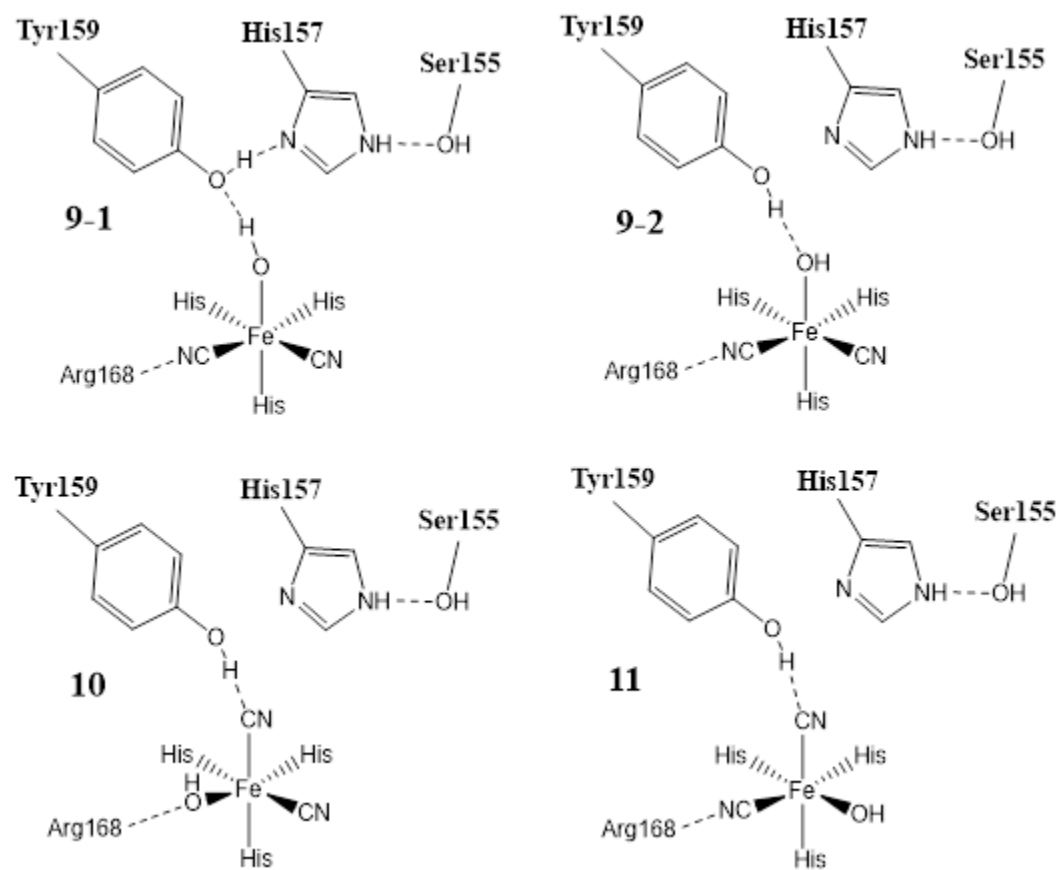


Figure A3.9. Illustrated models of species 1B of optimized structures for the cyanide-bound wild-type 3MDO active site.



CHAPTER 4:
SPECTROSCOPIC INVESTIGATION OF *Av*3MDO SIMULTANEOUSLY BOUND
TO CYANIDE AND NITRIC OXIDE

4.1 Introduction

Enzymes regarding sulfur chemistry are of interest due to their possible relation the medical conditions. Sulfur metabolism imbalances have been linked to diseases such as Alzheimer's, Parkinson's, and motor neuron disease (1-3). Similarly, sulfur oxidizing enzymes have been drug targets for inflammatory disease therapies, cancer therapies, and antimicrobial applications (4-7). 3-Mercaptopropionate dioxygenase (3MDO) is a thiol dioxygenase with an iron active site bound to three protein derived histidines (8). The histidines form a facial triad leaving three open coordination sites all *cis* to each other. *Av*3MDO from *Azotobacter vinelandii* catalyzes the oxidation of 3-mercaptopropionate (**3MPA**) to 3-sulfinopropionate using molecular O₂ (9-11).

Until very recently, substrate binding for 3MDO has been a topic of contention among the literature (12-14). For mammalian cysteine dioxygenase, cysteine (**CYS**) is shown to bind iron in a bidentate manner through the thiolate and amine group (15). In addition, two studies have been presented within this dissertation which show **3MPA** binds to *Av*3MDO iron via bidentate coordination. The first study (Chapter 2) featured a crystal structure which showed bidentate coordination of inhibitor, 3-hydroxypropionic acid (**3HPA**). **3HPA** is structurally very

similar to **3MPA** and the binding mode was used to model native substrate binding. This mode features the hydroxyl moiety (thiolate for **3MPA**) bound to iron *trans* to His92 with the carboxylate bound *trans* to His142 while forming a salt bridge with nearby Arg168. The crystal structure show chloride bound in the remaining axial position *trans* to His90. However, this position is hypothesized to be occupied by a solvent (H_2O , OH^-) in the resting state or the point of O_2 binding during catalytic turnover. This model was verified with a combination of EPR spectroscopy and computational modeling using the $S=3/2$ (**3MPA/NO**)-bound 3MDO complex, which has been studied previously (8,13). This complex was modeled with **3MPA** as stated above and nitric oxide in the axial position as would be predicted for O_2 . The optimized structure is shown in Figure 4.1, panel B. Pulsed EPR HYSCORE spectra were accurately replicated using theoretically calculated hyperfine couplings and Euler angles of hydrogens within the 3MDO active site. Given the sensitivity of hyperfine coupling and Euler angles on the simulation of HYSCORE data, the good agreement between experimental and theoretical data strongly suggested a physically accurate model.

The second study (Chapter 3) investigated the 3MDO active site in the inactive ferric state using cyanide as a spectroscopic probe. Like the study mentioned above, a combination of EPR, UV-vis spectroscopy, and computational modeling verified the mode of **3MPA** binding. Using CASSCF/NEVPT2 methods, g -values were calculated with very high accuracy compared to experimentally observed values. This model featured **3MPA** bound bidentate with thiolate and carboxylate in the equatorial positions and cyanide in the axial position.

Together, these studies together make a compelling case for bidentate binding of **3MPA**. However, the model fails to describe binding for substrates which are shown to be active yet have no carboxylate (cysteamine) as well as no amine (ethanethiol). Ethanethiol has no

functional group which would allow bidentate coordination still initiates O₂ consumption upon binding with Av3MDO (8). Therefore, while bidentate coordination is seemingly preferred, it is not strictly necessary.

The work presented here illustrates how both cyanide and nitric oxide can be used simultaneously to probe ligand binding and interactions with the outer-sphere SHY proton relay network within the Av3MDO active site. Given iron is bound to 3MDO by three histidines, there are three remaining coordination sites. The work presented below shows the simultaneous coordination of both cyanide and nitric oxide to the active site, leaving only one site for substrate to bind. Cyanide will bind without the presence of substrate, as seen in Chapter 3 and the crystal structure of thiocyanate bound to Av3MDO (shown in Figure 4.1, panel A). Both spectroscopic probes have been shown to bind in the axial position; therefore, the following work aims to elucidate where each ligand is coordinated in the iron active site. By determining ligands coordination, insights may be made upon the mechanism of which native substrates **3MPA** and O₂ bind.

4.2 MATERIALS AND METHODS

Enzyme Expression and Purification. Av3MDO was expressed and purified as previously described (8,9). To summarize the procedure, the Av3MDO expression vector was transformed into chemically competent BL21(DE3) *E. coli* and grown overnight at 37 °C on a 100 mg/L ampicillin LB-agar plate. A single colony was selected liquid LB media prior to inoculation of the 10-L BF-110 fermenter (New Brunswick Scientific) at 37 °C. Cell growth was monitored by optical density at 600 nm (OD 600). When the OD 600 reached a value of ~4, 1.0 g isopropyl β-D-1-thiogalactopyranoside (IPTG), 78 mg ferrous ammonium sulfate, and 20 g casamino acids was added for induction. The fermenter temperature was dropped to 25 °C with continued

stirring for four hours. Cells were then harvested and pelleted by centrifugation at 5,000 rpm (Beckman-Coulter Avanti J-E, JA 10.5 rotor). The pelleted cell paste was frozen and stored at -80 °C.

In a typical purification, ~20 g frozen cell paste was added to 20 mM 4-(2-hydroxyethyl)-1-piperazineethanesulfonic acid (HEPES), 50 mM NaCl, pH 8.0. Lysozyme, ribonuclease and deoxyribonuclease were added for a final concentration of 10 µg/mL each and stirred slowly on ice for ~20 min before pulse sonication (Bronson Digital 250/450). The sonicated mixture was centrifuged at 48,000 x g for 1 hour at 4 °C. The supernatant was then loaded onto a DEAE 155epharose fast flow anion exchange column (GE Life Sciences #17070901) pre-equilibrated with 20 mM HEPES, 50 mM NaCl, pH 8.0. One column volume 20 mM HEPES, 50 mM NaCl, pH 8.0 was used to wash the column of non-retaining particles before starting a linear NaCl gradient (50 mM – 350 mM).

Fractions were collected and pooled based on SDS PAGE as described elsewhere (13). The pooled enzyme solution was concentrated to ~50 mL using an Amicon stir cell and YM-10 ultrafiltration membrane. The C-terminal His-tag was removed by thrombin protease (Biopharma Laboratories) overnight at 4 °C with gentle stirring. The enzyme solution was then further concentrated with Amicon 10Kda spin concentrators at 5,000 rpm to ~ 5mL before freezing in liquid nitrogen and storing at -80 °C. Iron content was determined for both ferric and ferrous concentration using 2,4,6-tripyridyl-s-triazine (TPTZ) in a method previously described .

EPR Spectroscopy. Samples were prepared in either 3- or 4-mm diameter quartz tubes. Samples prepared in 4 mm tubes had a final Fe(II) concentration of 300 µM with 12 mM sodium cyanide and approximately 3 mM nitric oxide. All stock solution were degassed by bubbling argon gas through each solution before transferring into a Coy anaerobic glove box. 3MDO purifications

usually yield 5-20% Fe(II) relative to total iron. The remaining ferric content was reduced with anaerobic dithionite and a catalytic amount of methyl viologen. Sodium cyanide was added from a stock solution of 300 mM NaCN in 200 mM HEPES buffer, with 50 mM NaCl, at pH 8.0. Nitric oxide stock solution was prepared by adding 10 mg PROLI NONOate to degassed 10 mM NaOH. The NONOate/NaOH solution was diluted by half by adding degassed 20 mM HEPES buffer with 50 mM NaCl at pH 8.0. Upon diluting with buffer, nitric oxide is released in 2 molar equivalents of the PROLI NONOate making a stock solution of approximately 250 mM. Additions of nitric oxide to the enzyme were done quickly as possible as the stock solution would release nitric oxide as gas. Substrate, **3MPA**, was added to the enzyme at a final concentration of 3 mM from a stock solution of 300 mM **3MPA**, 20 mM HEPES, 50 mM NaCl at pH 8.0. Samples prepared for 3 mm diameter tubes were prepared with increased 3MDO Fe(II) concentration of 700 uM. All other concentrations were scaled up accordingly to keep the relative concentrations constant with the exception of cyanide, which was found to work best at 20 molar equivalents to 3MDO iron (in this case, 14 mM).

CW EPR spectroscopy was done on a Bruker EMX Plus (Bruker-Biospin, Billerica, MA) with a bimodal resonator and an Oxford ESR900 cryostat and Oxford ITC 03 temperature controller for low temperature spectra analysis. Simulations of CW EPR spectra were done on Spincount (version 6.2) developed by Professor Michael Hendrich at Carnegie Mellon University by utilizing the general spin Hamiltonian seen in Equation 1.

$$\hat{H} = D \left[\hat{S}_Z^2 - \frac{S(S+1)}{3} \right] + E \left(\hat{S}_X^2 + \hat{S}_Y^2 \right) + \beta \mathbf{B} \cdot \mathbf{g} \cdot \mathbf{S} \quad \text{Equation 1.}$$

Variables D and E are respectively the axial and rhombic zero-field splitting parameters and g is the g -tensor. For spin=1/2 systems, both the D and E terms are zero, leaving only the Zeeman (right) term.

HYSCORE Spectroscopy. HYSCORE measurements were collected at 10 K using an ELEXSYS E680 EPR spectrometer (Bruker-Biospin, Billerica, MA) equipped with a Bruker Flexline ER 4118 CF cryostat and an ER 4118X-MD4 ENDOR resonator. The measurements were made at a microwave frequency of 9.78 GHz with a four-pulse sequence, $\pi/2-\tau-\pi/2-t_1-\pi-t_2-\pi/2-\tau$ -echo, which was repeated at a rate of 1.25 kHz. The lengths of the $\pi/2$ and π pulses were 16 and 18 ns, respectively. The times t_1 and t_2 were varied independently to create the two frequency axes of the spectrum, and the delay time τ was set to 140 ns. HYSCORE spectra were processed using custom-built scripts in MATLAB (Mathworks, 2020a). In brief, the complex raw data was phased to minimize the imaginary component, and the background decay was subtracted in each dimension by removing a third-degree polynomial. Following removal of the background decay, a diagonal Blackman apodization function was applied to minimize noise at larger values of t_1 and t_2 . The data was then zero-filled in both directions to 1024 points before calculating the two-dimensional Fourier transform. The absolute value of the real part of the Fourier transform is displayed. Processing for the $^{14}\text{N}/^{15}\text{N}$ difference spectra followed the same steps; however, the data were only zero-filled to 256 points, and the complex data from the Fourier transform was used to generate difference spectra. The ^{14}N spectrum was subtracted from the ^{15}N spectrum at each magnetic field, and the absolute value of the complex difference spectrum was taken for plots and simulations. HYSCORE simulations of coupled ^{15}N nuclei at each experimental magnetic field were calculated using the EasySpin toolbox in MATLAB (16). The g -values used in simulations were determined from the CW-EPR

spectrum, and hyperfine coupling parameters for ^{15}N nuclei were taken directly from the DFT EPR calculations.

Quantum Calculations. Initial coordinates were taken from PDB code: 6XB9. The residues extracted were His90, His92, His142, Arg168, Tyr159, His157, Ser155, along with iron, **3HPA**, and chloride. Residues were truncated at the α -carbons and capped as methyl groups. Initial optimizations changed only the hydrogens while constraining the orientation of methyl-capped hydrogens to align with the original structure of the peptide chain. Ligands of cyanide, nitric oxide, and chloride were used to displace bound 3HPA prior to further optimizations which only constrained the coordinates of the methyl-capped α -carbons. The positions of each ligand will be discussed in results.

All calculations were performed using Orca (Ver. 4.2.1) (17). Optimizations were done using the TPSS meta-GGA functional (18). Iron and all coordinated atoms (the whole ligand in regard to NO and CN) utilized the Ahlrich's def2-TZVP basis set with the remaining atoms using def2-SVP (19). Optimizations also utilized the resolution of Identity approximation (RI), Grimme's D3 dispersion correction, and a CPCM solvent model with $\epsilon=4$ to imitate a protein environment (20-23).

Single point calculations were used to determine theoretical g -values, hyperfine coupling, and Euler angles for the optimized complexes. The TPSS functional was used for these single point calculations; TPSSh was also used but was found to underestimate the hyperfine couplings on the iron bound ligands (24). The CP(PPP) core potential basis set was used for iron with the radial integration accuracy set to 7 (25). The EPR-II basis set was used on all other atoms (26). EPR-III was attempted but resulted in convergence issues.

4.3 Results

EPR of 3MDO with cyanide and nitric oxide. Before adding substrate to the mixture, simultaneous binding of cyanide and nitric oxide was investigated as a control. Previous studies have shown that nitric oxide will not bind to Av3MDO without first binding substrate. Therefore, cyanide was added to the enzyme first, followed by nitric oxide. The resulting spectrum is shown as spectrum **A** in **Figure 4.2**. This spectrum was simulated as an $S = 1/2$ species with anisotropic g -values of $g_{1,2,3}(2.032, 2.005, 1.954)$. The g_2 signal was split into a triplet produced from hyperfine coupling of a ^{14}N ($I = 1$) nucleus. This triplet was simulated with hyperfine coupling of 66 MHz with good agreement to the experimental spectrum (**Figure 4.2, B**). Hyperfine couplings were not resolved for the g_1 or g_3 signals. However, the maximum possible hyperfine coupling was estimated by fitting the spectrum line width. These simulation parameters are shown in **Table 4.1**.

Interestingly, the observed spectrum shows remarkable similarity to a spectrum produced by Pierce et. al. of (NO/cysteine)-bound mammalian CDO (27,28). That spectrum also showed an $S = 1/2$ species with anisotropic g -values and a triplet on the middle g -value. Computational studies for the species showed the triplet originated from the nitrosyl ^{14}N . Counter to the spectrum shown herein, the CDO species had no bound cyanide. All coordination sites were occupied by the nitrosyl and bidentate coordination of cysteine through its thiolate and amine group.

Cyanide binding was confirmed by the addition of ^{13}C -labeled potassium cyanide. The resulting spectrum **C** is shown in **Figure 4.2**. Differences are minimal for g_1 or g_3 , but a broadening effect can be seen with the peaks of the middle g_2 triplet. This broadening is due to unresolved hyperfine from the $I = 1/2$ ^{13}C on cyanide. The simulation of this species (**Figure 4.2**,

D) treats the line broadening as hyperfine coupling from an $I = 1/2$ species. As shown in **Table 4.1**, the upper limit of hyperfine coupling from ^{13}C would be approximately 17 MHz. Studies of a similar complex with two cyanides bound found each ^{13}C had hyperfine couplings of ~ 15 MHz.

EPR of 3MDO with 3MPA, Cyanide, and Nitric Oxide. Now that the species attributed to cyanide and nitric oxide binding was accounted for, **3MPA** was added to the mixture to see if all three could bind simultaneously. Samples were prepared by adding **3MPA**, cyanide, and nitric oxide in that respective order. Previous work shows NO will not bind unless cyanide or **3MPA** are bound first, and nitric oxide binding to **3MPA**-bound 3MDO is a species already observed and characterized (13). The resulting spectrum of this mixture is shown in **Figure 4.3, A**. Initial inspection shows a clear difference in the middle g_2 signal as there is more negative signal appearing. However, when inspecting the broader magnetic field range (**Figure 4.3, B**), it is shown that this negative contribution arises from the $S = 3/2$ signal of the (**3MPA/NO**)-bound 3MDO species. This signal has been previously simulated, as shown in **Figure 4.3, C**. When taking the negative contribution into account, the remaining signal is simulated the same as seen previously without substrate. Therefore, the species shown are the (CN/NO)-bound 3MDO and (**3MPA/NO**)-bound 3MDO. No species attributing to simultaneous CN, NO, and **3MPA** bound to 3MDO was observed. Changing the order of ligand/substrate addition only resulted in slightly different ratios of both species. Addition of nitric oxide prior to cyanide resulted in a greater concentration of (**3MPA/NO**)-3MDO relative to (CN/NO)-3MDO. However, no new species were observed (data not shown).

HYSCORE of the (CN/NO)-bound 3MDO Complex. In order to determine why only two species are observed in the **3MPA/CN/NO** sample, identifying the structure of both species is

vital. The (3MPA/NO)-bound complex structure has been verified as seen in **Figure 4.1**, panel B. The structure of the (CN/NO)-bound complex is unknown. It is not known if there is a single cyanide ligand bound or two. Similarly, the orientation of the ligands is also unknown. Both CN and NO have been shown to bind to iron in the axial position. Therefore, either ligand could occupy the site in this species. Furthermore, if there is only one cyanide ligand bound, the third coordinated ligand could be a solvent water, hydroxide, or even a chloride. All three ligands have been shown to bind to 3MDO, either through crystallography or spectroscopically validated computational models (Chapters 2 and 3) as shown in **Figure 4.1**. The crystal structure (PDB: 6XB9) with 3HPA-bound also features a chloride bound to iron in the axial position. Giving credence to the possibility of a chloride ligand being bound to the species presented above.

Further experiments were performed to eliminate some of the numerous possibilities. First, ^{14}N -cyanide was substituted for ^{15}N -cyanide to see if differences in hyperfine coupling would help determine the number of cyanides bound. The resulting CW EPR spectrum is shown in **Figure 4.2, E**. Sharper peaks are observed in the g_2 triplet, opposed to the broadened peaks observed for ^{13}C -cyanide. Sharper peaks are expected as an unresolved triplet coupled to a $I = 1$ nucleus is replaced with an unresolved doublet coupled to a $I = 1/2$ nucleus. However, the ^{15}N couplings are still unresolved in the powder spectrum, so simulations were not able to reveal hyperfine couplings for the ^{15}N .

Hyperfine coupling of ^{15}N cyanide could not be resolved in CW EPR. Likely due to overlapping ^{14}N hyperfine contributions from iron-coordinated histidines. Therefore, pulsed EPR techniques were utilized to resolve the hyperfine contribution from ^{15}N -cyanide. HYSORE spectroscopy is a high-resolution two-dimensional pulsed EPR technique that directly observes magnetic nuclei coupled to a paramagnetic center. These measurements provide atomic-level

structural detail about the distance and position of coupled magnetic nuclei by probing the hyperfine interaction, which has an isotropic and an anisotropic component. The isotropic component represents the Fermi contact interaction from electron spin density delocalized onto the surrounding nuclei. The distance-dependent anisotropic component is a through-space interaction that is often approximates as a point-dipole (29). The HYSCORE spectra are divided into two quadrants, the (-, +) frequency quadrant, or the left half of the spectrum, and the (+, +) frequency quadrant, or the right half of the spectrum. The peaks in the (-, +) quadrant represent strongly coupled nuclei, such as the directly coordinated ^{14}N on the histidine residues in 3MDO. The (+, +) quadrant contains peak from weakly-coupled nuclei, typically those that are more distant and have a smaller hyperfine coupling, such as ^1H that are a few Å away from the paramagnetic center.

Figure 4.5 shows the HYSCORE spectrum of 3MDO with CN/NO added. HYSCORE peaks are roughly symmetric about the frequency diagonal, so for simplicity, peaks will be referred to hereafter in the format (ν_1, ν_2) . The spectrum contains several sets of peaks that encode information about ^{14}N and ^1H nuclei near the unpaired electron. In the case of ^1H ($I = 1/2$), peaks should show up at or near the ^1H Larmor frequency (~ 15 MHz at this magnetic field), and they would be shifted from the diagonal by the hyperfine coupling. As evident in **Figure 4.5**, there is a remarkable lack of peaks near (15, 15) MHz. The small peak centered at the ^1H Larmor frequency (15, 15) MHz is the matrix proton peak that represents all the weakly-coupled ^1H that are distant from the paramagnetic center. The lack of cross-peaks that are shifted out from the frequency diagonal suggests a lack of any strongly-coupled ^1H , such as those that would arise from a solvent-based ligand in close proximity to the center of spin density. This suggests that no

solvent-derived ligand is coordinated to the Fe site, which eliminates H₂O or OH⁻ as a potential ligand in the CN/NO complex.

While the ¹H region of the spectrum in **Figure 4.5** shows a lack of coupled nuclei, the ¹⁴N region below ~8 MHz contains several sets of peaks. In the case of ¹⁴N ($I = 1$), the electron spin states are split into three levels, each representing a quantum state of the ¹⁴N nucleus. The HYSCORE spectrum for a ¹⁴N nucleus contains cross-peaks from single-quantum and double-quantum nuclear transitions, and the intensity of these peaks varies with orientation and the presence of other coupled nuclei (30). In the case of nuclei where the hyperfine coupling is much larger than the ¹⁴N Larmor frequency ($A \gg 2\nu_I$), peaks will appear in the (-, +) quadrant of the HYSCORE spectrum. Accordingly, the (-, +) quadrant in **Figure 4.6** contains several sets of peaks below (8, 8) MHz that result from strongly-coupled ¹⁴N nuclei, namely the coordinated nitrogen from the three histidine residues and the ¹⁴N on NO. For weakly-coupled ¹⁴N where the hyperfine coupling is less than the ¹⁴N Larmor frequency ($A \ll 2\nu_I$), peaks will appear in the (+, +) quadrant of the HYSCORE spectrum. The (+, +) quadrant in **Figure 4.6** contains several peaks below (4, 4) MHz from weakly-coupled ¹⁴N nuclei. The remote nitrogen atoms on the coordinated histidine residues are likely to fall in this region, as they typically have much weaker hyperfine couplings (31). Nitrogen atoms from the second-sphere arginine residue as well as other nearby residues would also fall in this region.

Since there are multiple, overlapping ¹⁴N peaks in both the strong and weakly-coupled quadrants of the HYSCORE spectrum, the best method for observing a single ¹⁴N is via isotopic substitution with ¹⁵N ($S = 1/2$). As discussed earlier, the nuclear quadrupole for ¹⁴N results in multiple sets of peaks with varying intensities that depend heavily on the orientation of the nucleus. However, ¹⁵N peaks, like ¹H, show up at or near the nuclear Larmor frequency (~1.5

MHz in this case). Therefore, in order to determine how many CN⁻ ligands are present in the mixed CN/NO complex, analogous HYSCORE spectra on samples made with ¹⁵N-cyanide were measured. **Figure 4.6** shows a comparison between HYSCORE spectra taken with C¹⁴N and C¹⁵N plotted with the same contour levels for best peak intensity comparison. In the spectrum with ¹⁵N, there is an intense peak centered on the diagonal at 1.5 MHz; this peak is from at least one ¹⁵N nucleus and is not present in the corresponding ¹⁴N measurement. In the ¹⁴N measurement, a peak is shown at slightly higher frequency (~2 MHz), but it does not overlap with the ¹⁵N Larmor frequency. Still, the best way to visualize the ¹⁵N peak without contaminating ¹⁴N peaks is by looking at the difference spectrum between ¹⁵N and ¹⁴N measurements collected under the same conditions. **Figure 4.7** shows the difference spectra at each magnetic field. These spectra clearly demonstrate a ¹⁵N peak at 1.5 MHz that could either arise from one weakly-coupled ¹⁵N nucleus or two ¹⁵N nuclei with similar hyperfine couplings. The weak coupling makes resolving peaks difficult, but computational simulations can still shed light on the number of nuclei by comparing simulations of one and two coupled ¹⁵N to the experimental peak shape.

H157N Variant of 3MDO. Though a third ligand has not been identified, the active site of 3MDO presents an opportunity for inducing perturbations which could give insight into the orientation of known ligands. As shown in **Figure 4.1**, the SHY motif is positioned to potentially interact with the axial ligand bound to iron. Previous studies with NO and cyanide independently showed an interaction in the form a hydrogen bond donation from Tyr159. The exact method of interaction could not be ascertained in the case of NO, but cyanide studies clearly indicated that wild-type 3MDO features Tyr159 donating a hydrogen bond to the terminal nitrogen of an axial bound cyanide. In the case of the H157N variant, this hydrogen bond was removed from the iron

complex and directed toward the Asn157 carbonyl. A (CN/NO)-bound sample was prepared with the H157N 3MDO variant to discern if any shift in hydrogen bonding was shown and if it could be attributed to a specific ligand.

Spectrum **B** in **Figure 4.8** was observed upon addition of cyanide and nitric oxide to ferrous H157N 3MDO. In addition to the hyperfine triplet already observed in wild-type, there is an additional smaller triplet coupled to the middle g_2 signal. The g_1 signal also shows hyperfine coupling from a triplet, though it is not as well-resolved. Significant line broadening is seen in the g_3 signal. Simulation of this species results in the spectrum **C** shown in **Figure 4.8** and shows exceptional agreement with the experimental data. The hyperfine couplings for the nitrosyl nitrogen are virtually unchanged from that of wild type. The second triplet seen in the g_2 signal shows a splitting of 19 MHz. The hyperfine couplings are slightly larger for the g_1 and g_3 signal than seen in wild type. Presently, the contributions from individual $I = 1$ nuclei cannot be resolved for these peaks.

Qualitative inspection of the (CN/NO)-bound H157N species shows remarkable similarity to a (CN/NO)-bound Fe(II) nonheme enzyme, protocatechuate 3,4-dioxygenase (3,4-PCD) shown by Orville and Lipscomb (32). The 3,4-PCD species also featured an $S=1/2$ species with two resolved triplets in the middle g -value. The reported hyperfine couplings for this species were 64 and 23 MHz. The authors were able to determine the larger coupling originated from the nitrosyl ^{14}N nucleus. This is akin to the (NO/cysteine)-bound CDO and the MDO complexes presented herein. The authors also concluded that the smaller triplet arose from an ^{14}N nucleus of an iron-bound histidine *trans* to the bound nitrosyl and that two cyanides were simultaneously bound to the iron complex.

The similarity in hyperfine coupling between the species presented herein and those shown for 3,4-PCD and other examples in literature suggests the smaller hyperfine coupling does arise from a histidine *trans* to the nitrosyl (32,33). Three histidines are bound to the iron in a facial triad. Therefore, the coupling of a *trans* histidine does not help to elucidate the position of nitric oxide. The greatest insight from the resolved ^{14}N coupling is the fact that it is only observed with the H157N variant.

As stated above, a variation on the SHY motif would most likely perturb a ligand in the axial position, where the Tyr159 has been shown to donate a hydrogen bond. Clearly, some perturbation has occurred as the spectrum has changed to include more pronounced hyperfine structure. Studies with cyanide in the axial position revealed the perturbation induced from the H157N variant was the phenol hydrogen of Tyr159 reorienting to donate to Asn157 instead of cyanide. In this case, the removal of a hydrogen bond from the (CN/NO)-bound iron complex could result in a shift in the SOMO electron density, thus increasing the hyperfine coupling resolution of the histidine ^{14}N nucleus.

Computational Modeling. Three possible arrangements for nitrosyl binding to iron are shown in **Figure 4.9**. Each orientation shows a different interaction with the outer sphere residues. Orientation **A** shows the nitrosyl in the axial position receiving a hydrogen bond from Tyr159. Orientation **B** has the nitrosyl adjacent to cationic Arg168, whereas **C** shows no obvious interaction with outer sphere residues. The lack of strongly coupled protons in the HYSORE spectra suggest that (a) the nitric oxide is likely not accepting a hydrogen bond from Tyr159 and (b) it is not interacting with the guanidinium of Arg168. Furthermore, cyanide and chloride (if bound) would have a formal negative charge while the nitrosyl would be neutral. Therefore,

cyanide and chloride are more likely to be adjacent to Arg168. This leaves orientation **C** as the most likely for nitric oxide binding to iron.

While HYSCORE spectra cannot definitively determine the number of cyanide ligands bound, they suggest that the complex does not contain a solvent ligand. There are two remaining options for the third ligand: either a second cyanide or a chloride ligand. Based on the above deductions regarding the structure of the (CN/NO)-bound 3MDO complex, three structures were created based on the coordinates of PDB: 6XB9 and optimized by DFT. Each structure had the nitrosyl bound *trans* to His92 with the remaining positions occupied by either cyanide or chloride. **Figure 4.10** shows each of the three optimized structures. Structure 1 features two bound cyanides *trans* to His90 and His142. For simplicity, this structure will be denoted as NO/(CN)₂. Structure 2 in **Figure 4.10** has a cyanide bound *trans* to His142 and chloride *trans* to His90, denoted NO/CN₁₄₂/Cl₉₀. The final structure switches the cyanide and chloride and is labeled NO/CN₉₀/Cl₁₄₂. Each structure shows a strong interaction between Arg168 and adjacent iron-bound CN/Cl.

The *g*-values, hyperfine couplings, and Euler angles of relevant nuclei were calculated for each structure. Calculated *g*-values are shown in **Table 4.2** and select hyperfine values are shown in **Table 4.3**. The *g*-values for each structure agree with the experimental simulations within the error of DFT (27,28,34,35). The RMSDs comparing the calculated *g*-values to experimental are similar for each structure. As such, no structure can be excluded based on this parameter. As expected, each structure shows a large *A*₂ hyperfine coupling for the ¹⁴N of the nitrosyl. Though larger than experimental, these values line up well with previously calculated values for similar complexes (27). The ¹⁴N of His92 (*trans* to NO) showed the largest hyperfine coupling of all the bound histidines in each structure. Hyperfine values were calculated for ¹³C of cyanide as well.

Significant hyperfine is shown for ^{13}C in each structure, which agrees with simulated CW EPR parameters. The hyperfine coupling of the cyanide nitrogen was calculated as ^{15}N to be simulated with the HYSORE difference spectra. These values were all relatively small (<1.5 MHz) and variations between the structures are within error of DFT calculated values (data not shown). The inclusion of calculated Euler angles may still provide insight regarding simulating the HYSORE spectra, as will be discussed below.

Five-coordinate structures were also considered and optimized. The calculated g -values of these structures did not show good agreement with experimental as all three values were greater than $g = 2$ (not shown). As such, five coordinate structures were taken out of consideration.

Simulations of HYSORE spectra were completed using the calculated hyperfine couplings and Euler angles from single point DFT calculations. Simulations were compared to the $^{15}\text{N}/^{14}\text{N}$ difference spectra with isolated ^{15}N cyanide peaks. The nuclei taken into consideration for these simulations were limited to the ^{15}N -cyanide from each model. The simulation for each optimized model is shown in **Figures 4.11 – 4.13**. All simulations fit reasonably well as they all replicate a peak centered on the diagonal near (1.5, 1.5) MHz. Some error is predicted for DFT hyperfine couplings (36). As such, there is no clear argument to be made for which model fits best based on the weakly-coupled ^{15}N peak.

4.4 Discussion

A (CN/NO)-bound ferrous 3MDO species was produced which closely resembles the substrate-bound nitrosyl complex seen with mammalian CDO. Cyanide binding was confirmed based on isotopic substitutions. The exact structure of the (CN/NO)-bound species is unknown,

but some deductions can be made based on computational and spectroscopic evidence. Computational models immediately ruled out the possibility of a five-coordinate complex based on calculated *g*-values. A second nitrosyl ligand would result in a dinitrosyl-iron complex (DNIC). EPR spectra of DNICs are well characterized and do not fall within the spectral parameters shown herein (37-39). Therefore, the possibility of a second nitrosyl binding as the third ligand was not considered reasonable.

A lack of strongly coupled protons in HYSCORE spectra suggest the complex does not contain a water or hydroxide ligand. Therefore, the third bound ligand could be a chloride ((CN/Cl/NO)-3MDO) or a second cyanide (((CN₂)/NO)-3MDO). Both ligands have been shown to bind to the iron active site of 3MDO. Cyanide binding was presented in Chapter 3 and crystal structures reveal thiocyanate binding (PDB: 7HOV) and chloride binding (PDB: 6XB9). Two cyanides were confirmed to bind in the 3,4-PCD complex produced by Orville and Lipscomb (32). Logically, two cyanides bound agrees better when considering that only one species is observed. Because chloride and cyanide would show similar interactions with either Arg168 or Tyr159, it is easy to predict a mixture of species where the two ligands would exchange places. Theoretical calculations showed that switching the position of the cyanide and chloride would shift the *g*-values, so a mixture in solution would be observed if this was the case. However, there is also the possibility of chloride being bound to iron in a position with a favorable interaction (i.e. adjacent to Arg168) which would not be broken by addition of cyanide and nitric oxide, and thus resulting in a single species. Currently, neither possibility can be ruled out.

Much consideration was put into the positions of each ligand. Chloride, cyanide, and nitric oxide have all shown to be capable of binding to the axial position. Isotopic substitutions were limited in assigning a position of bound cyanide. The variant H157N was used as it would

most perturb the axial bound ligand. The resulting spectrum for this variant shows increased hyperfine resolution for a $I = 1$ nuclei. Based on literature it is presumed to be the ^{14}N of histidine *trans* to nitric oxide.(32,33) Initially, nitric oxide was concluded to be bound to the axial position and loss of a hydrogen bond from Tyr159 resulted in a shift in electron density towards the iron and *trans* histidine. The caveat to this model is shown in the HYSCORE spectra. No strongly coupled protons are observed for the wild type (CN/NO)-bound species. Based on the model of hydrogen bonding in the SHY motif, the change in H157N should be a result of a hydrogen bond being removed from the axial ligand. Meaning a hydrogen bond would be present in wild-type. However, if the ligand centered radical was accepting a hydrogen bond, a set of strongly coupled proton peaks should be observed in HYSCORE.

Because HYSCORE showed no strongly coupled protons, nitric oxide was determined to be position *trans* to His92 as seen in **Figure 4.9**, model C. Using nitric oxide position as a postulate, three models were conceived and optimized with DFT. EPR parameters were calculated from the optimized structures to compare with experimental data. Based on CW EPR simulations, each species shows g -values and hyperfine couplings, which qualitatively agree with experimental results. The calculated EPR parameters were used to simulate HYSCORE spectra for the isolated ^{15}N cyanide nuclei. Because each ^{15}N nucleus showed low hyperfine coupling, the differences are minimal.

The structural identification of the (CN/NO)-bound 3MDO species remains open until further data can be procured. Based on results currently available it can be concluded that simultaneous binding of cyanide and nitric oxide is observed on the ferrous 3MDO active site. Binding of substrate, **3MPA**, is not able to occur with both cyanide and nitric oxide, suggesting bidentate coordination of substrate is preferred. It was also shown that perturbations to the SHY

motif resulted in resolved hyperfine coupling not seen with the wild-type enzyme. This shows the SHY motif directly influences the spin density of the iron complex and, therefore, the electronic structure of the iron active site. Dissection of measurable shifts in the electronic structure of non-catalytic complexes as seen above can lead to insights for the SHY motif's role in catalytic enhancement.

4.5 Future work

Future experiments will focus on determining whether a chloride ligand is bound to the iron. This is to be addressed by two experiments. The first is to replicate the (CN/NO)-bound species in buffer with no NaCl. If chloride is bound in the observed species, a drastic drop in NaCl concentration would severely attenuate the observed signal. However, a decrease in EPR signal may be a result of overall protein structural instability from a lack of salt content. Therefore, a second experiment would be to produce the (CN/NO)-bound species in 50 mM sodium fluoride. This would match the ionic strength of the control sample with 50 mM NaCl without supplying chloride. There would also be an opportunity for fluoride to displace chloride in the (CN/NO)-bound species. This would be interesting from a spectroscopical perspective as ^{19}F has a nuclear spin of $I = 1/2$ and a gyromagnetic ratio which is an order of magnitude greater than ^{35}Cl or ^{37}Cl . If fluoride would bind to iron instead of chloride, there is a reasonable chance to observe resolved hyperfine coupling either by CW or pulsed EPR. A positive result from these experiments would confirm the presence of a chloride, or more inclusively, a halide bound to the (CN/NO)-iron complex. A lack of signal attenuation or fluoride binding would not necessarily rule out the possibility of chloride binding. If chloride is already bound to iron prior to addition of

reductant or cyanide and nitric oxide, then dialysis or other forms of buffer exchange may not be fruitful. Therefore, it would be useful to also test the alternative of two cyanides being bound.

The histidine variant gives an excellent opportunity for further isotopic substitution experiments. Based on previous literature and low values for calculated cyanide nitrogen hyperfine, it is assumed that the smaller triplet observed in the H157N variant arises from the histidine ^{14}N *trans* to NO. Isotopic substitution of ^{15}N cyanide could experimentally confirm the smaller triplet does not arise from bound cyanide. The H157N variant also shows much more resolved peaks in the g_2 region even though the overall signal intensity is considerably lower than that of wild type. These sharper peaks may also allow better resolution of coupling from ^{13}C cyanide. Orville and Lipscomb were able to determine two cyanides were bound to a similar (CN/NO)-bound iron complex using ^{13}C cyanide. Wild-type 3MDO did not show enough resolution to replicate these experiments, but it has yet to be seen in the H157N variant can show the needed resolution.

Finally, the samples described above as well as the H157N sample with natural abundance isotopes would be prepared at concentrations high enough for HYSCORE spectroscopy. The HYSCORE data presented above was invaluable in determining a lack of strongly coupled protons, which was crucial for the assignment of nitric oxide position on the iron complex. If a cyanide is bound in the axial position, it is possible a perturbation will be observed in a $^{15}\text{N}/^{14}\text{N}$ difference spectra. If achieved, a HYSCORE spectrum of a fluoride bound species could also yield information which could help elucidate its position on the iron.

Figures

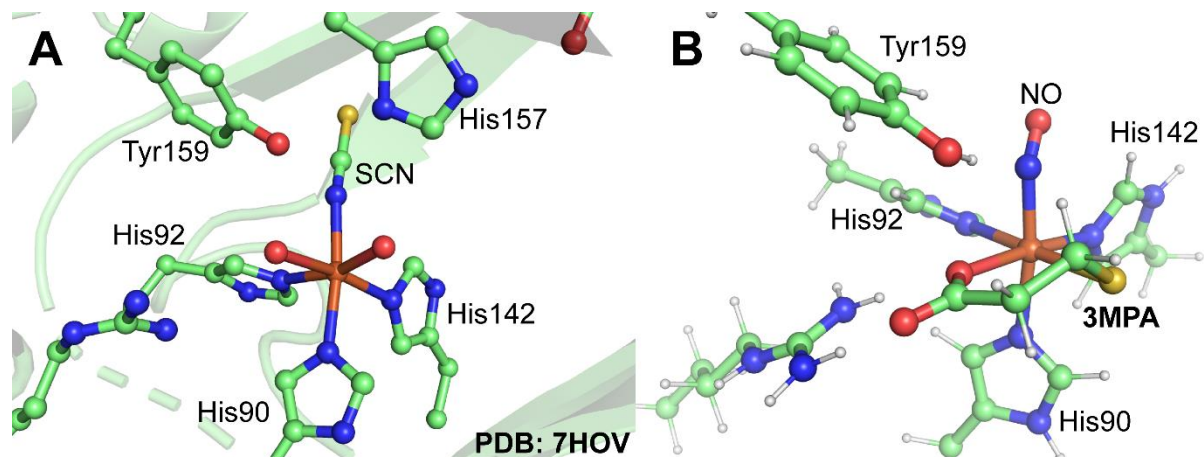


Figure 4.1: Panel A displays the crystal structure of Av3MDO bound to thiocyanate in the axial position *trans* to His90 with two water/solvent ligands bound in the equatorial positions *trans* to His92 and His142. Panel B displays the DFT optimized structure of **3MPA** bound to iron in the equatorial positions with nitric oxide bound axially.

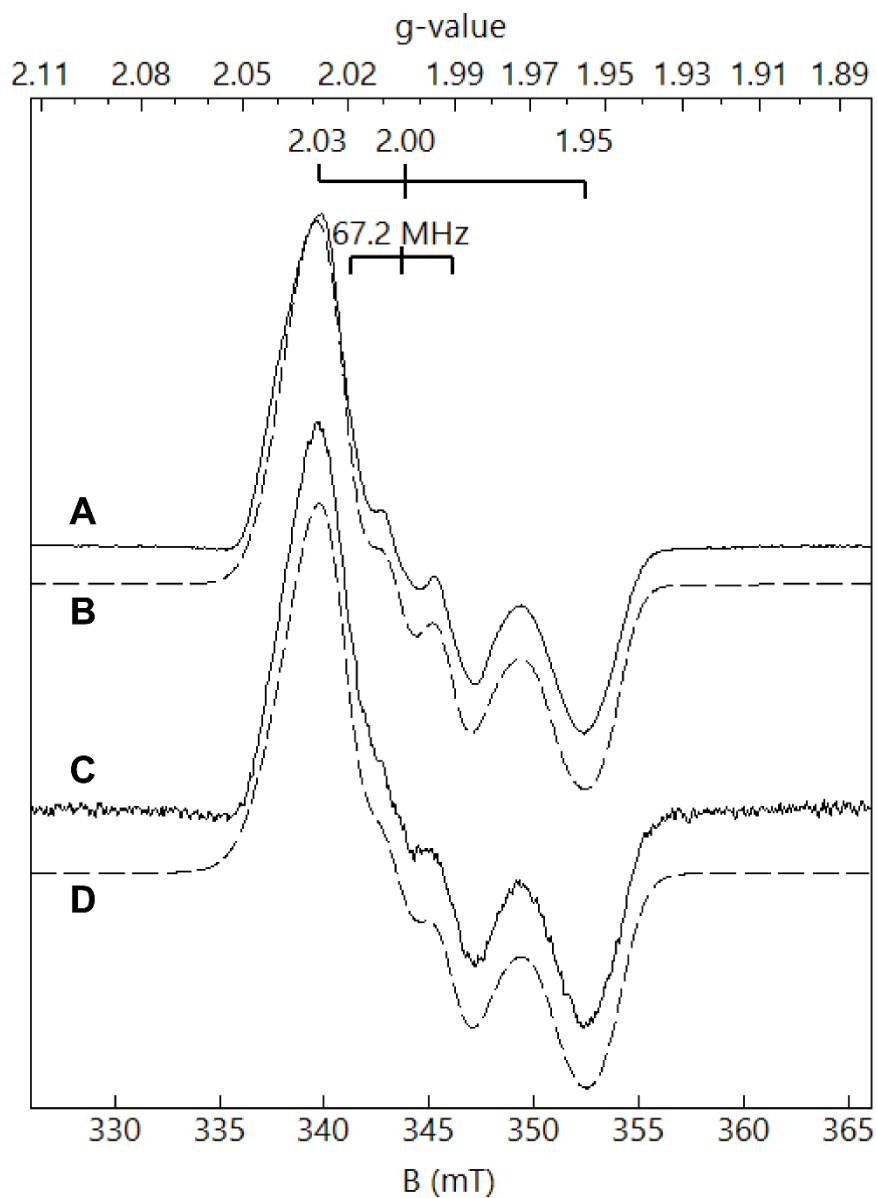


Figure 4.2: CW EPR spectra of Fe(II)-Av3MDO mixed with 20x KCN and 10x NO (*trace A*). A quantitative EPR simulations (*trace B*) is overlaid on the data for comparison. Shown in *trace C* is an equivalent sample prepared with $K^{13}CN$ and the corresponding simulated spectrum (**D**). Instrumental conditions: microwave frequency, 9.64 GHz, microwave power, 53 μW ; modulation amplitude, 0.2 mT; temperature, 10 K. Simulation parameters for **B** and **D** are provided in **Table 4.1**.

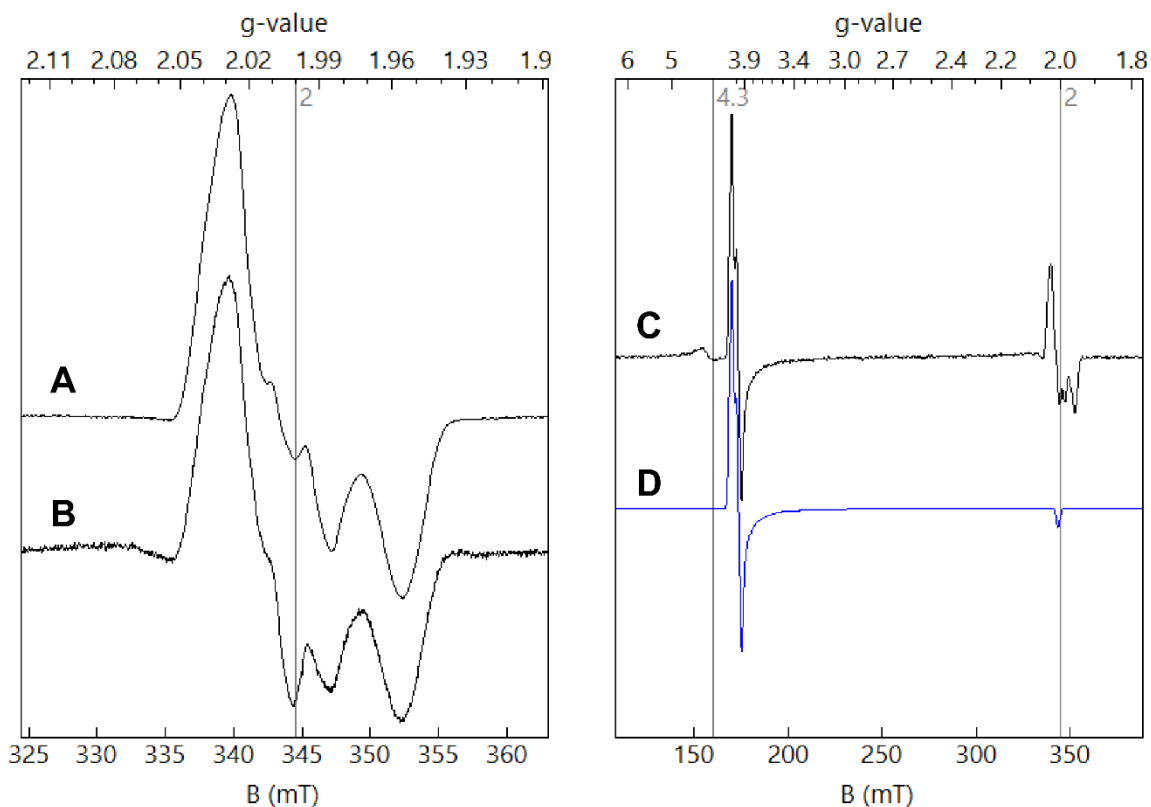


Figure 4.3: CW EPR spectrum **A** displayed the mixture of 3MDO with cyanide and nitric oxide as shown above. Spectrum **B** is the resulting spectrum when 10x relative concentration **3MPA** is added prior to cyanide or NO. Upon acquisition of this sample at a broader magnetic field range (**C**), it is concluded that the negative signal at $g = 2.00$ is due to the $S = 3/2$ (**3MPA/NO**)-bound 3MDO complex. The simulation of this species is shown in spectrum **D** in blue. Instrumental conditions: microwave frequency, 9.64 GHz, microwave power, 53 μ W; modulation amplitude, 0.9 mT; temperature, 10 K.

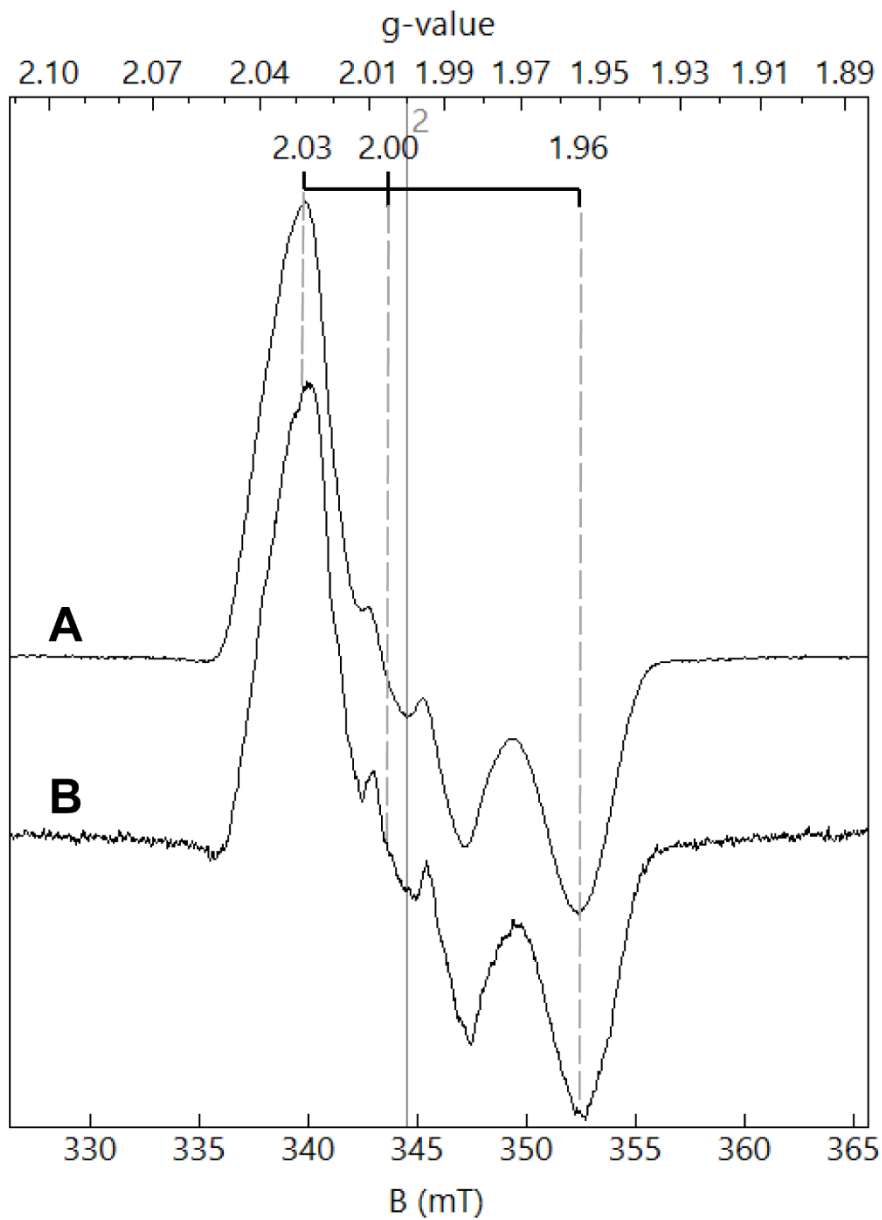


Figure 4.4: CW EPR spectra of Fe(II)-Av3MDO mixed with natural abundance CN and NO (**A**) and ^{15}N -CN and NO (**B**). Nitric oxide is the natural abundance of isotopes in both spectra. Instrumental conditions: microwave frequency, 9.64 GHz, microwave power, 53 μW ; modulation amplitude, 0.2 mT; temperature, 10 K.

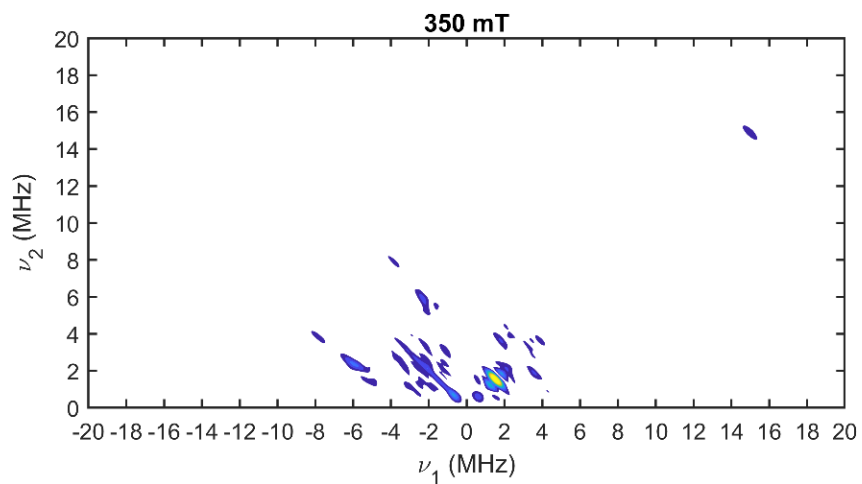


Figure 4.5: HYSCORE spectra of (CN/NO)-bound *Av3MDO*. Instrument parameters: microwave frequency, 9.78 GHz; field position of 350 mT; temperature, 10 K; pulse repetition rate, 1.25 kHz; τ , 140 ns.

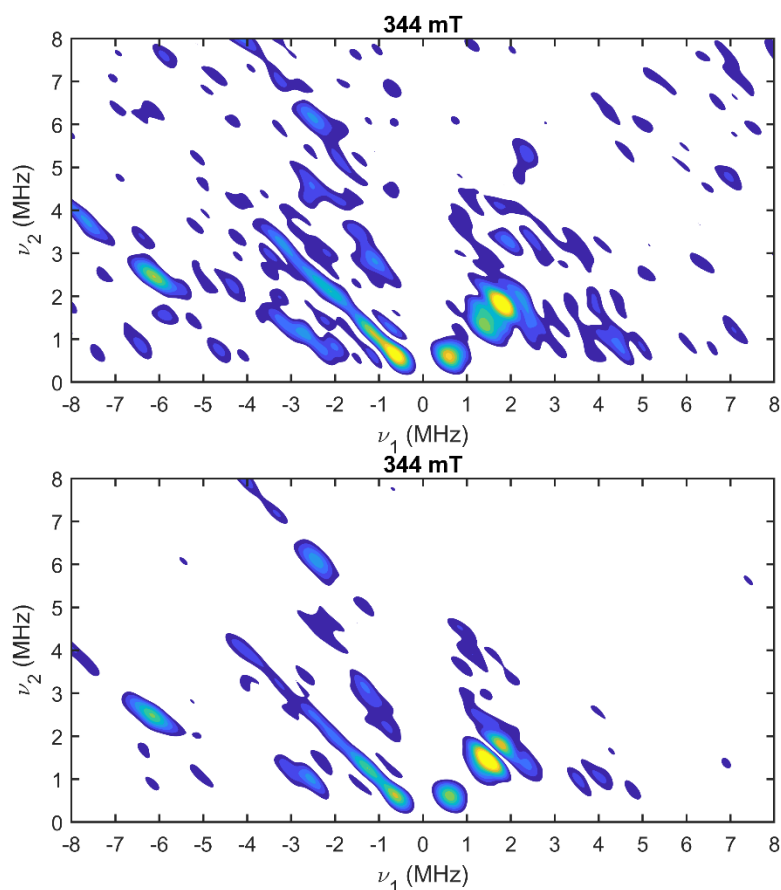


Figure 4.6: HSCORE spectra for (CN/NO)-bound Fe(II)-Av3MDO collected at 344 mT. Isotopic comparison was made by preparing equivalent enzyme samples for the ($C^{14}\text{N}/\text{NO}$)-bound (*top*) and ($C^{15}\text{N}/\text{NO}$)-bound (*bottom*) Fe-site. The two spectra were plotted using the same contour levels for best comparison of the $^{14}\text{N}/^{15}\text{N}$ peak intensity. Instrument parameters: microwave frequency, 9.78 GHz; field position of 344 mT; temperature, 10 K; pulse repetition rate, 1.25 kHz; τ , 140 ns.

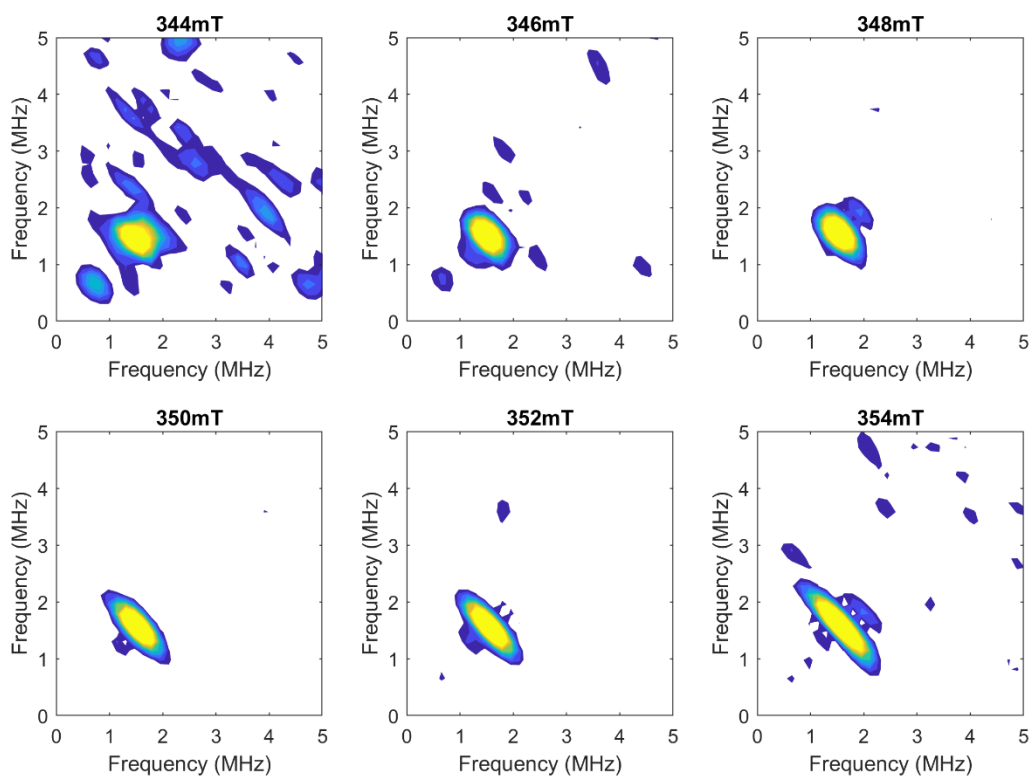


Figure 4.7: Field dependent HSCORE spectra of (CN/NO)-bound Av3MDO ($C^{15}N/C^{14}N$) difference spectra. Selected magnetic fields (344, 346, 348, 350, 352, 354 mT) span the g -values for the observed EPR spectrum. Instrument parameters: microwave frequency, 9.78 GHz; temperature, 10 K; pulse repetition rate, 1.25 kHz; τ , 140 ns.

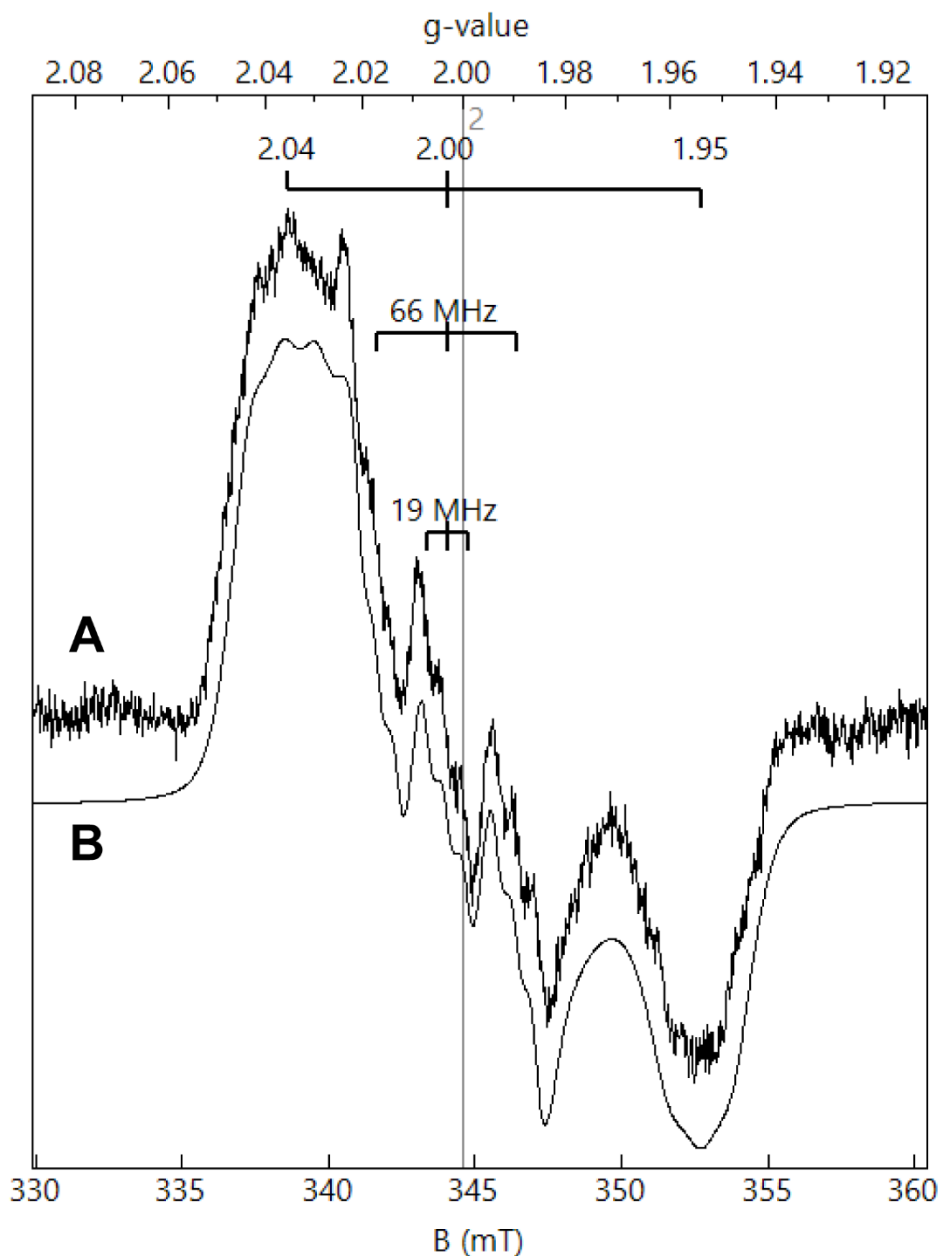


Figure 4.8: CW EPR spectrum (*trace A*) of the H157N (CN/NO)-bound Av3MDO variant. Samples were prepared under equivalent conditions as described in **Fig. 4.4**. A quantitative EPR simulation (*trace B*) is offset from the data to highlight the central g -value (g_2) hyperfine splitting from two inequivalent (^{14}N , $I = 1$) triplets. The ^{14}N -atoms A -values determined by simulation were 66 and 19 MHz. Instrumental conditions: microwave frequency, 9.64 GHz, microwave power, 53 μW ; modulation amplitude, 0.2 mT; temperature, 10 K.

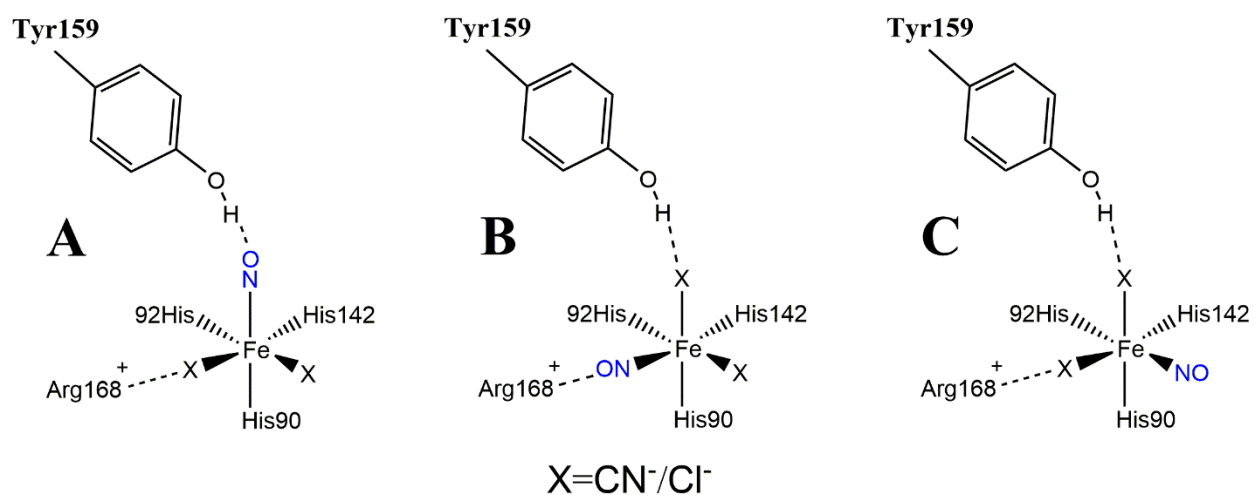


Figure 4.9: Schematic representation of possible orientations of the nitrosyl ligand on the His-bound facial triad of Av3MDO. Potential interactions with non-Fe-coordinating outer sphere residues are highlighted in blue. Model A shows nitrosyl accepting a hydrogen bond from Tyr159, model B shows the nitrosyl interacting with the cationic Arg168 residue, and model C shows no apparent interaction with the outer sphere.

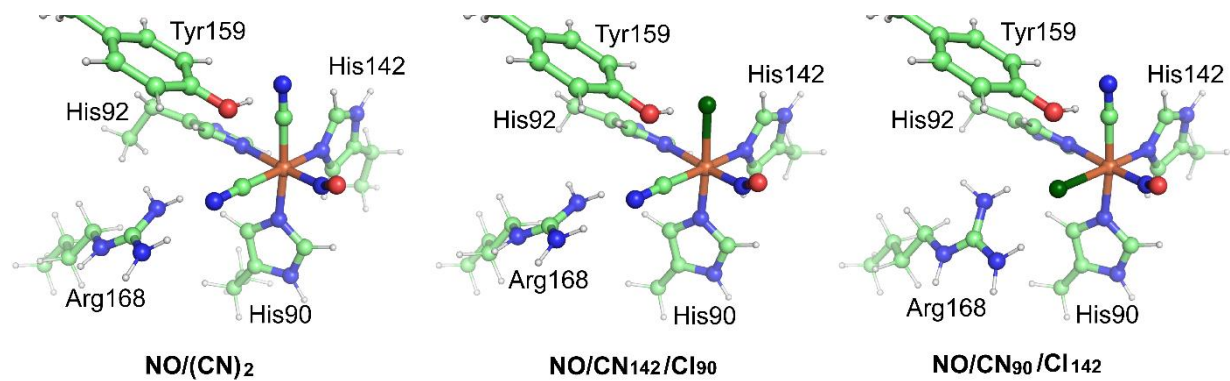


Figure 4.10: DFT optimized structures for possible ligand arrangement for the (CN/NO)-bound Av3MDO ($S = 1/2$) species. For clarity, numerical subscripts on selected ligands refer to the *trans* protein derived His ligand. Chlorine is displayed in dark green, oxygen in red, and nitrogen in blue.

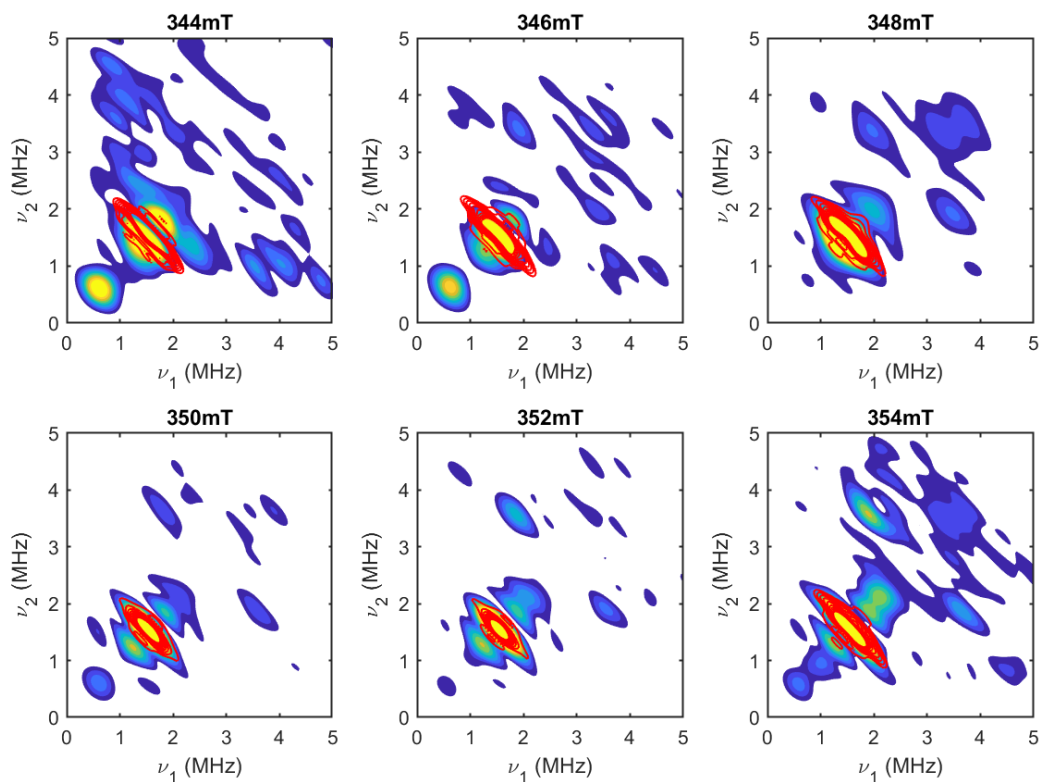


Figure 4.11: Simulated HYSORE spectra (red lines) based on calculated hyperfine couplings and Euler angles of ^{15}N -cyanide for the DFT optimized model NO/(CN) $_2$. Simulations are superimposed on $^{15}\text{N}/^{14}\text{N}$ difference spectra taken at six different magnetic fields (344, 346, 348, 350, 352, 354 mT) spanning the observed g -values for the (CN/NO)-bound Av3MDO ($S = 1/2$) species.

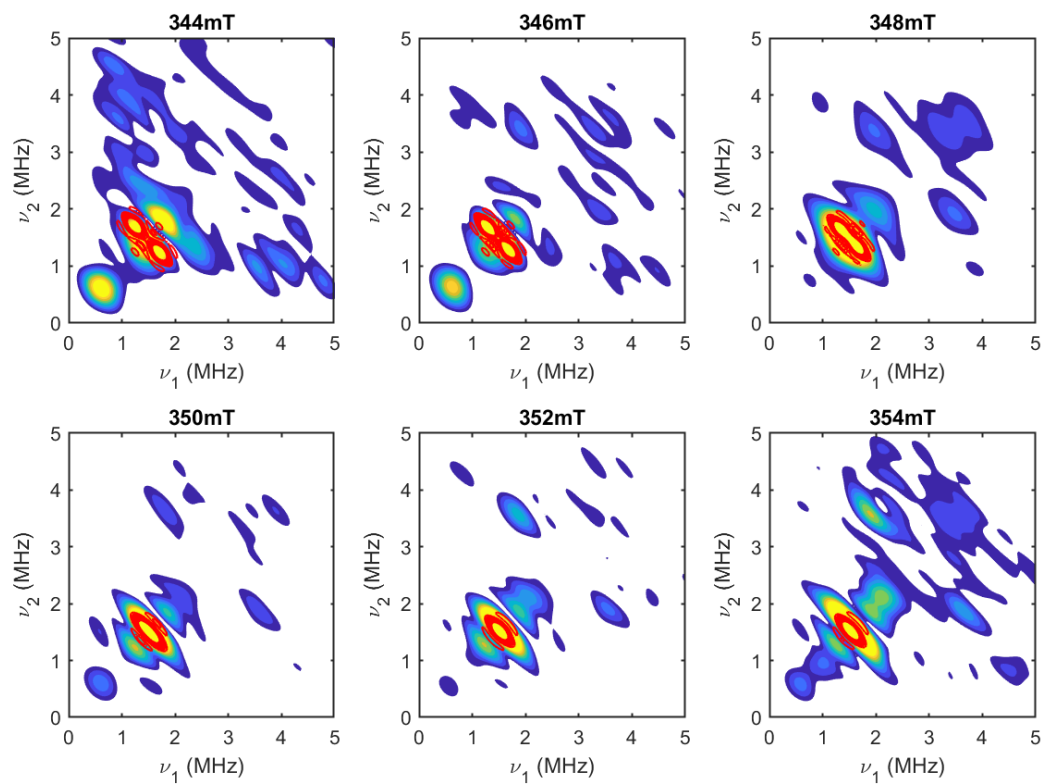


Figure 4.12: Simulated HYSORE spectra (red lines) based on calculated hyperfine couplings and Euler angles of ^{15}N -cyanide for the DFT optimized model NO/CN₁₄₂/Cl₉₀. Simulations are superimposed on $^{15}\text{N}/^{14}\text{N}$ difference spectra taken at six different magnetic fields (344, 346, 348, 350, 352, 354 mT) spanning the observed g -values for the (CN/NO)-bound Av3MDO ($S = 1/2$) species.

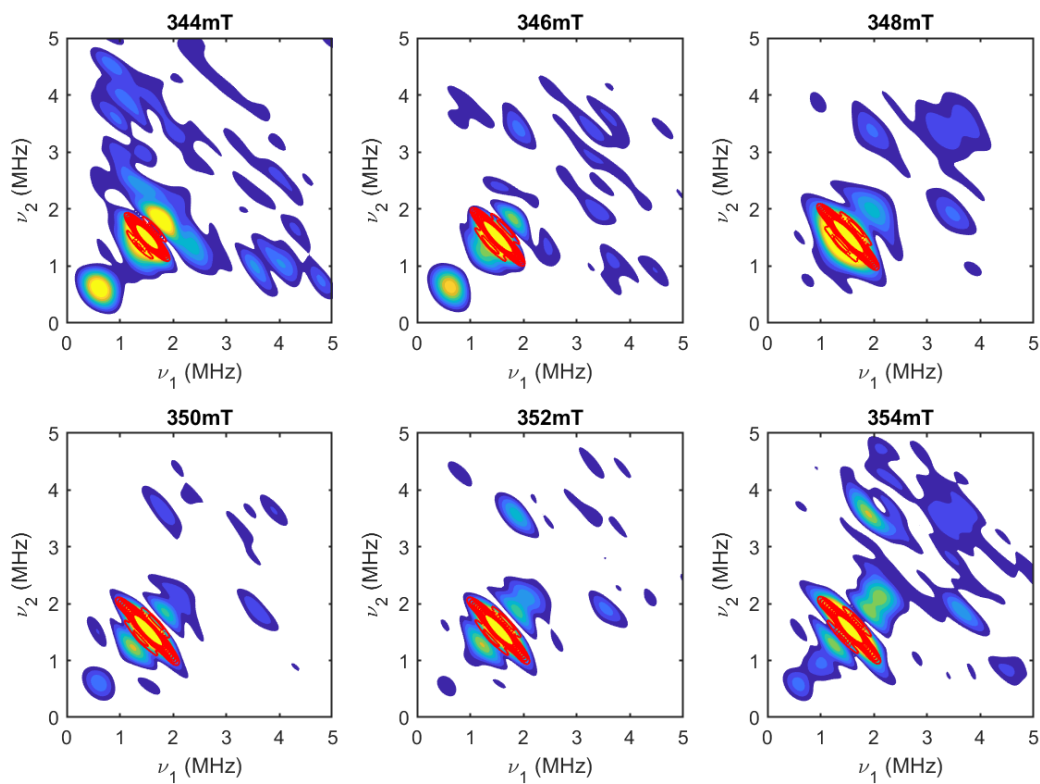


Figure 4.13: Simulated HYSORE spectra (red lines) based on calculated hyperfine couplings and Euler angles of ^{15}N -cyanide for the DFT optimized model NO/CN₉₀/Cl₁₄₂. Simulations are superimposed on $^{15}\text{N}/^{14}\text{N}$ difference spectra taken at six different magnetic fields (344, 346, 348, 350, 352, 354 mT) spanning the observed g -values for the (CN/NO)-bound $A\nu$ 3MDO ($S = 1/2$) species.

| | | | |
|-------------------------------|--------------|--------------|--------------|
| Wild-type | g_1 | g_2 | g_3 |
| | 2.032 | 2.005 | 1.955 |
| $^{14}\text{N}_{(\text{NO})}$ | σg_1 | σg_2 | σg_3 |
| | 0.0073 | 0.0052 | 0.0049 |
| $^{13}\text{C}_{(\text{CN})}$ | A_1 (MHz) | A_2 (MHz) | A_3 (MHz) |
| | 28.0 | 67.2 | 30.0 |
| H157N | g_1 | g_2 | g_3 |
| | 2.037 | 2.003 | 1.954 |
| $^{14}\text{N}_{(\text{NO})}$ | σg_1 | σg_2 | σg_3 |
| | 0.0052 | 0.0018 | 0.0053 |
| ^{14}N | A_1 (MHz) | A_2 (MHz) | A_3 (MHz) |
| | 33.3 | 66.2 | 30.5 |
| H157N - WT | A_1 (MHz) | A_2 (MHz) | A_3 (MHz) |
| | - | 19.1 | - |
| H157N - WT | Δg_1 | Δg_2 | Δg_3 |
| | 0.005 | 0.002 | 0.001 |

Table 4.1: Simulated EPR parameters for the (CN/NO)-bound ferrous 3MDO in wild-type and H157N variant.

| | g_1 | g_2 | g_3 | RMSD |
|--|-------|-------|-------|-------|
| exp | 2.032 | 2.005 | 1.955 | N/A |
| NO/(CN) ₂ | 2.017 | 2.001 | 1.971 | 0.013 |
| NO/CN ₉₀ /Cl ₁₄₂ | 2.021 | 2.001 | 1.970 | 0.011 |
| NO/CN ₁₄₂ /Cl ₉₀ | 2.021 | 2.003 | 1.973 | 0.012 |

Table 4.2: Calculated g -values for DFT optimized models of the (CN/NO)-bound 3MDO.

| NO/(CN) ₂ | A ₁ (MHz) | A ₂ (MHz) | A ₃ (MHz) | α (Deg) | β (Deg) | γ (Deg) |
|---|----------------------|----------------------|----------------------|---------|---------|---------|
| ¹⁴ N(NO) | 22.7 | 80.7 | 23.4 | -18 | 10 | 6 |
| ¹⁴ N(<i>trans</i> -His) | 19.1 | 14.9 | 15.2 | 95 | 18 | -129 |
| ¹³ C(CN <i>trans</i> His142) | -16.2 | -15.8 | -13.7 | 6 | 38 | 27 |
| ¹³ C(CN <i>trans</i> His90) | -14.0 | -14.5 | -11.6 | 125 | 46 | -152 |
| NO/CN ₉₀ /Cl ₁₄₂ | | | | | | |
| ¹⁴ N(NO) | 24.7 | 80.0 | 25.5 | 157 | 18 | -173 |
| ¹⁴ N(<i>trans</i> -His) | 17.3 | 13.5 | 13.7 | 56 | 17 | -96 |
| ¹³ C(CN <i>trans</i> His90) | -11.8 | -13.8 | -14.3 | -9 | 46 | 50 |
| NO/CN ₁₄₂ /Cl ₉₀ | | | | | | |
| ¹⁴ N(NO) | 26.4 | 79.0 | 25.7 | -159 | 41 | 153 |
| ¹⁴ N(<i>trans</i> -His) | 15.6 | 12.0 | 12.2 | 113 | 18 | -146 |
| ¹³ C(CN <i>trans</i> His142) | -17.5 | -16.9 | -15.0 | -16 | 39 | 47 |

Table 4.3: Calculated hyperfine values and Euler angles for selected nuclei of DFT optimized models of the (CN/NO)-bound 3MDO.

References

1. Gordon, C., Emery, P., Bradley, H., and Waring, R. H. (1992) Abnormal sulphur oxidation in systemic lupus erythematosus. *Lancet* **339**, 25-26
2. Dominy Jr, J. E., Simmons, C. R., Karplus, P. A., Gehring, A. M., and Stipanuk, M. H. (2006) Identification and characterization of bacterial cysteine dioxygenases: A new route of cysteine degradation for eubacteria. *J. Bacteriol.* **188**, 5561-5569
3. Heafield, M. T., Fearn, S., Steventon, G. B., Waring, R. H., Williams, A. C., and Sturman, S. G. (1990) Plasma cysteine and sulphate levels in patients with motor neurone, Parkinson's and Alzheimer's disease. *Neurosci. Lett.* **110**, 216-220
4. Reddie, K. G., and Carroll, K. S. (2008) Expanding the functional diversity of proteins through cysteine oxidation. *Curr. Opin. Chem. Biol.* **12**, 746-754
5. Winyard, P. G., Moody, C. J., and Jacob, C. (2005) Oxidative activation of antioxidant defence. *Trends Biochem. Sci* **30**, 453-461
6. Trachootham, D., Alexandre, J., and Huang, P. (2009) Targeting cancer cells by ROS-mediated mechanisms: a radical therapeutic approach? *Nat. Rev. Drug Discov.* **8**, 579-591
7. Bhave, D. P., Muse, W. B., 3rd, and Carroll, K. S. (2007) Drug targets in mycobacterial sulfur metabolism. *Infect. Disord. Drug Targets* **7**, 140-158
8. Pierce, B. S., Subedi, B. P., Sardar, S., and Crowell, J. K. (2015) The "Gln-Type" Thiol Dioxygenase from *Azotobacter vinelandii* Is a 3-Mercaptopropionic Acid Dioxygenase. *Biochemistry* **54**, 7477-7490
9. Crowell, J. K., Sardar, S., Hossain, M. S., Foss, F. W., and Pierce, B. S. (2016) Non-chemical proton-dependent steps prior to O₂-activation limit *Azotobacter vinelandii* 3-mercaptopropionic acid dioxygenase (MDO) catalysis. *Arch. Biochem. Biophys.* **604**, 86-94
10. Tchesnokov, E. P., Fellner, M., Siakkou, E., Kleffmann, T., Martin, L. W., Aloï, S., Lamont, I. L., Wilbanks, S. M., and Jameson, G. N. (2015) The cysteine dioxygenase homologue from *Pseudomonas aeruginosa* is a 3-mercaptopropionate dioxygenase. *J. Biol. Chem.* **290**, 24424-24437
11. Fellner, M., Aloï, S., Tchesnokov, E. P., Wilbanks, S. M., and Jameson, G. N. L. (2016) Substrate and pH-Dependent Kinetic Profile of 3-Mercaptopropionate Dioxygenase from *Pseudomonas aeruginosa*. *Biochemistry* **55**, 1362-1371
12. Fischer, A. A., Miller, J. R., Jodts, R. J., Ekanayake, D. M., Lindeman, S. V., Brunold, T. C., and Fiedler, A. T. (2019) Spectroscopic and Computational Comparisons of Thiolate-

- Ligated Ferric Nonheme Complexes to Cysteine Dioxygenase: Second-Sphere Effects on Substrate (Analogue) Positioning. *Inorg. Chem.* **58**, 16487-16499
13. Sardar, S., Weitz, A., Hendrich, M. P., and Pierce, B. S. (2019) Outer-Sphere Tyrosine 159 within the 3-Mercaptopropionic Acid Dioxygenase S-H-Y Motif Gates Substrate-Coordination Denticity at the Non-Heme Iron Active Site. *Biochemistry* **58**, 5135-5150
 14. Aloï, S., Davies, C. G., Karplus, P. A., Wilbanks, S. M., and Jameson, G. N. L. (2019) Substrate Specificity in Thiol Dioxygenases. *Biochemistry* **58**, 2398-2407
 15. Driggers, C. M., Cooley, R. B., Sankaran, B., Hirschberger, L. L., Stipanuk, M. H., and Karplus, P. A. (2013) Cysteine Dioxygenase Structures from pH4 to 9: Consistent Cys-Persulfenate Formation at Intermediate pH and a Cys-Bound Enzyme at Higher pH. *J. Mol. Biol.* **425**, 3121-3136
 16. Stoll, S., and Schweiger, A. (2006) EasySpin, a comprehensive software package for spectral simulation and analysis in EPR. *J. Magn. Reson.* **178**, 42-55
 17. Neese, F. (2017) Software update: the ORCA program system, version 4.0. *Wiley Interdiscip. Rev. Comput. Mol. Sci.* **8**, e1327
 18. Tao, J., Perdew, J. P., Staroverov, V. N., and Scuseria, G. E. (2003) Climbing the Density Functional Ladder: Nonempirical Meta--Generalized Gradient Approximation Designed for Molecules and Solids. *Phys. Rev. Lett.* **91**, 146401
 19. Weigend, F., and Ahlrichs, R. (2005) Balanced basis sets of split valence, triple zeta valence and quadruple zeta valence quality for H to Rn: Design and assessment of accuracy. *Phys. Chem. Chem. Phys.* **7**, 3297-3305
 20. Grimme, S., Antony, J., Ehrlich, S., and Krieg, H. (2010) A consistent and accurate ab initio parametrization of density functional dispersion correction (DFT-D) for the 94 elements H-Pu. *J. Chem. Phys.* **132**, 154104
 21. Vahtras, O., Almlöf, J., and Feyereisen, M. W. (1993) Integral approximations for LCAO-SCF calculations. *Chem. Phys. Lett.* **213**, 514-518
 22. Kendall, R. A., and Früchtl, H. A. (1997) The impact of the resolution of the identity approximate integral method on modern ab initio algorithm development. *Theor. Chem. Acc.* **97**, 158-163
 23. Cossi, M., Rega, N., Scalmani, G., and Barone, V. (2003) Energies, structures, and electronic properties of molecules in solution with the C-PCM solvation model. *J. Comput. Chem.* **24**, 669-681
 24. Staroverov, V. N., Scuseria, G. E., Tao, J., and Perdew, J. P. (2003) Comparative assessment of a new nonempirical density functional: Molecules and hydrogen-bonded complexes. *J. Chem. Phys.* **119**, 12129-12137

25. Römelt, M., Ye, S., and Neese, F. (2009) Calibration of modern density functional theory methods for the prediction of ^{57}Fe Mössbauer isomer shifts: meta-GGA and double-hybrid functionals. *Inorg. Chem.* **48**, 784-785
26. Rega, N., Cossi, M., and Barone, V. (1996) Development and validation of reliable quantum mechanical approaches for the study of free radicals in solution. *J. Chem. Phys.* **105**, 11060-11067
27. Pierce, B. S., Gardner, J. D., Bailey, L. J., Brunold, T. C., and Fox, B. G. (2007) Characterization of the Nitrosyl Adduct of Substrate-Bound Mouse Cysteine Dioxygenase by Electron Paramagnetic Resonance: Electronic Structure of the Active Site and Mechanistic Implications. *Biochemistry* **46**, 8569-8578
28. Blaesi, E. J., Gardner, J. D., Fox, B. G., and Brunold, T. C. (2013) Spectroscopic and Computational Characterization of the NO Adduct of Substrate-Bound Fe(II) Cysteine Dioxygenase: Insights into the Mechanism of O₂ Activation. *Biochemistry* **52**, 6040-6051
29. Cruce, A. A., Lockart, M. M., and Bowman, M. K. (2015) Chapter Twelve - Pulsed EPR in the Study of Drug Binding in Cytochrome P450 and NOS. in *Methods Enzymol.* (Qin, P. Z., and Warncke, K. eds.), Academic Press. pp 311-340
30. Chatterjee, R., Milikisiyants, S., and Lakshmi, K. (2012) Two-dimensional ^{14}N HYSCORE spectroscopy of the coordination geometry of ligands in dimanganese di- μ -oxo mimics of the oxygen evolving complex of photosystem II. *Phys. Chem. Chem. Phys.* **14**
31. Dikanov, S. A., Davydov, R. M., Gräslund, A., and Bowman, M. K. (1998) Two-Dimensional ESEEM Spectroscopy of Nitrogen Hyperfine Couplings in Methemerythrin and Azidomethemerythrin. *J. Am. Chem. Soc.* **120**, 6797-6805
32. Orville, A. M., and Lipscomb, J. D. (1997) Cyanide and Nitric Oxide Binding to Reduced Protocatechuate 3,4-Dioxygenase: Insight into the Basis for Order-Dependent Ligand Binding by Intradiol Catecholic Dioxygenases. *Biochemistry* **36**, 14044-14055
33. Stevens, T. H., and Chan, S. I. (1981) Histidine is the axial ligand to cytochrome alpha 3 in cytochrome c oxidase. *J. Biol. Chem.* **256**, 1069-1071
34. Neese, F. (2003) Quantum chemical calculations of spectroscopic properties of metalloproteins and model compounds: EPR and Mössbauer properties. *Curr. Opin. Chem. Biol.* **7**, 125-135
35. Neese, F. (2003) Metal and ligand hyperfine couplings in transition metal complexes: The effect of spin-orbit coupling as studied by coupled perturbed Kohn-Sham theory. *J. Chem. Phys.* **118**, 3939-3948
36. Neese, F. (2017) Quantum Chemistry and EPR Parameters. *eMagRes*, 1-22

37. Timoshin, A. A., Vanin, A. F., Orlova, T. R., Sanina, N. A., Ruuge, E. K., Aldoshin, S. M., and Chazov, E. I. (2007) Protein-bound dinitrosyl–iron complexes appearing in blood of rabbit added with a low-molecular dinitrosyl–iron complex: EPR studies. *Nitric Oxide* **16**, 286-293
38. Vanin, A. F. (2018) EPR Characterization of Dinitrosyl Iron Complexes with Thiol-Containing Ligands as an Approach to Their Identification in Biological Objects: An Overview. *Cell Biochem. Biophys.* **76**, 3-17
39. Vanin, A. F., Serezhenkov, V. A., Mikoyan, V. D., and Genkin, M. V. (1998) The 2.03 Signal as an Indicator of Dinitrosyl–Iron Complexes with Thiol-Containing Ligands. *Nitric Oxide* **2**, 224-234

CHAPTER 5: CONCLUSIONS

5.1 Substrate Binding to Av3MDO

The topic of substrate binding to Av3MDO was addressed in each preceding chapter. Chapter 2 showed a crystal structure with inhibitor, 3-hydroxypropionic acid, bound bidentate to the iron active site. This structure was used as a basis for modeling bidentate binding of substrate, 3-mercaptopropionic acid (**3MPA**). Bidentate binding of 3MPA was verified using DFT optimized models of the (**3MPA/NO**)-bound 3MDO $S = 3/2$ species in tandem with HYSORE spectroscopy. Chapter 3 addressed the mode of **3MPA** binding in the ferric, inactive enzyme using cyanide as a spectroscopic probe. Models of bidentate coordination were verified by accurate computational replication of experimentally observed spectral parameters. In chapter 4, the possibility of monodentate binding of **3MPA** was assessed by use of two different spectroscopic probes which would individually occupy iron coordination sites. However, no species was detected which could be attributed to monodentate substrate binding, suggesting bidentate coordination is the preferred method.

For clarity each verified structure showing bidentate binding for Av3MDO is shown in Figure 5.1. Each study presented above shows evidence of bidentate coordination, seemingly resolving a topic of contention among the literature (1,2).

5.2 Role of the SHY Motif

Similar to substrate binding, the role of the SHY motif was a key aspect in each chapter presented above. Based on the work presented, Tyr159 of the SHY motif was concluded to

stabilize bound nitric oxide in the (NO/**3MPA**)-bound *Av3MDO* $S=3/2$ species. A similar interaction is observed for the (CN/**3MPA**)-bound $S=1/2$ species presented in chapter 3. Experimental g -values for this species were only able to be replicated when Tyr159 was oriented to donate a hydrogen bond to the cyanide ligand. Results also showed that the variant H157N resulted in Tyr159 shifting to donate a hydrogen bond away from the iron active site. Both cyanide and nitric oxide are bound in the axial position where native substrate O_2 is expected to bind as well. It is possible that Tyr159 stabilizes the activated oxygen intermediate in the native catalytic mechanism or perhaps help facilitate the formation of said intermediate. In Chapter 4, the SHY motif was shown to have a direct influence on the electronic structure of the iron complex. Shifting the Tyr159 hydrogen bond away from the iron complex resulted in increased hyperfine structure concurrent with a shift in electron density. Clearly, the SHY motif plays an important role which has yet to be fully recognized.

5.3 Future Directions

This work has provided substantial evidence of **3MPA** binding to the iron active site of *Av3MDO* through its thiolate and carboxylate groups. It remains to be seen how non-native substrates bind to the active site. Substrates such as cysteamine and ethanethiol are shown to be active but have no carboxyl group to bind in the way of **3MPA** (3). It is important to also determine these non-native substrate's mode of binding as it may lead to insights for the catalytic mechanism. The promiscuous activity of *3MDO* is a major topic of interest among TDO research, and it is still not well understood (2). The next step in probing the unique reactivity of *3MDO* would be to determine how each substrate binds to iron. From there, additional experiments could be performed to help elucidate the mechanism by which *3MDO* proceeds.

The SHY motif's role within the catalytic mechanism is still largely unresolved. The studies above have shown how the Tyr159 donates a hydrogen bond to the axial bound ligand which is indicative of Tyr159's role in stabilizing the ES complex. However, it is not known if the direction of hydrogen bond donation is constant or if there are steps in the mechanism where Tyr159 shifts toward His157. The tyrosine's ability to donate a hydrogen bond either to or away from the iron complex may play an important role in initiating reactivity or gating substrate binding. Future experiments would be aimed to determine the role of the SHY motif during catalysis. This would ideally be investigated by characterizing reactive intermediates by methods such as pre-steady-state kinetics, stopped-flow measurements, and rapid freeze-quench. Characterizing a reactive intermediate through spectroscopic means creates the opportunity for modeling the structure through computational methods as shown within this manuscript.

Figures

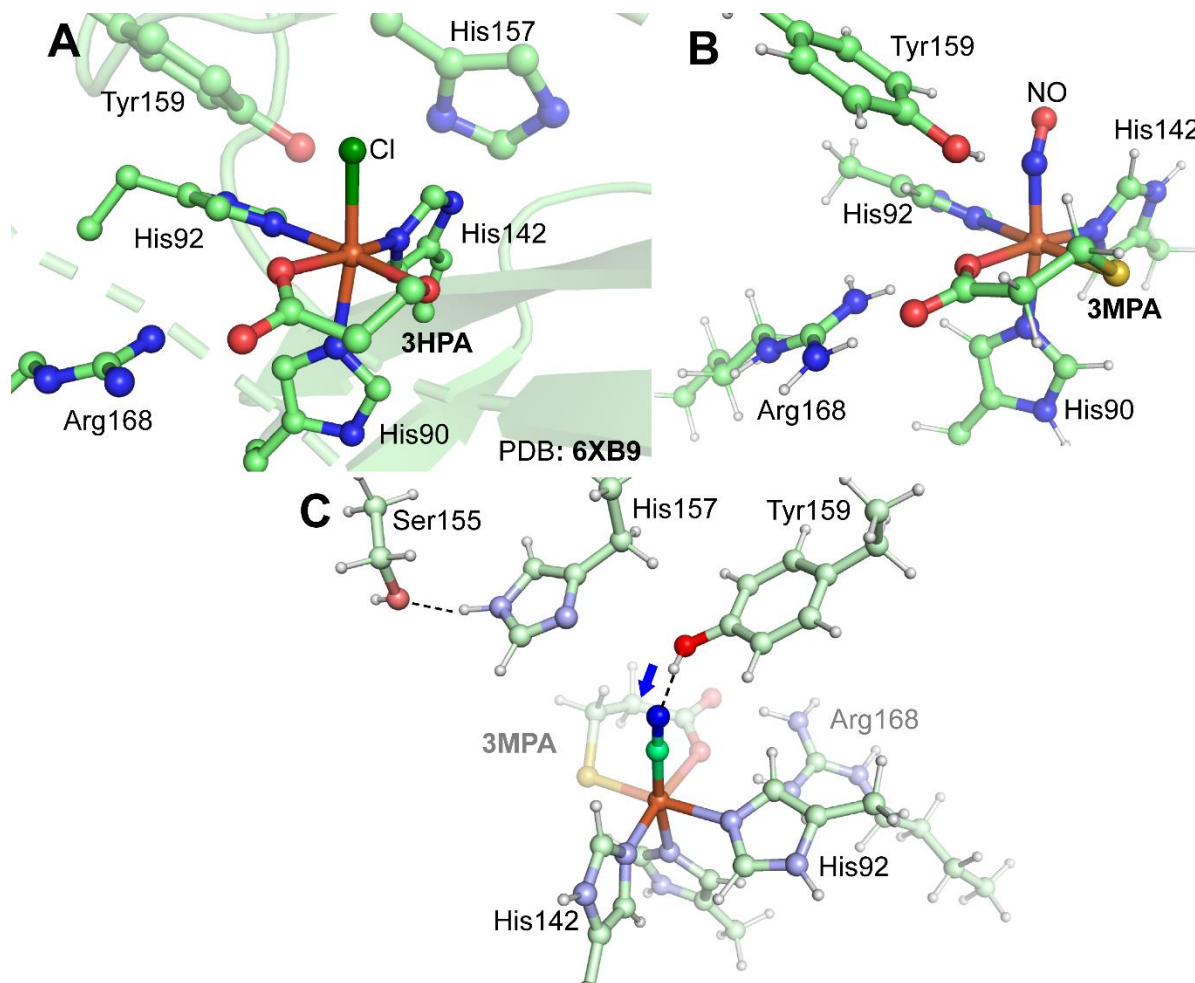


Figure 5.1: Three modes of binding to 3MDO iron seen throughout this dissertation. Panel **A** displays the crystal structure of **3HPA** binding to iron in a bidentate fashion. Panel **B** shows the DFT optimized structure of the (NO/**3MPA**)-bound 3MDO $S = 3/2$ species as seen in Chapter 2. Panel **C** shows the DFT optimized (CN/**3MPA**)-bound 3MDO $S = 1/2$ species with emphasis on the hydrogen bond donation of Tyr159 to the cyanide ligand as shown in Chapter 3.

References

1. Sardar, S., Weitz, A., Hendrich, M. P., and Pierce, B. S. (2019) Outer-Sphere Tyrosine 159 within the 3-Mercaptopropionic Acid Dioxygenase S-H-Y Motif Gates Substrate-Coordination Denticity at the Non-Heme Iron Active Site. *Biochemistry* **58**, 5135-5150
2. Aloi, S., Davies, C. G., Karplus, P. A., Wilbanks, S. M., and Jameson, G. N. L. (2019) Substrate Specificity in Thiol Dioxygenases. *Biochemistry* **58**, 2398-2407
3. Pierce, B. S., Subedi, B. P., Sardar, S., and Crowell, J. K. (2015) The “Gln-Type” Thiol Dioxygenase from *Azotobacter vinelandii* Is a 3-Mercaptopropionic Acid Dioxygenase. *Biochemistry* **54**, 7477-7490